Development and evaluation of interventional bioimplants as cancer cell traps for the treatment of glioblastoma

Rodolfo Molina Peña

THESE DE DOCTORAT

DE
L'UNIVERSITÉ D'ANGERS
SOUS LE SCEAU DE
LA COMUE ANGERS – LE MANS

ECOLE DOCTORALE N° 605
Biologie-Santé
Spécialité : *« Cancérologie »*

Par
« Rodolfo MOLINA PENA »

« Development and evaluation of interventional bioimplants as cancer cell traps for the treatment of glioblastoma »

Thèse présentée et soutenue à « Angers », le « 06/07/2023 »
Unité de recherche : CRCI²NA team 5 (GLIAD)
INSERM U1307 - CNRS U6075
Institut de Biologie en Santé (IBS), CHU Angers

Rapporteurs avant soutenance :

Sylvie FOURNEL	PEX1 HDR, Université de Strasbourg
Thierry VIROLLE	DR2 INSERM HDR, Université Côte d'Azur

Composition du Jury :

Président :	Prénom Nom	Fonction et établissement d'exercice *(à préciser après la soutenance)*
Examinateurs :	Sylvie FOURNEL	PEX1 HDR, Université de Strasbourg
	Thierry VIROLLE	DR2 INSERM HDR, Université Côte d'Azur
	Frédéric TEWES	MCU HDR Université de Poitiers
Directeur de thèse :	Frank BOURY	PU HDR, Université d'Angers
Codirecteur de thèse :	Emmanuel GARCION	DR2 INSERM HDR, Université d'Angers

RÉSUMÉ

La récidive de glioblastome (GB) après résection est aujourd'hui inévitable. Elle se produit dans 2 cm de la cavité de résection en raison de cellules GB infiltrantes. Les défis qui entravent l'efficacité thérapeutique comprennent 1) la résistance associée à l'hétérogénéité des GB et les capacités de survie, de réparation et d'infiltration des cellules ; 2) l'écosystème immunosuppresseur ; et 3) les barrières cérébrales et l'administration sous-optimale de médicaments. Une approche alternative pour cibler directement ces « cellules de guérilla » consiste plutôt à attirer la cible à un leurre en modifiant des éléments de l'écosystème du GB. Autrement dit, en remplaçant la niche de choix des cellules restantes de GB, il pourrait devenir possible de les diriger vers un emplacement contrôlé pour une élimination loco-régionale plus poussée. Ici, l'axe SDF-1α/CXCR4 s'est avéré diriger la migration des cellules U87MG-CXCR4+ humaines. Nous émettons l'hypothèse qu'il pourrait être possible d'attirer les cellules GB dans un piège en implantant un échafaudage à l'intérieur de la cavité de résection. À cette fin, deux nouveaux échafaudages implantables libérant du SDF-1α ont été développés et évalués en tant que pièges à cellules de GB. Le premier échafaudage est une éponge de fibroïne de soie avec de l'acide hyaluronique et de l'héparine, où l'héparine agit comme un agent de complexation pour le SDF-1α. Le second est constitué de SDF-1α nanoprécipité encapsulé dans des nanoparticules de PLGA-PEG intégrées dans une matrice fibreuse de chitosane électrofilé. Dans la présente thèse, la caractérisation et les interactions *in vitro* avec les cellules de GB pour les deux systèmes, ainsi que l'évaluation *in vivo* des éponges ont été réalisées. Les avantages et les inconvénients des deux systèmes sont discutés et des perspectives sur le piégeage des cellules de GB sont présentées.

mots-clés : Piège à tumeur ; Glioblastome ; Maladie résiduelle ; Bioimplants ; Fibroïne de soie ; Acide hyaluronique ; Eponges ; Nanofibres de chitosane ; Nanoparticules de PLGA-PEG ; SDF-1α

ABSTRACT

Glioblastoma (GB) recurrence after resection is today inevitable. It occurs within 2 cm from the resection cavity due to infiltrative GB cells. Challenges that hamper therapeutic efficacy include 1) resistance associated with GB heterogeneity, and cell survival, repairing and infiltration capacities; 2) the immunosuppressive ecosystem; and 3) the brain barriers and sub-optimal drug delivery. An alternative approach to directly targeting those "guerrilla cells" is rather to convey the target to a lure by altering elements of the GB ecosystem. That is, by substituting GB remnant cell's niche of choice, it might become possible to direct them toward a controlled location for further loco-regional elimination. Here, the SDF-1α/CXCR4 axis was found to direct the migration of human U87MG-CXCR4+ cells. We hypothesize that it might be possible to attract GB cells in a trap by implanting a scaffold inside the resection cavity. For this purpose, two novel implantable scaffolds releasing SDF-1α were developed and evaluated as GB cell traps. The first scaffold is a silk fibroin with hyaluronic acid and heparin sponge, where heparin acts as a complexation agent for SDF-1α. The second consists of nano-precipitated SDF-1α encapsulated in PLGA-PEG nanoparticles embedded in an electrospun chitosan fibrous matrix. In the present thesis, the characterization and *in vitro* interactions with GB cells for both systems, and the *in vivo* evaluation of sponges were performed. The advantages and disadvantages of both systems are discussed, and perspectives on the trapping of GB cells are presented.

keywords: Cancer cell trap, Glioblastoma, Residual disease, bioimplants, silk fibroin, hyaluronic acid, sponges, chitosan nanofibers, PLGA-PEG nanoparticles, SDF-1α

Présidence de l'université
40 rue de rennes – BP 73532
49035 Angers cedex
Tél. 02 41 96 23 23 | Fax 02 41 96 23 00

AKNOWLEDGMENTS

As indispensable as the signaling in keeping the route is, many people to whom I am infinitely thankful help me to follow the route providing me with their advice, encouragement, and support. I would like to thank Prof. Frank Boury who recruited me and was my supervisor, and Dr. Emmanuel Garcion, director of the laboratory for the Design and Application of Innovative Loco-regional Treatments in Glioblastoma (GLIAD), and was my co-supervisor, first for allowing me to undertake this project. And secondly, for their very useful guidance, support, and great encouragement during this endeavor.

I took part in the GLIAD lab with great pleasure. Many thanks for the nice welcome from their members. This undoubtedly helped me to integrate myself within the team and advance little by little with my project. I was impressed by the very interesting and high-quality innovative projects the team develops and the nice people I found not only in the lab but also in the SFR Santé (SFR ICAT 4208) at the University of Angers. This is a well-organized structure with different equipment and very professional people in charge, who make a great contribution to the experimental setting and advancement of the projects.

Many thanks to Prof. Christine Jerôme and Dr. Didier Wion, members of my thesis follow-up committee (CSI), for agreeing to read my reports every year and for their useful comments and support. Many thanks to Dr. Carmen Alvarez-Lorenzo and Prof. Christine Jerôme for making the collaborations possible, and for their disposition to discuss and contribute to this project with their expertise in biomaterials fabrication.

This work would not have been possible without the participation of the individual members of the team that was integrated into this project. This includes the work from past doctoral students, specially Mathie Najberg and Muhammad Haji Mansor who worked hard in the conception and design of silk fibroin hyaluronic acid sponges and nanoparticle-containing SDF-1α electrospun fibers, respectively, as alternative systems for SDF-1α release.

Many thanks to Sylvie Avril, Laurence Sindji, and Charlotte Roy, invaluable members of the lab, who from the beginning taught me the functioning of the lab and helped me with setting up experiments. Similarly, many thanks to senior members Anne Clavreul, Claudia Menei, Audrey Rousseau, and Francois Hindre for their kindness, useful comments, and time for discussion. Thanks to Clement Tetau, Mélodie Riaud, Laurence Sindji, Jérôme Roux, Emmanuel Garcion, and Anne Clavreul for their time to discuss their experience working with animal models.

AKNOWLEDGMENTS

I am very grateful to the in-vivo work team that was integrated by Natalia Ferreira, Charlotte Roy, Loris Roncalli, Sylvie Avril, and Emmanuel Garcion. It was a challenge from the beginning to set up experiments, but thanks to fruitful discussions and encouragement we could develop a working model. Special thanks to Natalia Ferreira, who accompanied me all through the last two years of this project and greatly contributed to it providing useful information, discussions, experimental help, and encouragement. I am very pleased to have formed part of this team.

Many thanks to Catherine Guillet, Jerome Cayon, and Lydie Bonneau from the PACEM platform; Rodolphe Perrot, Florence Manero, and Romain Mallet from SCIAM; and Florence Franconi, Laurent Lemaire et Samuel Bonet from the PRISM platform; for their professionalism and availability to discuss and help me perform different cellular, material and imaging analyses. Similarly, thanks to Aurelia Rolland and Fabienne Simonneau from IMAC (SFR Campus du Vegetal) for their time spent using the fluorescence imager and kindness in welcoming Natalia and me. Thanks also to Jerôme Roux, Elodie Guillet, and all the people from Scahu for their help and support with animal experimentation.

Thanks to the external members of the jury of my thesis defense committee: Sylvie Fournel, Thierry Virolle, and Frédéric Tewes, for kindly accepting to read my manuscript and provide feedback on it. And to all members, including Frank Boury and Emmanuel Garcion, for being present on the day of the defense.

I reiterate my thankfulness to all members of the lab and people I collaborated with within the doctoral school, the University of Angers, the CRCI2NA, and the Gliosilk consortium, and people I might have not mentioned (with no intention), for their support and useful discussions. This work would not have been possible without the financial or administrative support, or both, from the French "Ministère de l'Enseignement supérieur, de la recherche et de l'innovation" (MESRI) under the form of a doctoral fellowship, from INSERM, the Gliosilk consortium (French National Research Agency (ANR) under the frame of EuroNanoMed III) and the University of Angers.

Finally, I would like to thank my parents, my family, and friends for your infinite love and support. This work is dedicated to you.

Table of Contents

Chapter 1:
General Introduction

1. General Introduction

1.1. Glioblastoma facts and figures

Box 1

Glioblastoma facts and figures

Central Nervous System (CNS) cancers = 1.3 % of all cancers

Gliomas = 24 % of all CNS cancers

Glioblastoma = 59.2 % of all gliomas

Glioblastoma = 0.18 % of all cancers

Annual Incidence Cases /1 x 10^5 people/year	
EUA	3.26
England	5
Australia	3.4
France	3.34
Korea	0.59
Jordan	0.89

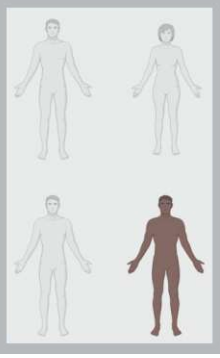

1.6 x more frequent in man

1.9 x more frequent in white people

Glioblastoma (GB) is one of the most complex, deadly, and treatment-resistant cancers ("About Glioblastoma," 2022). In the USA, according to the CBTRUS (Central Brain Tumor Registry of the United States) most recent report (2015 – 2019), GB is the most common malignant Central Nervous System (CNS) histopathology (Ostrom et al., 2022). It is also the most common type of glioma covering 59.2 % of all gliomas, which in turn represent 24 % of all CNS cancers (Ostrom et al., 2022). Although GB constitutes approximately only 0.18 % of all cancers (1.3 % x 0.24 x 0.592, according to data from the USA National Cancer Institute ("Cancer of the Brain and Other Nervous System - Cancer Stat Facts," 2022)), and hence is considered rare cancer, it is today lethal with a median overall survival of 3 months without treatment that increases to 15 months under the standard therapy after diagnosis (Thakkar et al., 2014).

The devasting nature of this cancer is due to its aggressive behavior, given the invasiveness and high proliferative potential of GB cells (Kanu et al., 2009). In addition, it is believed that the cellular heterogeneity of GB contributes to its resistance and recurrence (Kanu et al., 2009). Indeed, GB was also named "glioblastoma multiforme (GBM)", concerning not only the different cellular and tumor microenvironment components but also the broad genetic landscape within the tumor (Holland, 2000). To simplify, nowadays it is only named Glioblastoma (GB) with a specific molecular pattern, including IDH-wild-type-ness, in the WHO's 2021 CNS tumors classification (Louis et al., 2021).

Patients who suffer from GB are diagnosed in an advanced state. Symptoms start with health problems including head pain, periods of seizure, double or blurred vision, loss of appetite, vomiting, changes in mood and personality, and also in the ability to think and learn (Thakkar

et al., 2023). The diagnosis is confirmed by brain magnetic resonance imaging (MRI) (Thakkar et al., 2023). Unfortunately, when it is diagnosed, the tumor has already grown to 5 – 10 cm in the majority of cases (Kanderi and Gupta, 2022). At this time, the typical treatment is based on the standard protocol developed by Stupp et al. (Stupp et al., 2005), which includes the maximal extent resection of the tumor followed by a combination of temozolomide-based chemotherapy and radiotherapy. Despite the median overall survival being increased by 12 months compared to non-treated patients, GB is virtually recurrent and unfortunately lethal with a 5-year survival rate of 6.9 % (Ostrom et al., 2022).

The annual incidence of GB was 3.26 cases per 100 000 population (100k) during 2015 – 2019 in the USA (Ostrom et al., 2022). This figure did not change as compared to the 2013 CBTRUS document that reported 3.19 cases per 100k people (Ostrom et al., 2013). In contrast, in England, a gradual increase from 2.4 to 5 cases per 100k from 1995 to 2015 was reported (Philips et al., 2018). In Australia, the incidence was 3.4 / 100k during the 2000 – 2008 period (Tamimi and Juweid, 2017). In France, the annual incidence of malignant astrocytomas was 2.38 / 100k between 1983 and 1990 (Fleury et al., 1997); and more recently the rate of GB incidence was estimated to be 3.34 / 100k from data between 2006 and 2011 (Darlix et al., 2017). In contrast to an average of 3.28 (0.87) / 100k from all the previous figures, the incidence in countries such as Korea (2005) and Jordan (2012 – 2013) was 0.59 and 0.89 per 100k, respectively (Tamimi and Juweid, 2017).

GB is more common in older adults than in children. For example, in the USA, the adjusted annual incidence rate per 100k people was 0.15, 0.58, and 7.03, for population ages comprising children (0 – 14 years old), adolescents and young adults (15 – 39 years old), and older adults (+40 years old), respectively (Ostrom et al., 2022). However, this comparison is possible before the publication of the 2021 WHO classification, because in this recent classification, pediatric astrocytomas are set apart from GB, which is defined exclusively in adults. On the other hand, the median age of diagnosis was 65, and the highest incidence rate was for the subgroup comprising 75 – 84 age (Ostrom et al., 2022). GB was 1.6-fold more frequent in men than in women, and 1.9 times higher in people who are White than in people who are Black (Ostrom et al., 2022). GB's etiology is unknown, but there is an increased risk in people subjected to previous radiation and those less sensitive to allergy (Tamimi and Juweid, 2017) (See **Box 1** for a summary of facts and figures).

1.2 Overview of the brain as an organ with protective barriers

Human brain development begins in the third week of conception and extends to the third decade of life. The building of this complex organ is a process that requires the production of neural and non-neural components in adequate numbers and at the right location and time (Jiang and Nardelli, 2016). The brain is composed of two main classes of cells: neurons and glia (Gibb and Kovalchuk, 2018). Neurons are electrically active cells that constitute a network of excitatory projection neurons and inhibitory neurons. Glial cells support, modulate and

maintain neural function ("glia" = glue (from Greek)). Mature glial cells can be classified as macroglia or microglia. From the three layers that develop in early embryogenesis (ectoderm, mesoderm, and endoderm), the ectoderm gives origin to neuroectodermal stem cells that in turn give rise to neurons and glial cells. While macroglia are derived from the neuroectodermal layer, microglia originate in the mesodermal layer (Gibb and Kovalchuk, 2018). The three main types of macroglia are astrocytes, oligodendrocytes, and ependymal cells. Astrocytes are more abundant and play a role in the maintenance of neural networks, regulation of neural production, and modulation of neural activity and communication (Jernigan and Stiles, 2017). Oligodendrocytes produce myelin that insulates the axonal fibers lying in the white matter and provides an enhanced speed of neural transmission (Gibb and Kovalchuk, 2018). Ependymal cells localize in the brain's ventricular zone and constitute the choroid plexus in conjunction with the capillary beds. The choroid plexus produces cerebrospinal fluid (CSF) filling the ventricular system (Gibb and Kovalchuk, 2018). The ventricular system provides cushioning and protection of the brain, removal of waste material, and transport of hormones and other substances (Stiles and Jernigan, 2010). On the other hand, microglia monitor signs of infection, clear debris, and participate in the inflammatory and repair responses in brain injuries and disease. Other of their roles include the regulation of cell proliferation and synaptic pruning (Schafer and Stevens, 2015).

There are 7 phases of brain development: 1) cell birth (genesis of neurons and glia); 2) cell migration (toward functional positioning); 3) cell differentiation; 4) cell maturation (growth of cellular components); 5) synaptogenesis; 6) cell death and synaptic pruning (apoptosis and dismantling of unused circuitry); and 7) myelination (Gibb and Kovalchuk, 2018). During this orchestrated process, the endings of the first structure appearing, the neural plate, fuse into the neural tube. This is followed by cellular proliferation, migration, and differentiation, concomitant with an expansion of the brain. The walls of the ventricles are the site of most neuron production. Neurogenesis and brain architecture are largely completed at birth, while maturation of glial cells (astrocytes and oligodendrocytes), synaptogenesis, synapse pruning, and myelination undergo at the postnatal stage (Giedd, 1999). Intrinsic factors (genetics, cell characteristics, biological programs, etc.) and extrinsic factors (environmental clues including molecules such as cytokines, hormones, etc.) direct the process of brain development making an individual's brain unique (Stiles and Jernigan, 2010).

The CNS specializes in forming barriers that maintain the integrity of this system. These specialized neural barriers contain an arrangement of endothelial and other cells that limit the direct connection with the nervous tissue. They include the blood-brain barrier (BBB), the blood-CSF barrier (BCSFB), the meningeal barriers, and the blood-retinal barrier (Barichello et al., 2019; Swanson and McGavern, 2015; Zhang et al., 2022). The blood-brain barrier (BBB) keeps blood cells, neurotoxic molecules, and microorganisms outside the CNS, while it allows the permeation of some solutes in and out of the brain. The BBB is a fundamental component of the neurovascular unit (NVU). The NVU consists of neurons, astrocyte end-feet, microglia, oligodendrocytes, smooth muscle cells, and pericytes lying on the basal lamina, endothelial

cells, and extracellular matrix. The NVU reacts to physiological stimuli regulating permeability, and blood flow and triggering the neuro-immune response to keep the CNS homeostasis (Barichello et al., 2019). The BCSFB is a barrier mainly located in the ventricular system. It is composed of cuboidal epithelial cells contiguous to a layer of ependymal cells lining the ventricles forming the choroid plexus (CP), which main function is to secrete CSF into the ventricles (Swanson and McGavern, 2015). The three meninges (dura mater, arachnoid, and pia mater) constitute a protective layer surrounding the brain (Swanson and McGavern, 2015). The arachnoid barrier consists of endothelial cells lining the fenestrated capillaries of the arachnoid, and this barrier is also a BCSFB (Zhang et al., 2022). There is also a barrier between the CSF in the subarachnoid space and brain parenchyma. This CSF-brain barrier is constituted of pia matter in conjunction with glial cells (Zhang et al., 2022). Because the barriers of the CNS protect it from toxicological and infection insults, they also constitute an impediment to drug delivery into the CNS. Therefore, increasing efforts are directed toward the development of methods of drug delivery into the CNS including the engineering of molecules or vectors for enhanced delivery through systemic administration, the disruption of the barriers, and loco-regional administrations (Djoudi et al., 2022; Zhang et al., 2022) (See **Section 1.11**).

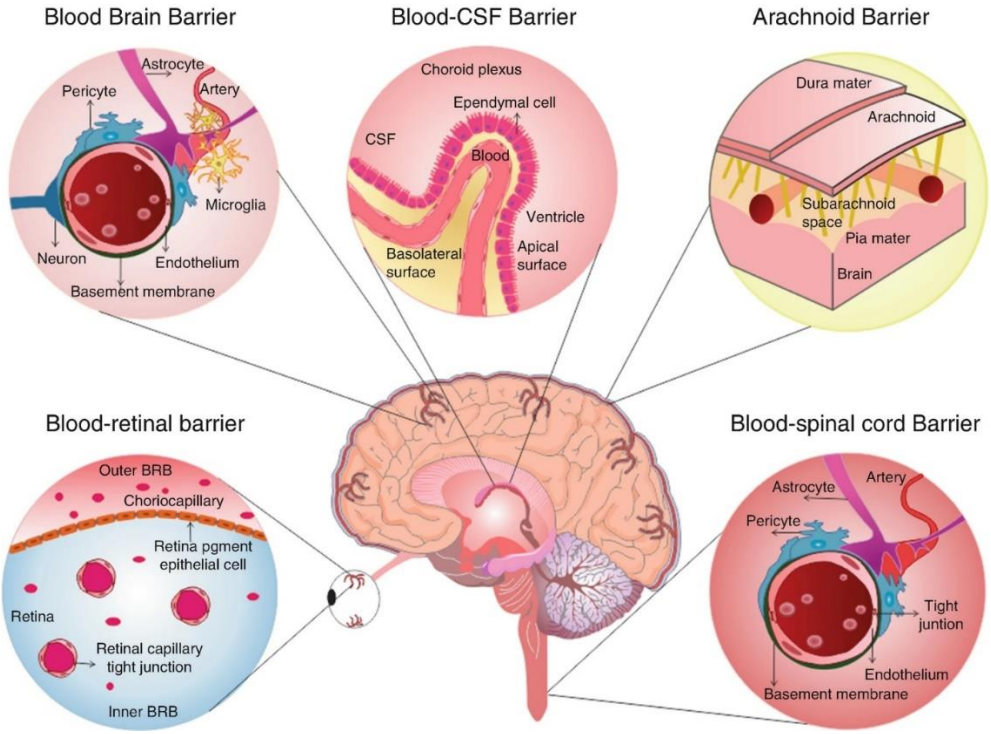

Figure 1.1. The specialized blood-neural barriers. Specialized barriers protect the neural tissue from neurotoxicological substances and help maintain CNS homeostasis. They can be grouped into three major barriers: the blood-brain barrier (BBB), the blood-cerebrospinal fluid barrier (BCSFB) mainly localized in the ventricular zone, but also present in the arachnoid barrier, and the CSF-brain barrier present between the CSF in the subarachnoid space and the brain parenchyma and of which the pia mater takes part. Reproduced from (Barichello et al., 2019) with permission from the publisher.

1.3. Cellular origin and classification of gliomas

In the USA, gliomas represented 24 % of all primary and other CNS tumors and the majority (80.9 %) of CNS malignant tumors (Ostrom et al., 2022). Although the cellular origin of gliomas remains controversial, most *in vivo* data suggest they might come from neural stem cells or progenitor cells that undergo genetic alterations in the course of their lineage differentiation (Alcantara Llaguno and Parada, 2016; Visvader, 2011) (**Fig. 1.2**). As terminal differentiated cells cannot proliferate or have reduced proliferative capacity, the probability of less differentiated cells, which can self-renew by symmetric division and differentiate through asymmetric divisions, is higher for them to accumulate mutations (Poppleton and Gilbertson, 2007; Visvader, 2011). For example, glial fibrillar acidic protein (GFAP) is a marker of both NSCs and post-mitotic astrocytes. It has been shown by GFAP-CreER-induced mutational experiments in mice that the majority of gliomas formed in zones where NSC populations reside. However, around 20 % of gliomas also developed in zones of less proliferation including the brain cortex, giving the possibility that astrocytes also generated gliomas (Chow et al., 2011). However, evidence exists that direct targeting of astrocytes in the brain parenchyma does not form gliomas straightforwardly (Alcantara Llaguno et al., 2009; Jacques et al., 2010). It is then suggested that NSCs and neural progenitors are more susceptible to transformation, but astrocytes cannot be excluded (Zong et al., 2015).

The genetic and cellular heterogeneity found in gliomas suggests the existence of tumor-initiating cells capable of giving rise to different clones. However, the tumor's evolution is probably dictated by developmental patterns, including mutational events, and environmental cues from the tumor microenvironment (Alcantara Llaguno and Parada, 2016). A recent example is shown in the case of ependymomas of type A that develop in the PF and can, in turn, be of subtypes 1 (mesenchymal) and 2 (ciliated) (Gillen et al., 2020). Although the cellular origin of ependymomas is thought to be an early glial progenitor cell called Radial Glia cells (Poppleton and Gilbertson, 2007), ependymomas can show different morphologies according to the predominant cell type. By single-cell RNA profiling, it was shown that both subtypes, mesenchymal and ciliated arose from a common progenitor, but it was the hypoxic environmental cues that directed the transformation into a mesenchymal phenotype 1, whereas type 2 followed the typical differentiation pattern of the progenitor towards ciliated-like cells (Gillen et al., 2020). This underscores the importance of the brain region and microenvironmental factors in the development of the complexity of gliomas.

Overall, gliomas are then classified according to the main histopathological component. For example, astrocytomas contain aberrant astrocyte-like cells. Similarly, gliomas with mostly oligodendrocyte components are called olygodendrocytoma, and gliomas with an ependymal cell-like component are called ependymomas. According to the 2015 – 2019 CBTRUS report, astrocytomas, including GB, represented most gliomas (78 %). At the same time, GB was the most common type of glioma covering 59.2 % of all gliomas. Oligodendrogliomas represented 5.3 %, and ependymomas 6.5 % of all gliomas, respectively (Ostrom et al., 2022).

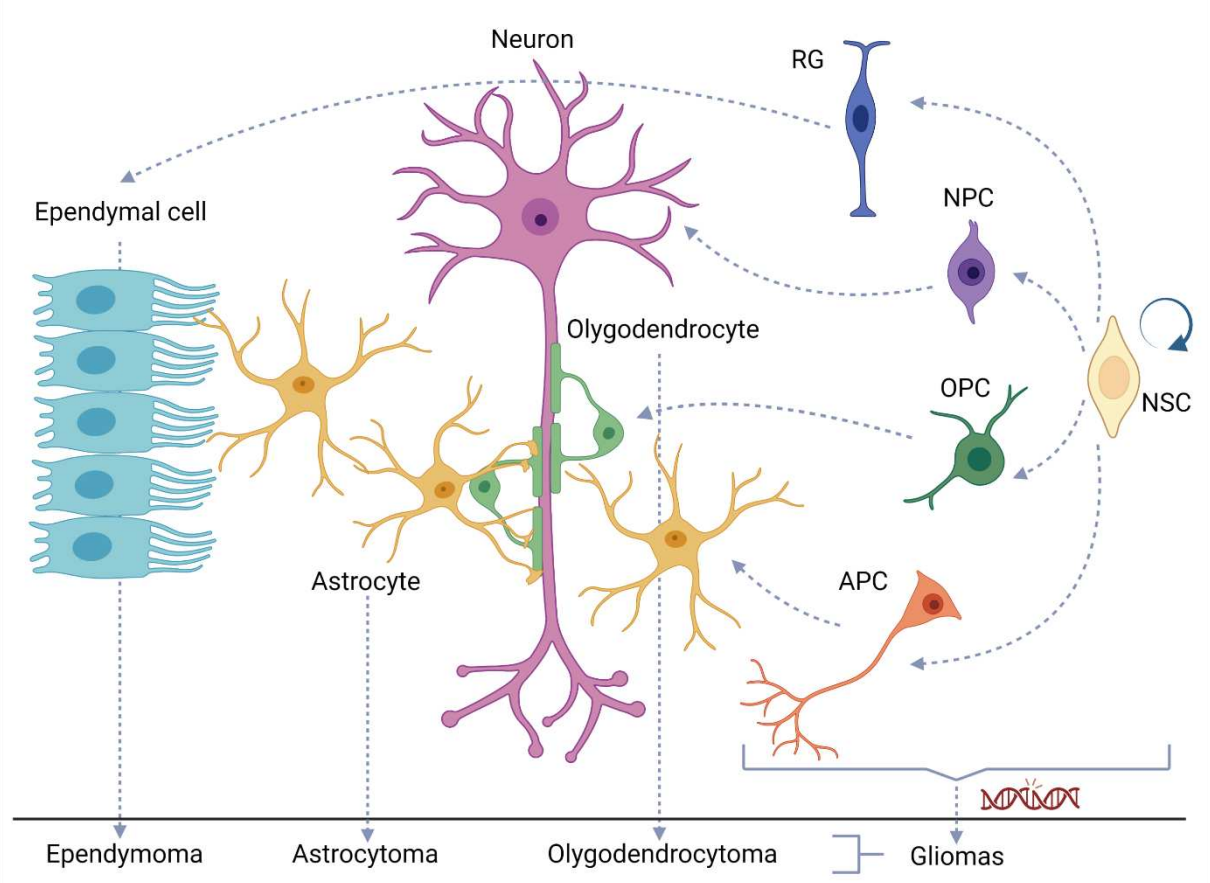

Figure 1.2. Cell lineage of gliomas. The diversity of glial cells and neurons originates from slow-cycling neural stem cells (NSCs) that can self-renew by symmetric divisions and give origin to different committed progenitors throughout asymmetric divisions. Progenitor cells divide more frequently and generate post-mitotic cells such as neurons, astrocytes, oligodendrocytes, and ependymal cells. Because of their lifespan and self-renewal capacity, NSCs and the array of progenitor cells may undergo genetic transformations leading to the accumulation of driver mutations that can generate complex gliomas. Gliomas are named according to the main histopathological component, e.g., astrocytoma containing astrocyte-like cells. Abbreviations stand for NPG = neural progenitor cells, RG = radial glia, OPC = oligodendrocyte progenitor cells, and APC = astrocyte progenitor cells.

1.4. Molecular markers of glioblastoma

Historically, the histological analysis of gliomas has been the first step used in the clinic for their classification. In addition, the molecular events characteristic of gliomas have been studied over the last four decades. This has resulted in the discovery of important molecular markers used for a more specific classification of gliomas, which include:

Isocitrate dehydrogenase (IDH). The new classification considers glioblastoma as IDH wildtype. Mutated IDH grade 4 astrocytoma was considered a secondary GB in the previous classification (**Fig. 1.3**) (Louis et al., 2021). Mutations in the IDH isoforms 1 and 2 (IDH1 and IDH2) induce the preference of the enzyme toward alpha-ketoglutarate instead of isocitrate

(Dang et al., 2009). This increases the accumulation of 2-hydroxyglutarate, an oncometabolite showing blockage of dioxygenase leading to hypermethylation of CpG islands, a phenomenon known as "glioma CpG-island methylator phenotype" (**G-CIMP**) (Noushmehr et al., 2010; Xu et al., 2011). IDH1 and 2 mutations are more frequent in low-grade astrocytomas but favor the progression to IDH-mutated grade 4 astrocytomas (Yan et al., 2009). However, IDH-mutated gliomas are positively correlated with patient survival (Yan et al., 2009). The reduction of glutamate, the precursor of glutathione, also accompanies IDH-mutated gliomas (Nagashima et al., 2016), which suggests an increasing demand on glutathione to mediate the scavenging of oxidative stress-related molecules (McBrayer et al., 2018; Tang et al., 2020). 2-hydroxyglutarate inhibits the BCAT transaminases resulting in a transamination-dependent glutamate biosynthesis defect (McBrayer et al., 2018). Further blockage of the alternative glutamate synthesis pathways by glutaminase inhibition (McBrayer et al., 2018) or the Nrf2/GSH metabolism (Tang et al., 2020) increases apoptosis under oxidative stress.

TERT (Telomerase Reverse Transcriptase). Mutations in this enzyme increase their activity involved in telomeres maintenance, which is essential for the continuity of cell division (Killela et al., 2013). TERT mutations are more frequent in gliomas with enhanced EGFR expression but are inversely correlated with IDH and TP53 mutations (Killela et al., 2013; Nonoguchi et al., 2013).

ATRX (a-thalassemia/mental-retardation-syndrome-X-linked). Located at Xq21.1, ARTX protein allows histone H3.3 to be incorporated into heterochromatin (Schwartzentruber et al., 2012). Mutations in this gene are presumed to cause genomic instability by an alternative and mutually exclusive pathway to telomere lengthening by TERT (Killela et al., 2013). ATRX mutations are more frequent in other astrocytomas than glioblastoma and are found together with IDH1/2 and TP53 mutations (Jiao et al., 2012; Liu et al., 2012).

TP53 (Tumor protein P53). TP53 is a tumor suppressor in regulating cell proliferation, survival, and genomic stability. Mutations in this gene result in protein inactivation which in turn allows for increased proliferation and decreased apoptosis (Djuzenova et al., 2015; Wang et al., 2001). Mutations of this gene are found more frequently in low-grade astrocytomas (Ohgaki and Kleihues, 2007).

EGFR (epidermal growth factor receptor). EGFR is a tyrosine kinase receptor. EGFR amplification and EGFR mutation EGFRvIII lead to constitutive activation of the receptor and the downstream MAPK and PI3K-Akt pathways, enhancing cell division and tumor invasiveness and resistance to RT and chemotherapy (Hatanpaa et al., 2010). EGFR amplification and mutations are more common in IDH-wildtype GB (Louis et al., 2016).

PTEN (Phosphatase and tensin homolog). PTEN is a tumor suppressor gene with protein and lipid phosphatase functions, and that is involved in the regulation of the phosphatidylinositol-3-kinase (PI3K) / Akt pathway. PTEN mutation or deletion results in loss of function and dysregulation of cell proliferation, survival, and migration (Hopkins et al.,

2014; Koul, 2008). PTEN mutations are more frequent in IDH-wildtype glioblastoma (Louis et al., 2016).

Loss of chromosome 9p21. Deletion of this chromosome involves the loss of the CDKN2A gene, which encodes for the cyclin-dependent kinase inhibitor A and AFR, and also the loss of CDKN2B, which encodes the cyclin-dependent kinase 4 inhibitor B (Masui et al., 2016). The resulting loss of these proteins leads to the deregulation of the cell cycle. Loss of CDKN2A/B is more frequent in IDH-mutant astrocytomas (Louis et al., 2021).

Losses on chromosome 10. Loss of the entire chromosome or only the short or long arms were reported (Ohgaki and Kleihues, 2007). PTEN, located in chromosome 10q23.3, is mutated or deleted because of this alteration (Koul, 2008). Losses on chromosome 10 are more frequent in IDH-wildtype glioblastoma (Louis et al., 2021).

Gain of chromosome 7. EGFR is located at chromosome 7p12, therefore this gain results in the amplification of the receptor. The gain of chromosome 7 is a characteristic of IDH-wildtype glioblastoma (Aldape et al., 2015).

Codeletion of chromosome arms 1p and 19q. An unbalanced translocation t(1;19)(q10;p10) results in the loss of heterozygosity (LOH) (Griffin et al., 2006). Although the biological effect remains unclear, the 1p/9q codeletion is a marker of oligodendrogliomas with better prognostic and predictive values (Idbaih and Touat, 2016).

MGMT (O6-methylguanine DNA methyl transferase). This enzyme removes the methyl groups resulting from alkylating agents such as temozolomide. When alkylation is effective, apoptosis is induced, but in the presence of MGMT glioma cells become resistant. Methylation of the DNA promoter of MGMT results in the silencing of the protein. Hence, the methylated status has a prognostic and predictive value compared to the promoter's non-methylated status, resulting in an advantage of approximately 7 months in patients receiving radiotherapy plus temozolomide (Hegi et al., 2005).

CIC. This is the protein homolog of Drosophila capicua, a transcriptional repressor and tumor suppressor-like protein (Bettegowda et al., 2011). Mutations in this gene were observed in 69 % of oligodendrogliomas samples and is a new marker for these tumors in the 2021 WHO CNS tumors classification (Louis et al., 2021).

These are the most used markers for the classification of the most common type of gliomas. According to the 2016 WHO classification, glioblastoma could be classified as primary and secondary GB (Louis et al., 2016) (**Fig. 1.3, left**). Primary or *de novo* GB referred to the spontaneous formation of these tumors in adults, and the main molecular marker was the absence of mutations in IDH (IDH-wild type). Secondary GB, in contrast, developed from gliomas of lower grade (II or III), which harbored IDH mutations as an early event but accumulated additional mutations, including TP53, AXTR loss, CDKN2A/B loss, for example, that eventually lead to GB, with assigned grade IV (Louis et al., 2016).

The new classification, reported in 2021 by the WHO (Louis et al., 2021), attributes the term glioblastoma to diffuse gliomas with an IDH-wildtype gene only (**Fig. 1.3, right**). IDH-mutant gliomas are set apart and classified according to additional molecular markers. For instance, astrocytoma: IDH-mutant, IDH1, IDH2, ATRX, TP53, and CDKN2A/B; and oligodendroglioma: IDH-mutant, and 1p/19q-codeleted, IDH1, IDH2, TERT promoter, CIC, FUBP1, NOTCH1. Pediatric GB is no longer considered as GB but enters a pediatric gliomas category. In addition, the grade is assigned in Arabic numbers, e.g., GB is of grade 4. Finally, the grade is assigned within subtypes of gliomas and grading is not expected to be correlated with prognosis (Louis et al., 2021).

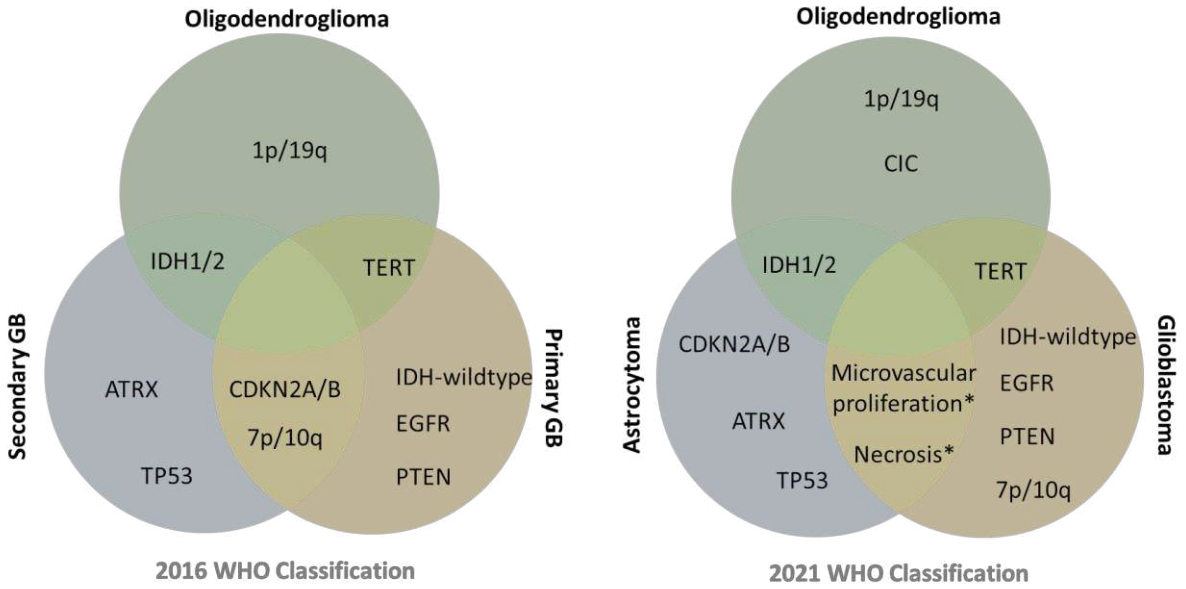

Figure 1.3. Evolution of glioblastoma classification. Classification of glioblastoma (GB) according to the WHO criteria from 2016 (left panel) compared to the 2021 classification (right panel). The main difference is the inclusion of secondary GB as astrocytomas harboring IDH mutations, i.e., GB is now defined as an IDH-wildtype glioma of grade 4, in which any of the mutations shown in the corresponding circumscribed region (right panel, orange circle) are more frequent, in addition to the presence of microvascular proliferation and/or necrosis. Importantly, astrocytomas, which are IDH-mutant, can be of grade 4 even if microvascular proliferation or necrosis (*) are not present but CDKN2A/B mutations are detected. Oligodendrogliomas share with astrocytomas the IDH mutations and with GB the TERT mutation, but they present the 1p/19q codeletion and CIC mutations, highlighting the relevance of the molecular profiling of gliomas. Adapted with data from: (Grochans et al., 2022; Louis et al., 2021, 2016; Reifenberger et al., 2017).

1.5. Cellular and physiological aspects of glioblastoma

Glioblastomas are most commonly diagnosed in the supratentorial region of the brain, which comprehends the frontal, temporal, parietal, and occipital lobes; and are rarely observed in the cerebellum and spinal cord (Adams et al., 2013; Engelhard et al., 2010). GB does not metastasize to regions external to the CNS (Kanu et al., 2009). GB may originate from NSCs or progenitor cells that undergo malignant transformation, as discussed in Section 1.1.2. The natural history of GB includes a series of molecular events such as the gain and loss of chromosomes (+7p/-10q), oncogenic events such as tyrosine kinase receptor constitutive activation and overexpression (e.g., EGFR), and the TERT promoter mutation; and tumor suppressor gene mutations such as in PTEN (**Section 1.4**).

The complexity of glioblastoma not only resides in the variety of molecular events but also in the physiological characteristics of the tumor. For instance, macroscopically, it shows regions of necrosis and hemorrhage; and microscopically, it shows regions of pseudo-palisading necrosis (GB cells form a palisade-like barrier around regions of necrosis), pleomorphic nuclei and cells, and microvascular proliferation (**Fig. 1.4-E**) (Holland, 2000). Indeed, the term "glioblastoma multiforme" introduced initially in 1927 by Bailey and Cushing, who were the first to attempt a classification of gliomas based on histological analysis, was given with regards to the "multiform" nature of glioblastoma, a brain tumor that would arise from primitive precursors of glial cells or "glioblasts" (Bailey and Harvey, 1927).

One of the main characteristics of glioblastoma is the infiltration ability of GB cells. This feature highlights the intrinsic nature of GB as a "diffuse glioma" of the CNS, about the diffusivity of GB into the brain parenchyma. Indeed, GB's recurrence is inevitable today due to the impossibility of removing all GB cells by resectioning the main tumor. While most tumor recurrences occur within 2 cm from the tumor proper considering the edges from the pre-operatory imaging MRI and/or CT scan (Giese et al., 2003), glioma cells can migrate even longer distances and transmigrate to the contralateral hemisphere (Claes et al., 2007). For example, Yamahara et al. 2010 found that most invading cells localize within 6 – 14 mm from the tumor edges (Yamahara et al., 2010). And Gaspar et al. 1992, found that 96 % of recurrent glioblastoma occurred within 2 cm of the MRI- or CT scan-imaged tumor margins (Gaspar et al., 1992). However, although in less proportion than within the main invading zone, Yamahara et al. 2010 also localized invading GB cells farther than 2 cm distances from the main tumor margins (Yamahara et al., 2010); and Gaspar et al. 1992 found that 100 % of recurrences occurred within the 4-cm contouring from the primary tumor edges (Gaspar et al., 1992). Furthermore, Silbergeld and Chicoine obtained GB cells from the normal parenchyma from distances greater than 4 cm from the gross tumor (Silbergeld and Chicoine, 1997). The extreme case is the condition named "*gliomatosis cerebri*" in which glioma cells invade the whole brain (Holland, 2000).

The highly infiltrative nature of GB cells is favored by the composition of the extracellular matrix and existing paths within the brain parenchyma. In 1940, Scherer was the first to

describe the migration patterns of glioma cells within the brain parenchyma (Holland, 2000). These patterns, known as the secondary structures of Scherer (Scherer, 1940), are the following: 1) GB cells can migrate throughout the perivascular space surrounding blood vessels (perivascular satellitosis) containing interstitial fluid and communicating with the cerebrospinal fluid (**Fig. 1.4-A**); 2) glioma cells can surround neurons, a condition called "perineural satellitosis" (**Fig. 1.4-B**). In addition, 3) glioma cells can spread following the white matter tracks of the brain parenchyma organized as fascicles within the *corona radiata* (**Fig. 1.4-D**) and throughout the *corpus callosum* (**Fig. 1.4-F**). This pattern of migration is called "intrafascicular spread". And finally, 4) glioma cells can collect in the subpial space, a condition called "subpial spread" (**Fig. 1.4-C**) (Claes et al., 2007; Holland, 2000; Scherer, 1940).

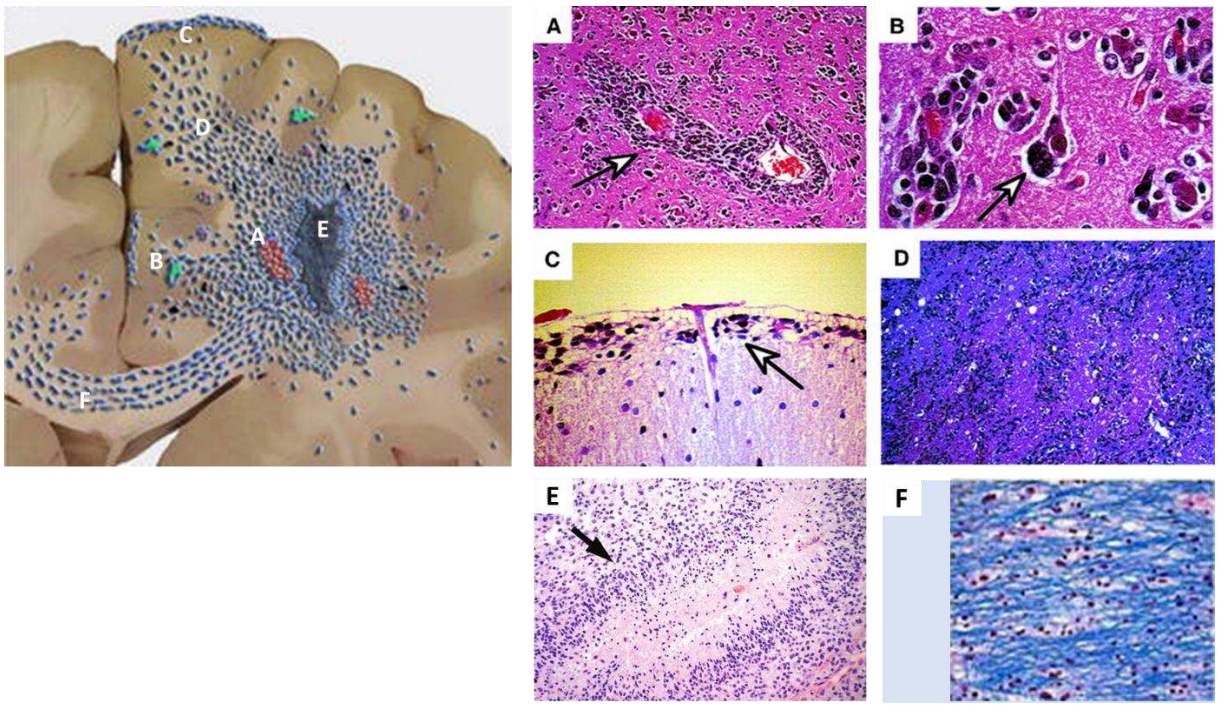

Figure 1.4. Patterns of glioma migration. Glioblastoma is characterized by the high heterogeneity of cells and morphological components containing pseudo-palisading necrosis zones (E) (cells forming a palisade-like barrier around necrotic zones), and zones of microvascular proliferation (A and E, red zones). Glioma cells are highly infiltrative in the brain parenchyma, and they follow defined patterns of migration and spreading known as secondary structures of Scherer: (A) glioma cells can migrate through the perivascular space and appear surrounding blood vessels (perivascular satellitosis), (B) glioma cells can spread around neurons (perineural satellitosis). Furthermore, glioma cells can migrate by using the white matter tracks of the *corona radiata* (D) and *corpus callosum* (F). Glioma cells can also accumulate in the margins of the subpial membrane (C). Left panel and F: Adapted from (Claes et al., 2007) under the CC BY-NC 2.0 license. A – D: reprinted from (Holland, 2000) with permission from the editor, "Copyright (2000) National Academy of Sciences, U.S.A." E: Reprinted from (Rong et al., 2006) by permission of Oxford University Press.

MRI imaging has benefitted the diagnosis of GB and other CNS tumors. The assessment of the disease is determined by the presence of the main tumor mass of about 5 – 10 cm (Urbańska et al., 2014). FLAIR (Fluid attenuated inversion recovery) MRI and administration of a contrast agent such as Gadolinium (Gd) are used to observe with more detail some macroscopic features of the disease, such as the presence of edema, necrosis, and spreading of the disease. For example, it is believed that the diffusivity of gliomas appears as hyper-signals in T2-weighted MRI (Pavlisa et al., 2009) and contrast-enhanced MRI (Rong et al., 2006) depicting zones of edema contouring the main tumor (**Fig. 1.5 A-C white arrows**). Of note is that other zones of infiltration do not always correspond to the zone of edema and tumorigenic cells, although in less proportion, are found in such zones (Yamahara et al., 2010); hence current MRI techniques used in the clinic remain limited for a complete assessment of the real extent of GB cell diffusivity. In contrast, large necrotic zones appear as hypo-signals in an enhanced-contrast T1-weighted MRI image, this is typically seen in the necrotic core of a GB tumor (**Fig. 1.5-C**).

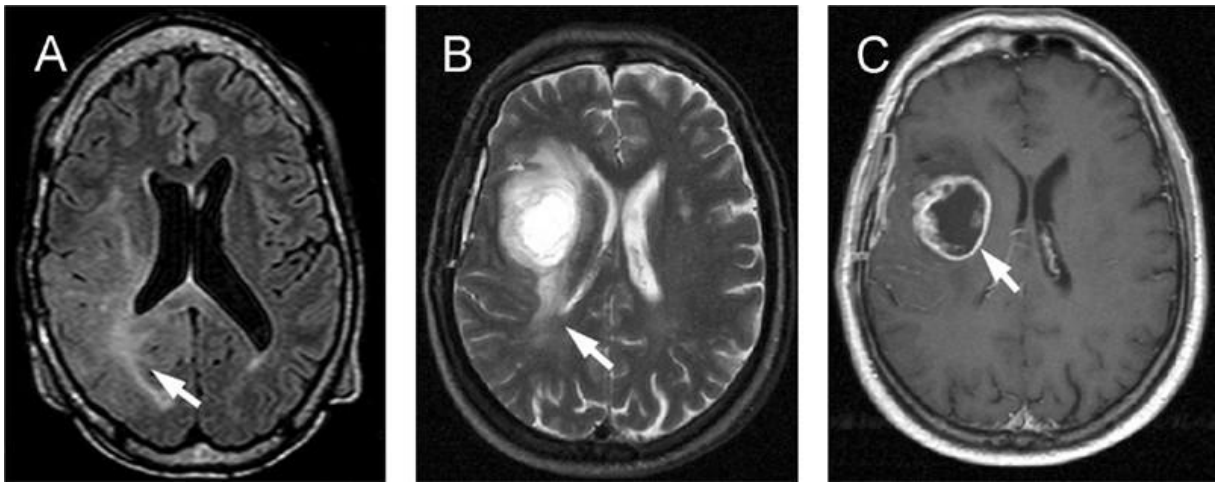

Figure 1.5. Growth patterns of malignant gliomas. A) FLAIR MRI imaging of an anaplastic astrocytoma grade 3 shows vasogenic edema reflecting glioma cells' infiltration (arrow). B) T2-weighted image of a glioblastoma also shows the presence of edema arising from infiltrative GB cells in the periphery of the main tumor mass. T1-weighted enhanced contrast MRI of the same GB showing the presence of a necrotic core and rapidly expanding leading edge of the main tumor. Reprinted from (Rong et al., 2006) with permission from Oxford University Press.

Notwithstanding the limitations of MRI imaging to completely determine the infiltration of GB cells, a combination of different modalities results in complementary information that is useful for both the clinician and researcher. For example, the diffusion pattern observed in the histological analysis shown in **Fig. 1.4-F**, in which glioma cells use the fasciculi of the *corpus callosum* to cross the hemisphere, can be interpreted in a T1-weighted contrast-enhanced MRI

of the condition called "butterfly glioma", because two lobes, one in each brain hemisphere, are observed interconnected by the *corpus callosum* (**Fig. 1.6-a**). In contrast, a T1-weighted MRI without contrast in another patient showed two focal points of GB in different hemispheres (**Fig. 1.6-c**). When contrast was used in a T1-weighted MRI, edema and necrotic centers are revealed, and no suspicion of interconnection between lobes could be implied (**Fig. 1.6-b&d**). However, a T2-weighted MRI suggested that both lobes were communicating via the *corpus callosum* (**Fig. 1.6-e, arrowhead**) (Claes et al., 2007).

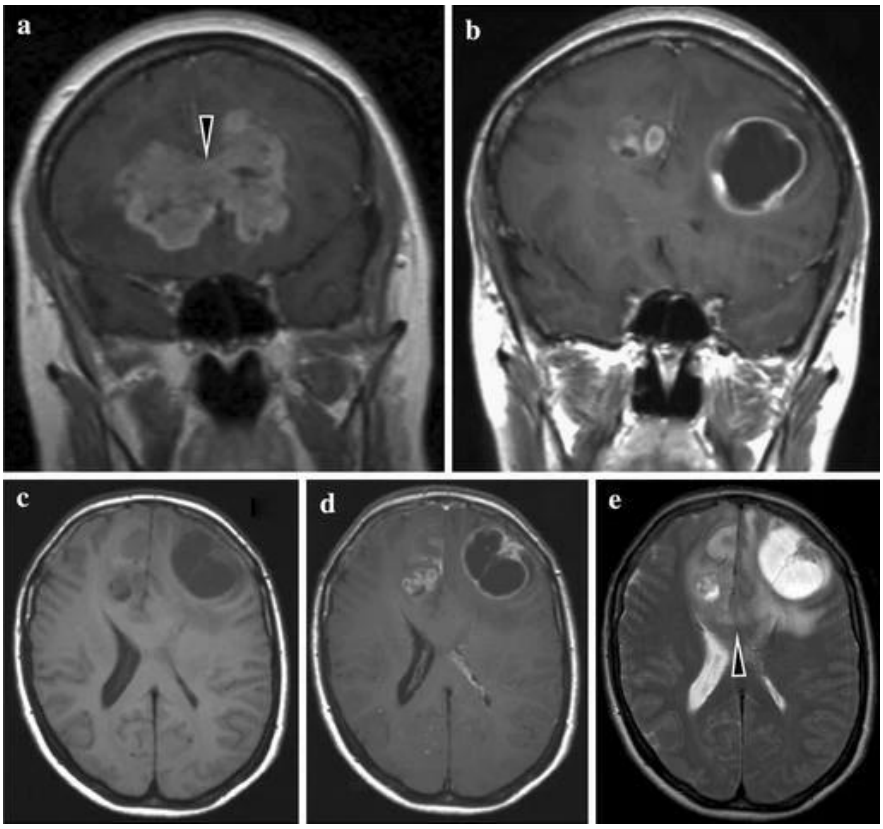

Figure 1.6. Examples of the use of MRI to assess the spreading of glioblastoma. a) T1-weighted MRI with Gadolinium contrast enhancement in a patient with the so-called "butterfly glioblastoma" showing two frontal lobes interconnected via the *corpus callosum*. In another patient (**b-e**), both normal (**c**) and contrast-enhanced (**b and d**) T1 MRIs suggest two independent lesions located in different brain hemispheres. However, a T2-weighted image (**e**) reveals that the *corpus callosum* (arrowhead) interconnected the two lesions. Reprinted from (Claes et al., 2007) under the CC BY-NC 2.0 license.

Box 2. Breakthroughs in GB treatment 1

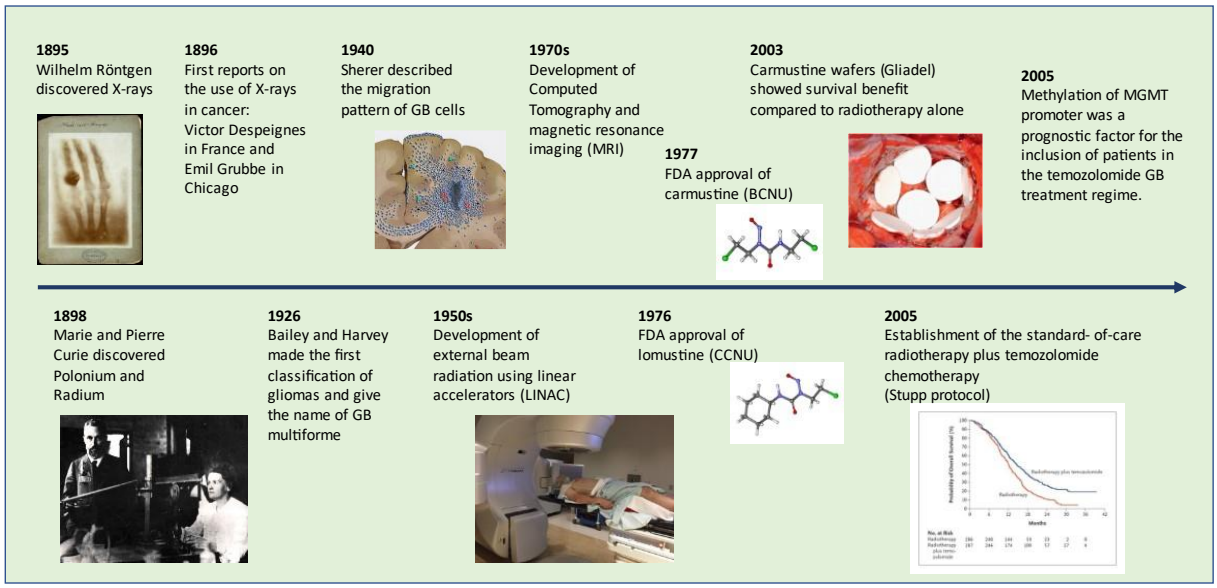

1.6. Current therapeutics approaches

After the discovery of malignant brain tumors, and their further classification (Bailey and Harvey, 1927), surgical resection was the first approach to treat gliomas. The median overall survival of patients was improved by 3 – 4 months to those that were only biopsied (Holland, 2000). The implementation of external beam radiation therapy using linear accelerators in the 1950s (Thwaites et al 2006), and the invention of computed tomography and magnetic resonance imaging in the 1970s, allowed the development of precision radiation therapy in oncology, considering the anatomical aspects of the disease (Connell and Hellman, 2009; Heilbrun et al., 1987). With radiation as adjuvant therapy, the median overall survival was increased for an additional 7 months, making a MOS of around 12 months (Holland, 2000). At the same time, systemic chemotherapy including nitrosoureas, procarbazine, carboplatin, or temozolomide, in addition to radiotherapy were investigated; however, none showed to be effective in double-blind, randomized controlled studies in patients with primary malignant glioma (Westphal et al., 2003), as shown representatively in **Fig. 1.7**.

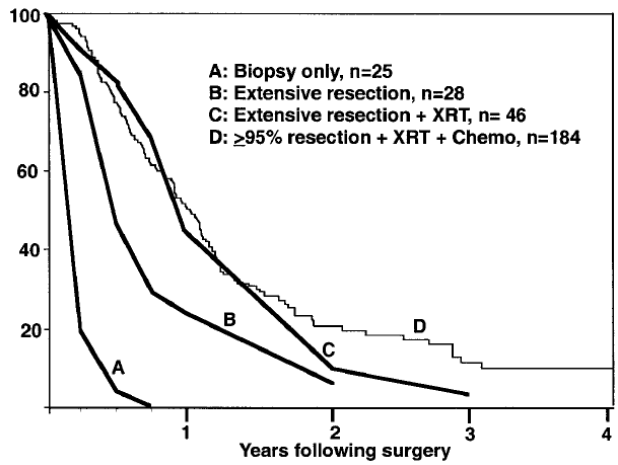

Figure 1.7. Kaplan–Meier survival plots for patients diagnosed with GBM from historical data before the implementation of Stupp's current standard of care. It can be observed no difference in the MOS of patients treated with ration + chemotherapy (curve D) vs radiation alone (curve C). Reprinted from (Holland, 2000) with permission from the PNAS.

Box 2 continued. Breakthroughs in GB treatment 2.

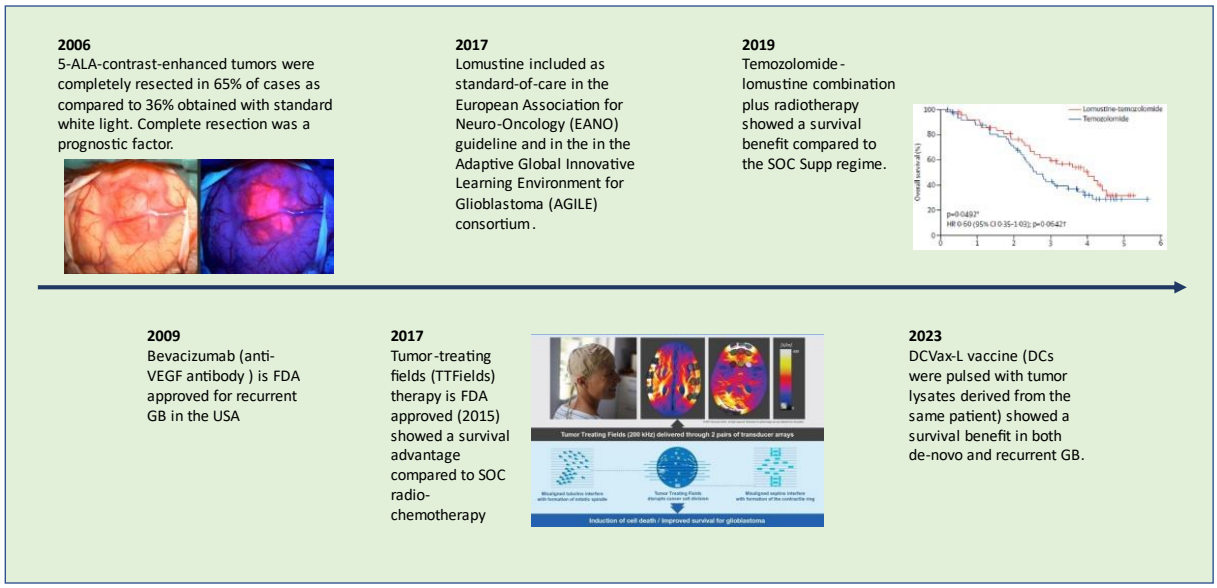

By 2002, nitrosoureas, in particular carmustine (3-bis (2-chloroethyl1)-1-nitrosourea (BCNU)), were frequently used due to the high permeability to the blood-brain barrier. However, their short 20-min half-life and systemic toxicity limit their efficacy. Different polymeric supports were tested to be placed directly in the resection cavities. Among them, Gliadel® wafers made of poly [carboxyphenoxy-propane/sebacic acid] anhydride containing 3.85% carmustine (7.7 mg/implant) were designed for carmustine sustained release over a 2 – 3-week period after placement of up to 8 wafers (61.6 mg carmustine). In a placebo-controlled, multicenter, multinational, double-blind, randomized, prospective phase 3 trial, BCNU wafers as local chemotherapy for malignant glioma at the time of primary surgical resection, showed an improvement in the median overall survival of 13.9 vs 11.6 in patients with placebo wafers (Westphal et al., 2003).

However, these findings were followed shortly after in 2005 by Stupp et al. reporting the results of a phase 3 trial including concomitant and adjuvant temozolomide in addition to radiotherapy. Temozolomide proved efficacy by its synergic effect with radiotherapy by incrementing the MOS from 12 to an average of 15 months. This became and continues to be the standard of care in glioblastoma for almost 2 decades. It consists of surgical removal of the tumor, followed by 60 Gy in 30 fractions of radiotherapy and concomitant daily temozolomide (75 mg/m²), followed by six cycles of maintenance temozolomide (150–200 mg/m² per day on the first 5 days of the 4-week course) (TMZ/RT → TMZ) (Herrlinger et al., 2019; Stupp et al., 2005). At the same time, the development of molecular biology techniques favored the molecular understanding of glioblastoma, and in the same year, Hegi et al. showed that the methylation of the MGMT promoter was a prognostic factor for the inclusion of patients in the temozolomide GB treatment regime (MOS of 21.7 vs 12.7 for methylated vs unmethylated status, respectively) (Hegi et al., 2005).

Exploration of the use of Gliadel® wafers in addition to the standard of care chemo-radiotherapy has not yet been performed in a clinical trial. However, a recent retrospective study of 83 adult patients with newly diagnosed GB that were treated with carmustine wafers in addition to other treatments, showed that the median OS was significantly longer in Stupp regimen patients (19.5 months) as compared with patients with other postoperative treatments (13 months) (Pavlov et al., 2015). Similarly, another retrospective study of 561 patients receiving Gliadel® wafers in addition to other treatments during 2014 – 2017 in Japan, showed that the MOS of those patients ≤ 70 years old receiving the SCO radio-chemotherapy had a MOS of 23.4 months (Iuchi et al., 2022). Although this prognostic association encourages the assessment of the postsurgical combination therapy in a controlled trial, the use of Gliadel® wafers has generated some controversy due to the high rate of post-surgical complications (Bregy et al., 2013; Buonerba et al., 2011; Yeini et al., 2021).

Although a better overall survival is related to the maximal extent of tumor resection (≥ 95%), complete resection is only achievable in a fraction of patients because it is difficult to define the limits of the tumor (Sage et al., 2018). Oral administration of 5-aminolevulinic acid (5-ALA) results in the accumulation of porphyrins in malignant glioma cells. After exposure to UV light, the surgeon can be guided thanks to the contrast offered by the fluorescence as compared to the surrounding white matter. In 2006, a phase 3 trial showed that 5-ALA-contrast-enhanced tumors were completely resected in 65% of cases as compared to 36% obtained with standard white light. Moreover, patients receiving 5-ALA had higher 6-month PFS than the control arm (41% vs 21.1%). Overall survival did not show a significant difference (median of 13.5 vs 15.2 months, hazard ratio 0.82 (0.62–1.07), log-rank p=0.1). However, when stratification was made according to complete resection as assessed by post-operative MRI, the MOS was 17.9 months for patients without residual-enhancing tumors vs 12.9 months for those showing a residual-enhancing tumor (Stummer et al., 2006).

No clinical trial has been reported using 5-ALA for resected tumors plus the standard of care temozolomide radio-chemotherapy. However, a recent phase 3 trial did explore the addition of Gliadel® wafers after 5-ALA-guided tumor resection. Results showed no improvement for patients receiving carmustine wafers compared to enhanced-resected tumors alone (MOS of 14.2 vs 14.3, respectively). In addition, there was a trend of higher incidence of wound infections in patients receiving the wafers (Sage et al., 2018).

In Europe, lomustine, also known as CCNU (chloroethyl-cyclohexyl-nitrosourea), is another nitrosourea that became the standard of care in recurrent GB as bevacizumab is not approved (Weller and Le Rhun, 2020). Studies backing up the use of lomustine in recurrent GB lack formalization of placebo and best standard of care control trials. However, the favorable data of trials using a combination of procarbazine (P), lomustine (C), and vincristine (V), the so-called PCV regime, in low-grade gliomas (2 and 3) in combination with radiotherapy, was probably the reason it was selected as a salvage therapy in recurrent GB. Meanwhile, the activity of PVC therapy had a better response in oligodendrogliomas and IDH-mutant

astrocytomas, and the meaningfulness in IDH-wildtype tumors is still uncertain because the latter were underrepresented in those trials (Weller and Le Rhun, 2020). Different agents have failed to prove an advantage over lomustine alone. For example, in recurrent GB the use of lomustine + bevacizumab in the EORTC 26101 phase 3 clinical trial showed no advantage of the combination therapy with a median overall survival of 9.1 months in the combination group and of 8.6 months in the lomustine monotherapy group (Wick et al., 2017). One possible exception may constitute the use of regorafenib, an oral multi-kinase inhibitor of angiogenic, stromal, and oncogenic receptor tyrosine kinases (Lombardi et al., 2019). In the randomized phase 2 REGOMA trial (n=119), MOS was superior in the regorafenib group (7.4 months) compared to the lomustine group (5.6 months). On the other hand, the use of lomustine in *de novo* GB patients has not been extensively explored apart from two negative trials assessing PVC therapy in the UK (Weller and Le Rhun, 2020). A recent randomized phase 3 trial (CeTeG) in newly diagnosed GB patients with methylated MGMT promoter status has shown encouraging results with prolonged overall survival for the temozolomide-lomustine combination plus radiotherapy (MOS = 48.1 months) over standard-of-care radio-chemotherapy (MOS = 31.4 months), which presumably has the potential to become an alternative to the standard of care (Herrlinger et al., 2019).

Other GB research tackling axes in the last two decades include antiangiogenic therapies, small molecule inhibitors, immunotherapies, and gene therapy. In particular, antiangiogenic therapy was expected to produce significant results due to the high microvascular proliferation observed in GB. Based on radiographic response ranging from 20 – 40 % and a presumed clinical benefit in two uncontrolled trials, antiangiogenic therapy with the anti-VEGF antibody bevacizumab was approved for the treatment of recurrent GB in the USA (Friedman et al., 2009; Kreisl et al., 2009). Despite bevacizumab providing a durable tumor response, it does not provide a survival benefit (Wick et al., 2017). Chinot et al. 2014 published their phase 3 clinical trial results showing that the addition of bevacizumab to the standard of care in de-novo GB patients did not improve overall survival and the rate of adverse effects was higher than in the placebo group (Chinot et al., 2014). There may be an exception for a subgroup of patients with a pro-neural gene-expression signature who may benefit from antiangiogenic therapy as shown in the AVAGlio phase III trial, which includes the use of bevacizumab in addition to standard chemoradiotherapy in newly diagnosed GB patients (Sandmann et al., 2015). However, several phase III trials testing small-molecule inhibitors of VEGF signaling, bevacizumab, and inhibition of integrins by a cyclic peptide (cilengitide) have resulted in negative outcomes (Chinot et al., 2014; Gilbert et al., 2014; Stupp et al., 2014; Wick et al., 2017, 2015).

In IDH-wild-type glioblastomas, EGFRvIII is a driver of epigenetic remodeling promoting tumor growth, and therefore it is a target for therapy. Rindopepimut is a peptide with homology to EGFRvIII designed as a targeted vaccine. Rindopepimut with temozolomide for patients with newly diagnosed EGFRvIII-expressing glioblastoma failed to demonstrate a survival benefit in the ACT IV randomized, double-blind, international phase 3 trial (Weller et al.,

2017). In further exploration, the double-blind randomized ReACT phase II trial in recurrent GB showed a PFS6 of 28% (10/36) of rindopepimut combined with bevacizumab compared to 16% (6/37) for bevacizumab + placebo, and a 3-month advantage on the MOS from 9 to 12 months (Reardon et al., 2020).

In another recent vaccination strategy, DCs were pulsed with tumor lysates derived from the same patient, in the DCVax-L study, a nonrandomized phase 3 trial investigating the use of DCVax-L plus standard of care vs contemporaneous matched external control patients treated with standard of care (Liau et al., 2023). Results showed a MOS of 19.3 vs 16.5 months from randomization, respectively, in *de novo* GB. And a MOS of 13.2 vs 7.8 months from relapse, respectively, in recurrent GB. On average, these results showed a MOS advantage of 3 months and 5 months for newly diagnosed and recurrent GB patients, respectively, relative to the standard of care.

Despite discouraging results of the phase III CheckMate 548 trial of nivolumab (anti-PD-1) therapy as an adjunct to standard chemoradiotherapy in patients with newly diagnosed MGMT-methylated glioblastoma showing no survival improvement as compared to the SOC (Lim et al., 2022), other recent ongoing immunotherapy studies include: the phase III CheckMate 143 trial of nivolumab (anti-PD-1) vs bevacizumab, and of nivolumab with or without Ipilimumab (anti-CTLA-4) in patients with recurrent glioblastoma (NCT02017717); the open-label phase III CheckMate 498 trial assessing the efficacy of nivolumab plus radiotherapy as an alternative to temozolomide plus radiotherapy in patients with newly diagnosed MGMT-unmethylated glioblastoma (NCT02617589); the phase 3 trial testing of ipilimumab and nivolumab plus radiation therapy compared to the standard temozolomide plus radiation therapy for newly diagnosed MGMT unmethylated Gb (NCT04396860); the phase 3 DEN-STEM trail evaluating dendritic cell immunotherapy against cancer stem cells in GB patients receiving standard therapy (NCT03548571). And early clinical trials using CAR T cells targeting EGFRvIII or HER2.

Other approaches consist of the evaluation of physical methods. Tumor-treating fields (TTFields) therapy interferes with GB cell division and organelle assembly by delivering low-intensity alternating electric fields to the tumor (Stupp et al., 2017). In this trial, TTFields were assessed in combination with standard of care (TTFields plus maintenance temozolomide chemotherapy) or temozolomide alone. Results showed a median overall survival of 20.9 months in the TTFields-temozolomide group vs 16.0 months in the temozolomide-alone group, which represents a median overall survival advantage of 5 months relative to the standard treatment (Stupp et al., 2017). This treatment has recently been incorporated as a standard of care (Lukas et al., 2019). Other physical approaches under investigation include: stereotactical photodynamic therapy with 5-aminolevulinic acid (Gliolan®) in recurrent glioblastoma (NOA11) (NCT04469699, phase 2), sonodynamic therapy with ExAblate system (Sonic ALA) (NCT04845919, phase 2), radiodynamic therapy (RDT) with Gliolan® in patients with first recurrence of brain tumor (ALA-RDTinGBM) (NCT05590689, phase 2), and PD L 506 for

stereotactic interstitial photodynamic therapy of newly diagnosed IDH wild-type glioblastoma (NCT03897491, phase 2).

1.7. The combinatorial and systems perspective

Despite the tremendous efforts in the treatment of GB ranging from molecularly targeted therapies, anti-vascular therapies, and recent immunotherapies, the classical treatment modality involving surgery, radio- and chemotherapy, remains the mainstay of therapy. The exploration of different combinatorial therapies is in progress, and this is because individual targeting strategies have failed to provide a survival advantage. This can be explained by the intrinsic complexity of GB, which involves its infiltration ability, cellular heterogeneity, mosaicism of genomic alterations, the clonal selection and the tumor evolution induced by the treatment, and the immunosuppressive microenvironment of the GB ecosystem (Reifenberger et al., 2017). In addition, treatments are constrained by dose-limited toxicities, and pharmacokinetic and pharmacodynamic issues (Le Rhun et al., 2023). Examples of combinatorial therapies showing a positive but limited effect on survival are the recent temozolomide-lomoustine combination for *de novo* GB (Herrlinger et al., 2019), and recent trials involving a dendritic cell vaccine in combination with the standard of care (Liau et al., 2023) (See **Box 2 and Section 1.6**). Current phase 3 trials in progress involve for example the blockage of multiple immune checkpoint inhibitors such as anti-PD-1 plus anti-CTL4 (NCT02017717). Interestingly, in a diffuse GB murine model, it was shown that the synergy between the blockage of an immune checkpoint plus immune-stimulation by multivalent vaccination substantially improved survival as compared to the individual strategies (Liu et al., 2020), which suggests the synergy of this combination strategy. However, this does not mean that all combination strategies will be effective, as shown by many different phase 3 clinical trials combining immunotherapies with the standard of care and anti-angiogenic therapy which have failed as mentioned in the previous section. The optimal therapy will depend on the patient's age, clinical performance status, stage of the tumor, and its molecular biomarkers, from the clinal point of view (Reifenberger et al., 2017). Bioinformatics analysis will aid in the selection of targets as recently demonstrated in a preclinical model where the identification and prioritization of neoantigens were performed in silico (Liu et al., 2020). In addition, exploration of GB as an ecosystem's disease may offer new opportunities linked to the behavior of the GB ecosystem including the possible interactions and evolution of its components according to the stages of treatment.

1.8. The glioblastoma ecosystem

The complexity of GB is linked to its tumor ecosystem. Studying the GB ecosystem has revealed some important features of the disease. For instance, the elucidation of the cell migration patterns of GB cells, which take advantage of the structural paths in the brain parenchyma (**Fig. 1.4, Section 1.5**). Another phenomenon, pseudo-palisading necrosis can be explained by a mechanism that involves the formation of a hypoxic environment due to the leaking aberrant blood vessels that impede the correct irrigation of the tumor (Rong et al., 2006). This unfavorable environment makes cells migrate away from the necrotic zone forming a surrounding barrier of aligned cells known as "pseudo-palisade" GB cells (**Fig. 1.4-E and Fig. 1.8, hypoxic niche**).

The main invasion routes of GB cells are the perivascular space and white matter tracks. Different signals, apart from the structural support provided by the brain parenchyma, are involved in the infiltrative behavior of GB cells. These comprehend chemotaxis gradients including SDF-1α and bradykinin provided within the vasculature; and a variety of axonal guidance molecules including netrins and ephrins within the white matter tracks (De Vleeschouwer and Bergers, 2017). The brain niches providing such signals are of interest as parts of the GB ecosystem promoting the spreading of the cellular glial components. These preinvasion niches are important not only as a target but to understand which pathways are the primary option for GB cell migration away from the primary tumor.

Three main niches can be identified in the GB ecosystem. The vascular/angiogenic, hypoxic, and invasive niches (Barthel et al., 2022). The vascular niche is characterized by pronounced angiogenesis with the secretion of VEGF and accumulation of tumor macrophages. The hypoxic niche resulting from a deficient vasculature induces the expression of HIF and PTEN. The invasive niche contains normal vessel distribution and morphology and connects to the normal brain parenchyma. Particularly, glioma stem cells are found in the perivascular space and their presence is correlated with the expression of CD133 (Barthel et al., 2022). In addition, they are associated with endothelial cells via the CXCR4/SDF1a axis (Cheng et al., 2013).

The GB microenvironment is known to be immunosuppressive. For instance, GB cells secrete M-CSF, TGFβ-1, and IL-10 that modulate macrophages towards an M2 phenotype (Nduom et al., 2015), which is correlated with vessel dilation and malignancy in different human glioma samples (Mathivet et al., 2017). Moreover, normal monocytes exposed to glioma cells acquire properties of myeloid-derived suppressor cells (MDSCs) (Rodrigues et al., 2010). In addition, VEGF inhibits the maturation of dendritic cells, hinders infiltration of effector T-cells, and activates antigen-specific regulatory T cells (Motz and Coukos, 2013); and reactive astrogliosis produces growth factors, cytokines, and metabolites that promote gliomagenesis (De Vleeschouwer and Bergers, 2017).

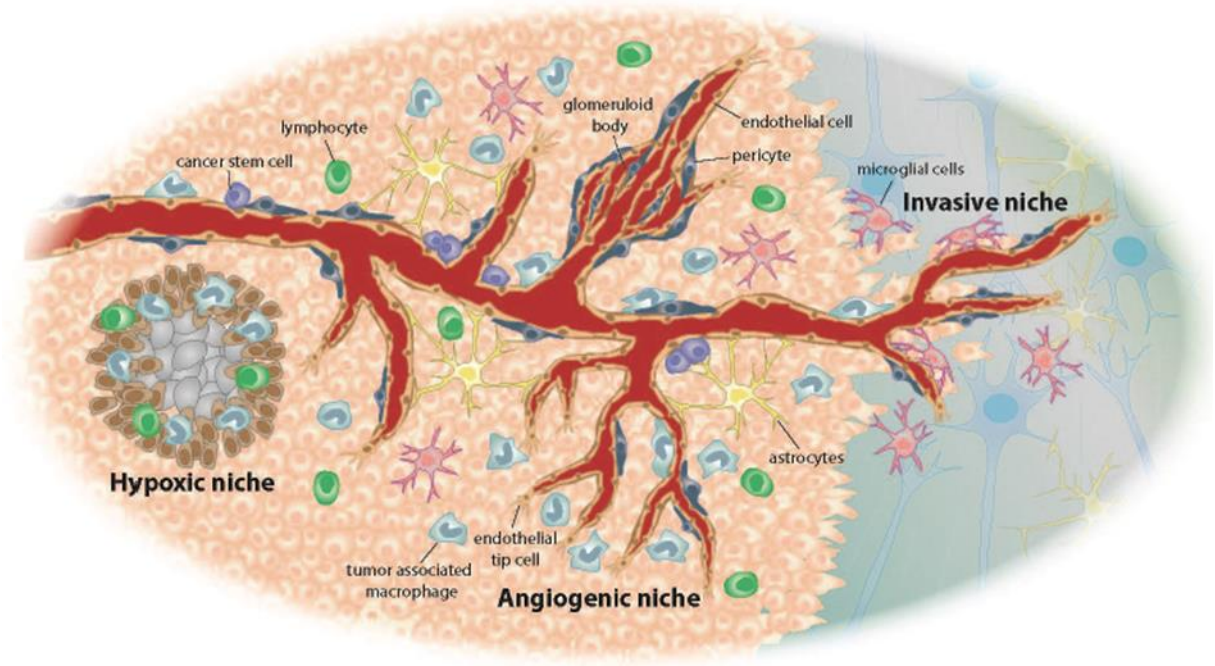

Figure 1.8. The GB ecosystem. Overview of the GB ecosystem comprising different niches including hypoxic, vascular/angiogenic, and invasive niches. Reproduced from (De Vleeschouwer and Bergers, 2017) under the Creative Commons CC BY 4 license.

1.9. Luring the tumor by altering elements of its ecosystem

1.9.1. Evolutionary and ecological traps

An overall understanding of the functioning of the GB ecosystem can help in the development of novel targeting strategies. The knowledge that has been generated at the macroscopic level in natural ecosystems might help comprehend the tumoral counterpart from a complex system perspective. For instance, an evolutionary trap is when a sudden change in the ecosystem cause the organism to prefer new signals without a long-term adaptation (Singer and Parmesan, 2018); that is, the sudden elimination of the new signal in the new context in which the organism is at the expense of its limiting survival abilities, will then die. This maladaptation can be interpreted as the luring of the organism because the trap compromises its survival in the absence of the development of a survival advantage (Robertson and Blumstein, 2019). For example, in a newly documented evolutionary trap, Edith's checkerspot butterflies preferred the exotic plant Plantago (introduced by farmers) over the native Collinsia which was abandoned entirely, because the exotic host plant allowed better survival of offspring. However, when cattle were abruptly removed, the growing grass hid access and cooled Plantago by reducing the microenvironment temperature by 7°C, and hence the thermophilic butterflies suffered local extinction (Singer and Parmesan, 2018) (**Fig. 1.9**).

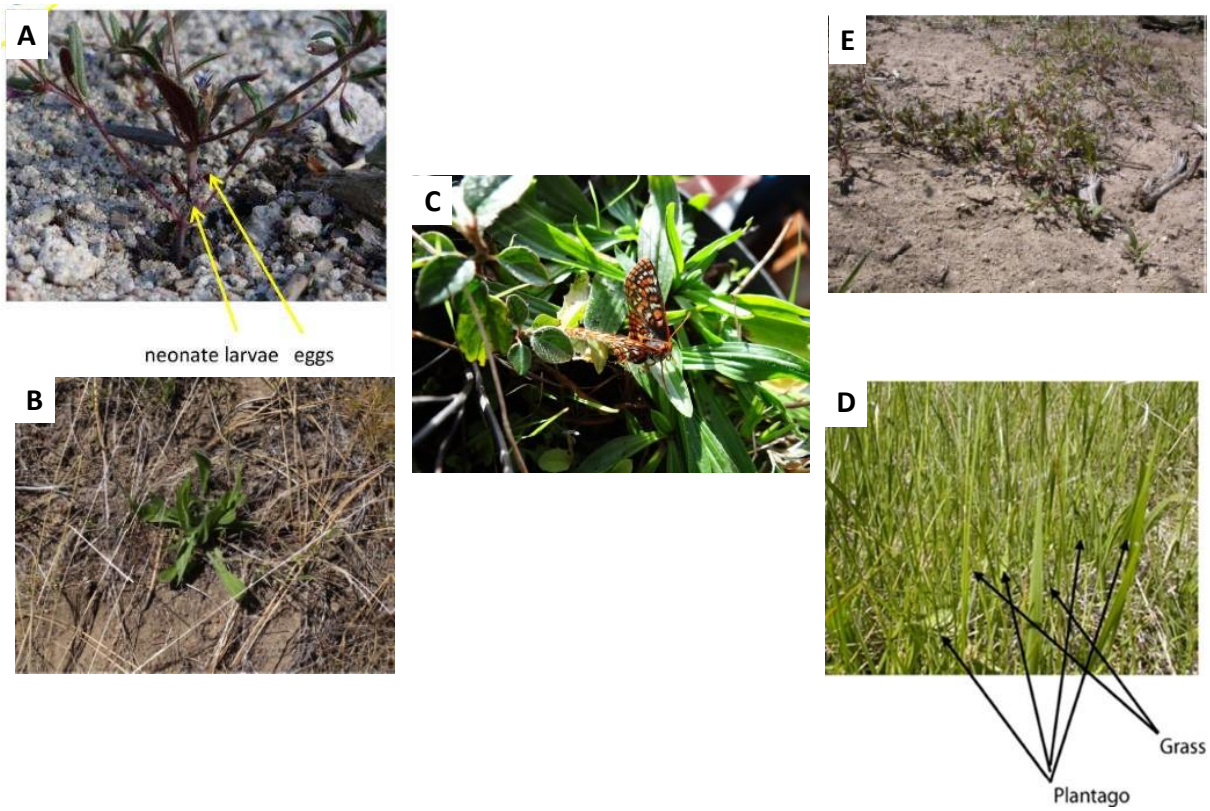

Figure 1.9. Edith's checkerspot butterflies are lured into an evolutionary trap. Edith's checkerspot butterflies used to hatch their eggs on the native Collinsia (A) at the time the exotic Plantago was introduced (B). Butterflies changed preference to Plantago and completely abandoned Collinsia (C). When the cattle were removed cessation of grazing occurred and the Plantago plants were embedded in the growing grass (D). This not only prevented access of butterflies to Plantago but hindered the plants/ground from solar radiation cooling the microenvironment both events causing local extinction of the thermophilic butterfly. In contrast to Plantago the native Collinsa remained unaffected, but hatching did not occur on them. Adapted from (Singer and Parmesan, 2018) with permission from the publisher.

When the trap does not involve a high fitness (producing offspring) on an exotic resource, it is then called an "ecological trap" (Singer and Parmesan, 2018). Examples of this phenomenon are widely seen as herbivores feeding on toxic exotic plants, insects and turtle hatchings migrating towards polluting light, etc. (**Fig. 1.10**). When the ecological trap entails migration or displacement of the species, it may be called "environmental lure" because the trap compromises the survival of the lured animal (Robertson and Blumstein, 2019).

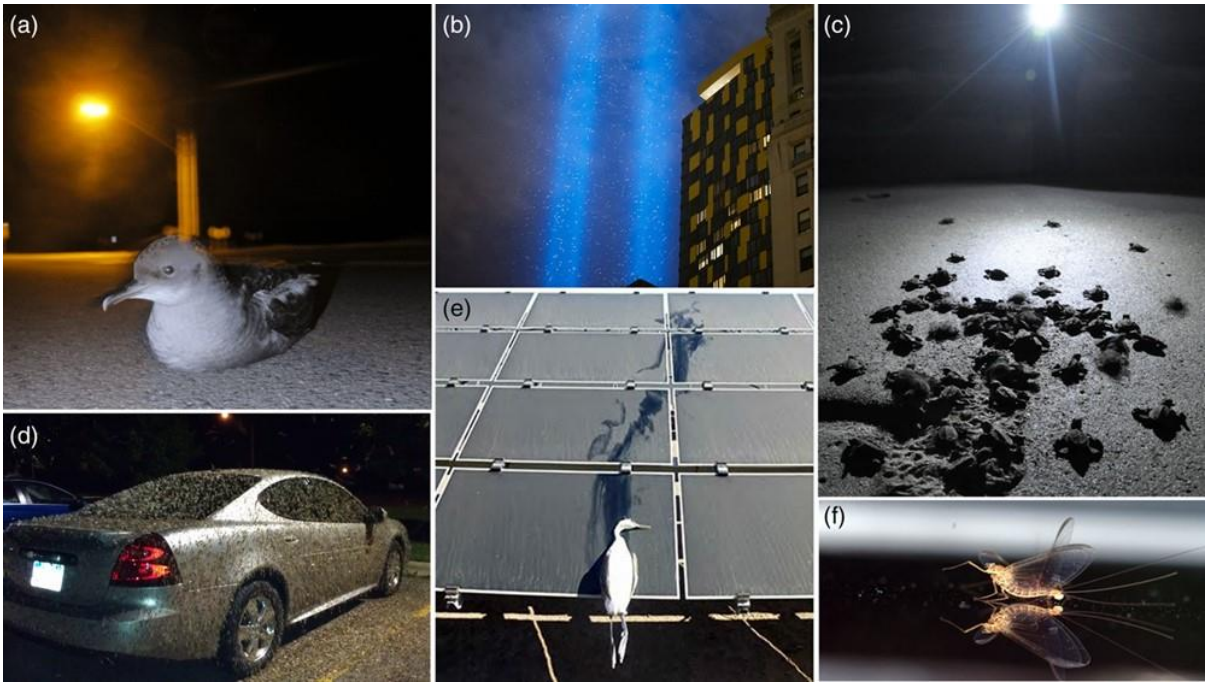

Figure 1.10. Examples of ecological traps. Burrow-nesting petrels (a), migrant birds (b), and turtle nestlings (c) are attracted to artificial light and become disorientated experiencing high mortality rates. Aquatic insects (d & f) and migrating birds are attracted to polarized light from car surfaces, asphalt, and photovoltaic panels. Reproduced from (Robertson and Blumstein, 2019) under a Creative Commons Attribution License.

1.9.2. The translation of an ecological trap into cancer therapy

The translation of an ecological trap to cancer therapy has been recently explored in different types of cancers (Azarin et al., 2015; de la Fuente et al., 2015; Jain et al., 2014; Moreau et al., 2007). By implantation of a biocompatible device within the body it is expected that it can trap cancer cells by luring them into an environment of preference (Najberg et al., 2019; Van Der Sanden et al., 2013). Although this strategy is new, and few traps have been developed, two approaches can be identified for this purpose. One is the use of biomimetic scaffolds resembling the extracellular matrix characteristics of the tissue in context, and the other is the use of scaffolds modulating the local immune environment (**Fig. 1.11**), both functioning as premetastatic niches.

It is known that bone is a predilected site of breast cancer metastasis (Weigelt et al., 2005; Weilbaecher et al., 2011). It is then plausible to develop tissue engineering strategies to recapitulate the site of breast cancer cell migration and homing. Moreau et al. developed a porous silk fibroin scaffold that was functionalized either by coupling with BMP-2 or by pre-seeding with bone marrow stromal cells (BMSC) (Moreau et al., 2007). Scaffolds were implanted subcutaneously in a human breast cancer orthotopic model in mice and human bone grafts were used as controls. Interestingly colonization of scaffolds was observed for both types of functionalization conditions and bone controls, but only in 1-day-culture BMSCs-seeded

and no older cultured scaffolds (4 and 7 weeks). Moreover, the combination of BMP-2/BMSCs had a reduced effectivity (17%). The authors suggested that early signaling may be important for establishing a homing environment. Less differentiated cells would promote cancer metastasis and BMP-2 would attract stem cells promoting the adaptation of the microenvironmental conditions including the vasculature for homing cancer cells (Moreau et al., 2007).

It is also known that extracellular vesicles are involved in the communication between the site of metastasis and the primary tumor (Feng et al., 2019). De la Fuente et al. developed a polyurethane collagen-coated scaffold that was implanted in the intraperitoneal cavity of mice bearing ovarian cancer tumors (de la Fuente et al., 2015). Extracellular vesicles recovered from ascites, which are the site of predilected metastases, were used as the bait signal that was loaded into the scaffolds. The scaffolds were hot spots of cancer metastasis and improved overall survival (de la Fuente et al., 2015). Chemoattractive signals have also been embedded within scaffolds. As breast cancer, prostate cancer metastasizes to bone and one of the mechanisms involves the CXCR4/SDF-1α axis (Sun et al., 2005). In addition, erythropoietin (EPO) has been found to attract prostate cancer cells (Ko et al., 2012). Huang et al. 2020 developed SDF-1α and EPO-loaded HA microparticles that upon subcutaneous injection captured circulating intravenously injected prostate cancer cells and reduced metastases (Huang et al., 2020). Another strategy is related to mechanical and topographic cues resembling the pattern of migration of cancer cells. This strategy was employed by Jain and coworkers to guide and direct glioblastoma cells from the primary tumor to an extracortical killing sink employing a film of aligned fibers placed perpendicular and in direct contact with the GB primary site. Their results showed an enhanced colonization of the conduit containing aligned fibers versus empty conduits, and a reduced tumor volume at the primary site (Jain et al., 2014).

The just enumerated strategies aimed at reproducing certain conditions involving either the structural composition or embedded signals or both, to emulate the site of cancer cell distant colonization. A different strategy takes advantage of the growing knowledge of the interplay between the immune system and the tumor ecosystem. For example, it is known that the sites of cancer cell metastasis are preconditioned by the recruitment of Gr-1^{+}CD11b^{+} myeloid-derived suppressor cells that induce the secretion of diverse cytokines as the medium to communicate distantly to attract cancer cells (Yan et al., 2010). In this regard, Azarin et al. developed a PLG porous scaffold that was implanted in the intraperitoneal fad pads of mice and was colonized by breast cancer cells from the primary tumor site in the mammary fat pads. The premetastatic potential was orchestrated first by the recruitment of immune cells that in turn secreted factors attracting metastatic cells (Azarin et al., 2015). In further exploration of this strategy, scaffold implantation in a model of resected tumors showed reduced metastases to the brain and liver and increased overall survival of mice (Rao et al., 2016). Whether this immunomodulatory strategy could be applied to glioblastoma remains to be explored due to the restricted conditions of the GB tumor microenvironment, i.e., the slow permeation due to BBB and the fact that GB cells do not metastasize out of the brain environment.

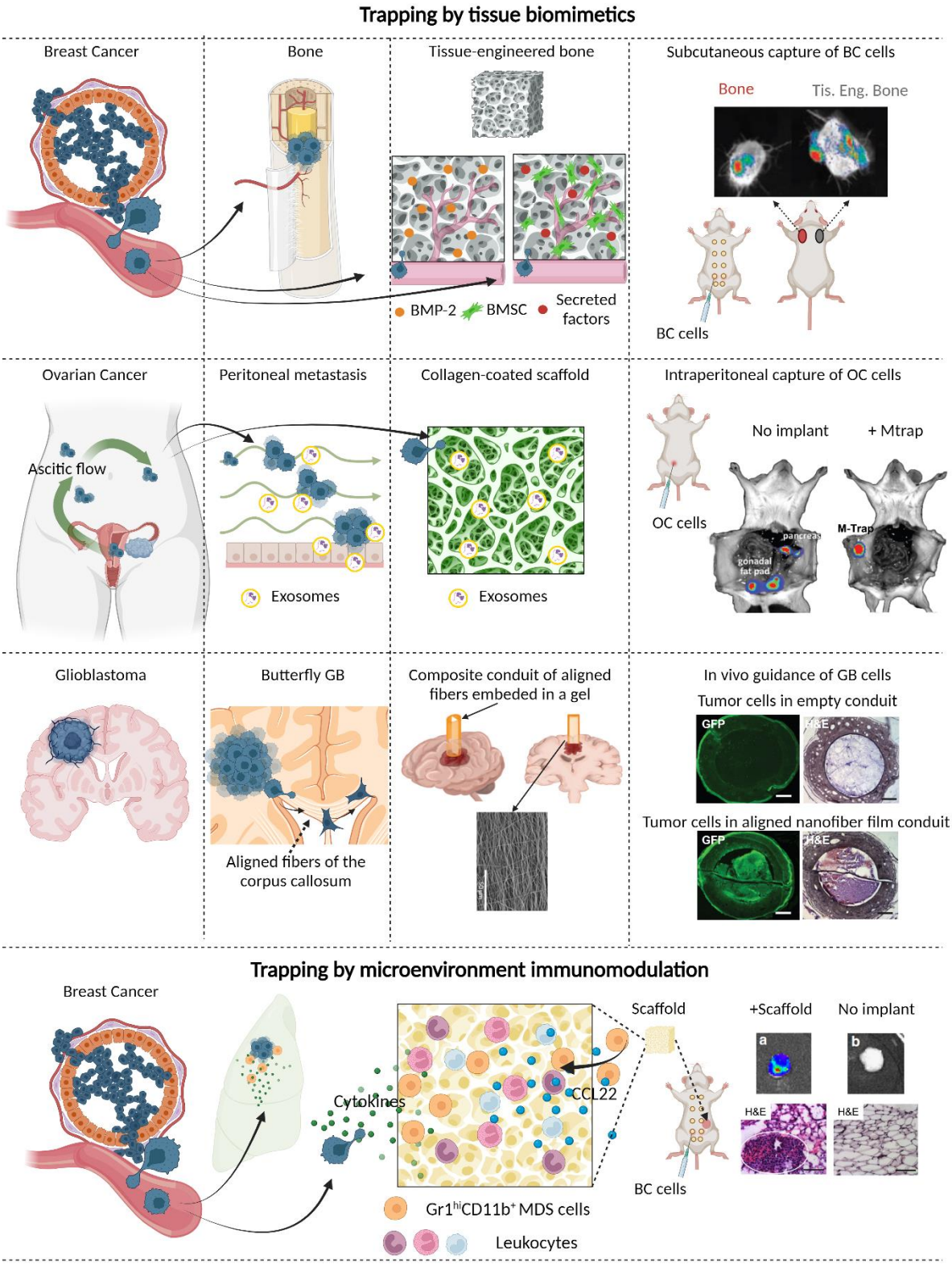

Figure 1.11. Cancer cell trapping strategies. New strategies aiming at the recruitment of cancer cells can be categorized as those reproducing the tissue characteristics of the main metastatic site (tissue biomimetics) using tissue engineering methods, and the second cohort aiming at controlling the immune response of the luring trap to establish a communication with the primary tumor ecosystem and attract cancer cells. From top to bottom: 1) Breast cancer

cells metastasize to bone and tissue-engineered bone containing either bone morphogenic protein-2 (BMP-2) or bone marrow stromal cells (BMSC) precultured for 1 day before s.c. implantation in mice (right panel) (Moreau et al., 2007). 2) Ovarian cancer (OC) can metastasize to the peritoneal cavity. Implantation of an ascites-exosome loaded collagen-coated polyurethane scaffold (so-called M-trap device) in the peritoneal cavity in mice reduces the multifocal to a mono-focal disease where the M-trap device acted as a trap of OC cells (right panel) (de la Fuente et al., 2015). 3) The invasive behavior of glioblastoma (GB) cells taking advantage of one of the Scherer's structures (the aligned fibers of the *corpus callosum*) is recapitulated in a scaffold of aligned PCL fibers placed in direct contact with the primary tumor. Right panel: colonization of the scaffold at 4.5 mm from the primary tumor is observed only in the conduit containing the aligned fibers (Jain et al., 2014). 4) Breast cancer also metastasizes to the lungs by a different mechanism involving immunomodulation of the local environment. Implantation of a PLG scaffold in the peritoneal cavity in mice reproduces in part this mechanism by recruitment of immune cells that secrete the cytokine CCL22 which in turn attracts $Gr\text{-}1^{+}CD11b^{+}$ myeloid-derived suppressor cells (MDSC) found also in the premetastatic niche in the lungs. The secretion of other cytokines is involved in the attraction of breast cancer cells to the immune preconditioned niche. The right panel shows the colonization of the site of implantation containing the scaffold versus mock surgery. (Azarin et al., 2015). Last-column images: adapted with permission from the publishers. Created with Biorender.

1.10. Designing of scaffolds as interactive biodeposits for the trapping of cancer cells

A biodeposit may be defined as an implantable device containing signals rendering the local environment biologically active for a specific purpose. Scaffolds for tissue engineering (TE) might be considered biodeposits aiming at regenerating or recapitulating the tissue of interest. From the instauration of tissue engineering for regenerative medicine, the "scaffold – signals – cells" triad has remained as the conceptual baseline in practice (Murphy et al., 2013), which is also of relevance for application in cancer research (**Fig. 1.12**). To design a biodeposit as a cancer cell trap, the three elements of the TE triad can be incorporated. For this, a scaffold made of biocompatible materials is needed to receive and home cancer cells. Typically, biomaterials for TE are biopolymers that can be self-assembled or cross-linked. The second element to consider comprises the signals that can be embedded within the scaffold matrix. Biochemical signals such as growth factors and cytokines have been incorporated by adsorption or absorption into the polymeric matrix, covalent bonding, or encapsulation in polymeric micro- and nanoparticles followed by incorporation into a polymeric matrix or assembling of individual particles. In terms of structural design, the scaffold's architecture might be developed to meet a particular characteristic, for example, a porous scaffold resembling the highly porous architecture of bone for bone TE, or a conduit with aligned fibers

for the reconstruction of nerves. Importantly, pore sizes > 8 µm are fundamental for cell infiltration (Wolf et al., 2013) and the interconnectivity between pores is indispensable for cell colonization of the scaffold (Annabi et al., 2010). The third element for TE association is constituted by cells. Indeed, cells might be incorporated into the scaffold, or the scaffold engineered for the attraction of a specific cell type. As this is the aim in the case of the cancer cell trap, knowledge of the physiological behavior of the cancer cell type and the interactions between cells and components of the tumor ecosystem including the primary and metastatic tumoral matrix become advantageous. Therefore, in the design of a cancer trap biodeposit, it becomes important to consider the type of cell migration that can be exploited ranging from structural cell guidance such as those cues provided by aligned fibers or channels of TE-nerve-cell conduits, haptotaxis by embedding signals in the matrix structure, chemotaxis by developing a strategy for the controlled release of a chemoattractant, or durotaxis by tunning the mechanical properties of the scaffold featuring a greater stiffness as means of conducting migration in a stiffness gradient. The positive interplay between the TE trinity will allow for the success of the trapping strategy.

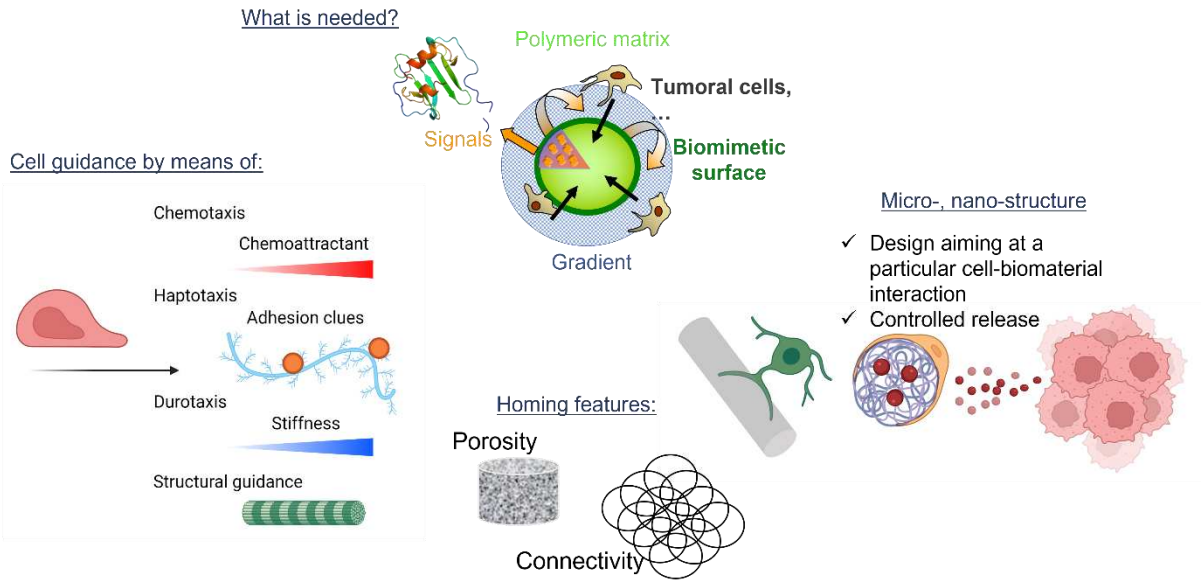

Figure 1.12. Designing aspects for a cancer cell trap. The design of an interactive biodeposit as a cancer cell trap relies on the interplay of the tissue-engineering triad. A scaffold with adequate porosity and interconnectivity to support cell growth, signals that induce the attraction of cancer cells, and previous knowledge of matrix-cell interactions constitute the three elements of the TE triad. Scaffold's micro or nanostructure might be devised to induce cancer cell migration using structural cell guidance, haptotaxis, chemotaxis, durotaxis, or a combination of them. Created with Biorender.

1.10.1. Biomaterials

The main characteristic of biomaterials is that they are biocompatible and hence can be implantable. Biomaterials for tissue engineering can be classified as inorganic biomaterials which comprise metals (e.g., titanium and its alloys) and bioceramics (e.g., calcium phosphates, calcium carbonates, bioactive glasses, alumina, and zirconia), and synthetic and natural biomaterials. Among synthetic materials are polymers such as poly-L-lactide acid (PLLA), polyethylene glycol (PEG), poly-lactic-co-glycolic acid (PLGA), polycaprolactone (PCL), polyurethane (PU), pluronics also known as poloxamers, and poly-acrylates (Collins et al., 2021; Kong et al., 2017; Santoro et al., 2017; Zarrintaj et al., 2020). Natural biomaterials are often extracted from natural resources and comprehend collagen, silk fibroin, chitosan, cellulose, agarose, alginate, glycosaminoglycans (GAGs) such as hyaluronic acid, heparan sulfate, and heparin, and extracellular matrix extracts, also known as decellularized tissues (Brovold et al., 2018; Collins et al., 2021; Joyce et al., 2021) (**Fig. 1.13**).

Hyaluronic acid

Hyaluronic acid or hyaluronan (HA) is present in the extracellular matrix (ECM) of almost all tissues and fluids within the body (Fraser et al., 1997). It is an anionic non-sulfated glycosaminoglycan (GAG) composed of repeating units of D-glucuronic acid and N-acetyl-D-glucosamine linked by a glucuronide β (1→3) bond (**Fig. 1.13**). Its molecular weight ranges between 0.2 and 10 MDa (Passi and Vigetti, 2019). HA is produced by extraction from animal tissues such as chicken combs and from bacteria (Vigetti et al., 2014). The versatility of HA resides in its ability to form hydrogels, a network of polymeric chains that retain water. It also increases the viscosity of the fluids as in the synovial fluid. It is not covalently attached to a protein core but can form aggregates with proteins via the hyaluronic acid-binding protein (HABP) linker. The biological functions of HA include hydration, lubrication of joints, a space-filling capacity, wound healing, and the framework through which cells migrate (Fraser et al., 1997; Passi and Vigetti, 2019; Vigetti et al., 2014). Being a constitutive element of the brain ECM, HA represents an interesting compound in the fabrication of biomimetic scaffolds for brain tissue engineering (see (Djoudi et al., 2022) in **Annexes** for a review).

Sulfated GAGs

Proteoglycans consist of a core protein and one or more chains of glycosaminoglycans (GAGs) covalently linked except for HA (**Fig. 1.14**). GAGs consist of linear polysaccharides containing an amino sugar N-acetylated glucosamine [GlcNAc], N-sulfated glucosamine [GlcNS] or N-acetylgalactosamine [GalNAc], and a uronic acid (glucuronic acid [GlcA] or iduronic acid [IdoA]) or galactose (Gal). The biological activities of proteoglycans are determined by the structure of the protein core and the composition of the glycosaminoglycan chains (Merry et al., 2022).

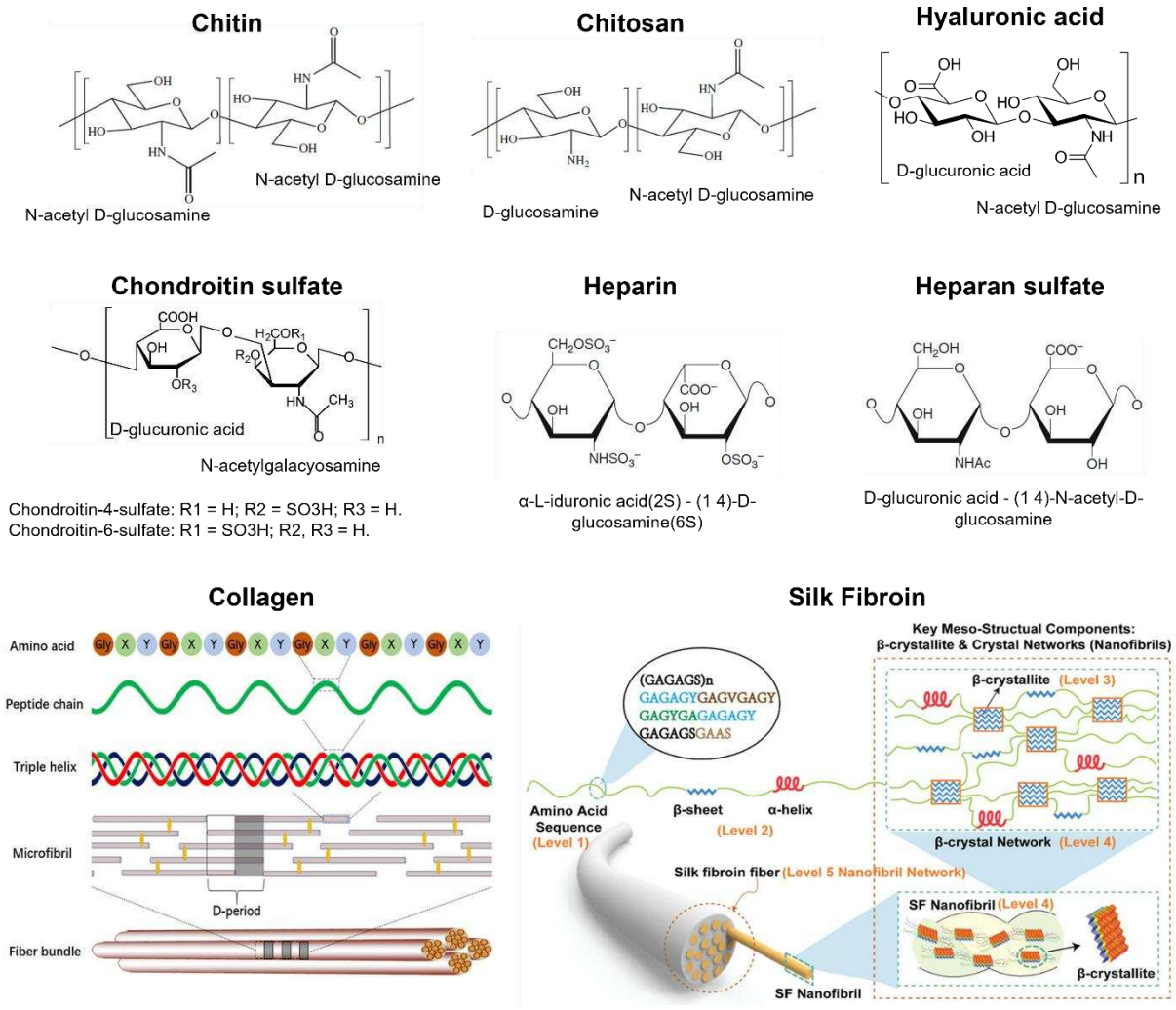

Figure 1.13. Natural biopolymers are used for the fabrication of scaffolds. Chitosan is a polysaccharide derived from chitin. Glycosaminoglycans such as Hyaluronic acid (HA), Chondroitin sulfate, heparan sulfate, and heparin are often incorporated in the fabrication of scaffolds for CNS tissue engineering. Heparin is a sulfated form of heparan sulfate. HA is a non-sulfated GAG. Other macromolecules are frequently used in tissue engineering including collagen and silk fibroin, both of which form fibers, and hence can be used to reproduce the structure of fibrous tissues. Bottom left panel: collagen structure: from Glycine (Gly) – X – Y repeating units, where X and Y represent most often proline and hydroxyproline, to its tridimensional structure featuring complex fibers. Reprinted from (He et al., 2021) under the CC BY 4.0 license. Bottom right panel: different levels of structural organization of silk fibroin (SF): level 1 (primary structure), level 2 (secondary structure α-helix and β-sheet), level 3 (β-crystallite), level 4 (SF nanofibrils-β-crystal network), and level 5 (bundle/network of nanofibrils). Reproduced from (Ma et al., 2020) with permission from the editor.

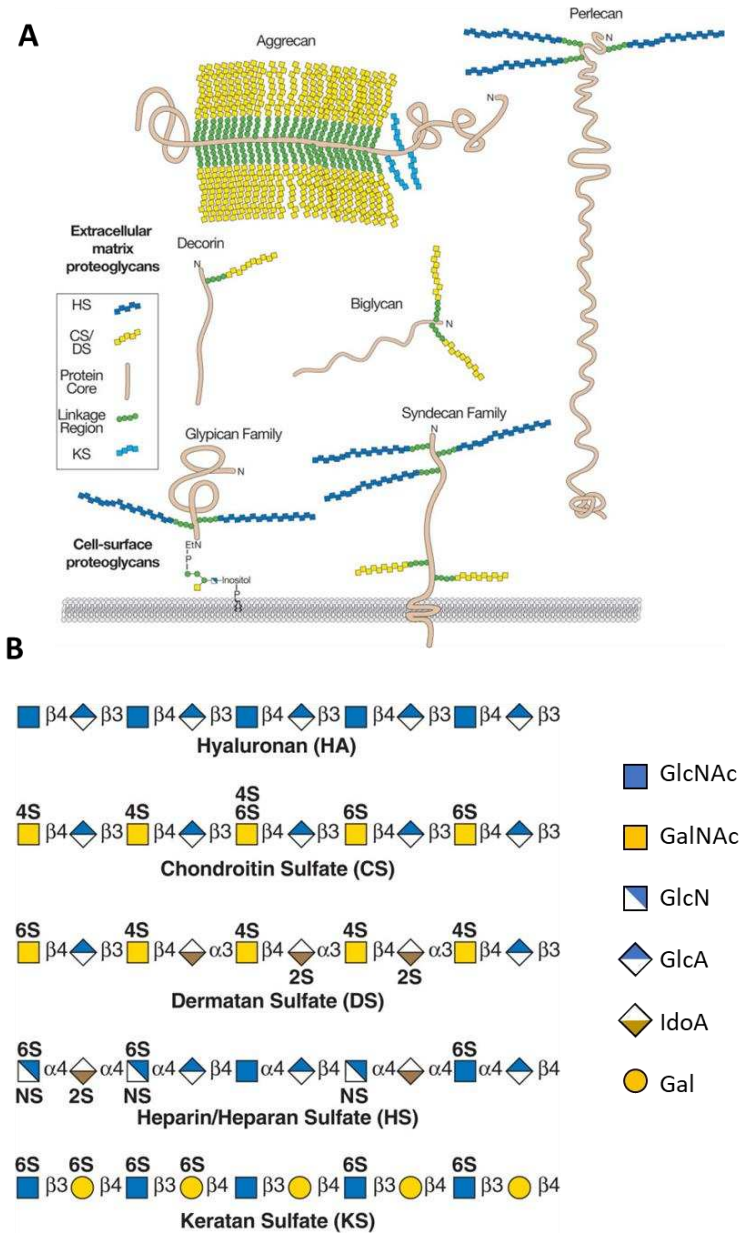

Figure 1.14. Main proteoglycans and glycosaminoglycans (GAGs) in the cell surface and ECM of mammalian cells. A) Proteoglycans are constituted by a core protein (brown) and covalently attached GAGs such as Heparan sulfate (HS), Chondroitin sulfate (CS), Dermatan sulfate (DS), and Keratan sulfate (KS). Hyaluronic acid (HA), a non-sulfated GAG, can also associate (not shown) without forming a covalent bond. B) Examples of glycosaminoglycans (GAGs). GAGs are polysaccharides of 2 or 3 repeating units. Hyaluronic acid is composed of N-acetyl-glucosamine (GlcNac) and Glucoronic acid (GlcA) units. Chondroitin sulfate is composed of N-acetyl-galactosamine (GalNAc) and GlcA. Dermatan sulfate is composed of GalNAc, Gand lcA with intercalation of or iduronic acid (IdoA). Heparan sulfate is constituted of N-acetyl-glucosamine, N-glucosamine, iduronic and glucuronic acid. The degree of sulfation in heparin is greater than in HS. Reproduced from (Merry et al., 2022) under a CC BY-NC-ND 4.0 license.

Chitosan

Chitosan is a polysaccharide composed of (1-4)-2-acetamido-2-deoxy-b-D-glucan (N-acetyl D-glucosamine) and (1-4)-2-amino-2-deoxy-b-D-glucan (D-glucosamine) units (**Fig. 1.13**). It is obtained from the deacetylation of chitin, the natural polymer that is present in the shell of crustaceans, the cuticles of insects, and the walls of mushrooms, green algae, and yeast. The preferred form for biomedical applications is vegetable chitin, which then is hydrolyzed under severe alkaline conditions or enzymatic treatment to obtain chitosan under a controlled purification process (Croisier and Jérôme, 2013).

The deacetylation degree is calculated by the number of D-glucosamine units divided by the total units including both D-glucosamine and N-acetyl D-glucosamine units. Chitosan has a deacetylation degree of >= 60% and its molecular weight varies between 300 and 1000 KDa. MW is directly correlated to viscosity. The greater the MW, the greater the viscosity is. Chitosan has the advantage over chitin that it is soluble in acidic conditions thanks to the protonation of the free amino groups. This offers the possibility of using chitosan for the formulation of different biomedical products ranging from antimycotic solutions, films, hydrogels, porous scaffolds, and fiber mats (Croisier and Jérôme, 2013; Ojeda-Hernández et al., 2020).

Chitosan is a β-glucan and shares the glucosamine unit with other glycosaminoglycans (GAGs) such as hyaluronic acid, heparan sulfate, and heparin (**Fig. 1.13**). Although their properties of GAGs substantially differ according to the presence of the accompanied monomer in the disaccharide structure, the polymeric structure of chitosan seems quite adaptable for applications in brain tissue engineering thanks to its excellent compatibility (Gnavi et al., 2013; Ojeda-Hernández et al., 2020). Interestingly chitosan in physiological conditions holds a positive charge, which can be of interest for biological applications such as complexation with factors and molecules showing a negative charge such as nucleic acids (Croisier and Jérôme, 2013).

Collagen

Collagen is the main structural protein appearing in mammals (Ricard-Blum, 2011). It is the main constituent of the ECM of tissues such as the skin, bone, cartilage, and cornea (Amirrah et al., 2022). Of 28 known forms of collagen, fibrillar collagens (types I, II, III, V, and XI), which provide the structural strength of tissues, are the most prominent in humans. Other types such as collagens IV and VII facilitate the network constitution of basement membranes (Ricard-Blum, 2011). Collagen type I is the most frequently used collagen for tissue engineering and scaffolding for drug delivery (Bettini et al., 2015; Irawan et al., 2018). This is because of its ubiquitous compatibility and clinical approval (Irawan et al., 2018). The molecular composition of collagen type I is rich in the Gly-X-Y sequence where glycine (Gly) repeats every third amino acid and X and Y can be any amino acid, but proline and hydroxyproline are fundamental for collagen properties such as gelation (**Fig. 1.13**). Together

these three amino acids account for more than 50% of the collagen composition. At the structural level, collagen chains appear as α helices that assemble in triads to form a triple helix or tropocollagen. They in turn interact mainly by hydrogen bonding to form microfibrils, which finally assemble into supramolecular complexes of fibrillar collagen whose dimensions depend on the tissue context (Ricard-Blum, 2011).

Silk Fibroin

Silk fibroin is a fibrous protein with a semi-crystalline structure providing stiffness and strength. The use of silk is best known in the textile industry. Different sources are silkworms, spiders, and butterflies (Qi et al., 2017). However, the silk from Bombyx mori has been used for 4 millenniums as a textile component and as a biomaterial for centuries and is still the most utilized source of silk fibers (Porter and Vollrath, 2009; Vepari and Kaplan, 2007). It is recognized as safe for biomedical applications by the FDA (Melke et al., 2016). The raw material contains 20–30% of sericin and 70–80% of silk fibroin (SF). Sericin is a gum-like protein that coats silk fibers that functions to bind SF fibers together. Sericin induces body immunoreaction; therefore, a degumming procedure is necessary. This is accomplished by boiling the raw fibers in a sodium carbonate solution (Koh et al., 2015). The structure of SF consists of a heavy chain (H ~ 390 KDa) and a light chain (L ~26 KDa) bounded at the H-chain C-terminus by a single disulfide bond. Silk fibroin is rich in glycine (43%), alanine (3,0%), and serine (12%). The H-chain's hydrophobic domains consist of Gly-Ala-Gly-Ala-Gly-Ser and Gly-X (X = Ala, Ser or Tyr) repeating units, allowing the formation of stable anti-parallel β-sheet crystallites (**Fig. 1.13**). L-chain's amino acid sequence is non-repetitive, more hydrophilic, and relatively elastic (Inoue et al., 2000; Vepari and Kaplan, 2007). There are 2 types of SF crystal structures (Silk I and II). Silk I belongs to the orthorhombic structure and is metastable appearing as a mixture of α-helices, β-sheets, and random coils. Silk II features the monoclinic system showing as an anti-parallel β-sheet structure that is stabilized by hydrogen bonds. The transition of silk I to II can be achieved by methanol or potassium phosphate treatment (Valluzzi et al., 1999; Wilson et al., 2000).

1.10.2. Delivery systems of therapeutics

Direct administration of drugs can be subjected to different processes of biological and chemical degradation. This process might be overcome with the help of carriers that allow a durable and gradual release of therapeutics. Carriers that have been used for drug delivery include micro and nanoparticles. Special interest has been given to nanoparticles (NPs) in the last few years because they can be engineered to navigate across biological barriers. Different types of NPs have been developed and include polymeric particles (e.g. polymersomes, dendrimers, polymer micelles, and nanospheres), inorganic NPs (e.g. silica NPs, quantum dots, iron oxide NPs, and gold NPs), and lipid-based NPs (e.g. liposomes, lipid NPs such as micelles, and emulsions) (**Fig. 1.15-A**) (Mitchell et al., 2021). The selection depends first on the application and then on 1) the target, 2) the stability of the particles within the body, 3) the stability of the drug within the particles, and 4) the releasing profile. Biological-derived or inspired NPs have also been investigated and include cell-derived extracellular vesicles and micro-organism-derived oncolytic viruses, virus-like particles and bacterial minicells (Briolay et al., 2021).

Another form of device that can carry active pharmaceutical ingredients (API) is scaffolds. They can be classified as hydrogels, solid porous scaffolds (such as sponges, wafers, and rigid matrices), and fibers (e.g., electrospun fibers). (**Fig. 1.15-B**). APIs can be adsorbed onto the surface of the matrix walls or fibers, or crosslinked. Moreover, NPs loaded with APIs can be incorporated into the matrix of the scaffold, to create a hybrid system, either by adsorption, embedding/entrapping into the polymer matrix, or crosslinking (**Fig. 1.15-C**) (Onaciu et al., 2019; Shin et al., 2021; Szentivanyi et al., 2011; Yoo et al., 2009).

Enhanced API delivery is an important feature often searched to attain the site of biological relevance. This aspect includes the crossing of biological barriers, adequate biodistribution, stability of the system, and adequate releasing profile. Scaffolds for drug delivery offer an opportunity to bypass biological barriers by implantation as drug delivery systems (DDS) at the site of intervention. This approach results interesting in CNS diseases to cross the BBB. On the other hand, NPs can be surface engineered to attain a target by providing their surface with properties that allow better-intended interaction with biological barriers, matrices, or cells. The design parameters comprise 1) the architecture of the NPs (size, shape, charge), 2) surface and material properties (PEGylation, cell coating, self peptides), and 3) targeting features (vectorization with for example carbohydrates, antibodies, receptors, vitamins, aptamers) (**Fig. 1.15-D**) (Mitchell et al., 2021). NPs can also be designed to react to endogenous and exogenous stimuli. Endogenous stimuli include microenvironment properties (acidic, hypoxic, etc.). Exogenous stimuli include physical signals such as light and sound.

In the context of brain tumor treatment, recent developments show the use of NPs, hydrogels, hybrid systems including micro-/nano- particles and hydrogels, and, to a lesser extent, fibers, as shown in **Table 1.1.** Novel strategies include the use of NPs and extracellular vesicles decorated with the RGD (Arg-Gly-Asp) peptide for enhanced systemic administration.

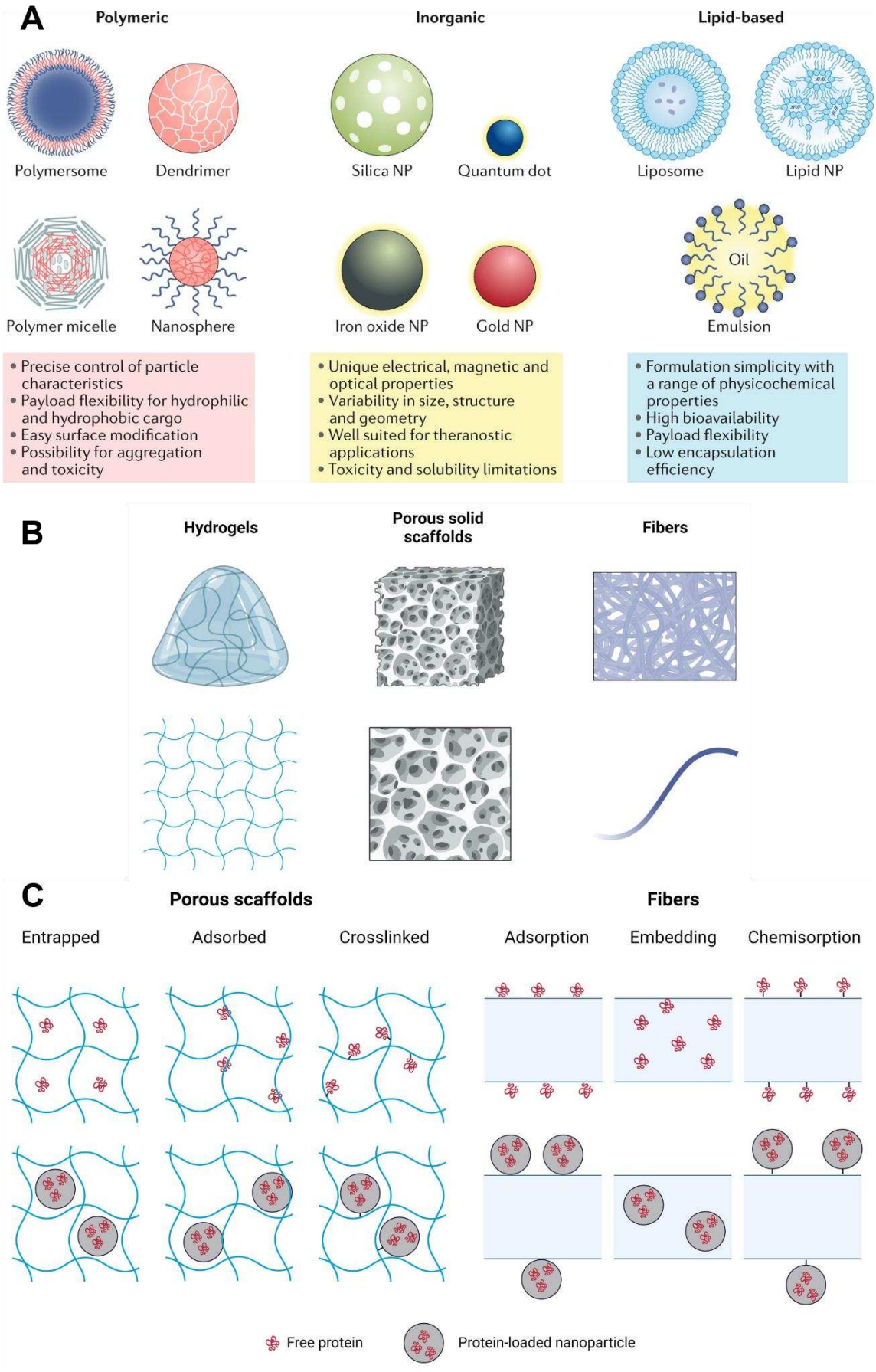

Figure 1.15. Examples of drug delivery systems. (Caption on the next page).

Figure 1.15. (Previous page). Examples of drug delivery systems. A) Different types of nanoparticles (NPs) based on polymeric, inorganic, or lipid-based materials. Reproduced with permission from (Mitchell et al., 2021). B) Different types of scaffolds as drug-loading matrices for the release of active pharmaceutical ingredients (APIs). C) Loading of proteins or protein-loaded NPs into scaffolds can be achieved by adsorption, entrapping/embedding, or crosslinking (Onaciu et al., 2019; Shin et al., 2021; Szentivanyi et al., 2011; Yoo et al., 2009).

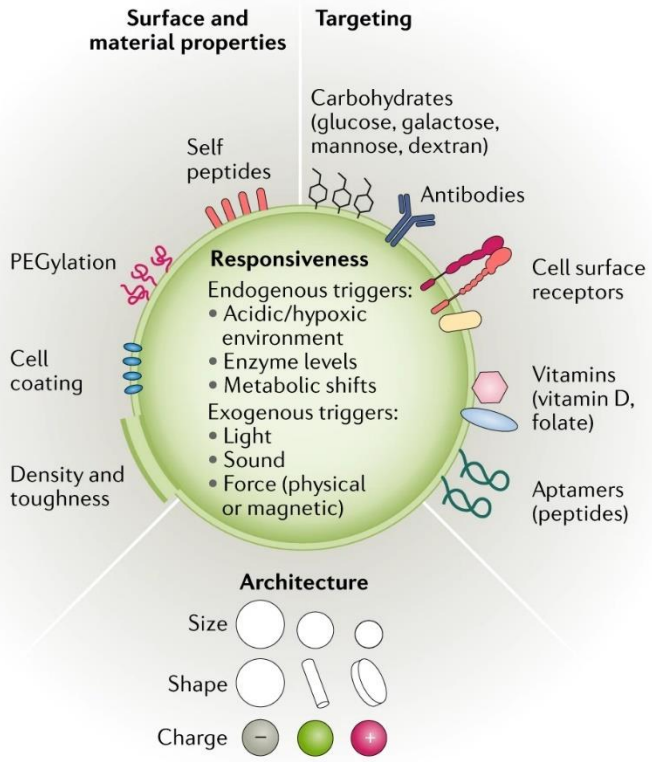

Figure 1.15-D. Examples of drug delivery systems (continued). Engineering of nanoparticles (NPs) by the design of their 1) architecture, 2) surface and material properties, and 3) vectorization agent to reach the target. NPs can be designed to respond to endogenous or exogenous stimuli. Reproduced with permission from (Mitchell et al., 2021).

The RGD peptide allows the interaction with $\alpha_v\beta_3$ integrin, which is overexpressed in endothelial and cancer cells of GB (Ellert-Miklaszewska et al., 2020). The internalization of nanobodies via RGD is thanks to a process of transcytosis (Gregory et al., 2020). Interestingly, the use of a short-burst radiation improves the delivery of nanobodies into brain tumors by a tumor-associated macrophage (TAM)-dependent fashion (Tian et al., 2022). Other innovative developments include the use of lipid nanocapsules containing ^{188}Re and functionalized with an anti-CXCR4 blocking antibody locally administered by convection enhanced delivery (CED) (Séhédic et al., 2017). There is also increased interest in locally administered responsive gels (e.g., to temperature or radiation) containing NPs for the controlled delivery of loco-regional therapeutics (Bouché et al., 2021; Gherardini et al., 2023) (**Table 1.1**).

Table 1.1. Examples of drug delivery systems for brain tumors

System	Composition	Agent	Admin.	Outcome	Ref.
NPs	PLGA nanoparticles overcoated with poloxamer 188	Doxorubicin		*In vitro* on U87MG cells.	(Malinovskaya et al., 2017)
NPs	PLGA NPs functionalized with an OX26 type monoclonal antibody for transferrin receptor	Temozolo-mide		*In vitro* on U87MG and U215 cells.	(Ramalho et al., 2018)
NPs	Polyethylene glycol (PEG) modified and chitosan-coated PLGA NPs	R-flurbiprofen and paclitaxel	Systemic	Reduced tumor *in vivo* in RG2 model in Wistar rats.	(Caban-Toktas et al., 2020)
NPs	Silk fibroin	Indocyanine green	Systemic	Reduction in the tumor volume after IR irradiation of C6 glioma-bearing subcutaneous xenografts in nude mice.	(Xu et al., 2018)
NPs	PLGA/PEG-PLGA	SDF-1α		*In vitro* attraction of U87MG cells.	(Haji Mansor et al., 2018)
NPs	Chitosan-Alginate	SDF-1α		*In vitro* attraction of F98 cells.	(Gascon et al., 2020)
NPs	Synthetic protein nanoparticles (SPNPs) coated with the transcytotic peptide iRGD	CXCR4 antagonist (AMD3100)	Systemic	*In vivo* reduction of both tumor growth and infiltration of myeloid-derived suppressor cells in C57BL/6 mice bearing ovalbumin-expressing glioma cells after synergic radiation treatment.	(Alghamri et al., 2022)
NPs	Lipophilic thiobenzoate complexes of rhenium-188 lipid nanocapsules (LNC188Re) with a function-blocking antibody anti-CXCR4	188Re	Local by CED	Improved survival of Scid mice bearing CXCR4-positive U87MG xenografts.	(Séhédic et al., 2017)
Micro-particles	166Ho microparticles	166Ho	Local intra-tumoral injection by micro brachy-therapy	Improved overall survival in a minipig glioblastoma model bearing U87MG tumors.	(Khoshnevis et al., 2022)

Table 1.1 Continued. Examples of drug delivery systems for brain tumors

System	Composition	Agent	Admin.	Outcome	Ref.
Extra-cellular vesicles (EV)	RGDyK coated EV	siRNA against PD-L1	Systemic	Short-burst radiation improved delivery in GL261 GB tumors effectively attenuating radiation-induced PD-L1 expression on TAMCs as well as tumor cells. Activation of T cells led to prolonged survival of C57BL/6 mice.	(Tian et al., 2022)
Hydrogel	Poly(ethylene glycol)-g-Chitosan	T-cells		*In vitro* on U87MG cells.	(Tsao et al., 2014)
Hydrogel	Chitosan/β-glycerophosphate(Ch/β-GP)	Ellagic acid		*In vitro* on U87MG and C6 glioma cells.	(Kim et al., 2010)
Hydrogel	Hyaluronic acid crosslinked with adipic acid dihydrazide	Human urotensin II (hUII) and doxorubicin		*In vitro* chemoattraction and chemotherapy of U87MG cells.	(Kasapidou et al., 2021)
Hydrogel/ NPs	Chitosan-β-glycerophosphate-based thermogel containing mesoporous SiO2 NPs or polycaprolactone microparticles	Temozolo-mide	Local	Reduction in local recurrences in U87MG tumor xenografts in nude mice.	(Gherardini et al., 2023)
Hydrogel/ NPs	Di(carboxylatophenoxy) phosphazene selenocystamine cross-linked hydrogel loaded with Au NPs	Quisinostat and Au NPs as contrast agent	Local	Radiation-induced release of quinosinat from intratumorally injected hydrogels in subcutaneous NS039 xenografts allowed a 67% response rate in nude mice.	(Bouché et al., 2021)
Lipid nano-capsules	Lipid nanocapsule-based hydrogel	Lauroyl-gemcitabine	Local	Sustained drug release. Significant increase of survival in a U87MG tumor xenograft mice model.	(Bastiancich et al., 2017)
Fibers	PEG–PLLA	Carmustine		*In vitro* testing on Glioma C6 cells.	(Xu et al., 2006)
NPs/ Nano-fibers	PLGA/PEG-PLGA NPs embedded in chitosan nanofibers	SDF-1α	Local	*In vitro* attraction of U87MG cells and *in vivo* feasibility.	(Molina-Peña et al., 2021)

1.10.3. Examples of nanoparticles fabrication processes

Different methods of NPs fabrication techniques for protein encapsulation include solvent evaporation, spray-drying, and phase separation (Makadia and Siegel, 2011). In the solvent evaporation method, a hydrophobic polymer and the APIs are dissolved in a water-immiscible and volatile organic solvent. The solution is then dispersed in a water-based solution containing stabilizers by continuous agitation giving origin to an oil-in-water (O/W) emulsion. NPs containing APIs are then formed upon evaporation of the organic solvent, separated, washed, and optionally processed for storage. The disadvantage when encapsulating proteins is that they are hydrophilic and hence tend to diffuse into the aqueous phase. Therefore, a modification of the previous method is to first dissolve the proteins in water and then disperse this into an organic phase containing the dissolved polymer to form a water-in-oil emulsion (W/O). The addition of a second aqueous phase under continuous agitation allows the formation of a W/O/W emulsion from which solvent evaporation induces the formation of NPs (Sokolsky-Papkov et al., 2007). NPs can also be formed by simultaneous spraying and drying of the W/O/W emulsion (Makadia and Siegel, 2011). In the phase separation method, the addition of an organic non-solvent to the polymer is used to extract the first organic solvent, inducing the concentration of the polymer in a liquid phase containing the drug (coacervate) that upon completion of the separation process induces the solidification of the coacervate to produce drug-loaded NPs (Ding and Zhu, 2018). A variation of this process is the use of water-soluble organic solvent for the dissolution of the polymer followed by the separation of the solvent by using an aqueous solution, which results advantageous as a green chemistry process (Tran et al., 2012) (**Fig. 1.16**).

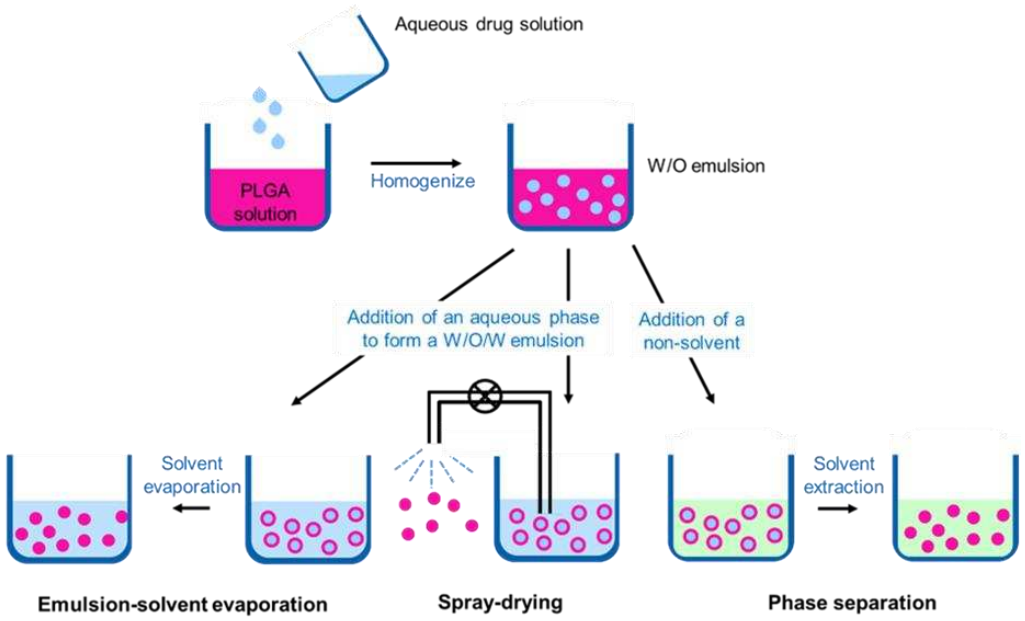

Figure 1.16. Examples of nano/micro particle preparation processes (previous page)**.** Loading of proteins into NPs can be achieved by water in oil (W/O) dispersion followed by a second dispersion in water (W/O/W emulsion) under continuous agitation which induces the formation of a coacervate containing the polymer and the active pharmaceutical ingredient

(API). The NPs can be formed by solvent evaporation or spray-drying. Another approach is to add a non-solvent to the polymer to extract the first organic solvent and induce the formation of solid NPs. (Fig. reproduced from (Haji Mansor, 2019) under the CC BY-NC-ND 2.0 FR license.

1.10.4. Fabrication of scaffolds for tissue engineering

Scaffolds for tissue engineering usually consist of biomaterials that are biocompatible and biodegradable. They can be fabricated by gelation processes forming hydrogels, and by techniques such as freeze dying and electrospinning, to produce porous sponges and fiber mats, respectively (Collins et al., 2021). Biodegradable hydrogels offer the advantage that can be self-assembled or crosslinked to meet certain tissue specificities, with the technical plus that can be injectable. They can cover small and ample volumes and at the same time make good contact with the tissue zone needing treatment (Shin et al., 2021). Freeze-dried sponges also fit medium to large areas and offer the possibility of mixing different biomaterials that may gel or not before the lyophilization step (Najberg et al., 2020). On the other hand, electrospun scaffolds have been postulated to mimic the nanofibrous characteristics of extracellular matrices (Cavo et al., 2020).

Hydrogels

Hydrogels are 3D water-swelling polymer networks formed by chemical and/or physical interactions. The main advantage of using hydrogels in tissue engineering constructs is that they are not only easy to process and mold, but also can be adapted to mechanical and biochemical properties to mimic soft tissues (See (Djoudi et al., 2022) in Annexes for a review of HA hydrogels for CNS applications). Hydrogels can be formed by spontaneous assembly of polymeric chains in a physical process that depends on the temperature, and by crosslinking by different techniques (Hu et al., 2019). One of the most used techniques corresponds to the carbodiimide hydrochloride (EDC) & N-hydroxy-succinimide (NHS) crosslinking (EDC/NHS) crosslinking by creating amide bounds. Aldehydes are also used, but toxicity is of concern. Glyoxal represents an alternative to glutaraldehyde for example because is less toxic (Oryan et al., 2018). Other techniques include the functionalization of the polymeric chains to induce an intrinsic reaction of the molecules in solution, by a change in temperature or photo-stimulation for example (Hu et al., 2019).

Sponges and porous solid scaffolds

Porous scaffolds consist of a solid structure that contains pores that can be interconnected or not depending on the fabrication method. The most used fabrication techniques for polymer biomaterials are shown in **Fig. 1.17**. Sponges are particularly interesting because they can trap water and fit cavities. Moreover, their stiffness can be varied by blending different materials

and varying the crosslinker concentration. The porosity can be tuned by varying the ratio of solid matter and by varying the concentration of crosslinker if used (Annabi et al., 2010). Sponges are mostly fabricated by conventional methods such as freeze drying (a.k.a. lyophilization) (**Fig. 1.17-B**). For instance, a polymeric solution/emulsification is cast in a mold and frozen. Lyophilization is then achieved by reducing the pressure of the chamber allowing for removal of the solvent and non-solvent. Another conventional technique is porogen leaching. It consists of the leaching of particles of different forms, e.g., balls and fibers that have been included within a polymeric matrix, and that can be removed by a specific solvent not affecting the polymer network. After leaching, the pores and their network remain within the structure of the solid scaffold (Viera Rey and St-Pierre, 2019). 3D printing (a.k.a. additive manufacturing) has become an area of intensive research because of the diversity of forms that can be achieved. 3D-printed scaffolds have been used in bone tissue engineering in preclinical and clinical settings (Collins et al., 2021). 3D-printed scaffolds might be tailored to respond to different stimuli such as a temperature change in time, and can be referred to as 4D-printed scaffolds (Kirillova et al., 2021). Nonwoven scaffolds are fibrous mats that resemble films and have the advantage of a greater surface area. However, their 3D design is limited. Nonwoven scaffolds include electrospinned fiber mats (Kirillova et al., 2021).

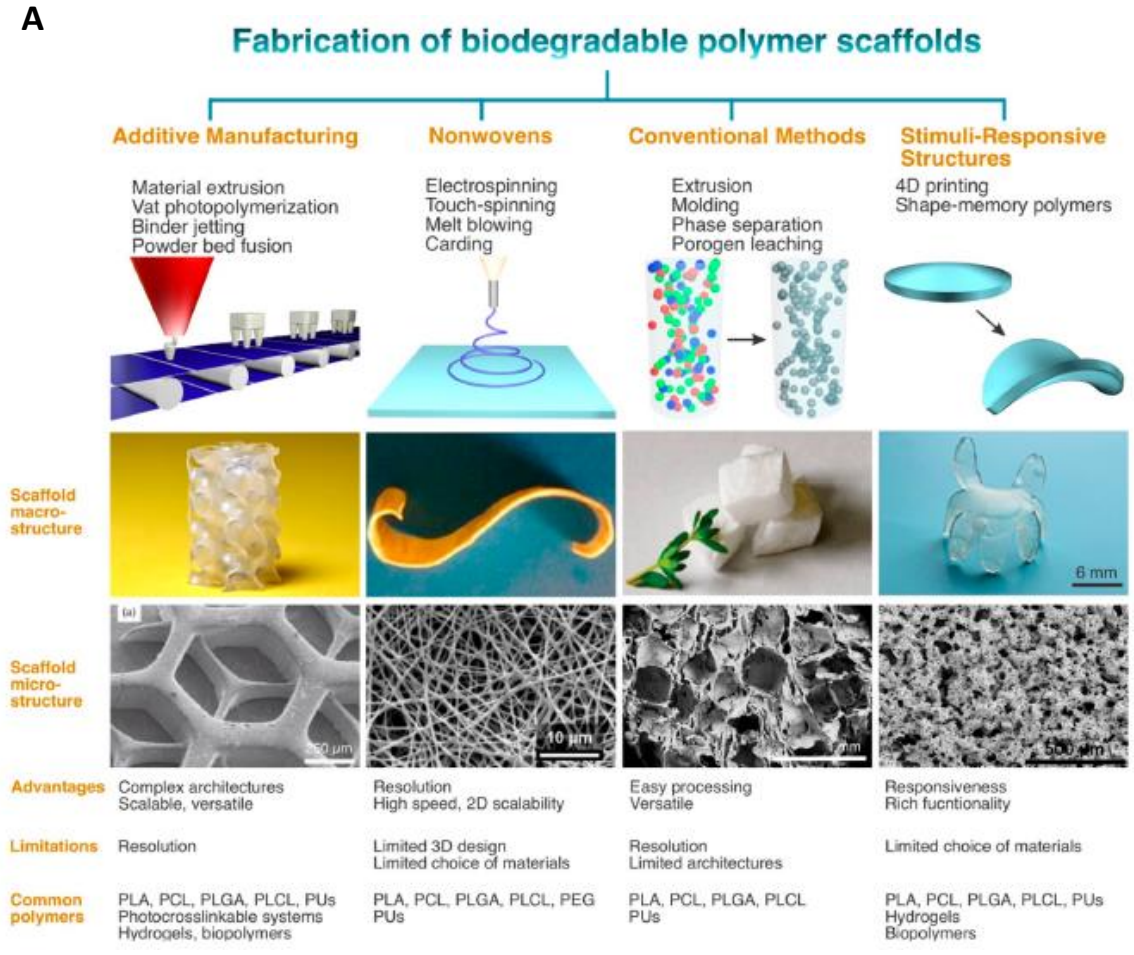

Figure 1.17. Examples of fabrication techniques of biodegradable polymeric scaffolds.

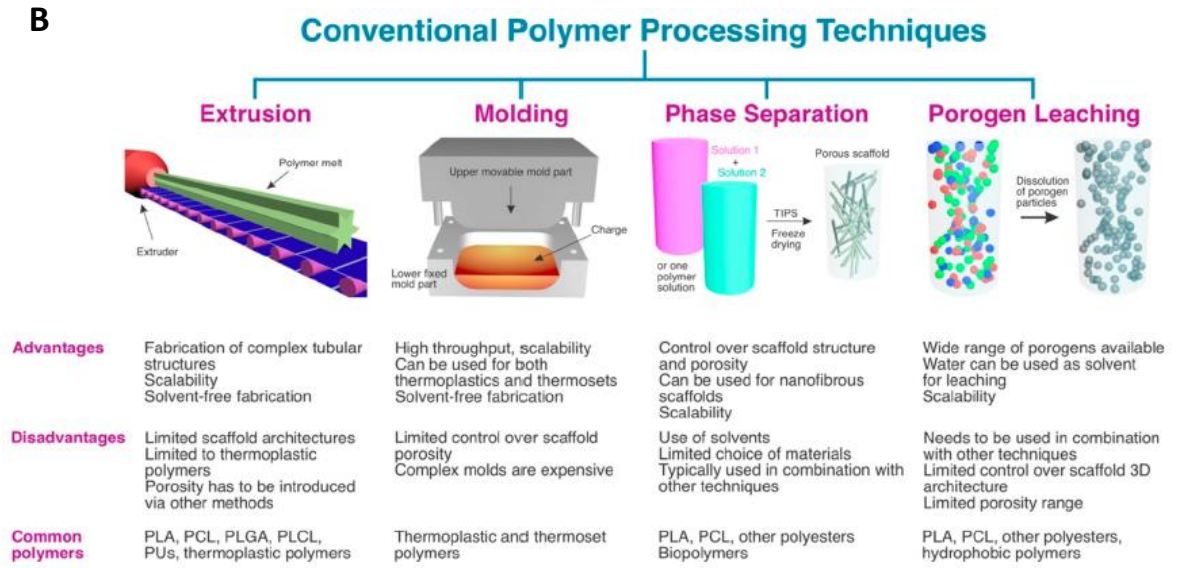

Figure 1.17 (continued). Examples of fabrication techniques of biodegradable polymeric scaffolds. A) (previous page) Biodegradable polymer scaffolds can be produced by 1) active manufacturing (3D printing), 2) nonwoven techniques including electrospinning, 3) more conventional methods such as porogen leaching and phase separation (e.g., freeze-drying), and 4) 4D printing which gives a time dimensionality. **B)** Conventional methods include 1) extrusion, in which a molten polymer is deposited to form tubular structures, 2) molding, which uses prefabricated molds, 3) phase separation, in which removal of a or several phases leaves a porous structure, and 4) porogen leaching, in which after the incorporated porogen is removed, the structure become porous. Conventional methods are not mutually exclusive and can benefit from combination approaches. Reprinted from (Kirillova et al., 2021) with permission from the American Chemical Society.

Electrospinning

Electrospinning involves the passage of an electrically charged polymer in a viscous state or solution into fibers by the process of drawing a stream in a powerful electrical field. Different polymers ranging from synthetic to natural ones have been processed by electrospinning including PLGA, PCL, PEG, alginate, silk fibroin, hyaluronan, collagen, and chitosan. A basic electrospinning system comprehends a syringe pump, the power supply, a metallic needle to allow the electricity to move into the polymeric solution, and a metallic collector for fiber collection (Cavo et al., 2020). The characteristics of the fiber mats can be optimized not only by tunning of the electrospinning instrument settings such as applied voltage, tip-to-collector distance, the shape of the spinneret, the shape of the collector, and flow rate, but also of the solution characteristics such as solute concentration and MW, type of solvent, additives, viscosity, and acetylation degree in the case of chitosan (Croisier and Jérôme, 2013) (**Fig. 1.18**).

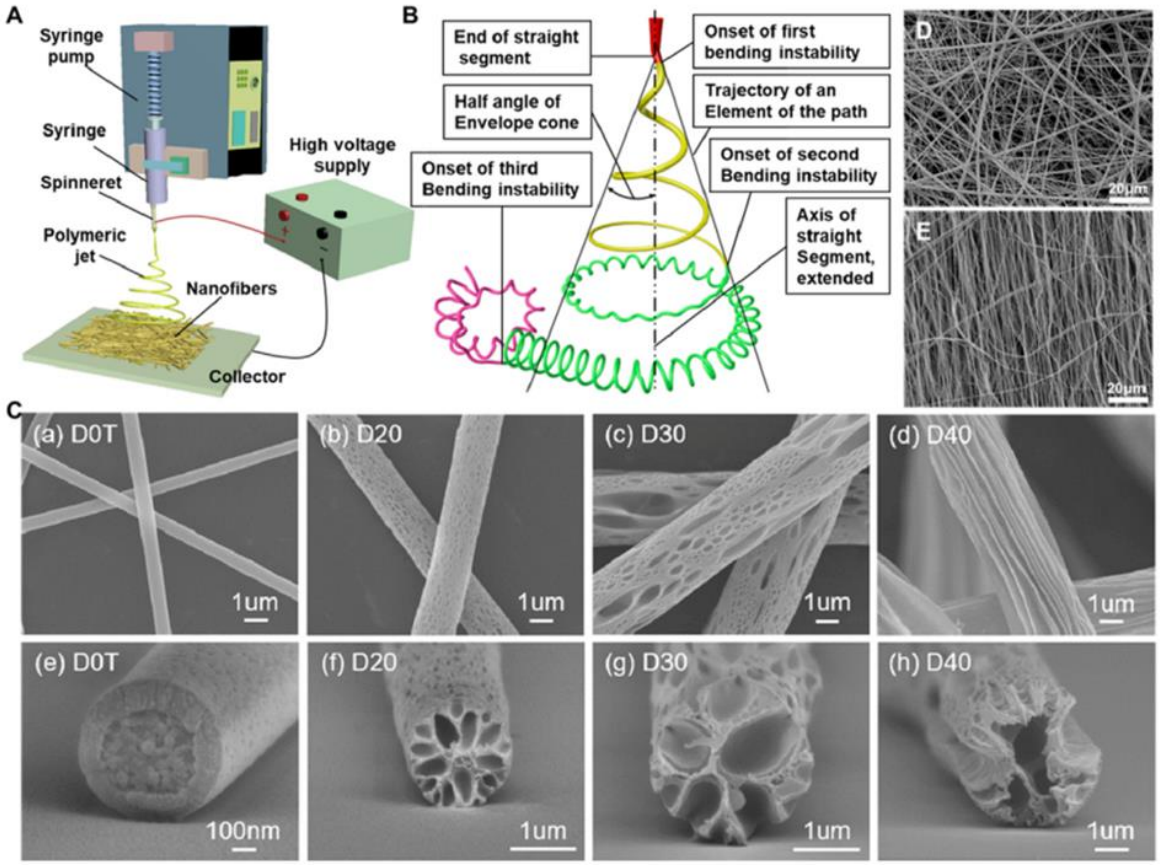

Figure 1.18. Electrospinning examples. A) Representation of the basic configuration of the electrospinning set-up. B) Representation of the stability of the polymeric electrospun jets. C) Examples of the surface morphology of fibers (a-d) and cross-section structures (e-h). D) Random fiber deposition. E) Aligned fiber deposition. Reprinted with permission from (Li et al., 2022).

1.11. Locoregional administration of therapeutics for GB treatment

The constraint imposed by the blood-brain barrier for the delivery of therapeutics to the central nervous system (CNS) including the brain, pushes efforts toward the development of strategies to circumvent such limitations (**Fig. 1.19**). Physical methods such as focused ultrasound permit the permeation of the blood-brain barrier, and hence facilitate the infiltration of therapeutics, these are then called enhanced administration methods. Different routes have been explored for direct administration including the intraparenchymal, intraventricular, intranasal, and intrathecal administration (see **Annexes** (Djoudi et al., 2022) for a more detailed description).

Convection-enhanced delivery (CED) offers the opportunity to gradually deliver a compound and circumvent the intraparenchymal pressure, therefore allowing a more homogeneous distribution within the loco-regional environment. Particularly interesting for the application of local delivery of therapeutics are volume-filling scaffolds such as hydrogels and sponges that are biocompatible and implantable. Moreover, they might be fictionalized or embedded with carrier particles for the sustained delivery of therapeutics (See **Table 1.1**).

Figure 1.19 (next page). Routes of administration into the CNS. (A) Enhanced administration of molecules and nanobodies by osmotic or focused ultrasound (FU) disruption of the BBB. (B) Direct administration: 1.1. Intraparenchymal injection. A brain tumor case is schematized where hydrogel injection might be performed intratumorally or after resection around the cavity edges. 1.2. Intraparenchymal injection assisted by CED (convection-enhanced delivery). Depicted is the case where soluble compounds are evenly distributed by CED within the tumor before a gelation reaction is induced by photoirradiation. The resulting embedded gel can be used as a platform for the sustained release of active compounds (Mukerji et al., 2016). 2. Intracerebroventricular administration of drugs directly into the cerebrospinal fluid (CSF). The Ommaya reservoir consists of a catheter connected to one lateral ventricle and a reservoir implanted under the scalp (Zubair and De Jesus, 2023). 3. Intrathecal injection. Lumbar puncture showing the direct administration of a drug directly into the CSF. 4. Intranasal delivery. 4.1 Intranasal application of modified HA in the nasal endothelium. Upon in situ polymerization the generated patch might be used as a reservoir for sustained release of compounds (Kiparissides et al., 2020). 4.2 After permeation of the nasal barrier, HA nanogels may be used to enhance the intracellular trafficking of drugs in CD44-expressing cells (Wei et al., 2013). 5. Keyhole surgery (Boahene et al., 2010) might be used as an alternative access route to the implantation of hydrogels into the brain. Credits: Figure 2B-1.2: reprinted from (Mukerji et al., 2016), with permission from Elsevier. Figure 2B-2: reprinted from the public domain access at https://en.wikipedia.org/wiki/Ommaya_reservoir#/media/File:Ommaya_01.png (accessed on 5 October 2022) Lynch PJ. Figure 2B-4.1: reprinted from (Kiparissides et al., 2020), with permission from ACS. Figure 2B-4.2: reprinted from (Wei et al., 2013), with permission from ACS. Figure 2B-5: reprinted from (Jandial, 2019), with permission from Elsevier. Central and additional figures were created with BioRender.com. The collage figure and caption are reprinted from the authors' manuscript (see **Annexes** (Djoudi et al., 2022)) with permission from the editor.

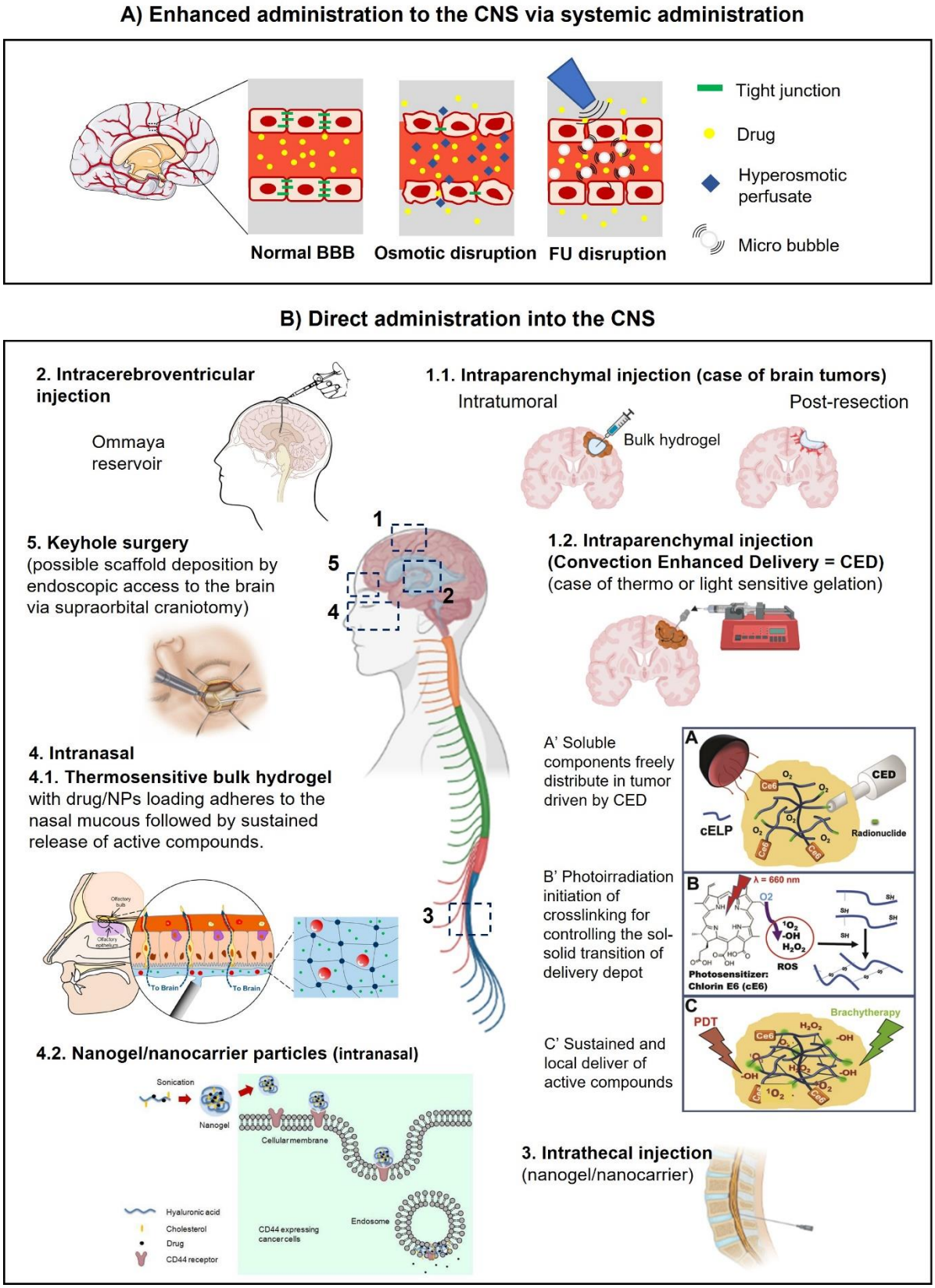

Figure 1.19. Routes of administration into the CNS. (Caption in the previous page).

1.12. The CXCR4/ SDF-1α axis in glioblastoma

The CXCR4/ SDF-1α signaling is used for the recruitment of hematopoietic stem cells from the bone marrow to a site of injury. The enhanced secretion of SDF-1α to the site of injury creates a chemical gradient that attracts stem cells to orchestrate the regeneration process (Ratajczak et al., 2004). This pathway (**Fig. 1.20-A**) seems to be hijacked to form metastases by different types of cancer cells including breast (Kang et al., 2003), prostate (Sun et al., 2007), and ovarian cancers (Rusetska et al., 2022), which cellular components overexpress the CXCR4 receptor. Interestingly glioblastoma cells have been found to express the CXCR4 receptor in *de novo* and recurrent GB-derived cell lines, but they more often do not produce SDF-1α (Zhou et al., 2002). One explanation of the migration patterns of Scherer's structures (**Section 1.5**) is the expression of SDF-1α on the paths leading to their formation, and overexpression of the CXR4 receptor on the leading edge of GB tumors (Zagzag et al., 2008). Recently, it has been demonstrated that U87MG cells transduced with the CXCR4 receptor are infiltrative (**Fig. 1.20-B**) and resemble the increased diffusion pattern of GB, in contrast to more localized U87MG without receptor expression (Séhédic et al., 2017; Toussaint et al., 2012). In addition, CXCR4-knockdown mouse glioma GL26-Cit tumors are less invasive (Yadav et al., 2016). Interestingly GB cells have been found to migrate to blood vessels through the perivascular space and that blocking of CXCR4 reduces invasion (Yadav et al., 2016; Zagzag et al., 2008). Therefore, these observations highlight the role of the CXCR4/ SDF-1α pathway in the invasion potential of GB cells. Furthermore, the expression of CXCR4 is overexpressed in cancer stem cells (Dubrovska et al., 2012; Fujita et al., 2015; Jung et al., 2013; López-Gil et al., 2021). Glioma stem cells are attracted towards endothelial cells in the perivascular niche, and they can differentiate into pericytes predominantly by transforming growth factor β (Cheng et al., 2013). The CXCR4/SDF-1α axis in cancer is also related to enhanced cell survival and proliferation (Guo et al., 2016; Jung et al., 2013; Yadav et al., 2016). Recently, it has been found that the CXCL12/CXCR4 axis enhanced temozolomide resistance in GB cells via Forkhead box protein M1 (FOXM1), a nuclear transcription factor related to cell proliferation and cell cycle regulation (Wang et al., 2020).

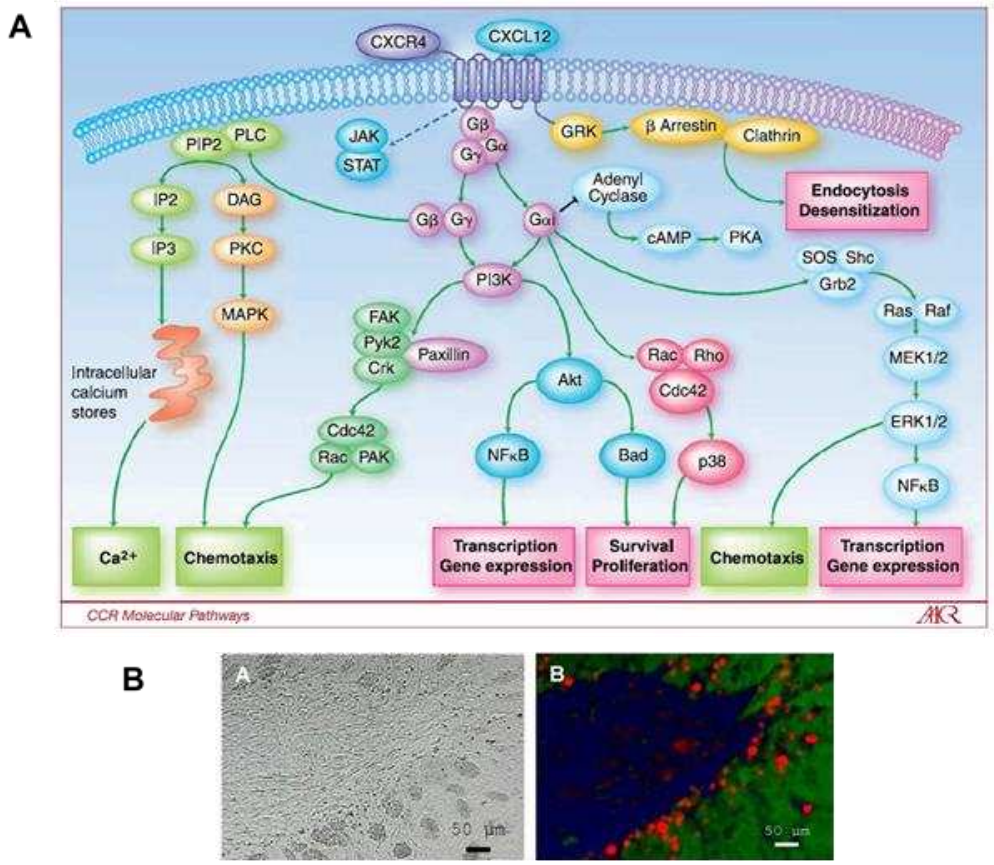

Figure 1.20. A) The CXCR4/ SDF-1α pathway in cancer. Reproduced from (Teicher and Fricker, 2010) with permission. B) CXCR4-expressing GB cells are infiltrative. RFP-CXCR4-positive cell migratory front (in red) throughout the tumor margin. Reproduced from (Séhédic et al., 2017) under a CC BY-NC 4.0 license.

1.13. The cancer cell trap in glioblastoma

In the GB context, the cell trapping strategy can be applied by on-purpose alteration of the GB ecosystem. That is if the environment of choice of residual tumoral cells after resection could be settled into the loco-regional space of the resection cavity, remnant infiltrative GB cells might be lured towards a confined location which could facilitate their further elimination. Here it is hypothesized that GB cells can be attracted toward an interactive biodeposit serving as a trap making use of the SDF-1α/CXCR4 pathway as a luring strategy. Once confined or concentrated in a controlled space, cells might be eliminated by the application of a loco-regional treatment such as focalized radiotherapy. This thesis aims to explore the use of biomaterial-designed scaffolds as a means of trapping GB cells.

1.14. References

About Glioblastoma [WWW Document], 2022. . National Brain Tumor Society. URL https://braintumor.org/events/glioblastoma-awareness-day/about-glioblastoma/ (accessed 1.23.23).

Adams, H., Chaichana, K.L., Avendaño, J., Liu, B., Raza, S.M., Quiñones-Hinojosa, A., 2013. Adult cerebellar glioblastoma: understanding survival and prognostic factors using a population-based database from 1973 to 2009. World Neurosurg 80, e237-243. https://doi.org/10.1016/j.wneu.2013.02.010

Alcantara Llaguno, S., Chen, J., Kwon, C.-H., Jackson, E.L., Li, Y., Burns, D.K., Alvarez-Buylla, A., Parada, L.F., 2009. Malignant Astrocytomas Originate from Neural Stem/Progenitor Cells in a Somatic Tumor Suppressor Mouse Model. Cancer Cell 15, 45–56. https://doi.org/10.1016/j.ccr.2008.12.006

Alcantara Llaguno, S.R., Parada, L.F., 2016. Cell of origin of glioma: biological and clinical implications. Br J Cancer 115, 1445–1450. https://doi.org/10.1038/bjc.2016.354

Aldape, K., Zadeh, G., Mansouri, S., Reifenberger, G., von Deimling, A., 2015. Glioblastoma: pathology, molecular mechanisms and markers. Acta Neuropathol 129, 829–848. https://doi.org/10.1007/s00401-015-1432-1

Alghamri, M.S., Banerjee, K., Mujeeb, A.A., Mauser, A., Taher, A., Thalla, R., McClellan, B.L., Varela, M.L., Stamatovic, S.M., Martinez-Revollar, G., Andjelkovic, A.V., Gregory, J.V., Kadiyala, P., Calinescu, A., Jiménez, J.A., Apfelbaum, A.A., Lawlor, E.R., Carney, S., Comba, A., Faisal, S.M., Barissi, M., Edwards, M.B., Appelman, H., Sun, Y., Gan, J., Ackermann, R., Schwendeman, A., Candolfi, M., Olin, M.R., Lahann, J., Lowenstein, P.R., Castro, M.G., 2022. Systemic Delivery of an Adjuvant CXCR4–CXCL12 Signaling Inhibitor Encapsulated in Synthetic Protein Nanoparticles for Glioma Immunotherapy. ACS Nano 16, 8729–8750. https://doi.org/10.1021/acsnano.1c07492

Amirrah, I.N., Lokanathan, Y., Zulkiflee, I., Wee, M.F.M.R., Motta, A., Fauzi, M.B., 2022. A Comprehensive Review on Collagen Type I Development of Biomaterials for Tissue Engineering: From Biosynthesis to Bioscaffold. Biomedicines 10, 2307. https://doi.org/10.3390/biomedicines10092307

Annabi, N., Nichol, J.W., Zhong, X., Ji, C., Koshy, S., Khademhosseini, A., Dehghani, F., 2010. Controlling the porosity and microarchitecture of hydrogels for tissue engineering. Tissue Eng Part B Rev 16, 371–383. https://doi.org/10.1089/ten.TEB.2009.0639

Azarin, S.M., Yi, J., Gower, R.M., Aguado, B.A., Sullivan, M.E., Goodman, A.G., Jiang, E.J., Rao, S.S., Ren, Y., Tucker, S.L., Backman, V., Jeruss, J.S., Shea, L.D., 2015. In vivo capture and label-free detection of early metastatic cells. Nature Communications 6, 8094. https://doi.org/10.1038/ncomms9094

Bailey, P., Harvey, C., 1927. A classification of the tumours of the glioma group on a histogenetic basis, with a correlated study of prognosis. By Percival Bailey and Harvey Cushing. Medium 8vo. Pp. 175, with 108 illustrations. 1926. Philadelphia, London, and Montreal: J. B. Lippincott Company. 21s. net. British Journal of Surgery 14, 554–555. https://doi.org/10.1002/bjs.1800145540

Barichello, T., Collodel, A., Hasbun, R., Morales, R., 2019. An Overview of the Blood-Brain Barrier, in: Barichello, T. (Ed.), Blood-Brain Barrier, Neuromethods. Springer, New York, NY, pp. 1–8. https://doi.org/10.1007/978-1-4939-8946-1_1

Barthel, L., Hadamitzky, M., Dammann, P., Schedlowski, M., Sure, U., Thakur, B.K., Hetze, S., 2022. Glioma: molecular signature and crossroads with tumor microenvironment. Cancer Metastasis Rev 41, 53–75. https://doi.org/10.1007/s10555-021-09997-9

Bastiancich, C., Bianco, J., Vanvarenberg, K., Ucakar, B., Joudiou, N., Gallez, B., Bastiat, G., Lagarce, F., Préat, V., Danhier, F., 2017. Injectable nanomedicine hydrogel for local chemotherapy of glioblastoma after surgical resection. J Control Release 264, 45–54. https://doi.org/10.1016/j.jconrel.2017.08.019

Bettegowda, C., Agrawal, N., Jiao, Y., Sausen, M., Wood, L.D., Hruban, R.H., Rodriguez, F.J., Cahill, D.P., McLendon, R., Riggins, G., Velculescu, V.E., Oba-Shinjo, S.M., Marie, S.K.N., Vogelstein, B., Bigner, D., Yan, H., Papadopoulos, N., Kinzler, K.W., 2011. Mutations in CIC

and FUBP1 contribute to human oligodendroglioma. Science 333, 1453–1455. https://doi.org/10.1126/science.1210557

Bettini, S., Bonfrate, V., Syrgiannis, Z., Sannino, A., Salvatore, L., Madaghiele, M., Valli, L., Giancane, G., 2015. Biocompatible Collagen Paramagnetic Scaffold for Controlled Drug Release. Biomacromolecules 16, 2599–2608. https://doi.org/10.1021/acs.biomac.5b00829

Boahene, K.D.O., Lim, M., Chu, E., Quinones-Hinojosa, A., 2010. Transpalpebral Orbitofrontal Craniotomy: A Minimally Invasive Approach to Anterior Cranial Vault Lesions. Skull Base 237–244. https://doi.org/10.1055/s-0030-1249247

Bouché, M., Dong, Y.C., Sheikh, S., Taing, K., Saxena, D., Hsu, J.C., Chen, M.H., Salinas, R.D., Song, H., Burdick, J.A., Dorsey, J., Cormode, D.P., 2021. Novel Treatment for Glioblastoma Delivered by a Radiation Responsive and Radiopaque Hydrogel. ACS Biomater. Sci. Eng. 7, 3209–3220. https://doi.org/10.1021/acsbiomaterials.1c00385

Bregy, A., Shah, A.H., Diaz, M.V., Pierce, H.E., Ames, P.L., Diaz, D., Komotar, R.J., 2013. The role of Gliadel wafers in the treatment of high-grade gliomas. Expert Review of Anticancer Therapy 13, 1453–1461. https://doi.org/10.1586/14737140.2013.840090

Briolay, T., Petithomme, T., Fouet, M., Nguyen-Pham, N., Blanquart, C., Boisgerault, N., 2021. Delivery of cancer therapies by synthetic and bio-inspired nanovectors. Molecular Cancer 20, 55. https://doi.org/10.1186/s12943-021-01346-2

Brovold, M., Almeida, J.I., Pla-Palacín, I., Sainz-Arnal, P., Sánchez-Romero, N., Rivas, J.J., Almeida, H., Royo Dachary, P., Serrano-Aulló, T., Soker, S., Baptista, P.M., 2018. Naturally-Derived Biomaterials for Tissue Engineering Applications. Adv Exp Med Biol 1077, 421–449. https://doi.org/10.1007/978-981-13-0947-2_23

Buonerba, C., Di Lorenzo, G., Marinelli, A., Federico, P., Palmieri, G., Imbimbo, M., Conti, P., Peluso, G., De Placido, S., Sampson, J.H., 2011. A comprehensive outlook on intracerebral therapy of malignant gliomas. Crit Rev Oncol Hematol 80, 54–68. https://doi.org/10.1016/j.critrevonc.2010.09.001

Caban-Toktas, S., Sahin, A., Lule, S., Esendagli, G., Vural, I., Karlı Oguz, K., Soylemezoglu, F., Mut, M., Dalkara, T., Khan, M., Capan, Y., 2020. Combination of Paclitaxel and R-flurbiprofen loaded PLGA nanoparticles suppresses glioblastoma growth on systemic administration. International Journal of Pharmaceutics 578, 119076. https://doi.org/10.1016/j.ijpharm.2020.119076

Cancer of the Brain and Other Nervous System - Cancer Stat Facts [WWW Document], 2022. . SEER. URL https://seer.cancer.gov/statfacts/html/brain.html (accessed 1.23.23).

Cavo, M., Serio, F., Kale, N.R., D'Amone, E., Gigli, G., Mercato, L.L. del, 2020. Electrospun nanofibers in cancer research: from engineering of in vitro 3D cancer models to therapy. Biomater. Sci. 8, 4887–4905. https://doi.org/10.1039/D0BM00390E

Cheng, L., Huang, Z., Zhou, W., Wu, Q., Donnola, S., Liu, J.K., Fang, X., Sloan, A.E., Mao, Y., Lathia, J.D., Min, W., McLendon, R.E., Rich, J.N., Bao, S., 2013. Glioblastoma Stem Cells Generate Vascular Pericytes to Support Vessel Function and Tumor Growth. Cell 153, 139–152. https://doi.org/10.1016/j.cell.2013.02.021

Chinot, O.L., Wick, W., Mason, W., Henriksson, R., Saran, F., Nishikawa, R., Carpentier, A.F., Hoang-Xuan, K., Kavan, P., Cernea, D., Brandes, A.A., Hilton, M., Abrey, L., Cloughesy, T., 2014. Bevacizumab plus Radiotherapy–Temozolomide for Newly Diagnosed Glioblastoma. N Engl J Med 370, 709–722. https://doi.org/10.1056/NEJMoa1308345

Chow, L.M.L., Endersby, R., Zhu, X., Rankin, S., Qu, C., Zhang, J., Broniscer, A., Ellison, D.W., Baker, S.J., 2011. Cooperativity within and among Pten, p53, and Rb Pathways Induces High-Grade Astrocytoma in Adult Brain. Cancer Cell 19, 305–316. https://doi.org/10.1016/j.ccr.2011.01.039

Claes, A., Idema, A.J., Wesseling, P., 2007. Diffuse glioma growth: a guerilla war. Acta Neuropathol 114, 443–458. https://doi.org/10.1007/s00401-007-0293-7

Collins, M.N., Ren, G., Young, K., Pina, S., Reis, R.L., Oliveira, J.M., 2021. Scaffold Fabrication Technologies and Structure/Function Properties in Bone Tissue Engineering. Advanced Functional Materials 31, 2010609. https://doi.org/10.1002/adfm.202010609

Connell, P.P., Hellman, S., 2009. Advances in Radiotherapy and Implications for the Next Century: A Historical Perspective. Cancer Research 69, 383–392. https://doi.org/10.1158/0008-5472.CAN-07-6871

Croisier, F., Jérôme, C., 2013. Chitosan-based biomaterials for tissue engineering. European Polymer Journal, Biobased Polymers and Related Materials 49, 780–792. https://doi.org/10.1016/j.eurpolymj.2012.12.009

Dang, L., White, D.W., Gross, S., Bennett, B.D., Bittinger, M.A., Driggers, E.M., Fantin, V.R., Jang, H.G., Jin, S., Keenan, M.C., Marks, K.M., Prins, R.M., Ward, P.S., Yen, K.E., Liau, L.M., Rabinowitz, J.D., Cantley, L.C., Thompson, C.B., Vander Heiden, M.G., Su, S.M., 2009. Cancer-associated IDH1 mutations produce 2-hydroxyglutarate. Nature 462, 739–744. https://doi.org/10.1038/nature08617

Darlix, A., Zouaoui, S., Rigau, V., Bessaoud, F., Figarella-Branger, D., Mathieu-Daudé, H., Trétarre, B., Bauchet, F., Duffau, H., Taillandier, L., Bauchet, L., 2017. Epidemiology for primary brain tumors: a nationwide population-based study. J Neurooncol 131, 525–546. https://doi.org/10.1007/s11060-016-2318-3

de la Fuente, A., Alonso-Alconada, L., Costa, C., Cueva, J., Garcia-Caballero, T., Lopez-Lopez, R., Abal, M., 2015. M-Trap: Exosome-Based Capture of Tumor Cells as a New Technology in Peritoneal Metastasis. J Natl Cancer Inst 107. https://doi.org/10.1093/jnci/djv184

De Vleeschouwer, S., Bergers, G., 2017. Glioblastoma: To Target the Tumor Cell or the Microenvironment?, in: De Vleeschouwer, S. (Ed.), Glioblastoma. Codon Publications, Brisbane (AU).

Ding, D., Zhu, Q., 2018. Recent advances of PLGA micro/nanoparticles for the delivery of biomacromolecular therapeutics. Mater Sci Eng C Mater Biol Appl 92, 1041–1060. https://doi.org/10.1016/j.msec.2017.12.036

Djoudi, A., Molina-Peña, R., Ferreira, N., Ottonelli, I., Tosi, G., Garcion, E., Boury, F., 2022. Hyaluronic Acid Scaffolds for Loco-Regional Therapy in Nervous System Related Disorders. International Journal of Molecular Sciences 23, 12174. https://doi.org/10.3390/ijms232012174

Djuzenova, C.S., Fiedler, V., Memmel, S., Katzer, A., Hartmann, S., Krohne, G., Zimmermann, H., Scholz, C.-J., Polat, B., Flentje, M., Sukhorukov, V.L., 2015. Actin cytoskeleton organization, cell surface modification and invasion rate of 5 glioblastoma cell lines differing in PTEN and p53 status. Experimental Cell Research 330, 346–357. https://doi.org/10.1016/j.yexcr.2014.08.013

Dubrovska, A., Hartung, A., Bouchez, L.C., Walker, J.R., Reddy, V.A., Cho, C.Y., Schultz, P.G., 2012. CXCR4 activation maintains a stem cell population in tamoxifen-resistant breast cancer cells through AhR signalling. Br J Cancer 107, 43–52. https://doi.org/10.1038/bjc.2012.105

Ellert-Miklaszewska, A., Poleszak, K., Pasierbinska, M., Kaminska, B., 2020. Integrin Signaling in Glioma Pathogenesis: From Biology to Therapy. International Journal of Molecular Sciences 21, 888. https://doi.org/10.3390/ijms21030888

Engelhard, H.H., Villano, J.L., Porter, K.R., Stewart, A.K., Barua, M., Barker, F.G., Newton, H.B., 2010. Clinical presentation, histology, and treatment in 430 patients with primary tumors of the spinal cord, spinal meninges, or cauda equina. J Neurosurg Spine 13, 67–77. https://doi.org/10.3171/2010.3.SPINE09430

Feng, W., Dean, D.C., Hornicek, F.J., Shi, H., Duan, Z., 2019. Exosomes promote pre-metastatic niche formation in ovarian cancer. Molecular Cancer 18, 124. https://doi.org/10.1186/s12943-019-1049-4

Fleury, A., Menegoz, F., Grosclaude, P., Daures, J.P., Henry-Amar, M., Raverdy, N., Schaffer, P., Poisson, M., Delattre, J.Y., 1997. Descriptive epidemiology of cerebral gliomas in France. Cancer 79, 1195–1202. https://doi.org/10.1002/(sici)1097-0142(19970315)79:6<1195::aid-cncr19>3.0.co;2-v

Fraser, J.R., Laurent, T.C., Laurent, U.B., 1997. Hyaluronan: its nature, distribution, functions and turnover. J Intern Med 242, 27–33. https://doi.org/10.1046/j.1365-2796.1997.00170.x

Friedman, H.S., Prados, M.D., Wen, P.Y., Mikkelsen, T., Schiff, D., Abrey, L.E., Yung, W.K.A., Paleologos, N., Nicholas, M.K., Jensen, R., Vredenburgh, J., Huang, J., Zheng, M., Cloughesy, T., 2009. Bevacizumab Alone and in Combination With Irinotecan in Recurrent Glioblastoma. JCO 27, 4733–4740. https://doi.org/10.1200/JCO.2008.19.8721

Fujita, T., Chiwaki, F., Takahashi, R., Aoyagi, K., Yanagihara, K., Nishimura, T., Tamaoki, M., Komatsu, M., Komatsuzaki, R., Matsusaki, K., Ichikawa, H., Sakamoto, H., Yamada, Y., Fukagawa, T., Katai, H., Konno, H., Ochiya, T., Yoshida, T., Sasaki, H., 2015. Identification and Characterization of CXCR4-Positive Gastric Cancer Stem Cells. PLOS ONE 10, e0130808. https://doi.org/10.1371/journal.pone.0130808

Gascon, S., Giraldo Solano, A., El Kheir, W., Therriault, H., Berthelin, P., Cattier, B., Marcos, B., Virgilio, N., Paquette, B., Faucheux, N., Lauzon, M.-A., 2020. Characterization and Mathematical Modeling of Alginate/Chitosan-Based Nanoparticles Releasing the Chemokine CXCL12 to Attract Glioblastoma Cells. Pharmaceutics 12, 356. https://doi.org/10.3390/pharmaceutics12040356

Gaspar, L.E., Fisher, B.J., Macdonald, D.R., Leber, D.V., Halperin, E.C., Schold, S.C., Cairncross, J.G., 1992. Supratentorial malignant glioma: Patterns of recurrence and implications for external beam local treatment. International Journal of Radiation Oncology*Biology*Physics 24, 55–57. https://doi.org/10.1016/0360-3016(92)91021-E

Gherardini, L., Vetri Buratti, V., Maturi, M., Inzalaco, G., Locatelli, E., Sambri, L., Gargiulo, S., Barone, V., Bonente, D., Bertelli, E., Tortorella, S., Franci, L., Fioravanti, A., Comes Franchini, M., Chiariello, M., 2023. Loco-regional treatment with temozolomide-loaded thermogels prevents glioblastoma recurrences in orthotopic human xenograft models. Sci Rep 13, 4630. https://doi.org/10.1038/s41598-023-31811-5

Gibb, R., Kovalchuk, A., 2018. Chapter 1 - Brain Development, in: Gibb, R., Kolb, B. (Eds.), The Neurobiology of Brain and Behavioral Development. Academic Press, pp. 3–27. https://doi.org/10.1016/B978-0-12-804036-2.00001-7

Giedd, J., 1999. Brain Development, IX. AJP 156, 4–4. https://doi.org/10.1176/ajp.156.1.4

Giese, A., Bjerkvig, R., Berens, M.E., Westphal, M., 2003. Cost of migration: invasion of malignant gliomas and implications for treatment. J Clin Oncol 21, 1624–1636. https://doi.org/10.1200/JCO.2003.05.063

Gilbert, M.R., Dignam, J.J., Armstrong, T.S., Wefel, J.S., Blumenthal, D.T., Vogelbaum, M.A., Colman, H., Chakravarti, A., Pugh, S., Won, M., Jeraj, R., Brown, P.D., Jaeckle, K.A., Schiff, D., Stieber, V.W., Brachman, D.G., Werner-Wasik, M., Tremont-Lukats, I.W., Sulman, E.P., Aldape, K.D., Curran, W.J., Mehta, M.P., 2014. A Randomized Trial of Bevacizumab for Newly Diagnosed Glioblastoma. New England Journal of Medicine 370, 699–708. https://doi.org/10.1056/NEJMoa1308573

Gillen, A.E., Riemondy, K.A., Amani, V., Griesinger, A.M., Gilani, A., Venkataraman, S., Madhavan, K., Prince, E., Sanford, B., Hankinson, T.C., Handler, M.H., Vibhakar, R., Jones, K.L., Mitra, S., Hesselberth, J.R., Foreman, N.K., Donson, A.M., 2020. Single-Cell RNA Sequencing of Childhood Ependymoma Reveals Neoplastic Cell Subpopulations That Impact Molecular Classification and Etiology. Cell Reports 32, 108023. https://doi.org/10.1016/j.celrep.2020.108023

Gnavi, S., Barwig, C., Freier, T., Haastert-Talini, K., Grothe, C., Geuna, S., 2013. Chapter One - The Use of Chitosan-Based Scaffolds to Enhance Regeneration in the Nervous System, in: Geuna, S., Perroteau, I., Tos, P., Battiston, B. (Eds.), International Review of Neurobiology, Tissue Engineering of the Peripheral Nerve. Academic Press, pp. 1–62. https://doi.org/10.1016/B978-0-12-420045-6.00001-8

Gregory, J.V., Kadiyala, P., Doherty, R., Cadena, M., Habeel, S., Ruoslahti, E., Lowenstein, P.R., Castro, M.G., Lahann, J., 2020. Systemic brain tumor delivery of synthetic protein nanoparticles for glioblastoma therapy. Nat Commun 11, 5687. https://doi.org/10.1038/s41467-020-19225-7

Griffin, C.A., Burger, P., Morsberger, L., Yonescu, R., Swierczynski, S., Weingart, J.D., Murphy, K.M., 2006. Identification of der(1;19)(q10;p10) in five oligodendrogliomas suggests mechanism of concurrent 1p and 19q loss. J Neuropathol Exp Neurol 65, 988–994. https://doi.org/10.1097/01.jnen.0000235122.98052.8f

Grochans, S., Cybulska, A.M., Simińska, D., Korbecki, J., Kojder, K., Chlubek, D., Baranowska-Bosiacka, I., 2022. Epidemiology of Glioblastoma Multiforme–Literature Review. Cancers 14, 2412. https://doi.org/10.3390/cancers14102412

Guo, F., Wang, Y., Liu, J., Mok, S.C., Xue, F., Zhang, W., 2016. CXCL12/CXCR4: a symbiotic bridge linking cancer cells and their stromal neighbors in oncogenic communication networks. Oncogene 35, 816–826. https://doi.org/10.1038/onc.2015.139

Haji Mansor, M., 2019. Functionalized polymer implants for the trapping of glioblastoma cells (Doctoral Thesis). Univerité d'Angers.

Haji Mansor, M., Najberg, M., Contini, A., Alvarez-Lorenzo, C., Garcion, E., Jérôme, C., Boury, F., 2018. Development of a non-toxic and non-denaturing formulation process for encapsulation of SDF-1α into PLGA/PEG-PLGA nanoparticles to achieve sustained release. Eur J Pharm Biopharm 125, 38–50. https://doi.org/10.1016/j.ejpb.2017.12.020

Hatanpaa, K.J., Burma, S., Zhao, D., Habib, A.A., 2010. Epidermal growth factor receptor in glioma: signal transduction, neuropathology, imaging, and radioresistance. Neoplasia 12, 675–684. https://doi.org/10.1593/neo.10688

He, X., Xie, L., Zhang, X., Lin, F., Wen, X., Teng, B., 2021. The Structural Characteristics of Collagen in Swim Bladders with 25-Year Sequence Aging: The Impact of Age. Applied Sciences 11, 4578. https://doi.org/10.3390/app11104578

Hegi, M.E., Diserens, A.-C., Gorlia, T., Hamou, M.-F., de Tribolet, N., Weller, M., Kros, J.M., Hainfellner, J.A., Mason, W., Mariani, L., Bromberg, J.E.C., Hau, P., Mirimanoff, R.O., Cairncross, J.G., Janzer, R.C., Stupp, R., 2005. MGMT Gene Silencing and Benefit from Temozolomide in Glioblastoma. New England Journal of Medicine 352, 997–1003. https://doi.org/10.1056/NEJMoa043331

Heilbrun, M.P., Sunderland, P.M., McDonald, P.R., Jr, T.H.W., Cosman, E., Ganz, E., 1987. Brown-Roberts-Wells Stereotactic Frame Modifications to Accomplish Magnetic Resonance Imaging Guidance in Three Planes. SFN 50, 143–152. https://doi.org/10.1159/000100700

Herrlinger, U., Tzaridis, T., Mack, F., Steinbach, J.P., Schlegel, U., Sabel, M., Hau, P., Kortmann, R.-D., Krex, D., Grauer, O., Goldbrunner, R., Schnell, O., Bähr, O., Uhl, M., Seidel, C., Tabatabai, G., Kowalski, T., Ringel, F., Schmidt-Graf, F., Suchorska, B., Brehmer, S., Weyerbrock, A., Renovanz, M., Bullinger, L., Galldiks, N., Vajkoczy, P., Misch, M., Vatter, H., Stuplich, M., Schäfer, N., Kebir, S., Weller, J., Schaub, C., Stummer, W., Tonn, J.-C., Simon, M., Keil, V.C., Nelles, M., Urbach, H., Coenen, M., Wick, W., Weller, M., Fimmers, R., Schmid, M., Hattingen, E., Pietsch, T., Coch, C., Glas, M., 2019. Lomustine-temozolomide combination therapy versus standard temozolomide therapy in patients with newly diagnosed glioblastoma with methylated MGMT promoter (CeTeG/NOA–09): a randomised, open-label, phase 3 trial. The Lancet 393, 678–688. https://doi.org/10.1016/S0140-6736(18)31791-4

Holland, E.C., 2000. Glioblastoma multiforme: The terminator. Proc Natl Acad Sci U S A 97, 6242–6244.

Hopkins, B.D., Hodakoski, C., Barrows, D., Mense, S.M., Parsons, R.E., 2014. PTEN function: the long and the short of it. Trends in Biochemical Sciences 39, 183–190. https://doi.org/10.1016/j.tibs.2014.02.006

Hu, W., Wang, Z., Xiao, Y., Zhang, S., Wang, J., 2019. Advances in crosslinking strategies of biomedical hydrogels. Biomater. Sci. 7, 843–855. https://doi.org/10.1039/C8BM01246F

Huang, Y., Hakamivala, A., Li, S., Nair, A., Saxena, R., Hsieh, J.-T., Tang, L., 2020. Chemokine releasing particle implants for trapping circulating prostate cancer cells. Sci Rep 10, 4433. https://doi.org/10.1038/s41598-020-60696-x

Idbaih, A., Touat, M., 2016. 1p/19q Co-deletion in Glioma: ESMO Biomarker Factsheet [WWW Document]. URL https://oncologypro.esmo.org/education-library/factsheets-on-biomarkers/1p-19q-co-deletion-in-glioma (accessed 2.1.23).

Inoue, S., Tanaka, K., Arisaka, F., Kimura, S., Ohtomo, K., Mizuno, S., 2000. Silk fibroin of Bombyx mori is secreted, assembling a high molecular mass elementary unit consisting of H-chain, L-chain, and P25, with a 6:6:1 molar ratio. J Biol Chem 275, 40517–40528. https://doi.org/10.1074/jbc.M006897200

Irawan, V., Sung, T.-C., Higuchi, A., Ikoma, T., 2018. Collagen Scaffolds in Cartilage Tissue Engineering and Relevant Approaches for Future Development. Tissue Eng Regen Med 15, 673–697. https://doi.org/10.1007/s13770-018-0135-9

Iuchi, T., Inoue, A., Hirose, Y., Morioka, M., Horiguchi, K., Natsume, A., Arakawa, Y., Iwasaki, K., Fujiki, M., Kumabe, T., Sakata, Y., 2022. Long-term effectiveness of Gliadel implant for

malignant glioma and prognostic factors for survival: 3-year results of a postmarketing surveillance in Japan. Neuro-Oncology Advances 4, vdab189. https://doi.org/10.1093/noajnl/vdab189

Jacques, T.S., Swales, A., Brzozowski, M.J., Henriquez, N.V., Linehan, J.M., Mirzadeh, Z., O' Malley, C., Naumann, H., Alvarez-Buylla, A., Brandner, S., 2010. Combinations of genetic mutations in the adult neural stem cell compartment determine brain tumour phenotypes. The EMBO Journal 29, 222–235. https://doi.org/10.1038/emboj.2009.327

Jain, A., Betancur, M., Patel, G.D., Valmikinathan, C.M., Mukhatyar, V.J., Vakharia, A., Pai, S.B., Brahma, B., MacDonald, T.J., Bellamkonda, R.V., 2014. Guiding intracortical brain tumour cells to an extracortical cytotoxic hydrogel using aligned polymeric nanofibres. Nature Mater 13, 308–316. https://doi.org/10.1038/nmat3878

Jandial, R., 2019. Core Techniques in Operative Neurosurgery - 2nd Edition, 2nd ed.

Jernigan, T.L., Stiles, J., 2017. Construction of the human forebrain. WIREs Cognitive Science 8, e1409. https://doi.org/10.1002/wcs.1409

Jiang, X., Nardelli, J., 2016. Cellular and molecular introduction to brain development. Neurobiology of Disease, Development Disorders of the immature brain 92, 3–17. https://doi.org/10.1016/j.nbd.2015.07.007

Jiao, Y., Killela, P.J., Reitman, Z.J., Rasheed, A.B., Heaphy, C.M., de Wilde, R.F., Rodriguez, F.J., Rosemberg, S., Oba-Shinjo, S.M., Nagahashi Marie, S.K., Bettegowda, C., Agrawal, N., Lipp, E., Pirozzi, C., Lopez, G., He, Y., Friedman, H., Friedman, A.H., Riggins, G.J., Holdhoff, M., Burger, P., McLendon, R., Bigner, D.D., Vogelstein, B., Meeker, A.K., Kinzler, K.W., Papadopoulos, N., Diaz, L.A., Yan, H., 2012. Frequent ATRX, CIC, FUBP1 and IDH1 mutations refine the classification of malignant gliomas. Oncotarget 3, 709–722. https://doi.org/10.18632/oncotarget.588

Joyce, K., Fabra, G.T., Bozkurt, Y., Pandit, A., 2021. Bioactive potential of natural biomaterials: identification, retention and assessment of biological properties. Sig Transduct Target Ther 6, 1–28. https://doi.org/10.1038/s41392-021-00512-8

Jung, M.-J., Rho, J.-K., Kim, Y.-M., Jung, J.E., Jin, Y.B., Ko, Y.-G., Lee, J.-S., Lee, S.-J., Lee, J.C., Park, M.-J., 2013. Upregulation of CXCR4 is functionally crucial for maintenance of stemness in drug-resistant non-small cell lung cancer cells. Oncogene 32, 209–221. https://doi.org/10.1038/onc.2012.37

Kanderi, T., Gupta, V., 2022. Glioblastoma Multiforme, in: StatPearls. StatPearls Publishing, Treasure Island (FL).

Kang, Y., Siegel, P.M., Shu, W., Drobnjak, M., Kakonen, S.M., Cordón-Cardo, C., Guise, T.A., Massagué, J., 2003. A multigenic program mediating breast cancer metastasis to bone. Cancer Cell 3, 537–549. https://doi.org/10.1016/s1535-6108(03)00132-6

Kanu, O.O., Mehta, A., Di, C., Lin, N., Bortoff, K., Bigner, D.D., Yan, H., Adamson, D.C., 2009. Glioblastoma multiforme: a review of therapeutic targets. Expert Opinion on Therapeutic Targets 13, 701–718. https://doi.org/10.1517/14728220902942348

Kasapidou, P.M., Montullé, E.L. de, Dembélé, K.-P., Mutel, A., Desrues, L., Gubala, V., Castel, H., 2021. Hyaluronic acid-based hydrogels loaded with chemoattractant and anticancer drug – new formulation for attracting and tackling glioma cells. Soft Matter 17, 10846–10861. https://doi.org/10.1039/D1SM01003D

Khoshnevis, M., Brown, R., Belluco, S., Zahi, I., Maciocco, L., Bonnefont-Rebeix, C., Pillet-Michelland, E., Tranel, J., Roger, T., Nennig, C., Oudoire, P., Marcon, L., Tillement, O., Louis, C., Gehan, H., Bardiès, M., Mariani, M., Muzio, V., Meunier, J.-P., Duchemin, C., Michel, N., N'Tsiba, E., Haddad, F., Buronfosse, T., Carozzo, C., Ponce, F., 2022. Therapeutic efficacy of 166Holmium siloxane in microbrachytherapy of induced glioblastoma in minipig tumor model. Frontiers in Oncology 12.

Killela, P.J., Reitman, Z.J., Jiao, Y., Bettegowda, C., Agrawal, N., Diaz, L.A., Friedman, A.H., Friedman, H., Gallia, G.L., Giovanella, B.C., Grollman, A.P., He, T.-C., He, Y., Hruban, R.H., Jallo, G.I., Mandahl, N., Meeker, A.K., Mertens, F., Netto, G.J., Rasheed, B.A., Riggins, G.J., Rosenquist, T.A., Schiffman, M., Shih, I.-M., Theodorescu, D., Torbenson, M.S., Velculescu, V.E., Wang, T.-L., Wentzensen, N., Wood, L.D., Zhang, M., McLendon, R.E., Bigner, D.D., Kinzler, K.W., Vogelstein, B., Papadopoulos, N., Yan, H., 2013. TERT promoter mutations

occur frequently in gliomas and a subset of tumors derived from cells with low rates of self-renewal. Proceedings of the National Academy of Sciences 110, 6021–6026. https://doi.org/10.1073/pnas.1303607110

Kim, S., Nishimoto, S.K., Bumgardner, J.D., Haggard, W.O., Gaber, M.W., Yang, Y., 2010. A chitosan/β-glycerophosphate thermo-sensitive gel for the delivery of ellagic acid for the treatment of brain cancer. Biomaterials 31, 4157–4166. https://doi.org/10.1016/j.biomaterials.2010.01.139

Kiparissides, C., Vasileiadou, A., Karageorgos, F., Serpetsi, S., 2020. A Computational Systems Approach to Rational Design of Nose-to-Brain Delivery of Biopharmaceutics. Ind. Eng. Chem. Res. 59, 2548–2565. https://doi.org/10.1021/acs.iecr.9b04885

Kirillova, A., Yeazel, T.R., Asheghali, D., Petersen, S.R., Dort, S., Gall, K., Becker, M.L., 2021. Fabrication of Biomedical Scaffolds Using Biodegradable Polymers. Chem. Rev. 121, 11238–11304. https://doi.org/10.1021/acs.chemrev.0c01200

Ko, C.-Y., Wu, L., Nair, A.M., Tsai, Y.-T., Lin, V.K., Tang, L., 2012. The use of chemokine-releasing tissue engineering scaffolds in a model of inflammatory response-mediated melanoma cancer metastasis. Biomaterials 33, 876–885. https://doi.org/10.1016/j.biomaterials.2011.10.002

Koh, L.-D., Cheng, Y., Teng, C.-P., Khin, Y.-W., Loh, X.-J., Tee, S.-Y., Low, M., Ye, E., Yu, H.-D., Zhang, Y.-W., Han, M.-Y., 2015. Structures, mechanical properties and applications of silk fibroin materials. Progress in Polymer Science 46, 86–110. https://doi.org/10.1016/j.progpolymsci.2015.02.001

Kong, X.-B., Tang, Q.-Y., Chen, X.-Y., Tu, Y., Sun, S.-Z., Sun, Z.-L., 2017. Polyethylene glycol as a promising synthetic material for repair of spinal cord injury. Neural Regen Res 12, 1003–1008. https://doi.org/10.4103/1673-5374.208597

Koul, D., 2008. PTEN Signaling pathways in glioblastoma. Cancer Biology & Therapy 7, 1321–1325. https://doi.org/10.4161/cbt.7.9.6954

Kreisl, T.N., Kim, L., Moore, K., Duic, P., Royce, C., Stroud, I., Garren, N., Mackey, M., Butman, J.A., Camphausen, K., Park, J., Albert, P.S., Fine, H.A., 2009. Phase II Trial of Single-Agent Bevacizumab Followed by Bevacizumab Plus Irinotecan at Tumor Progression in Recurrent Glioblastoma. JCO 27, 740–745. https://doi.org/10.1200/JCO.2008.16.3055

Le Rhun, E., Oppong, F.B., van den Bent, M., Wick, W., Brandes, A.A., Taphoorn, M.JB., Platten, M., Idbaih, A., Clement, P.M., Preusser, M., Golfinopoulos, V., Gorlia, T., Weller, M., 2023. Thrombocytopenia limits the feasibility of salvage lomustine chemotherapy in recurrent glioblastoma: a secondary analysis of EORTC 26101. European Journal of Cancer 178, 13–22. https://doi.org/10.1016/j.ejca.2022.10.006

Li, Y., Dong, T., Li, Z., Ni, S., Zhou, F., Alimi, O.A., Chen, S., Duan, B., Kuss, M., Wu, S., 2022. Review of advances in electrospinning-based strategies for spinal cord regeneration. Materials Today Chemistry 24, 100944. https://doi.org/10.1016/j.mtchem.2022.100944

Liau, L.M., Ashkan, K., Brem, S., Campian, J.L., Trusheim, J.E., Iwamoto, F.M., Tran, D.D., Ansstas, G., Cobbs, C.S., Heth, J.A., Salacz, M.E., D'Andre, S., Aiken, R.D., Moshel, Y.A., Nam, J.Y., Pillainayagam, C.P., Wagner, S.A., Walter, K.A., Chaudhary, R., Goldlust, S.A., Lee, I.Y., Bota, D.A., Elinzano, H., Grewal, J., Lillehei, K., Mikkelsen, T., Walbert, T., Abram, S., Brenner, A.J., Ewend, M.G., Khagi, S., Lovick, D.S., Portnow, J., Kim, L., Loudon, W.G., Martinez, N.L., Thompson, R.C., Avigan, D.E., Fink, K.L., Geoffroy, F.J., Giglio, P., Gligich, O., Krex, D., Lindhorst, S.M., Lutzky, J., Meisel, H.-J., Nadji-Ohl, M., Sanchin, L., Sloan, A., Taylor, L.P., Wu, J.K., Dunbar, E.M., Etame, A.B., Kesari, S., Mathieu, D., Piccioni, D.E., Baskin, D.S., Lacroix, M., May, S.-A., New, P.Z., Pluard, T.J., Toms, S.A., Tse, V., Peak, S., Villano, J.L., Battiste, J.D., Mulholland, P.J., Pearlman, M.L., Petrecca, K., Schulder, M., Prins, R.M., Boynton, A.L., Bosch, M.L., 2023. Association of Autologous Tumor Lysate-Loaded Dendritic Cell Vaccination With Extension of Survival Among Patients With Newly Diagnosed and Recurrent Glioblastoma: A Phase 3 Prospective Externally Controlled Cohort Trial. JAMA Oncology 9, 112–121. https://doi.org/10.1001/jamaoncol.2022.5370

Lim, M., Weller, M., Idbaih, A., Steinbach, J., Finocchiaro, G., Raval, R.R., Ansstas, G., Baehring, J., Taylor, J.W., Honnorat, J., Petrecca, K., De Vos, F., Wick, A., Sumrall, A., Sahebjam, S., Mellinghoff, I.K., Kinoshita, M., Roberts, M., Slepetis, R., Warad, D., Leung, D., Lee, M., Reardon, D.A., Omuro, A., 2022. Phase III trial of chemoradiotherapy with temozolomide plus

nivolumab or placebo for newly diagnosed glioblastoma with methylated MGMT promoter. Neuro-Oncology 24, 1935–1949. https://doi.org/10.1093/neuonc/noac116

Liu, C.J., Schaettler, M., Blaha, D.T., Bowman-Kirigin, J.A., Kobayashi, D.K., Livingstone, A.J., Bender, D., Miller, C.A., Kranz, D.M., Johanns, T.M., Dunn, G.P., 2020. Treatment of an aggressive orthotopic murine glioblastoma model with combination checkpoint blockade and a multivalent neoantigen vaccine. Neuro-Oncology 22, 1276–1288. https://doi.org/10.1093/neuonc/noaa050

Liu, X.-Y., Gerges, N., Korshunov, A., Sabha, N., Khuong-Quang, D.-A., Fontebasso, A.M., Fleming, A., Hadjadj, D., Schwartzentruber, J., Majewski, J., Dong, Z., Siegel, P., Albrecht, S., Croul, S., Jones, D.T.W., Kool, M., Tonjes, M., Reifenberger, G., Faury, D., Zadeh, G., Pfister, S., Jabado, N., 2012. Frequent ATRX mutations and loss of expression in adult diffuse astrocytic tumors carrying IDH1/IDH2 and TP53 mutations. Acta Neuropathol 124, 615–625. https://doi.org/10.1007/s00401-012-1031-3

Lombardi, G., De Salvo, G.L., Brandes, A.A., Eoli, M., Rudà, R., Faedi, M., Lolli, I., Pace, A., Daniele, B., Pasqualetti, F., Rizzato, S., Bellu, L., Pambuku, A., Farina, M., Magni, G., Indraccolo, S., Gardiman, M.P., Soffietti, R., Zagonel, V., 2019. Regorafenib compared with lomustine in patients with relapsed glioblastoma (REGOMA): a multicentre, open-label, randomised, controlled, phase 2 trial. The Lancet Oncology 20, 110–119. https://doi.org/10.1016/S1470-2045(18)30675-2

López-Gil, J.C., Martin-Hijano, L., Hermann, P.C., Sainz, B., 2021. The CXCL12 Crossroads in Cancer Stem Cells and Their Niche. Cancers 13, 469. https://doi.org/10.3390/cancers13030469

Louis, D.N., Perry, A., Reifenberger, G., von Deimling, A., Figarella-Branger, D., Cavenee, W.K., Ohgaki, H., Wiestler, O.D., Kleihues, P., Ellison, D.W., 2016. The 2016 World Health Organization Classification of Tumors of the Central Nervous System: a summary. Acta Neuropathol 131, 803–820. https://doi.org/10.1007/s00401-016-1545-1

Louis, D.N., Perry, A., Wesseling, P., Brat, D.J., Cree, I.A., Figarella-Branger, D., Hawkins, C., Ng, H.K., Pfister, S.M., Reifenberger, G., Soffietti, R., von Deimling, A., Ellison, D.W., 2021. The 2021 WHO Classification of Tumors of the Central Nervous System: a summary. Neuro-Oncology 23, 1231–1251. https://doi.org/10.1093/neuonc/noab106

Lukas, R.V., Wainwright, D.A., Ladomersky, E., Sachdev, S., Sonabend, A.M., Stupp, R., 2019. Newly Diagnosed Glioblastoma: A Review on Clinical Management. Oncology (Williston Park) 33, 91–100.

Ma, L., Liu, Q., Wu, R., Meng, Z., Patil, A., Yu, R., Yang, Y., Zhu, S., Fan, X., Hou, C., Li, Y., Qiu, W., Huang, L., Wang, J., Lin, N., Wan, Y., Hu, J., Liu, X.Y., 2020. From Molecular Reconstruction of Mesoscopic Functional Conductive Silk Fibrous Materials to Remote Respiration Monitoring. Small 16, 2000203. https://doi.org/10.1002/smll.202000203

Makadia, H.K., Siegel, S.J., 2011. Poly Lactic-co-Glycolic Acid (PLGA) as Biodegradable Controlled Drug Delivery Carrier. Polymers 3, 1377–1397. https://doi.org/10.3390/polym3031377

Malinovskaya, Y., Melnikov, P., Baklaushev, V., Gabashvili, A., Osipova, N., Mantrov, S., Ermolenko, Y., Maksimenko, O., Gorshkova, M., Balabanyan, V., Kreuter, J., Gelperina, S., 2017. Delivery of doxorubicin-loaded PLGA nanoparticles into U87 human glioblastoma cells. International Journal of Pharmaceutics 524, 77–90. https://doi.org/10.1016/j.ijpharm.2017.03.049

Masui, K., Mischel, P.S., Reifenberger, G., 2016. Molecular classification of gliomas. Handb Clin Neurol 134, 97–120. https://doi.org/10.1016/B978-0-12-802997-8.00006-2

Mathivet, T., Bouleti, C., Van Woensel, M., Stanchi, F., Verschuere, T., Phng, L.-K., Dejaegher, J., Balcer, M., Matsumoto, K., Georgieva, P.B., Belmans, J., Sciot, R., Stockmann, C., Mazzone, M., De Vleeschouwer, S., Gerhardt, H., 2017. Dynamic stroma reorganization drives blood vessel dysmorphia during glioma growth. EMBO Molecular Medicine 9, 1629–1645. https://doi.org/10.15252/emmm.201607445

McBrayer, S.K., Mayers, J.R., DiNatale, G.J., Shi, D.D., Khanal, J., Chakraborty, A.A., Sarosiek, K.A., Briggs, K.J., Robbins, A.K., Sewastianik, T., Shareef, S.J., Olenchock, B.A., Parker, S.J., Tateishi, K., Spinelli, J.B., Islam, M., Haigis, M.C., Looper, R.E., Ligon, K.L., Bernstein, B.E., Carrasco, R.D., Cahill, D.P., Asara, J.M., Metallo, C.M., Yennawar, N.H., Vander Heiden, M.G., Kaelin, W.G., 2018. Transaminase Inhibition by 2-Hydroxyglutarate Impairs Glutamate

Biosynthesis and Redox Homeostasis in Glioma. Cell 175, 101-116.e25. https://doi.org/10.1016/j.cell.2018.08.038

Melke, J., Midha, S., Ghosh, S., Ito, K., Hofmann, S., 2016. Silk fibroin as biomaterial for bone tissue engineering. Acta Biomater 31, 1–16. https://doi.org/10.1016/j.actbio.2015.09.005

Merry, C.L.R., Lindahl, U., Couchman, J., Esko, J.D., 2022. Proteoglycans and Sulfated Glycosaminoglycans, in: Varki, A., Cummings, R.D., Esko, J.D., Stanley, P., Hart, G.W., Aebi, M., Mohnen, D., Kinoshita, T., Packer, N.H., Prestegard, J.H., Schnaar, R.L., Seeberger, P.H. (Eds.), Essentials of Glycobiology. Cold Spring Harbor Laboratory Press, Cold Spring Harbor (NY).

Mitchell, M.J., Billingsley, M.M., Haley, R.M., Wechsler, M.E., Peppas, N.A., Langer, R., 2021. Engineering precision nanoparticles for drug delivery. Nat Rev Drug Discov 20, 101–124. https://doi.org/10.1038/s41573-020-0090-8

Molina-Peña, R., Haji Mansor, M., Najberg, M., Thomassin, J.-M., Gueza, B., Alvarez-Lorenzo, C., Garcion, E., Jérôme, C., Boury, F., 2021. Nanoparticle-containing electrospun nanofibrous scaffolds for sustained release of SDF-1α. Int J Pharm 610, 121205. https://doi.org/10.1016/j.ijpharm.2021.121205

Moreau, J.E., Anderson, K., Mauney, J.R., Nguyen, T., Kaplan, D.L., Rosenblatt, M., 2007. Tissue-Engineered Bone Serves as a Target for Metastasis of Human Breast Cancer in a Mouse Model. Cancer Research 67, 10304–10308. https://doi.org/10.1158/0008-5472.CAN-07-2483

Motz, G.T., Coukos, G., 2013. Deciphering and Reversing Tumor Immune Suppression. Immunity 39, 61–73. https://doi.org/10.1016/j.immuni.2013.07.005

Mukerji, R., Schaal, J., Li, X., Bhattacharyya, J., Asai, D., Zalutsky, M.R., Chilkoti, A., Liu, W., 2016. Spatiotemporally photoradiation-controlled intratumoral depot for combination of brachytherapy and photodynamic therapy for solid tumor. Biomaterials 79, 79–87. https://doi.org/10.1016/j.biomaterials.2015.11.064

Murphy, C.M., O'Brien, F.J., Little, D.G., Schindeler, A., 2013. Cell-scaffold interactions in the bone tissue engineering triad. Eur Cell Mater 26, 120–132. https://doi.org/10.22203/ecm.v026a09

Nagashima, H., Tanaka, K., Sasayama, T., Irino, Y., Sato, N., Takeuchi, Y., Kyotani, K., Mukasa, A., Mizukawa, K., Sakata, J., Yamamoto, Y., Hosoda, K., Itoh, T., Sasaki, R., Kohmura, E., 2016. Diagnostic value of glutamate with 2-hydroxyglutarate in magnetic resonance spectroscopy for IDH1 mutant glioma. Neuro-Oncology 18, 1559–1568. https://doi.org/10.1093/neuonc/now090

Najberg, M., Haji Mansor, M., Boury, F., Alvarez-Lorenzo, C., Garcion, E., 2019. Reversing the Tumor Target: Establishment of a Tumor Trap. Frontiers in Pharmacology 10, 887. https://doi.org/10.3389/fphar.2019.00887

Najberg, M., Haji Mansor, M., Taillé, T., Bouré, C., Molina-Peña, R., Boury, F., Cenis, J.L., Garcion, E., Alvarez-Lorenzo, C., 2020. Aerogel sponges of silk fibroin, hyaluronic acid and heparin for soft tissue engineering: Composition-properties relationship. Carbohydrate Polymers 237, 116107. https://doi.org/10.1016/j.carbpol.2020.116107

Nduom, E.K., Weller, M., Heimberger, A.B., 2015. Immunosuppressive mechanisms in glioblastoma. Neuro Oncol 17 Suppl 7, vii9–vii14. https://doi.org/10.1093/neuonc/nov151

Nonoguchi, N., Ohta, T., Oh, J.-E., Kim, Y.-H., Kleihues, P., Ohgaki, H., 2013. TERT promoter mutations in primary and secondary glioblastomas. Acta Neuropathol 126, 931–937. https://doi.org/10.1007/s00401-013-1163-0

Noushmehr, H., Weisenberger, D.J., Diefes, K., Phillips, H.S., Pujara, K., Berman, B.P., Pan, F., Pelloski, C.E., Sulman, E.P., Bhat, K.P., Verhaak, R.G.W., Hoadley, K.A., Hayes, D.N., Perou, C.M., Schmidt, H.K., Ding, L., Wilson, R.K., Van Den Berg, D., Shen, H., Bengtsson, H., Neuvial, P., Cope, L.M., Buckley, J., Herman, J.G., Baylin, S.B., Laird, P.W., Aldape, K., 2010. Identification of a CpG Island Methylator Phenotype that Defines a Distinct Subgroup of Glioma. Cancer Cell 17, 510–522. https://doi.org/10.1016/j.ccr.2010.03.017

Ohgaki, H., Kleihues, P., 2007. Genetic Pathways to Primary and Secondary Glioblastoma. Am J Pathol 170, 1445–1453. https://doi.org/10.2353/ajpath.2007.070011

Ojeda-Hernández, D.D., Canales-Aguirre, A.A., Matias-Guiu, J., Gomez-Pinedo, U., Mateos-Díaz, J.C., 2020. Potential of Chitosan and Its Derivatives for Biomedical Applications in the Central Nervous System. Frontiers in Bioengineering and Biotechnology 8.

Onaciu, A., Munteanu, R.A., Moldovan, A.I., Moldovan, C.S., Berindan-Neagoe, I., 2019. Hydrogels Based Drug Delivery Synthesis, Characterization and Administration. Pharmaceutics 11, 432. https://doi.org/10.3390/pharmaceutics11090432

Oryan, A., Kamali, A., Moshiri, A., Baharvand, H., Daemi, H., 2018. Chemical crosslinking of biopolymeric scaffolds: Current knowledge and future directions of crosslinked engineered bone scaffolds. International Journal of Biological Macromolecules 107, 678–688. https://doi.org/10.1016/j.ijbiomac.2017.08.184

Ostrom, Q.T., Gittleman, H., Farah, P., Ondracek, A., Chen, Y., Wolinsky, Y., Stroup, N.E., Kruchko, C., Barnholtz-Sloan, J.S., 2013. CBTRUS Statistical Report: Primary Brain and Central Nervous System Tumors Diagnosed in the United States in 2006-2010. Neuro-Oncology 15, ii1–ii56. https://doi.org/10.1093/neuonc/not151

Ostrom, Q.T., Price, M., Neff, C., Cioffi, G., Waite, K.A., Kruchko, C., Barnholtz-Sloan, J.S., 2022. CBTRUS Statistical Report: Primary Brain and Other Central Nervous System Tumors Diagnosed in the United States in 2015–2019. Neuro Oncol 24, v1–v95. https://doi.org/10.1093/neuonc/noac202

Passi, A., Vigetti, D., 2019. Hyaluronan: Structure, Metabolism, and Biological Properties, in: Cohen, E., Merzendorfer, H. (Eds.), Extracellular Sugar-Based Biopolymers Matrices, Biologically-Inspired Systems. Springer International Publishing, Cham, pp. 155–186. https://doi.org/10.1007/978-3-030-12919-4_4

Pavlisa, Goran, Rados, M., Pavlisa, Gordana, Pavic, L., Potocki, K., Mayer, D., 2009. The differences of water diffusion between brain tissue infiltrated by tumor and peritumoral vasogenic edema. Clin Imaging 33, 96–101. https://doi.org/10.1016/j.clinimag.2008.06.035

Pavlov, V., Page, P., Abi-Lahoud, G., Nataf, F., Dezamis, E., Robin, A., Varlet, P., Turak, B., Dhermain, F., Domont, J., Louvel, G., Souillard-Scemama, R., Parraga, E., Meder, J.-F., Chrétien, F., Devaux, B., Pallud, J., 2015. Combining intraoperative carmustine wafers and Stupp regimen in multimodal first-line treatment of primary glioblastomas. British Journal of Neurosurgery 29, 524–531. https://doi.org/10.3109/02688697.2015.1012051

Philips, A., Henshaw, D.L., Lamburn, G., O'Carroll, M.J., 2018. Brain Tumours: Rise in Glioblastoma Multiforme Incidence in England 1995–2015 Suggests an Adverse Environmental or Lifestyle Factor. Journal of Environmental and Public Health 2018, e7910754. https://doi.org/10.1155/2018/7910754

Poppleton, H., Gilbertson, R.J., 2007. Stem cells of ependymoma. Br J Cancer 96, 6–10. https://doi.org/10.1038/sj.bjc.6603519

Porter, D., Vollrath, F., 2009. Silk as a Biomimetic Ideal for Structural Polymers. Advanced Materials 21, 487–492. https://doi.org/10.1002/adma.200801332

Qi, Y., Wang, H., Wei, K., Yang, Y., Zheng, R.-Y., Kim, I.S., Zhang, K.-Q., 2017. A Review of Structure Construction of Silk Fibroin Biomaterials from Single Structures to Multi-Level Structures. Int J Mol Sci 18, 237. https://doi.org/10.3390/ijms18030237

Ramalho, M.J., Sevin, E., Gosselet, F., Lima, J., Coelho, M.A.N., Loureiro, J.A., Pereira, M.C., 2018. Receptor-mediated PLGA nanoparticles for glioblastoma multiforme treatment. International Journal of Pharmaceutics 545, 84–92. https://doi.org/10.1016/j.ijpharm.2018.04.062

Rao, S.S., Bushnell, G.G., Azarin, S.M., Spicer, G., Aguado, B.A., Stoehr, J.R., Jiang, E.J., Backman, V., Shea, L.D., Jeruss, J.S., 2016. Enhanced Survival with Implantable Scaffolds That Capture Metastatic Breast Cancer Cells In Vivo. Cancer Research 76, 5209–5218. https://doi.org/10.1158/0008-5472.CAN-15-2106

Ratajczak, M.Z., Kucia, M., Reca, R., Majka, M., Janowska-Wieczorek, A., Ratajczak, J., 2004. Stem cell plasticity revisited: CXCR4-positive cells expressing mRNA for early muscle, liver and neural cells 'hide out' in the bone marrow. Leukemia 18, 29–40. https://doi.org/10.1038/sj.leu.2403184

Reardon, D.A., Desjardins, A., Vredenburgh, J.J., O'Rourke, D.M., Tran, D.D., Fink, K.L., Nabors, L.B., Li, G., Bota, D.A., Lukas, R.V., Ashby, L.S., Duic, J.P., Mrugala, M.M., Cruickshank, S., Vitale, L., He, Y., Green, J.A., Yellin, M.J., Turner, C.D., Keler, T., Davis, T.A., Sampson, J.H., for the ReACT trial investigators, 2020. Rindopepimut with Bevacizumab for Patients with Relapsed EGFRvIII-Expressing Glioblastoma (ReACT): Results of a Double-Blind

Randomized Phase II Trial. Clinical Cancer Research 26, 1586–1594. https://doi.org/10.1158/1078-0432.CCR-18-1140

Reifenberger, G., Wirsching, H.-G., Knobbe-Thomsen, C.B., Weller, M., 2017. Advances in the molecular genetics of gliomas — implications for classification and therapy. Nat Rev Clin Oncol 14, 434–452. https://doi.org/10.1038/nrclinonc.2016.204

Ricard-Blum, S., 2011. The Collagen Family. Cold Spring Harb Perspect Biol 3, a004978. https://doi.org/10.1101/cshperspect.a004978

Robertson, B.A., Blumstein, D.T., 2019. How to disarm an evolutionary trap. Conservation Science and Practice 1, e116. https://doi.org/10.1111/csp2.116

Rodrigues, J.C., Gonzalez, G.C., Zhang, L., Ibrahim, G., Kelly, J.J., Gustafson, M.P., Lin, Y., Dietz, A.B., Forsyth, P.A., Yong, V.W., Parney, I.F., 2010. Normal human monocytes exposed to glioma cells acquire myeloid-derived suppressor cell-like properties. Neuro-Oncology 12, 351–365. https://doi.org/10.1093/neuonc/nop023

Rong, Y., Durden, D.L., Van Meir, E.G., Brat, D.J., 2006. "Pseudopalisading" necrosis in glioblastoma: a familiar morphologic feature that links vascular pathology, hypoxia, and angiogenesis. J Neuropathol Exp Neurol 65, 529–539. https://doi.org/10.1097/00005072-200606000-00001

Rusetska, N., Kowalski, K., Zalewski, K., Zięba, S., Bidziński, M., Goryca, K., Kotowicz, B., Fuksiewicz, M., Kopczynski, J., Bakuła-Zalewska, E., Kowalik, A., Kowalewska, M., 2022. CXCR4/ACKR3/CXCL12 axis in the lymphatic metastasis of vulvar squamous cell carcinoma. Journal of Clinical Pathology 75, 324–332. https://doi.org/10.1136/jclinpath-2020-206917

Sage, W., Guilfoyle, M., Luney, C., Young, A., Sinha, R., Sgubin, D., McAbee, J.H., Ma, R., Jefferies, S., Jena, R., Harris, F., Allinson, K., Matys, T., Qian, W., Santarius, T., Price, S., Watts, C., 2018. Local alkylating chemotherapy applied immediately after 5-ALA guided resection of glioblastoma does not provide additional benefit. J Neurooncol 136, 273–280. https://doi.org/10.1007/s11060-017-2649-8

Sandmann, T., Bourgon, R., Garcia, J., Li, C., Cloughesy, T., Chinot, O.L., Wick, W., Nishikawa, R., Mason, W., Henriksson, R., Saran, F., Lai, A., Moore, N., Kharbanda, S., Peale, F., Hegde, P., Abrey, L.E., Phillips, H.S., Bais, C., 2015. Patients With Proneural Glioblastoma May Derive Overall Survival Benefit From the Addition of Bevacizumab to First-Line Radiotherapy and Temozolomide: Retrospective Analysis of the AVAglio Trial. JCO 33, 2735–2744. https://doi.org/10.1200/JCO.2015.61.5005

Santoro, R., Venkateswaran, S., Amadeo, F., Zhang, R., Brioschi, M., Callanan, A., Agrifoglio, M., Banfi, C., Bradley, M., Pesce, M., 2017. Acrylate-based materials for heart valve scaffold engineering. Biomater. Sci. 6, 154–167. https://doi.org/10.1039/C7BM00854F

Schafer, D.P., Stevens, B., 2015. Microglia Function in Central Nervous System Development and Plasticity. Cold Spring Harb Perspect Biol 7, a020545. https://doi.org/10.1101/cshperspect.a020545

Scherer, H.J., 1940. THE FORMS OF GROWTH IN GLIOMAS AND THEIR PRACTICAL SIGNIFICANCE. Brain 63, 1–35. https://doi.org/10.1093/brain/63.1.1

Schwartzentruber, J., Korshunov, A., Liu, X.-Y., Jones, D.T.W., Pfaff, E., Jacob, K., Sturm, D., Fontebasso, A.M., Quang, D.-A.K., Tönjes, M., Hovestadt, V., Albrecht, S., Kool, M., Nantel, A., Konermann, C., Lindroth, A., Jäger, N., Rausch, T., Ryzhova, M., Korbel, J.O., Hielscher, T., Hauser, P., Garami, M., Klekner, A., Bognar, L., Ebinger, M., Schuhmann, M.U., Scheurlen, W., Pekrun, A., Frühwald, M.C., Roggendorf, W., Kramm, C., Dürken, M., Atkinson, J., Lepage, P., Montpetit, A., Zakrzewska, M., Zakrzewski, K., Liberski, P.P., Dong, Z., Siegel, P., Kulozik, A.E., Zapatka, M., Guha, A., Malkin, D., Felsberg, J., Reifenberger, G., von Deimling, A., Ichimura, K., Collins, V.P., Witt, H., Milde, T., Witt, O., Zhang, C., Castelo-Branco, P., Lichter, P., Faury, D., Tabori, U., Plass, C., Majewski, J., Pfister, S.M., Jabado, N., 2012. Driver mutations in histone H3.3 and chromatin remodelling genes in paediatric glioblastoma. Nature 482, 226–231. https://doi.org/10.1038/nature10833

Séhédic, D., Chourpa, I., Tétaud, C., Griveau, A., Loussouarn, C., Avril, S., Legendre, C., Lepareur, N., Wion, D., Hindré, F., Davodeau, F., Garcion, E., 2017. Locoregional Confinement and Major Clinical Benefit of 188Re-Loaded CXCR4-Targeted Nanocarriers in an Orthotopic Human to Mouse Model of Glioblastoma. Theranostics 7, 4517–4536. https://doi.org/10.7150/thno.19403

Shin, G.R., Kim, H.E., Kim, J.H., Choi, S., Kim, M.S., 2021. Advances in Injectable In Situ-Forming Hydrogels for Intratumoral Treatment. Pharmaceutics 13, 1953. https://doi.org/10.3390/pharmaceutics13111953

Silbergeld, D.L., Chicoine, M.R., 1997. Isolation and characterization of human malignant glioma cells from histologically normal brain. J Neurosurg 86, 525–531. https://doi.org/10.3171/jns.1997.86.3.0525

Singer, M.C., Parmesan, C., 2018. Lethal trap created by adaptive evolutionary response to an exotic resource. Nature 557, 238–241. https://doi.org/10.1038/s41586-018-0074-6

Sokolsky-Papkov, M., Agashi, K., Olaye, A., Shakesheff, K., Domb, A.J., 2007. Polymer carriers for drug delivery in tissue engineering. Adv Drug Deliv Rev 59, 187–206. https://doi.org/10.1016/j.addr.2007.04.001

Stiles, J., Jernigan, T.L., 2010. The Basics of Brain Development. Neuropsychol Rev 20, 327–348. https://doi.org/10.1007/s11065-010-9148-4

Stummer, W., Pichlmeier, U., Meinel, T., Wiestler, O.D., Zanella, F., Reulen, H.-J., 2006. Fluorescence-guided surgery with 5-aminolevulinic acid for resection of malignant glioma: a randomised controlled multicentre phase III trial. The Lancet Oncology 7, 392–401. https://doi.org/10.1016/S1470-2045(06)70665-9

Stupp, R., Hegi, M.E., Gorlia, T., Erridge, S.C., Perry, J., Hong, Y.-K., Aldape, K.D., Lhermitte, B., Pietsch, T., Grujicic, D., Steinbach, J.P., Wick, W., Tarnawski, R., Nam, D.-H., Hau, P., Weyerbrock, A., Taphoorn, M.J.B., Shen, C.-C., Rao, N., Thurzo, L., Herrlinger, U., Gupta, T., Kortmann, R.-D., Adamska, K., McBain, C., Brandes, A.A., Tonn, J.C., Schnell, O., Wiegel, T., Kim, C.-Y., Nabors, L.B., Reardon, D.A., van den Bent, M.J., Hicking, C., Markivskyy, A., Picard, M., Weller, M., 2014. Cilengitide combined with standard treatment for patients with newly diagnosed glioblastoma with methylated MGMT promoter (CENTRIC EORTC 26071-22072 study): a multicentre, randomised, open-label, phase 3 trial. The Lancet Oncology 15, 1100–1108. https://doi.org/10.1016/S1470-2045(14)70379-1

Stupp, R., Mason, W.P., van den Bent, M.J., Weller, M., Fisher, B., Taphoorn, M.J.B., Belanger, K., Brandes, A.A., Marosi, C., Bogdahn, U., Curschmann, J., Janzer, R.C., Ludwin, S.K., Gorlia, T., Allgeier, A., Lacombe, D., Cairncross, J.G., Eisenhauer, E., Mirimanoff, R.O., 2005. Radiotherapy plus Concomitant and Adjuvant Temozolomide for Glioblastoma. New England Journal of Medicine 352, 987–996. https://doi.org/10.1056/NEJMoa043330

Stupp, R., Taillibert, S., Kanner, A., Read, W., Steinberg, D.M., Lhermitte, B., Toms, S., Idbaih, A., Ahluwalia, M.S., Fink, K., Di Meco, F., Lieberman, F., Zhu, J.-J., Stragliotto, G., Tran, D.D., Brem, S., Hottinger, A.F., Kirson, E.D., Lavy-Shahaf, G., Weinberg, U., Kim, C.-Y., Paek, S.-H., Nicholas, G., Bruna, J., Hirte, H., Weller, M., Palti, Y., Hegi, M.E., Ram, Z., 2017. Effect of Tumor-Treating Fields Plus Maintenance Temozolomide vs Maintenance Temozolomide Alone on Survival in Patients With Glioblastoma: A Randomized Clinical Trial. JAMA 318, 2306–2316. https://doi.org/10.1001/jama.2017.18718

Sun, Y.-X., Fang, M., Wang, J., Cooper, C.R., Pienta, K.J., Taichman, R.S., 2007. Expression and activation of alpha v beta 3 integrins by SDF-1/CXC12 increases the aggressiveness of prostate cancer cells. Prostate 67, 61–73. https://doi.org/10.1002/pros.20500

Sun, Y.-X., Schneider, A., Jung, Y., Wang, Jianhua, Dai, J., Wang, Jingcheng, Cook, K., Osman, N.I., Koh-Paige, A.J., Shim, H., Pienta, K.J., Keller, E.T., McCauley, L.K., Taichman, R.S., 2005. Skeletal Localization and Neutralization of the SDF-1(CXCL12)/CXCR4 Axis Blocks Prostate Cancer Metastasis and Growth in Osseous Sites In Vivo. Journal of Bone and Mineral Research 20, 318–329. https://doi.org/10.1359/JBMR.041109

Swanson, P.A., McGavern, D.B., 2015. Portals of Viral Entry into the Central Nervous System, in: The Blood-Brain Barrier in Health and Disease, Volume Two. CRC Press.

Szentivanyi, A., Chakradeo, T., Zernetsch, H., Glasmacher, B., 2011. Electrospun cellular microenvironments: Understanding controlled release and scaffold structure. Advanced Drug Delivery Reviews, FROM TISSUE ENGINEERING TO REGENERATIVE MEDICINE - THE POTENTIAL AND THE PITFALLS 63, 209–220. https://doi.org/10.1016/j.addr.2010.12.002

Tamimi, A.F., Juweid, M., 2017. Epidemiology and Outcome of Glioblastoma, in: De Vleeschouwer, S. (Ed.), Glioblastoma. Codon Publications, Brisbane (AU).

Tang, X., Fu, X., Liu, Y., Yu, D., Cai, S.J., Yang, C., 2020. Blockade of Glutathione Metabolism in IDH1-Mutated Glioma. Molecular Cancer Therapeutics 19, 221–230. https://doi.org/10.1158/1535-7163.MCT-19-0103

Teicher, B.A., Fricker, S.P., 2010. CXCL12 (SDF-1)/CXCR4 Pathway in Cancer. Clinical Cancer Research 16, 2927–2931. https://doi.org/10.1158/1078-0432.CCR-09-2329

Thakkar, J.P., Dolecek, T.A., Horbinski, C., Ostrom, Q.T., Lightner, D.D., Barnholtz-Sloan, J.S., Villano, J.L., 2014. Epidemiologic and Molecular Prognostic Review of Glioblastoma. Cancer Epidemiology, Biomarkers & Prevention 23, 1985–1996. https://doi.org/10.1158/1055-9965.EPI-14-0275

Thakkar, J.P., Peruzzi, P.P., Prabhu, V.C., 2023. Glioblastoma Multiforme – Symptoms, Diagnosis and Treatment Options [WWW Document]. URL https://www.aans.org/ (accessed 1.23.23).

Tian, T., Liang, R., Erel-Akbaba, G., Saad, L., Obeid, P.J., Gao, J., Chiocca, E.A., Weissleder, R., Tannous, B.A., 2022. Immune Checkpoint Inhibition in GBM Primed with Radiation by Engineered Extracellular Vesicles. ACS Nano 16, 1940–1953. https://doi.org/10.1021/acsnano.1c05505

Toussaint, L.G., Nilson, A.E., Goble, J.M., Ballman, K.V., James, C.D., Lefranc, F., Kiss, R., Uhm, J.H., 2012. Galectin-1, a gene preferentially expressed at the tumor margin, promotes glioblastoma cell invasion. Molecular Cancer 11, 32. https://doi.org/10.1186/1476-4598-11-32

Tran, M.-K., Swed, A., Boury, F., 2012. Preparation of polymeric particles in CO(2) medium using non-toxic solvents: formulation and comparisons with a phase separation method. Eur J Pharm Biopharm 82, 498–507. https://doi.org/10.1016/j.ejpb.2012.08.005

Tsao, C.-T., Kievit, F.M., Ravanpay, A., Erickson, A.E., Jensen, M.C., Ellenbogen, R.G., Zhang, M., 2014. Thermoreversible Poly(ethylene glycol)-g-Chitosan Hydrogel as a Therapeutic T Lymphocyte Depot for Localized Glioblastoma Immunotherapy. Biomacromolecules 15, 2656–2662. https://doi.org/10.1021/bm500502n

Urbańska, K., Sokołowska, J., Szmidt, M., Sysa, P., 2014. Glioblastoma multiforme - an overview. Contemp Oncol (Pozn) 18, 307–312. https://doi.org/10.5114/wo.2014.40559

Valluzzi, R., Gido, S.P., Muller, W., Kaplan, D.L., 1999. Orientation of silk III at the air-water interface. International Journal of Biological Macromolecules 24, 237–242. https://doi.org/10.1016/S0141-8130(99)00002-1

Van Der Sanden, B., Appaix, F., Berger, F., Selek, L., Issartel, J.-P., Wion, D., 2013. Translation of the ecological trap concept to glioma therapy: the cancer cell trap concept. Future Oncol 817–824. https://doi.org/10.2217/fon.13.30

Vepari, C., Kaplan, D.L., 2007. Silk as a Biomaterial. Prog Polym Sci 32, 991–1007. https://doi.org/10.1016/j.progpolymsci.2007.05.013

Viera Rey, D.F., St-Pierre, J.-P., 2019. 6 - Fabrication techniques of tissue engineering scaffolds, in: Mozafari, M., Sefat, F., Atala, A. (Eds.), Handbook of Tissue Engineering Scaffolds: Volume One, Woodhead Publishing Series in Biomaterials. Woodhead Publishing, pp. 109–125. https://doi.org/10.1016/B978-0-08-102563-5.00006-X

Vigetti, D., Karousou, E., Viola, M., Deleonibus, S., De Luca, G., Passi, A., 2014. Hyaluronan: biosynthesis and signaling. Biochim Biophys Acta 1840, 2452–2459. https://doi.org/10.1016/j.bbagen.2014.02.001

Visvader, J.E., 2011. Cells of origin in cancer. Nature 469, 314–322. https://doi.org/10.1038/nature09781

Wang, S., Chen, C., Li, J., Xu, X., Chen, W., Li, F., 2020. The CXCL12/CXCR4 axis confers temozolomide resistance to human glioblastoma cells via up-regulation of FOXM1. Journal of the Neurological Sciences 414, 116837. https://doi.org/10.1016/j.jns.2020.116837

Wang, T.-J., Huang, M.-S., Hong, C.-Y., Tse, V., Silverberg, G.D., Hsiao, M., 2001. Comparisons of Tumor Suppressor p53, p21, and p16 Gene Therapy Effects on Glioblastoma Tumorigenicity in Situ. Biochemical and Biophysical Research Communications 287, 173–180. https://doi.org/10.1006/bbrc.2001.5565

Wei, X., Senanayake, T.H., Warren, G., Vinogradov, S.V., 2013. Hyaluronic Acid-Based Nanogel–Drug Conjugates with Enhanced Anticancer Activity Designed for the Targeting of CD44-Positive and Drug-Resistant Tumors. Bioconjugate Chem. 24, 658–668. https://doi.org/10.1021/bc300632w

Weigelt, B., Peterse, J.L., van't Veer, L.J., 2005. Breast cancer metastasis: markers and models. Nat Rev Cancer 5, 591–602. https://doi.org/10.1038/nrc1670

Weilbaecher, K.N., Guise, T.A., McCauley, L.K., 2011. Cancer to bone: a fatal attraction. Nat Rev Cancer 11, 411–425. https://doi.org/10.1038/nrc3055

Weller, M., Butowski, N., Tran, D.D., Recht, L.D., Lim, M., Hirte, H., Ashby, L., Mechtler, L., Goldlust, S.A., Iwamoto, F., Drappatz, J., O'Rourke, D.M., Wong, M., Hamilton, M.G., Finocchiaro, G., Perry, J., Wick, W., Green, J., He, Y., Turner, C.D., Yellin, M.J., Keler, T., Davis, T.A., Stupp, R., Sampson, J.H., Butowski, N., Campian, J., Recht, L., Lim, M., Ashby, L., Drappatz, J., Hirte, H., Iwamoto, F., Mechtler, L., Goldlust, S., Becker, K., Barnett, G., Nicholas, G., Desjardins, A., Benkers, T., Wagle, N., Groves, M., Kesari, S., Horvath, Z., Merrell, R., Curry, R., O'Rourke, J., Schuster, D., Wong, M., Mrugala, M., Jensen, R., Trusheim, J., Lesser, G., Belanger, K., Sloan, A., Purow, B., Fink, K., Raizer, J., Schulder, M., Nair, S., Peak, S., Perry, J., Brandes, A., Weller, M., Mohile, N., Landolfi, J., Olson, J., Finocchiaro, G., Jennens, R., DeSouza, P., Robinson, B., Crittenden, M., Shih, K., Flowers, A., Ong, S., Connelly, J., Hadjipanayis, C., Giglio, P., Mott, F., Mathieu, D., Lessard, N., Sepulveda, S.J., Lövey, J., Wheeler, H., Inglis, P.-L., Hardie, C., Bota, D., Lesniak, M., Portnow, J., Frankel, B., Junck, L., Thompson, R., Berk, L., McGhie, J., Macdonald, D., Saran, F., Soffietti, R., Blumenthal, D., André de, S.B.C.M., Nowak, A., Singhal, N., Hottinger, A., Schmid, A., Srkalovic, G., Baskin, D., Fadul, C., Nabors, L., LaRocca, R., Villano, J., Paleologos, N., Kavan, P., Pitz, M., Thiessen, B., Idbaih, A., Frenel, J.S., Domont, J., Grauer, O., Hau, P., Marosi, C., Sroubek, J., Hovey, E., Sridhar, P.S., Cher, L., Dunbar, E., Coyle, T., Raymond, J., Barton, K., Guarino, M., Raval, S., Stea, B., Dietrich, J., Hopkins, K., Erridge, S., Steinbach, J.-P., Pineda, L.E., Balana, Q.C., Sonia del, B.B., Wenczl, M., Molnár, K., Hideghéty, K., Lossos, A., Myra van, L., Levy, A., Harrup, R., Patterson, W., Lwin, Z., Sathornsumetee, S., Lee, E.-J., Ho, J.-T., Emmons, S., Duic, J.P., Shao, S., Ashamalla, H., Weaver, M., Lutzky, J., Avgeropoulos, N., Hanna, W., Nadipuram, M., Cecchi, G., O'Donnell, R., Pannullo, S., Carney, J., Hamilton, M., MacNeil, M., Beaney, R., Fabbro, M., Schnell, O., Fietkau, R., Stockhammer, G., Malinova, B., Odrazka, K., Sames, M., Miguel Gil, G., Razis, E., Lavrenkov, K., Castro, G., Ramirez, F., Baldotto, C., Viola, F., Malheiros, S., Lickliter, J., Gauden, S., Dechaphunkul, A., Thaipisuttikul, I., Thotathil, Z., Ma, H.-I., Cheng, W.-Y., Chang, C.-H., Salas, F., Dietrich, P.-Y., Mamot, C., Nayak, L., Nag, S., 2017. Rindopepimut with temozolomide for patients with newly diagnosed, EGFRvIII-expressing glioblastoma (ACT IV): a randomised, double-blind, international phase 3 trial. The Lancet Oncology 18, 1373–1385. https://doi.org/10.1016/S1470-2045(17)30517-X

Weller, M., Le Rhun, E., 2020. How did lomustine become standard of care in recurrent glioblastoma? Cancer Treatment Reviews 87, 102029. https://doi.org/10.1016/j.ctrv.2020.102029

Westphal, M., Hilt, D.C., Bortey, E., Delavault, P., Olivares, R., Warnke, P.C., Whittle, I.R., Jääskeläinen, J., Ram, Z., 2003. A phase 3 trial of local chemotherapy with biodegradable carmustine (BCNU) wafers (Gliadel wafers) in patients with primary malignant glioma. Neuro-Oncology 5, 79–88. https://doi.org/10.1093/neuonc/5.2.79

Wick, W., Brandes, AA., Gorlia, T., Bendszus, M., Sahm, F., Taal, W., Taphoorn, M., Domont, J., Idbaih, A., Campone, M., Clement, P.M., Stupp, R., Fabbro, M., Dubois, F., Bais, C., Musmeci, D., Platten, M., Weller, M., Golfinopoulos, V., van den Bent, M., 2015. LB-05PHASE III TRIAL EXPLORING THE COMBINATION OF BEVACIZUMAB AND LOMUSTINE IN PATIENTS WITH FIRST RECURRENCE OF A GLIOBLASTOMA: THE EORTC 26101 TRIAL. Neuro-Oncology 17, v1. https://doi.org/10.1093/neuonc/nov306

Wick, W., Gorlia, T., Bendszus, M., Taphoorn, M., Sahm, F., Harting, I., Brandes, A.A., Taal, W., Domont, J., Idbaih, A., Campone, M., Clement, P.M., Stupp, R., Fabbro, M., Le Rhun, E., Dubois, F., Weller, M., von Deimling, A., Golfinopoulos, V., Bromberg, J.C., Platten, M., Klein, M., van den Bent, M.J., 2017. Lomustine and Bevacizumab in Progressive Glioblastoma. New England Journal of Medicine 377, 1954–1963. https://doi.org/10.1056/NEJMoa1707358

Wilson, D., Valluzzi, R., Kaplan, D., 2000. Conformational transitions in model silk peptides. Biophys J 78, 2690–2701. https://doi.org/10.1016/S0006-3495(00)76813-5

Wolf, K., Te Lindert, M., Krause, M., Alexander, S., Te Riet, J., Willis, A.L., Hoffman, R.M., Figdor, C.G., Weiss, S.J., Friedl, P., 2013. Physical limits of cell migration: control by ECM space and

nuclear deformation and tuning by proteolysis and traction force. J Cell Biol 201, 1069–1084. https://doi.org/10.1083/jcb.201210152

Xu, H.-L., ZhuGe, D.-L., Chen, P.-P., Tong, M.-Q., Lin, M.-T., Jiang, X., Zheng, Y.-W., Chen, B., Li, X.-K., Zhao, Y.-Z., 2018. Silk fibroin nanoparticles dyeing indocyanine green for imaging-guided photo-thermal therapy of glioblastoma. Drug Delivery 25, 364–375. https://doi.org/10.1080/10717544.2018.1428244

Xu, W., Yang, H., Liu, Y., Yang, Y., Wang, Ping, Kim, S.-H., Ito, S., Yang, C., Wang, Pu, Xiao, M.-T., Liu, L., Jiang, W., Liu, J., Zhang, J., Wang, B., Frye, S., Zhang, Y., Xu, Y., Lei, Q., Guan, K.-L., Zhao, S., Xiong, Y., 2011. Oncometabolite 2-Hydroxyglutarate Is a Competitive Inhibitor of α-Ketoglutarate-Dependent Dioxygenases. Cancer Cell 19, 17–30. https://doi.org/10.1016/j.ccr.2010.12.014

Xu, Xiuling, Chen, X., Xu, Xiaoyi, Lu, T., Wang, X., Yang, L., Jing, X., 2006. BCNU-loaded PEG–PLLA ultrafine fibers and their in vitro antitumor activity against Glioma C6 cells. Journal of Controlled Release 114, 307–316. https://doi.org/10.1016/j.jconrel.2006.05.031

Yadav, V.N., Zamler, D., Baker, G.J., Kadiyala, P., Erdreich-Epstein, A., DeCarvalho, A.C., Mikkelsen, T., Castro, M.G., Lowenstein, P.R., 2016. CXCR4 increases in-vivo glioma perivascular invasion, and reduces radiation induced apoptosis: A genetic knockdown study. Oncotarget 7, 83701–83719. https://doi.org/10.18632/oncotarget.13295

Yamahara, T., Numa, Y., Oishi, T., Kawaguchi, T., Seno, T., Asai, A., Kawamoto, K., 2010. Morphological and flow cytometric analysis of cell infiltration in glioblastoma: a comparison of autopsy brain and neuroimaging. Brain Tumor Pathol 27, 81–87. https://doi.org/10.1007/s10014-010-0275-7

Yan, H., Parsons, D.W., Jin, G., McLendon, R., Rasheed, B.A., Yuan, W., Kos, I., Batinic-Haberle, I., Jones, S., Riggins, G.J., Friedman, H., Friedman, A., Reardon, D., Herndon, J., Kinzler, K.W., Velculescu, V.E., Vogelstein, B., Bigner, D.D., 2009. IDH1 and IDH2 Mutations in Gliomas. New England Journal of Medicine 360, 765–773. https://doi.org/10.1056/NEJMoa0808710

Yan, H.H., Pickup, M., Pang, Y., Gorska, A.E., Li, Z., Chytil, A., Geng, Y., Gray, J.W., Moses, H.L., Yang, L., 2010. Gr-1+CD11b+ Myeloid Cells Tip the Balance of Immune Protection to Tumor Promotion in the Premetastatic Lung. Cancer Research 70, 6139–6149. https://doi.org/10.1158/0008-5472.CAN-10-0706

Yeini, E., Ofek, P., Albeck, N., Rodriguez Ajamil, D., Neufeld, L., Eldar-Boock, A., Kleiner, R., Vaskovich, D., Koshrovski-Michael, S., Dangoor, S.I., Krivitsky, A., Burgos Luna, C., Shenbach-Koltin, G., Goldenfeld, M., Hadad, O., Tiram, G., Satchi-Fainaro, R., 2021. Targeting Glioblastoma: Advances in Drug Delivery and Novel Therapeutic Approaches. Advanced Therapeutics 4, 2000124. https://doi.org/10.1002/adtp.202000124

Yoo, H.S., Kim, T.G., Park, T.G., 2009. Surface-functionalized electrospun nanofibers for tissue engineering and drug delivery. Advanced Drug Delivery Reviews, Nanofibers in Regenerative Medicine and Drug Delivery 61, 1033–1042. https://doi.org/10.1016/j.addr.2009.07.007

Zagzag, D., Esencay, M., Mendez, O., Yee, H., Smirnova, I., Huang, Y., Chiriboga, L., Lukyanov, E., Liu, M., Newcomb, E.W., 2008. Hypoxia- and vascular endothelial growth factor-induced stromal cell-derived factor-1alpha/CXCR4 expression in glioblastomas: one plausible explanation of Scherer's structures. Am J Pathol 173, 545–560. https://doi.org/10.2353/ajpath.2008.071197

Zarrintaj, P., Ramsey, J.D., Samadi, A., Atoufi, Z., Yazdi, M.K., Ganjali, M.R., Amirabad, L.M., Zangene, E., Farokhi, M., Formela, K., Saeb, M.R., Mozafari, M., Thomas, S., 2020. Poloxamer: A versatile tri-block copolymer for biomedical applications. Acta Biomaterialia 110, 37–67. https://doi.org/10.1016/j.actbio.2020.04.028

Zhang, S., Gan, L., Cao, F., Wang, H., Gong, P., Ma, C., Ren, L., Lin, Y., Lin, X., 2022. The barrier and interface mechanisms of the brain barrier, and brain drug delivery. Brain Research Bulletin 190, 69–83. https://doi.org/10.1016/j.brainresbull.2022.09.017

Zhou, Y., Larsen, P.H., Hao, C., Yong, V.W., 2002. CXCR4 is a major chemokine receptor on glioma cells and mediates their survival. J Biol Chem 277, 49481–49487. https://doi.org/10.1074/jbc.M206222200

Zong, H., Parada, L.F., Baker, S.J., 2015. Cell of Origin for Malignant Gliomas and Its Implication in Therapeutic Development. Cold Spring Harb Perspect Biol a020610. https://doi.org/10.1101/cshperspect.a020610

Zubair, A., De Jesus, O., 2023. Ommaya Reservoir, in: StatPearls. StatPearls Publishing, Treasure Island (FL).

Chapter 2:
Thesis aim and objectives

2. Thesis aim and objectives

Glioblastoma is a lethal cancer and novel approaches are needed to improve the survival of patients. The infiltrative nature of residual GB cells after resection might be exploited by attracting them towards a lure. It has been reported that infiltrative GBM cells overexpress the C-X-C chemokine receptor type 4 (CXCR4) (Ehtesham et al., 2006; Zagzag et al., 2008; Zhou et al., 2002). This receptor binds the chemoattractant stromal cell-derived factor 1 α (SDF-1α). A gradient of this chemokine induces an attraction of GB cells expressing the CXCR4 receptor (Bian et al., 2007; Hira et al., 2017; Kim et al., 2016; Tabouret et al., 2015; Zhou et al., 2002). Therefore***, the hypothesis is that it might be possible to attract and confine infiltrative glioblastoma cells in a trap by implanting a scaffold inside the resection cavity that makes available a gradient of SDF-1α. The aim of this thesis is therefore to evaluate two different biodeposits containing SDF-1a as means of luring them toward a confined site in the resection cavity (Figure 2.1).***

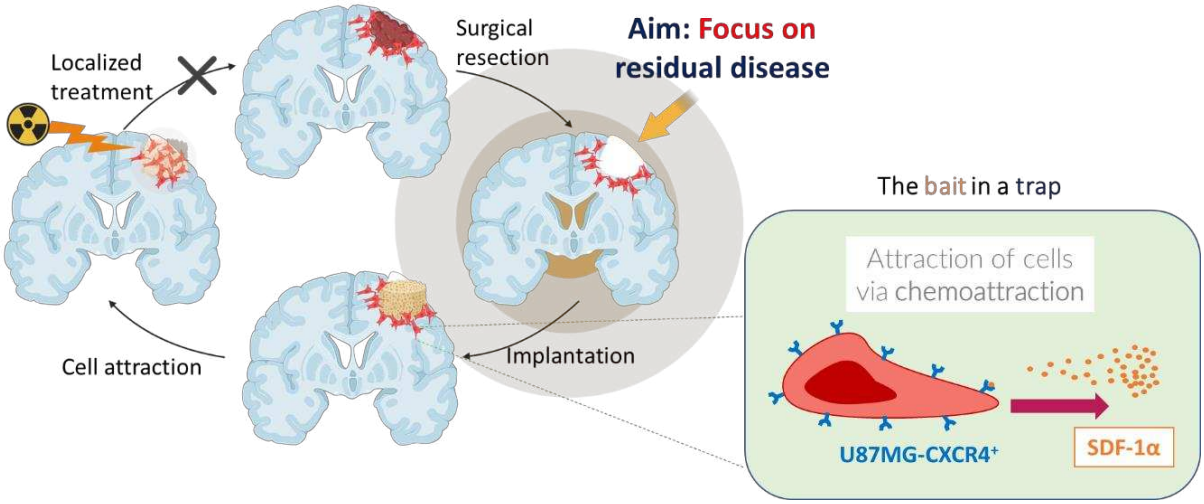

Figure 2.1. Evaluation of scaffolds as glioblastoma cell traps. The focus is on residual disease. The aim is to evaluate an interactive scaffold containing SDF-1α as a means to attract CXCR4-expressing GB cells.

2.1. Research questions

To inquiry about this hypothesis, the following questions are addressed:

1. Can glioblastoma cells be attracted by SDF-1α?

1.1. What GB cell lines express the CXCR4 receptor?

1.2. Can a GB model cell line with stable expression of CXCR4 be established?

1.3. Is the cell line responsive to SDF-1α by activation of relevant pathways?

1.4. Is the cell line responsive to SDF-1α in a functional assay of migration?

2. What kind of scaffold can be employed as a biointeractive deposit as a glioblastoma cell trap?

2.1. What biomaterials could be used for implantation in the brain cortex?

2.2. Is scaffold biocompatible?

2.3. What is its biodegradability? Does it last enough in physiological conditions to serve as a sink to receive cancer cells?

2.4. Does it release the bait (SDF-1α) to make available a chemoattraction gradient?

3. What is the bioperformance of the scaffold *in vitro*?

3.1. What kind of *in vitro* model is the most suitable according to the biological question?

3.2. Do cancer cells interact with the scaffolds by direct seeding? What is the cancer cell adhesion capacity of scaffolds?

3.3. Can the scaffold attract GB cells *in vitro*?

3.4. Can the scaffolds be colonized by cancer cells *in vitro*?

4. What is the bioperformance of the scaffold *in vivo*?

4.1. What animal model can be used to study the residual disease of GB?

4.2. Can the scaffold attract GB cells *in vivo*?

4.3. How do tumors behave in the presence of scaffolds?

4.4. What is the effect of the scaffold on survival?

2.2. General and specific objectives

Two different novel scaffolds releasing SDF-1α to be tested as GBM cell traps have been developed in our lab. The first scaffold is a silk fibroin (SF) with hyaluronic acid (HA) and heparin (Hep) (SF-HA-Hep) sponge, where heparin acts as a complexation agent for SDF-1α (Najberg et al., 2020). The second consists of nano-precipitated SDF-1α encapsulated in PLGA-PEG nanoparticles embedded in an electrospun chitosan fibrous matrix (Haji Mansor et al., 2018; Molina-Peña et al., 2021).

The general and specific objectives of this thesis are therefore:

1. **Scaffolds' synthesis**
   - 1.1. To produce SF-HA-Hep sponges (collaboration with Dr. Carmen Alvarez-Lorenzo, University of Santiago de Compostela, Spain) so that they are structurally stable, with high porosity and good pore connectivity.
   - 1.2. To produce nanofibrous chitosan scaffolds containing SDF-1α-loaded PLGA nanoparticles (collaboration with Prof. Christine Jérôme, University of Liege, Belgium).
2. **Selection of a cellular model**
   - 2.1. To *characterize different glioblastoma cell lines* for the expression of the CXCR4 receptor.
   - 2.2. To establish a cell line constitutively expressing the CXCR4 receptor and a fluorescent marker (Red fluorescent protein, RFP) to facilitate their tracking.
   - 2.3. To characterize their **molecular response** to SDF-1α (activation of relevant pathways) by Western blotting analysis.
   - 2.4. To characterize their **functional response** to SDF-1α by using Boyden chamber, agarose drop, and agarose spot bioassays.
3. **Development of an *in vivo* model**
   - 3.1. Development of an orthotopic/resection model for U87MG-CXCR4$^+$ tumors in nude rats.
   - 3.2. Development of a syngeneic orthotopic/resection model for RG2 tumors in Fischer rats.
4. **Evaluation of scaffold biodegradability and cytocompatibility**
   - 4.1. To evaluate the **scaffold's biodegradability** *in vitro* by incubation in an appropriate buffer; and *in vivo* by implantation of scaffolds in the resection cavity, and further measurement of the scaffold's volume by magnetic resonance imaging (MRI), and assessment of their biodegradation by histological analysis.
   - 4.2. To evaluate their **cytocompatibility** *in vitro* by testing the direct and indirect contact methods on relevant cell lines; and *in vivo* by short-term (1 week) and long-term (3

months) histological analyses of the immunological response in the implantation zone and the brain resection periphery.

5. **Evaluation of the *in vitro* bioperformance of scaffolds**

   5.1. To evaluate the interaction of GBM cells with scaffolds, by testing their *in-vitro* cell **adhesion capacity** by assessing the viability of adhered cells by the MTS assay; and by revealing the cell/bio-interphase contact interactions by electron microscopy.

   5.2. To evaluate their **capacity to attract glioblastoma cells** from a distant site *in vitro*, by using an under-agarose migration assay to observe and quantify the directional migration of cells towards the scaffolds versus controls.

   5.3. To evaluate their **capacity to host infiltrative glioblastoma cells** *in vitro*, by using a glioma-spheroid assay to observe the infiltration of GBM cells in direct contact with the scaffolds.

6. **Evaluation of the bioperformance of scaffolds *in vivo***

   6.1. To evaluate their **capacity to attract and host infiltrative glioblastoma cells from the resection edges** of the resection cavity of a tumor: by implantation of scaffolds in the tumor resection cavity.

   6.2. To evaluate their **capacity to attract glioblastoma cells from a distant site** from the scaffold: by implantation of cells and scaffolds separated by either 1-mm or 3-mm distances.

2.3. General plan flow chart

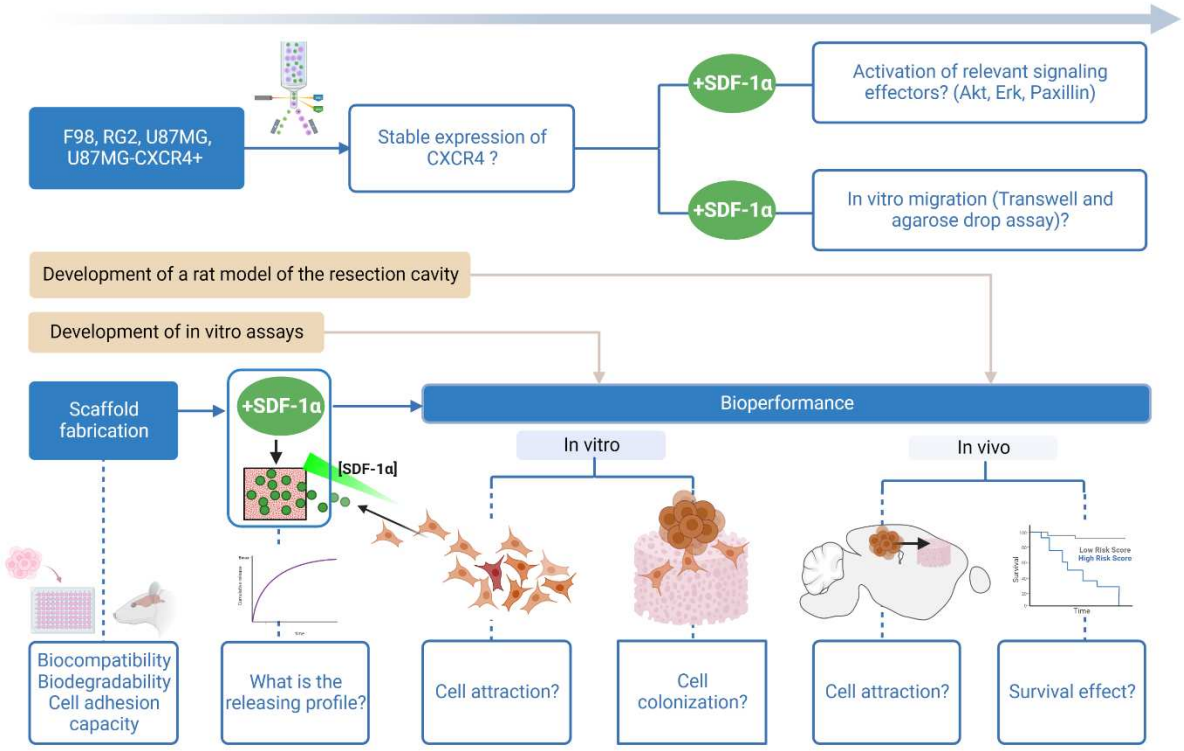

Figure 2.2. Flow chart for the evaluation of scaffolds as glioblastoma cell traps. The timeline on top indicates early events and rows are considered steps done in parallel. Therefore, the first step consisted of the characterization of different cell lines and the establishment of a cell line with stable expression of CXCR4. The next steps consisted of the evaluation of the response of cells expressing the CXCR4 receptor to SDF-1α. The synthesis of scaffolds was achieved with collaborations; and their biocompatibility, biodegradability, and adhesion capacity were performed during this work. In parallel, the development of *in vitro* models and an *in vivo* model to evaluate the scaffolds' bioperformance was done. Created with Biorender.

2.4. Overview of the presented polymeric scaffolds

As presented in the objectives of this thesis, two polymeric systems have been developed in our laboratory. The luring principle that is aimed to be exploited is based on the SDF-1α/CXCR4 axis for both types of scaffolds. Hence, they both are designed to contain SDF-1α. The first system consists of porous sponges fabricated by lyophilization (collaboration with Dr. Carmen Alvarez-Lorenzo, U. of Santiago de Compostela) made of silk fibroin (SF), hyaluronic acid (HA), and heparin (Hep). SF is used as the main structural component, HA is used also as a structural component but in addition it provides a biomimetic aspect, and Hep is used as a complexation agent for SDF-1α. The second scaffold consists of fiber mats fabricated by electrospinning (collaboration with Prof. Christine Jerôme, U. of Liège). The main structural component is chitosan fibers, into which PLGA nanoparticles have been incorporated containing SDF-1α. As observed (Figure 2.3) the systems are completely different in terms of structure and composition, therefore, in the present work, their pros and cons as implantable devices serving to attract glioblastoma cells are aimed to be compared.

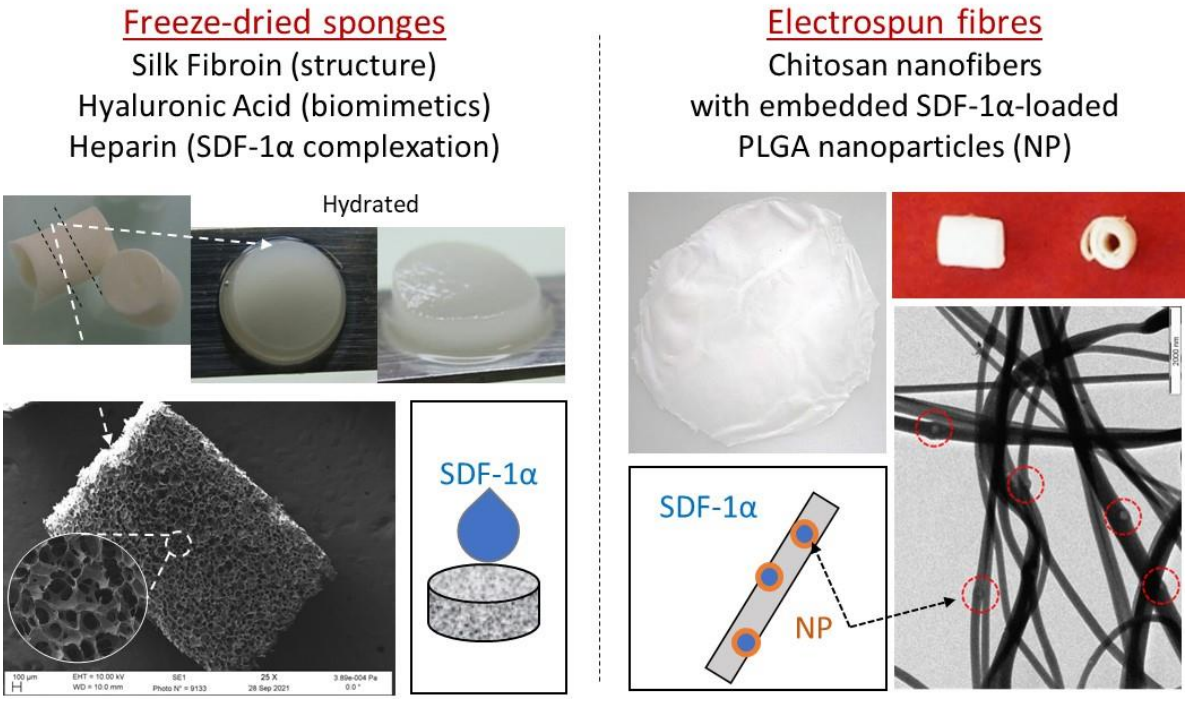

Figure 2.3. Polymeric scaffolds for evaluation as glioblastoma cell traps. Left panel: silk fibroin hyaluronic acid aerogel freeze-dried sponges. Right panel: chitosan electrospun fibers with embedded nanoparticles (NP). The loading of SDF-1α is performed by complexation in the case of sponges, whereas electrospun mats contain chitosan nanofibers with embedded nanoparticles containing SDF-1α.

2.5. References

Bian, X., Yang, S., Chen, J., Ping, Y., Zhou, X., Wang, Q., Jiang, X., Gong, W., Xiao, H., Du, L., Chen, Z., Zhao, W., Shi, J., Wang, J.M., 2007. PREFERENTIAL EXPRESSION OF CHEMOKINE RECEPTOR CXCR4 BY HIGHLY MALIGNANT HUMAN GLIOMAS AND ITS ASSOCIATION WITH POOR PATIENT SURVIVAL. Neurosurgery 61, 570–579. https://doi.org/10.1227/01.NEU.0000290905.53685.A2

Ehtesham, M., Winston, J.A., Kabos, P., Thompson, R.C., 2006. CXCR4 expression mediates glioma cell invasiveness. Oncogene 25, 2801–2806. https://doi.org/10.1038/sj.onc.1209302

Haji Mansor, M., Najberg, M., Contini, A., Alvarez-Lorenzo, C., Garcion, E., Jérôme, C., Boury, F., 2018. Development of a non-toxic and non-denaturing formulation process for encapsulation of SDF-1α into PLGA/PEG-PLGA nanoparticles to achieve sustained release. Eur J Pharm Biopharm 125, 38–50. https://doi.org/10.1016/j.ejpb.2017.12.020

Hira, V.V.V., Verbovšek, U., Breznik, B., Srdič, M., Novinec, M., Kakar, H., Wormer, J., der Swaan, B.V., Lenarčič, B., Juliano, L., Mehta, S., Van Noorden, C.J.F., Lah, T.T., 2017. Cathepsin K cleavage of SDF-1α inhibits its chemotactic activity towards glioblastoma stem-like cells. Biochim Biophys Acta Mol Cell Res 1864, 594–603. https://doi.org/10.1016/j.bbamcr.2016.12.021

Kim, H., Roh, H.S., Kim, J.E., Park, S.D., Park, W.H., Moon, J.-Y., 2016. Compound K attenuates stromal cell-derived growth factor 1 (SDF-1)-induced migration of C6 glioma cells. Nutr Res Pract 10, 259–264. https://doi.org/10.4162/nrp.2016.10.3.259

Molina-Peña, R., Haji Mansor, M., Najberg, M., Thomassin, J.-M., Gueza, B., Alvarez-Lorenzo, C., Garcion, E., Jérôme, C., Boury, F., 2021. Nanoparticle-containing electrospun nanofibrous scaffolds for sustained release of SDF-1α. Int J Pharm 610, 121205. https://doi.org/10.1016/j.ijpharm.2021.121205

Najberg, M., Haji Mansor, M., Taillé, T., Bouré, C., Molina-Peña, R., Boury, F., Cenis, J.L., Garcion, E., Alvarez-Lorenzo, C., 2020. Aerogel sponges of silk fibroin, hyaluronic acid and heparin for soft tissue engineering: Composition-properties relationship. Carbohydrate Polymers 237, 116107. https://doi.org/10.1016/j.carbpol.2020.116107

Tabouret, E., Tchoghandjian, A., Denicolai, E., Delfino, C., Metellus, P., Graillon, T., Boucard, C., Nanni, I., Padovani, L., Ouafik, L., Figarella-Branger, D., Chinot, O., 2015. Recurrence of glioblastoma after radio-chemotherapy is associated with an angiogenic switch to the CXCL12-CXCR4 pathway. Oncotarget 6, 11664–11675.

Zagzag, D., Esencay, M., Mendez, O., Yee, H., Smirnova, I., Huang, Y., Chiriboga, L., Lukyanov, E., Liu, M., Newcomb, E.W., 2008. Hypoxia- and vascular endothelial growth factor-induced stromal cell-derived factor-1alpha/CXCR4 expression in glioblastomas: one plausible explanation of Scherer's structures. Am J Pathol 173, 545–560. https://doi.org/10.2353/ajpath.2008.071197

Zhou, Y., Larsen, P.H., Hao, C., Yong, V.W., 2002. CXCR4 is a major chemokine receptor on glioma cells and mediates their survival. J Biol Chem 277, 49481–49487. https://doi.org/10.1074/jbc.M206222200

Chapter 3:

Development and evaluation of silk fibroin hyaluronic acid aerogel sponges

3. Development and evaluation of silk fibroin hyaluronic acid aerogel sponges

3.1. Introduction

This chapter concerns the synthesis and evaluation of aerogel sponges as an implantable device for the trapping of glioblastoma cells. The process of synthesis was the subject of the thesis by (Najberg et al., 2020) (See the publication in **Annexes**). In this thesis, the process of production is retaken, and the synthesis is performed in collaboration with Dr. Alvarez-Lorenzo at the University of Santiago de Compostela in Spain. In summary, the process involves the production of a gel in which the watery component is replaced by air (aerogel), forming a sponge. This is achieved by mixing the three components: silk fibroin (SF), hyaluronic acid (HA), and heparin (Hep), followed by crosslinking by amide bonding, and finally by lyophilization. This creates porous sponges with an average pore size of 69 µm. Compared to hydrogels, these sponges are easily hydrated and can fit cavities providing solid support which is an advantage for the looked application. SDF-1α is loaded into the sponges by depositing a drop of the chemoattractant solution, afterwards, SDF-1α is complexed with its heparin-binding domain (Najberg et al., 2020). The releasing profile of SDF-1α was completed during this work and included in the previously published paper (Annexes). In addition, the *in vitro* and *in vivo* biocompatibility and biodegradability were completed as well as their bioperformance (See flow chart, **Fig. 2.2** in **Chapter 2**). To achieve this, different *in vitro* models were used including an under-agarose migration assay and a neurospheroid colonization assay. In addition, an *in vivo* model of the resection cavity in rats was developed and tumor evolution was followed by MRI.

3.2. CXCR4 expressing cell lines

GBM human U87MG, U87MG-CXCR4+, and rat F98 and RG2 cells were evaluated by flow cytometry for expression of the CXCR4 receptor under standard 2D culture conditions (**Table 3.1**). To produce U87MG-CXCR4+ cells, the parental cell line was transduced with the following construction:

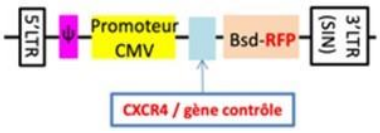

Figure 3.1

Sorted CXCR4+/RFP(red fluorescent protein)+ high cells were kept for further experiments and checked for stable expression of CXCR4 during different passages. These cells when cultured in 3D spheroid conditions maintained the expression of both CXCR4 and RFP (**Table 3.1**).

Table 3.1. Model cell lines

Cell line	Organism	Nature	CXCR4 expression (as assessed by FC)	Tumorgenicity in rats? (Our data)
U87MG	Human	Parental	No	Yes (Nude rats)
U87MG-CXCR4+	Human	Transduced for CXCR4 and RFP	++++ Both in 2D and 3D culture conditions	Yes (Nude rats)
RG2	Rat	Parental	++	Yes (Fischer rats)
F98	Rat	Parental	++	Yes (Fischer rats)

3.3. Orthotopic model

U87MG-CXCR4+ cells were selected for *in vivo* experiments since they presented a stable expression of the CXCR4 receptor and they have been demonstrated to be infiltrative into the brain parenchyma (Séhédic et al., 2017). U87MG-CXCR4+ cells were implanted in the cortex of nude rats and evaluation of tumor formation was assessed by MRI. The optimal concentration was 5 x 10^3 cells, with the endpoint reached by day 21. Similarly, for the syngeneic model, 5 x 10^3 RG2 cells were implanted in Fischer rats, with the endpoint reached by day 21.

A resection protocol was implemented in the right hemisphere. A burr hole was made using a high-speed driller and the brain tissue was cut using a biopsy punch. The cut brain was then aspirated with a needle. For evaluation of biocompatibility and biodegradability, the scaffolds were implanted in the resection cavities of Fischer rats, and animals were euthanized after 1 week and 3 months.

For the evaluation of the scaffolds' *in-vivo* bioperformance, two types of experiments were set. The first was the resection of tumors after 10 days of cell inoculation, followed by the implantation of scaffolds, and evaluation of the scaffolds' cell colonization after 1 week. The second was the placement of scaffolds and cells at distant sites (~ either 1 mm or 3 mm) at the same time to observe if the scaffolds can attract GB cells from different distances.

3.4. Results

3.4.1. Manuscript draft published in Acta Biomaterialia

Implantable SDF-1α-loaded silk fibroin hyaluronic acid aerogel sponges as an instructive component of the glioblastoma ecosystem: between chemoattraction and tumor shaping into resection cavities.

Rodolfo Molina-Peña[1,*], Natalia Helen Ferreira[1,*], Charlotte Roy[1], Loris Roncali[1], Mathie Najberg[1], Sylvie Avril[1], Mariana Zarur[2], William Bourgeois[3], Alba Ferreiros[7], Chiara Lucchi[5], Francesco Cavalieri[4], François Hindré[1], Giovani Tosi[6], Giuseppe Biagini[5], Franco Valzania[4], François Berger[3], Miguel Abal[7], Audrey Rousseau[1], Frank Boury[1], Carmen Alvarez-Lorenzo[2,°,#], Emmanuel Garcion[1,°,#].

[*, °] *Eq contribution*

[1] *Univ Angers, Université de Nantes, Inserm U1307, CRCI2NA, SFR ICAT, F-49000 Angers, France.* [2] *Departamento de Farmacología, Farmacia y Tecnología Farmacéutica, ID Farma (GI-1645), Facultad de Farmacia, and Health Research Institute of Santiago de Compostela (IDIS), Universidade de Santiago de Compostela, 15782 Santiago de Compostela, Spain.*
[3] *Inserm UMR1205, Brain Tech Lab, Grenoble Alpes University Hospital (CHUGA), Grenoble, 38000, France.*
[4] *Neuromotor Department, Neurology Unit, Azienda USL-IRCCS of Reggio Emilia, Reggio Emilia, Italy.*
[5] *Department of Biomedical & Neural Sciences, University of Modena and Reggio Emilia, 41125 Modena, Italy.*
[6] *Department of Life Sciences, University of Modena and Reggio Emilia, 41125 Modena, Italy.*
[7] *NASASBIOTECH S.L., Cantón Grande nº 9, 15003, A Coruña, Spain.*

[#] Corresponding authors e-mail addresses: emmanuel.garcion@univ-angers.fr (E. Garcion); carmen.alvarez.lorenzo@usc.es (C. Alvarez-Lorenzo).

Highlights

- U87MG cells expressing the CXCR4 receptor (U87MG-CXCR4+), are responsive to SDF-1α in a similar molecular pattern to de-novo and recurrent- GB patient-derived cell lines.
- SF-HA-Hep sponges retained SDF-1α *in vivo* acting as a chemokine reservoir.
- SDF-1α-loaded SF-HA-Hep sponges can attract U87MG-CXCR4+ cells *in vitro* and *in vivo*, shaping and localizing tumors into resection cavities.
- SF-HA-Hep sponges are well tolerated *in vivo*, absorbable, and can be colonized by other cell types including chronic inflammatory cells, persisting in resected zones.
- A reproducible rat model has been developed to evaluate locoregional functional effects of bioimplants near infiltrative GB cells in the brain parenchyma.

Graphical abstract

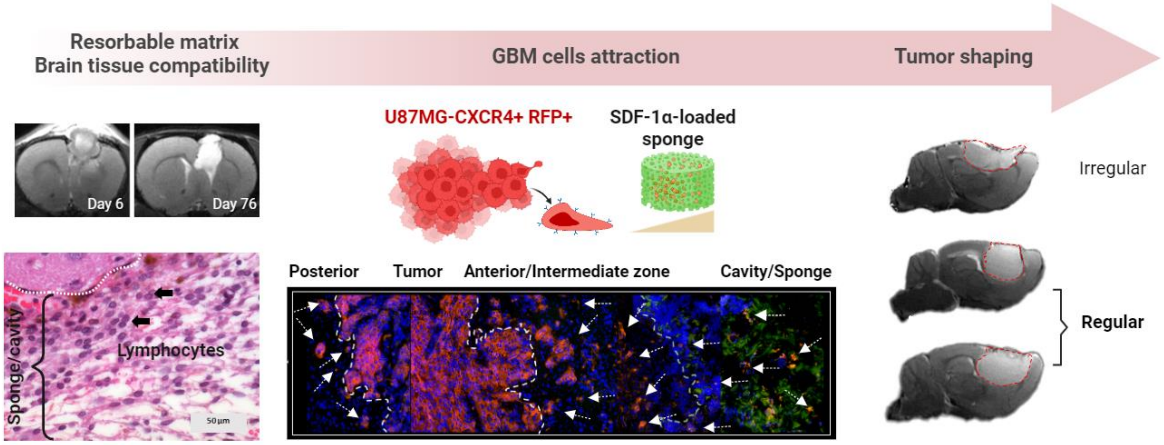

Abstract

In view of inevitable recurrences despite resection, glioblastoma (GB) is still an unmet clinical need. Dealing with the stromal-cell derived factor 1-alpha (SDF-1α)/CXCR4 axis as a hallmark of infiltrative GB tumors and with the resection cavity situation, the present study described the effects and relevance of a new engineered micro-nanostructured SF-HA-Hep aerogel sponges, made of silk fibroin (SF), hyaluronic acid (HA) and heparin (Hep) and loaded with SDF-1α, to interfere with the GB ecosystem and residual GB cells, attracting and confining them in a controlled area before elimination. 70 µm-pore sponges were designed as an implantable scaffold to trap GB cells. They presented shape memory and fit brain cavities. Histological results after implantation in brain immunocompetent Fischer rats revealed that SF-HA-Hep sponges are well tolerated for more than 3 months while moderately and reversibly colonized by immuno-inflammatory cells. The use of human U87MG GB cells overexpressing the CXCR4 receptor (U87MG-CXCR4+) and responding to SDF-1α allowed demonstrating directional GB cell attraction and colonization of the device *in vitro* and *in vivo* in orthotopic resection cavities in Nude rats. Not modifying global survival, aerogel sponge implantation strongly shaped U87MG-CXCR4+ tumors in cavities in contrast to random infiltrative growth in controls. Overall, those results support the interest of SF-HA-Hep sponges as modifiers of the GB ecosystem dynamics acting as "cell meeting rooms" and biocompatible niches whose properties deserve to be considered toward the development of new clinical procedures.

Statement of Significance

Brain tumor glioblastoma (GB) is one of the worst unmet clinical needs. To prevent the relapse in the resection cavity situation, new implantable biopolymer aerogel sponges loaded with a chemoattractant molecule were designed and preclinically tested as a prototype targeting the interaction between the initial tumor location and its attraction by the peritumoral environment. While not modifying global survival, biocompatible SDF1-loaded hyaluronic acid and silk fibroin sponges induce directional GB cell attraction and colonization *in vitro* and in rats *in vivo*. Interestingly, they strongly shaped GB tumors in contrast to random infiltrative growth in controls. These results provide original findings on application of exogenous engineered niches that shape tumors and serve as cell meeting rooms for further clinical developments.

Keywords

Resection cavity, Implantable device, Cancer cell trap, Chemoattraction, Ecosystem dynamic Cell homing

1. Introduction

Glioblastoma (GB) is a lethal tumor with high recurrence rates. Most recurrences occur within 2 cm of the resection cavity due to the infiltration of GB cells into the brain parenchyma (Birzu et al., 2021; Giese et al., 2003; Yamahara et al., 2010). Targeting residual tumor cells is crucial to improve patient outcomes. New strategies are needed to selectively kill these cells while minimizing damage to normal brain tissue.

In contrast to direct targeting strategies that vectorize killing agents toward cancer cells, the reversal approach involves bringing the target toward a site of confinement by mimicking the preferred environment of infiltrating tumor cells (Najberg et al., 2019; Van Der Sanden et al., 2013). Then, direct loco-regional delivery of a cell death signal, such as focalized radiotherapy or local delivery of cytotoxic chemotherapeutic agents, could be applied for more effective treatment.

The tumor cell trapping strategy has been applied by a few groups like De la Fuente et al. who designed a polyurethane scaffold coated with collagen that was able to confine metastatic ovarian cancer cells in mice peritonea showing an improvement in survival (de la Fuente et al., 2015). Jain et al. designed aligned fibers of polycaprolactone to direct GB cells toward an extracortical killing sink (Jain et al., 2014). Reduced tumor size was observed; however, the invasive behavior of GB cells did not allow for a complete recovery. More research in this area shall be beneficial for the development of more effective glioblastoma treatment.

For this purpose, biocompatible biomaterials that can support cell infiltration should be chosen (Sood et al., 2021; Xu et al., 2019). The scaffold should be biomimetically functionalized to adapt its structure and composition, including relevant extracellular matrix (ECM) components, such as hyaluronic acid (HA), which is a crucial element of the cerebral ECM (Jensen et al., 2020; Nicolas et al., 2020). Also, an active scaffold can contain specific cellular signals that respond to the desired application, such as a chemokine to increase the recruitment of cancer cells.

In this regard, it has been observed that infiltrative GB cells express the C-X-C chemokine receptor type 4 (CXCR4) (Ehtesham et al., 2006; Zagzag et al., 2008; Zhou et al., 2002). This receptor binds the chemoattractant stromal cell-derived factor 1 α (SDF-1α), also known as CXCL12. A gradient of this chemokine induces the attraction of cells expressing the CXCR4 receptor (Hira et al., 2017; Kim et al., 2016). Therefore, we hypothesize that implanting a scaffold containing SDF-1α in the resection cavity can attract and confine infiltrative GB cells into a specific site.

Previously, our group developed freeze-dried aerogel sponges for this purpose: a silk fibroin (SF) with Hyaluronic acid (HA) sponge (SF-HA), and a SF with HA and heparin (Hep) (SF-HA-Hep) sponge, where heparin acts as a complexation agent for SDF-1α (Najberg et al., 2020). This study aims to evaluate the capacity of this new scaffold to attract infiltrative GB cells in a rat model of the brain resection cavity.

The biocompatibility and biodegradability of sponges were first evaluated. Direct placement of GB cells and glioma spheroids in contact with the scaffolds was used to evaluate cellular interactions and their cell hosting capacity. SF-HA-Hep sponges were selected for further application based on their degradation profile and enhanced cell adhesion. Our results showed that SDF-1α-loaded sponges had a strong *in vitro* chemotactic response and enhanced colonization. *In vivo* assessment was conducted by the placement of sponges 1-mm away to human GB cells expressing the CXCR4 receptor. Sponges attracted GB cells and induced localized tumor development in the resection spaces, which can be potentially used for further focalized therapy in a concentrated area. The findings and limitations of this strategy are discussed for further development of a safer and more efficient GB cell confinement device.

2. Materials and methods

2.1. Materials

Hepes, bovine serum albumin (BSA), resazurin, paraformaldehyde (PFA), sucrose, low melting point low gelling temperature agarose, Sudan Black, Giemsa stain, Crystal violet, Phosphate Buffered Saline (PBS, pH 7.4), Dulbecco′s Modified Eagle′s Medium (DMEM) with high glucose and Aphidicolin (ADC) were purchased from Sigma-Aldrich; glycerol (86-89 wt%) from Fluka and heparin sodium salt (Mw 15,000 ± 2,000 g/mol) from Calbiochem (Billerca MA, USA), N-(3-dimethylaminopropyl)-N′-ethylcarbodiimide hydrochloride (EDC) and N-hydroxysulfosuccinimide sodium salt (NHS) from Acros Organics (New Jersey, USA). Hyaluronic acid (HA) (Mw 360,000 g/mol) was purchased from Guinama (Valencia, Spain). Silk fibroin (SF) 8 wt% in an aqueous solution was provided by IMIDA (Murcia, Spain). SDF-1α was purchased from Miltenyi Biotec (Paris, France).

2.1.1. Sponges' preparation and characterization

SF (4%) with HA (2%) (SF-HA) and SF (4%) with HA (2%) and heparin (1%) (SF-HA-hep) sponges were synthesized and physicochemically characterized as reported previously by Najberg et al. (2020) (Najberg et al., 2020). Briefly, HA was dissolved in Hepes buffer (C_{Hepes} = 20.10^{-3} M, C_{NaCl} = 0.15 M, pH=7.4) to obtain a final concentration of 4 % w/v. SF 8% w/v solution was gently mixed with an equivalent volume of HA 4% solution in Hepes buffer with or without heparin sodium salt (C_f = 1% w/v). The SF-HA mixture was crosslinked using 5 mg/mL EDC and 1.8 mg/mL NHS. For formulations with heparin, 15 mg/mL EDC and 5.5 mg/mL NHS were used. The solutions were poured into a 96-well plate, covered, and allowed to crosslink for 15 h at 4 °C. The gels were then frozen at -20 °C for 24 h and freeze-dried in a Telstar® LyoQuest at -70 °C and 0.01 mBar overnight. The stabilization occurred by annealing the sponges in ethanol vapors, followed by freeze-drying again.

The porosity, thickness, and pore size of the sponges (n=3) were evaluated by microcomputed tomography (microCT) using a Bruker SkyScan 1272 (Kontich, Belgium). Scans were acquired at a voltage of 50 kV and a current of 200 µA, with a rotation step of 0.3°, pixel size of 5 µm, and no filter. Reconstruction of the obtained tomograms was carried out using NRecon software (Bruker) and 3D rendered images of the samples were generated through original volumetric reconstructed images by CTVox (Bruker). The quantification of structure properties was evaluated using a cylindric volume of interest (VOI) of 30 mm^3 centered in the middle of the samples. Before the analysis, datasets were binarized using a global threshold of 70-255 and a 3D despeckle process was applied to reduce image noise. Finally, analysis was performed using CTAn software (Bruker).

Sponges, measuring 2 mm - height and 3 mm - diameter, underwent sterilization under UV light for 30 minutes on each side prior to both in vitro and in vivo procedures.

2.1.2. Cell lines and culture conditions

NIH3T3 mouse fibroblast cells (CRL-1658™) and U87-MG cells were acquired from ATCC (Rockville, Maryland, USA). U87-MG cells, transduced to express the CXCR4 receptor and red fluorescent protein (RFP) as previously described (Séhédic et al., 2017). Transduced cells were selected with Blasticidine treatment (10 µg/mL) followed by cell sorting of a pure subpopulation expressing RFP and the CXCR4 receptor. These cells were called here as U87MG-CXCR4$^+$. All cell lines were cultured at 37°C and 5% CO_2 in DMEM supplemented with 10% fetal bovine serum (FBS) and 1% penicillin/streptomycin and subcultured every 3.5 days.

2.2. *In vitro* methods

2.2.1. Flow cytometry

U87MG-CXCR4+ cells were dissociated with trypsin and incubated with 10 µg/mL anti-CXCR4 primary antibody clone 12G5, or IgG2a (Séhédic et al., 2017) in PBS containing 0.5% BSA for 40 min at 4°C. After washing with PBS/BSA, cells were incubated with 8 µg/mL secondary Ab (Polyclonal goat α-mouse IGs-FITC, Dako F0479) in PBS containing 0.5% BSA for 30 min at 4°C protected from light. After washing in PBS/BSA wells were analyzed in a MACSQuant® Analyzer 10 Flow Cytometer (Miltenyi Biotec).

2.2.2. Western blot

Total proteins were isolated from U87MG-CXCR4+ cells by sonication in a lysis buffer composed of 50 mM HEPES, pH 7.5, 150 mM NaCl, 1 mM EDTA, pH 8, 2.5 mM EGTA, pH 7.4, 0.1% Tween 20, 10% glycerol, 0.1 mM sodium orthovanadate, 1 mM sodium fluoride,

10 mM glycerophosphate and 0.1 mM phenylmethylsulphonyl fluoride (PMSF). After quantification by spectrophotometry (kit), equal amounts of proteins (20 µg) were loaded onto 10% polyacrylamide gels and transferred to an Amersham GE Healthcare nitrocellulose membrane (0.45 µm pore size; Fisher Scientific). The following antibodies were used according to the manufacturer's instructions: rabbit anti-human Akt (Cell Signaling, #9272), phosphor-Akt (Ser473; #9271), p44/42 MAPK Erk1/2 (#9102), phospho-p44/42 MAPK Erk1/2 (Thr202/Tyr204; #9101), paxillin (#2542), and phosphor-paxillin (Tyr118; #2541). A mouse anti-human actin (#MA5-11869, Invitrogen) was used as a loading control. Anti-Rabbit IgG Secondary Antibody, HRP conjugate (Fisher Scientific) was used at a dilution of 1:10,000. Detection was performed on SuperSignal™ West Femto Maximum Sensitivity Substrate (Fisher Scientific) with a ChemiCapt 3000 imaging system (Vilber Lourmat, Marne-la-Vallée France).

2.2.3. Viability assay

The cytotoxicity of sponges on NIH3T3 and U87MG cells was evaluated by the indirect and direct contact methods, by ISO 10993-5:2009, at 24 h and 72 h intervals. 4 x 10^4 NIH3T3 cells were seeded per well for the 24-h assay and 1 x 10^4 cells/well for the 72-h assay. 8 x 10^4 U87MG cells were seeded per well for the 24-h assay and 2 x 10^4 cells/well for the 72-h assay. Cells were kept at 37°C and 5% CO_2 for 24 h before adding the sponges. UV-sterilized 2 mm height and 3 mm diameter sponges were washed 3 times with PBS, for residual crosslinker removal, and equilibrated in complete medium before use. For the direct contact method, sponges were directly added on top of the cell monolayer. Wells without sponges were used as controls. 24 h or 72 h after, sponges were removed by aspiration, and the media was replaced with 500 µL of 44 µM resazurin. After 2 h, cell viability was estimated by the fluorescence intensity of the resorufin (545-600 nm) using the ClarioStar microplate fluorometer (BMG Labtech GmbH, Ortenberg, Germany). For the indirect contact method, suspended culture inserts with the sponges inside (MilliCell, PET, 8 µm) were placed in the wells containing cells. Inserts without sponges were used as controls. 200 µL of media was added to completely cover the sponges. The viability of the cells was measured as described above. Triplicates were performed for all used conditions.

2.2.4. Agarose drop assay

The ability of SDF-1α (Miltenyi Biotec) to induce the migration of U87MG-CXCR4+ cells was evaluated using an adapted agarose drop assay (Milner et al., 1996). Briefly, a 24-well plate was coated with the extracellular matrix from U87MG cells. To do so, wells were first coated with poly-D-lysine (PDL, Sigma), then 5 x 10^4 U87MG cells were cultured for 48 h, lysed with deionized water, washed with PBS, and air-dried under sterile conditions before use. Then, a 2 µL drop of 1% w/v agarose in PBS containing 1 x 10^5 cells was placed in the center of a well. The agarose was allowed to solidify at 4°C for 10 minutes. Then, 500 µL of serum-

free DMEM with or without the chemokine (40 ng/mL of SDF-1α), and with or without 20 µg/mL aphidicolin (ADC) acting as an inhibitor of proliferation, was added on top of the drops. Plates were incubated for 3 days at 37°C and 5% CO_2. The distance of migration was measured at 4 points of the drop between the edge of the drop and the front of migration with ImageJ (9 drops for each condition).

2.2.5. Boyden chamber assay

U87MG-CXCR4$^+$ cells were starved in serum-free DMEM (SFM) for 24 h. Then cells were collected with Acutase solution, washed with PBS and resuspended in SFM. 5 x 10^4 cells were deposited on top of 8-µm pore PET inserts (Corning 353097) in 100 µL of SFM. Then, 650 µL of SF DMEM containing 0, 40 or 120 ng/mL SDF-1α was deposited in the bottom well. After 18-h incubation cells were fixed with 4% PFA for 15 min at room temperature (RT) and stained with 0.1% crystal violet solution for 30 min. After washing, images were obtained in a VHX microscope, and cells were counted with the QuPath software.

2.2.6. U87MG cells interaction with sponges

The cell response of U87MG cells when cultured into the sponges matrix was evaluated by direct seeding of cells into the sponges. SF-HA and SF-HA-Hep (1% heparin) sponges were hydrated and cut in 2-mm height cylinders. After washing in PBS, they were sterilized by 30-min UV cycles each side. Sponges were washed with PBS and equilibrated in complete DMEM medium (10% FBS and 1% antibiotics). The excess medium was blotted in sterile gauzes for 20 seconds on each side. The sponges were then transferred to individual wells (24-well plate) and a drop containing 5 x 10^4 cells in 20 µL of medium was slowly deposited on top of the sponges. Sponges with cells were left for 30 min in the incubator to allow for cell adherence. Following this, 500 µL of complete DMEM was added and the sponges incubated for 2 days at 37°C and 5% CO_2. Revelation of the cellular response was performed by replacing the medium with complete DMEM containing 44 mM resazurin followed by incubation for 3 h. Controls well consisted in the same number of cells cultured on plastic.

The adherence and spreading of U87MG cells in SF-HA and SF-HA-Hep sponges were observed using a scanning electron microscope (SEM) Evo LS15 (Zeiss, USA). 60 µL DMEM containing 1 x 10^5 U87MG cells was deposited onto a 2-mm height sponge and cells were allowed to adhere for 1 h before the addition of 500 µL of complete DMEM in a 24-well plate. Constructs were cultured for 3 days at 37°C and 5% CO_2. 2.5% glutaraldehyde in 0.1 M phosphate buffer was used for fixation for 2h. After PBS and distilled water rinsing (1x for 5 min) constructs were incubated in 1% osmium tetroxide aqueous solution for 1 h at RT. The samples were cut in half then rinsed with distilled water (3x for 5 min), followed by dehydration performed in increasing concentrations of ethanol solutions 50, 70, and 95% for 20 min each, and 100%, (3x for 30 min). Desiccation was performed in ethanol:hexamethyldisilazane

(HDMS) 1:1 for 45 min, and HDMS overnight. A platinum coating was performed before the analysis of the surface and transverse sections of the different sponges.

2.2.7. Under agarose cell migration assay

The assay was adapted from Heit and Kubes, 2003 (Heit and Kubes, 2003). Agarose was dissolved in PBS by microwave heating and mixed with serum-free DMEM at 70 °C. The resulting mixture containing 1.2% agarose in 75% DMEM was sterile-filtered and equilibrated for 15 min at 37°C before depositing 3 mL into each well of a 6-well plate. Casted gels were left to solidify for 30 min at RT and 1 h at 4°C. Three punches were made in each gel using a homemade template and a 4-mm biopsy punch. The cut agarose was aspirated to create three reservoirs separated by equal distances of 2 mm. 5 x 10^4 U87MG-CXCR4+ cells previously treated with 1 µg/mL of ADC for 24 h in complete medium were seeded in 20 µL of DMEM containing either 1% FBS or 10% FBS, and 5 µg/mL of ADC, in the center well. Sterile sponges loaded with either 10 pmol or 100 pmol of SDF-1α were deposited in the right chamber and covered with 15 uL of serum-free DMEM. PBS was put in the left compartment acting as a control. To assess the effect of sponges without SDF-1α, the latter were evaluated against only PBS that was deposited in the left compartment. The comparison of the cell migration response to sponges loaded with SDF-1α (100 pmol) vs sponges alone was also carried out by placement of the former in the right wells and the sponges alone in the left well. After 3 days of incubation, the constructs were fixed with a mixture of methanol and acetic acid (3:1) and after removal of the gels, cells were stained with Giemsa stain (1:10), and washed 3x with distilled water. Pictures were taken with a VHX digital microscope and the areas of migration from the edge of the center well toward the left and right flanks were quantified with ImageJ.

2.2.8. Glioma spheroids assay

U87MG-CXCR4+ cells were cultured at a density of 6000 cells/cm^2 in defined medium consisting of a 1:1 mixture of low glucose DMEM and Ham's F12 supplemented with 20 ng/mL EGF and FGF-2, 5 µg/mL heparin, 1x B27 supplement and 1% v/v Penicillin/Streptomycin. Half of the medium was changed every 3.5 days and spheroids were cultivated every 7 days. A single D7-neurospheroid of around 200 µm was collected and deposited on top of a 2-mm height and 6-mm diameter UV-sterilized sponge that was previously loaded with 60 µL serum-free DMEM containing 100 pmol of SDF-1α. Sponges without SDF-1α were used as controls. After 1-h of incubation at 37°C and 5% CO_2, 400 µL of DMEM supplemented with 1% FBS, 1% N1, and 1% antibiotics was added carefully into the well (24 well plate). The constructs were left in culture for 6 days, fixed with 4% PFA, permeabilized, and stained with DAPI before incubation in 0.3% Soudan Black solubilized in 70% ethanol to reduce the autofluorescence of sponges. Confocal images were obtained from the top view and the cross-section of sliced constructs. The on-top cell area and the cross-section invaded area were analyzed with the QuPath software.

2.3. *In vivo* studies

2.3.1. Animals

Fischer and nude athymic female rats aged 8-10 weeks were obtained from Janvier Labs (Le Genest-Saint-Isle, France). The protocol was approved by the Ethical Committee for Animal Experimentation of Pays de la Loire region, France (authorization number APAFIS #25889-2020032620074335 v3).

2.3.2. Evaluation of the biocompatibility of sponges

2.3.2.1 Implantation of sponges

Fisher rats were anesthetized by intraperitoneal injection of a mixture of ketamine (80 mg/kg) and xylazine (10 mg/kg) with subcutaneous administration of ketoprofen (5 mg/Kg) and positioned in a Kopf stereotaxic instrument. A 10 mm-long incision was made along the midline to create access to the surface of the skull. Following this, a burr hole (stereotactic coordinates: P: +0.8 mm; L: -3 mm (right from the bregma)) was drilled into the skull using a high-speed drill to expose the brain tissues underneath. A portion of the brain cortex was then carefully cut using a biopsy punch device and subsequently removed using vacuum suction to create a cavity that was approximately 3 mm wide and 2 mm deep. SF-HA and SF-HA-hep sponges were swollen in PBS, cut transversely to obtain 2 mm height cylinders, and sterilized under UV light for 1 hour. The sponges were then cut one by one before implantation with a 3 mm diameter biopsy punch with a push-button and, immediately after, implanted in the cavity with the biopsy punch. The wound was sutured, and the rats were allowed to wake without any further intervention. All rats became fully conscious within 2 hours after surgery and did not display any sign of distress. In control rats, the same surgical procedure was also performed, but no scaffold was implanted. Ketoprofen was administered for 2 days after surgery. Two groups of rats were set up: one group consisted of 9 rats (3 implanted with SF-HA sponges, 3 implanted with SF-HA-hep sponges, and 3 cavity controls - with no implants), and was intended for the short-term study (euthanized after 7 days) while the other group, consisted of 12 rats (4 implanted with SF-HA sponges, 4 with SF-HA-hep sponges and 4 controls), was intended for the long-term follow-up (euthanized after 118 days). MRI follow-up was performed on days 7 and 76 post-implantation.

2.3.2.2 Histology

After euthanasia, the brains were collected and subsequently fixed in formalin for a duration of 10 days, followed by paraffin embedding. Next, 5 µm thick sections were obtained using an HM340E Microm Microtech microtome (France) and stained with hematoxylin and eosin (HE) for analysis. The histopathological parameters considered included multinucleated giant cells,

acute inflammatory cells, necrosis, chronic inflammatory cells, neoangiogenesis, hemorrhage, hemosiderin deposition, and mineralization. These parameters were evaluated in randomly selected fields under 40× magnification in the tissue sections. The analyses were conducted at the Department of Cellular and Tissue Pathology, Centre Hospitalier Universitaire d'Angers (CHU-Angers, France). Microscopic images were captured using an Olympus microscope.

2.3.4 Evaluation of SDF-1α release in rat brains

To study the potential release of SDF-1α from the sponge to the brain, an SDF-1α coupled with Alexa Fluor 647 (AF-SDF-1α) at the C terminal (Almac, Scotland) was used. The SF-HA-Hep sponge was used for further *in vivo* experiments, as the SF-HA sponge was mostly degraded after 7 days. The same methods to prepare the sponges, including cutting and sterilization, were used as cited before. Afterward, the 3 mm diameter sponges were taken out of the biopsy punch, the PBS excess was taken out by blotting them on a gauze, producing slight dehydration, and rehydrated by adding 3 µL of AF-SDF-1α (150 ng) on the top of the sponge to finally implant them in the cavity of Fischer rats as described in section 2.3.2.1. With this process, the full volume of AF-SDF-1α was absorbed by the sponge, resulting in a theoretical 100% loading. Rats were euthanized after 7 days, and the brains were snap-frozen in isopentane and stored at -80°C right after collection. Tissues were cut coronally in the region of interest with a Cryostat Leica CM3050 S (Leica Biosystems, Nussloch, Germany) to obtain 10 µm thick slices that were deposited on gelatinated Superfrost slides (Thermo Fisher Scientific, Braunschweig, Germany), and kept at -20°C until immunolabeling.

2.3.5 Evaluation of the sponge's performance *in vivo*

To assess the GB cell attractant capacity of sponges *in vivo*, two orthotopic models were tested in nude female rats, aged 8 to 10 weeks. In the first model, 5 x 10^3 U87MG-CXCR4+ cells were injected into the striatum (P: +0.8 mm; L: -3mm (right from the bregma); D: -2.5 mm from the cortex surface). After 10 days of tumor development, a 3-mm diameter and ~2-mm depth resection cavity was performed in the same vertical axis of cell injection using a biopsy punch. The tissue was then aspirated, and SF-HA-Hep sponges (3-mm diameter and 2-mm height) were implanted loaded or not with 100 pmol of SDF-1α. After 7 days, animals were euthanized, and brains were collected and snapfrozen at -80 °C until analysis. GB cell identification was performed by RFP, CXCR4 and Ki67 analysis by IHC-IF.

In the second model, a resection cavity was created (P: +0.8 mm; L: -2.9mmma; D: ~ -2 mm from the cortex surface). SF-HA-Hep sponges (3-mm diameter and 2-mm height) were implanted loaded or not with 100 pmol of SDF-1α in 5 µL of PBS. Following this, 2.5 x 10^4 U87MG-CXCR4+ cells were injected at 1 mm posterior from the edge of the resection (Stereotactic coordinates: P: -1.7, L: -2.9, D: -2 mm from the surface of the brain). Excess blood was removed with sterile gauze, the cavities were closed with non-absorbable bone wax and the wound was sutured.

The animals recovered after 2 hours and did not show signs of distress. Animals were monitored daily, observing food and water intake, also weights were recorded. After 7 days, euthanasia was conducted, and all brains were extracted, snap-frozen and kept at -80 °C until analysis. The experimental design consisted of three groups: resection control, PBS swollen sponges, and sponges loaded with SDF-1α (n=3). A survival experiment was performed using the same latter surgery procedures, but 1 x 10^3 U87MG-CXCR4+ cells were injected instead (n=6 per group). Animals were followed by MRI weekly and euthanized at defined endpoints.

2.3.6 MRI analysis

MRI scans were performed with a Bruker Biospec 70/20 system operating at 7T, under isoflurane (0.5% 1 L/min O2) anesthesia, with the monitoring of respiratory parameters. T2-weighted images were acquired with a multi-spin echo sequence [FOV = 30 x 30 mm, 9 axial 0.8 mm slices (gap = 0.1 mm), matrix 256 x 256, TR = 2.5 s, 25 TE = 30 ms].

2.3.7 Immunohistochemistry and Immunofluorescence

For the SDF-1α release study, 10 µm sections were fixed with PFA 4% (w/v) at 4°C for 20 min, permeabilized with 0.25% (w/v) Triton X-100 in PBS for 10 min and saturated with NGS 10% (w/v) in PBS for 2 h. They were then incubated overnight at 4°C with polyclonal rabbit IgG anti-SDF-1α (1:500) (Abcam, Cambridge) followed by 1 h incubation at RT with the secondary antibody goat anti-rabbit AF 488 (#4412 Cell Signaling). Cell nuclei were stained with DAPI (1:2000, Thermo Fisher Scientific, Waltham, MA) before mounting sections with Dako fluorescence mounting media (Dako, CA, USA). Stained sections were visualized using a confocal microscope Leica TCS SP8 AOBS (Leica Microsystems, Wetzlar, Germany).

For the sponge's bioperformance study, 16 µm sections were fixed for 10 min in methanol at -20°C and rehydrated in PBS (3 washes). After saturation in PBS/4%BSA/10%NGS/0.25% TritonX100 for 1 h, sections were probed with the primary antibodies as follows: anti-CXCR4 polyclonal (1:2500, #PA3-305-Invitrogen) which does not cross-react with rat tissue, or anti-Ki67 (1:200, ab16667-ABCAM), both overnight at 4°C in a humidified chamber. After washing (3x in PBS) the slices were incubated with a biotinylated secondary Ab (anti-mouse or anti-rabbit, 1:100 in PBS/4%BSA, Vector Laboratories) for 1 h at RT. Slices were rewashed and incubated with Streptavidin-FITC (1:500, Interchim) in PBS for 45 min at RT. After washing, slices were incubated with DAPI, and finally with Sudan Black for 15 min before mounting slides. Fluorescence was analyzed in a Leyca confocal microscope.

2.4 Statistical analysis

Data are presented as mean ± SEM. Data were statistically analyzed using an ANOVA test with Prism 7 software. Tukey's multiple comparison test was used to compare individual groups. For analysis considering only two groups, a two-tailed t test was performed. UACMA

data was analyzed with a two-tailed paired t test. In all statistical comparisons $p < 0.05$ was considered statistically significant. For the survival analysis, all and single groups were compared using the Log-rank (Mantel-Cox).

3. Results

In vitro studies

3.1. U87MG-CXCR4+ cells are responsive to SDF-1α

Human GB U87MG cells were transduced for the expression of the CXCR4 receptor (U87MG-CXCR4+) and the receptor expression was confirmed by flow cytometry (**Fig. 1A**). Then, their molecular response was evaluated by incubation of cells with serum-free medium containing 40 ng/mL of SDF-1α. Results showed an increased p-Akt/Akt ratio after 15 minutes, which was maintained at 1 h of incubation with SDF-1α, whereas the p-Erk/Erk ratio was increased after 15 min of incubation but then reduced at 1 h. These results match early findings on patient de-novo- and recurrent-derived GB cell lines (Ishii et al., 1999; Zhou et al., 2002). On the other hand, p-Paxillin/Paxillin ratio was gradually increased at 15 min and 1 h of evaluation (**Fig. 1B**), suggesting a gradual formation of focal adhesions (Hu et al., 2017).

To assess the functional response of U87MG-CXCR4+ cells to SDF-1α, first, their ability to migrate across an 8-μm porous membrane was evaluated in Boyden chambers. On average, a 3-fold increase in the number of migrating cells was observed after 18 h of incubation for both 40 and 120 ng/mL of SDF-1α as compared to controls (**Fig. 1C**). Then, the ability of U87MG-CXCR4+ cells to leave a confined spot of agarose was measured by the length of the migrating cell halo surrounding the cell-laden agarose drop (**Fig. 1D**). On average a 2-fold increase in the migrated distance was observed for cells treated with 40 ng/mL of SDF-1α relative to controls.

To discriminate against the effect of proliferation, the latter assay was performed in the presence of the proliferation inhibitor Aphidicolin (ADC). Although a reduced cell hallo was observed as compared to non-ADC treated cells, approximately the same ratio of 2-fold increase in the migrated length for SDF-1α treated drops was maintained relative to controls. This result suggests that the chemoattractant effect of SDF-1α was independent of cell proliferation. Moreover, U87MG cells without receptor expression (U87MG-CXCR4-) did not respond to SDF-1α, in terms of chemoattraction, as observed by the equal distances of migration for both non-treated and treated cells (**Fig. 1D**).

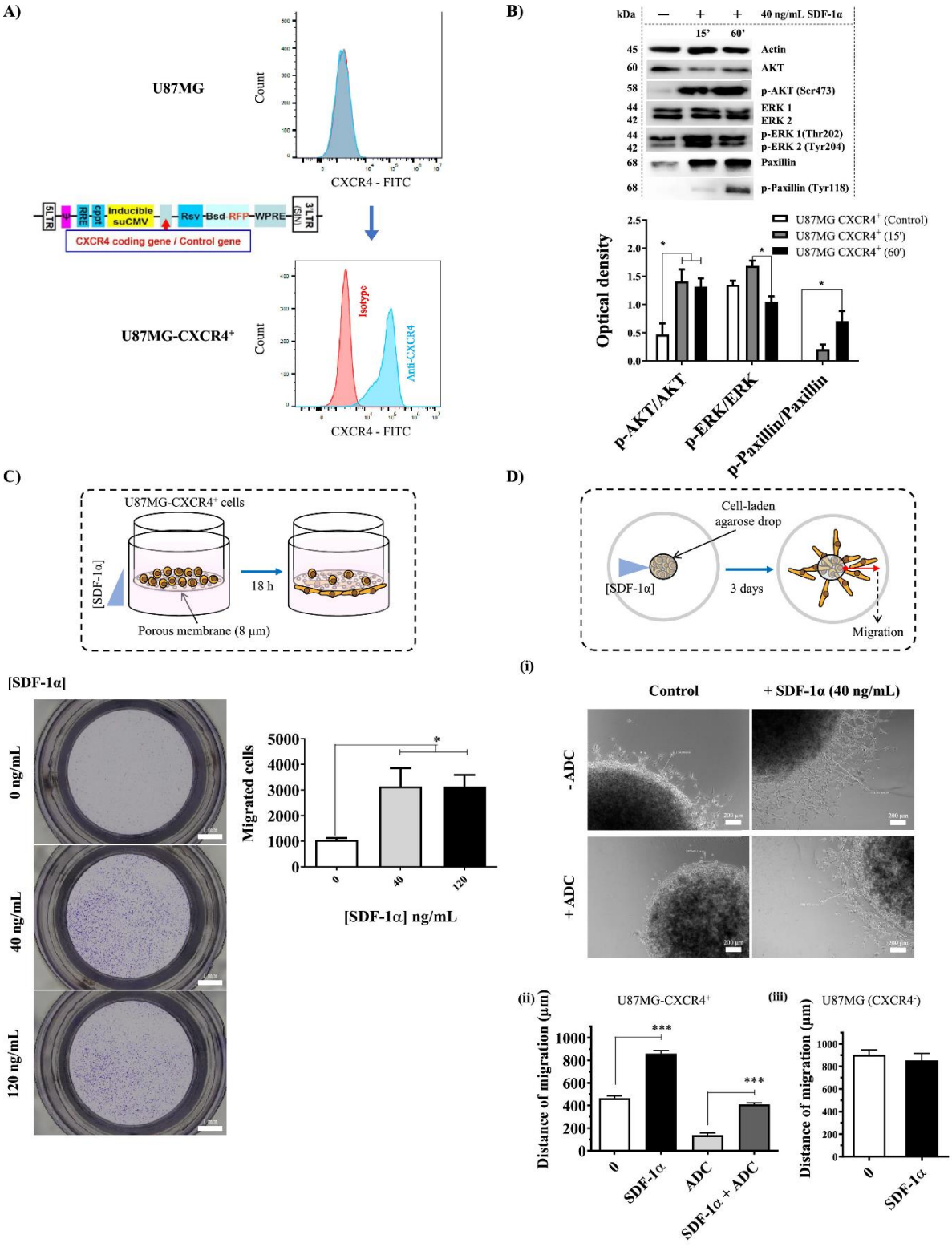

Fig. 1. Cellular model and its response to SDF-1α. A) Design of the cellular model: U87MG cells were transduced for constitutive expression of the CXCR4 receptor and red fluorescent protein (RFP). **B)** Molecular response: phosphorylation of Akt, Erk, and Paxillin shows the activation of the CXCR4/SDF-1α pathway in U87MG-CXCR4$^+$ cells in response to SDF-1α (n = 3). **C)** Transwell migration of U87MG-CXCR4$^+$ cells: after 18-h incubation of cells deposited on top of the porous membranes, migrating cells were more abundant in wells

containing both 40 and 120 ng/mL of SDF-1α compared to controls (n = 3–4 replicates, with three repetitions). **D)** Agarose drop assay. (i)(ii) Migration of U87MG-CXCR4$^+$ from a confined spot of agarose was higher for cells treated with 40 ng/mL of SDF-1α as compared to controls. Inhibition of cell proliferation by the addition of Aphidicolin (+ADC) reduced the measured distance of migration but did not change the ratio of migration respective to controls. (iii) U87MG cells without expression of the CXCR4 receptor (U87MG-CXCR4$^-$) did not show a significative difference when treated with SDF-1α compared to control drops (n = 3 replicates, with two repetitions). Levels of significance are: ∗: $p < 0.05$, ∗∗: $p < 0.01$, ∗∗∗: $p < 0.001$.

3.2. Sponges are highly porous, with interconnected pores and present shape memory

Aerogel sponges presented similar structure and physical appearance independently of heparin content **(Fig. 2A)**. A porosity of ~ 93 % was observed for both types of sponges SF-HA and SF-HA-Hep (1% heparin). However, the pore size distribution was affected by the presence of heparin (**Figure 2B**). A larger dispersion of pore sizes was observed in sponges without heparin 126.67 (90.84) µm, while sponges with heparin showed a narrower pore size distribution of on average 69.01 (22.53) µm. This reduction in the average pore size correlates to the higher content of total solids due to the addition of heparin.

The thickness of the pore walls was consistent between all types of sponges. On average, a 9.6 µm wall thickness, which represents a ~9.6/69 = ~14% of the diameter of a pore including walls for sponges containing heparin, reflects the spongy nature of the scaffolds. Thirdly, all sponges showed open, interconnected pores. This can be observed by tracking the maximal length of the path with troughs larger than 15 µm that can be followed without interruption in both orthogonal axes of the cross sections of sponges. Finally, all the sponges presented shape memory as observed by their capacity to regain their original shape upon an external force was applied, and then released, over the sponges' hydrated form (**Video S1**).

3.3. SF-HA-Hep sponges present mild to moderate cytotoxicity *in vitro*

The viability of NIH/3T3 mouse fibroblasts and U87MG glioblastoma cells was evaluated via the indirect and direct contact methods at 24 and 72 h incubation with SF-HA and SF-HA-Hep sponges **(Fig. 2C)**. NIH/3T3 cells were chosen due their high sensitivity to chemical-induced toxicities (Xia et al., 2008). After 72 h of direct contact, SF-HA sponges significantly decreased the viability only for NIH/3T3 cells (71 ± 14%). SF-HA-Hep sponges, however, presented mild cytotoxicity after 72 h of indirect contact (63 ± 19% viability), and moderate cytotoxicity after 72 h of direct contact with NIH/3T3 cells (39 ± 9% viability). Mild cytotoxicity was seen on U87MG cells after direct contact with SF-HA-Hep sponges at 24 (76 ± 9% viability) and 72 h (64 ± 9% viability).

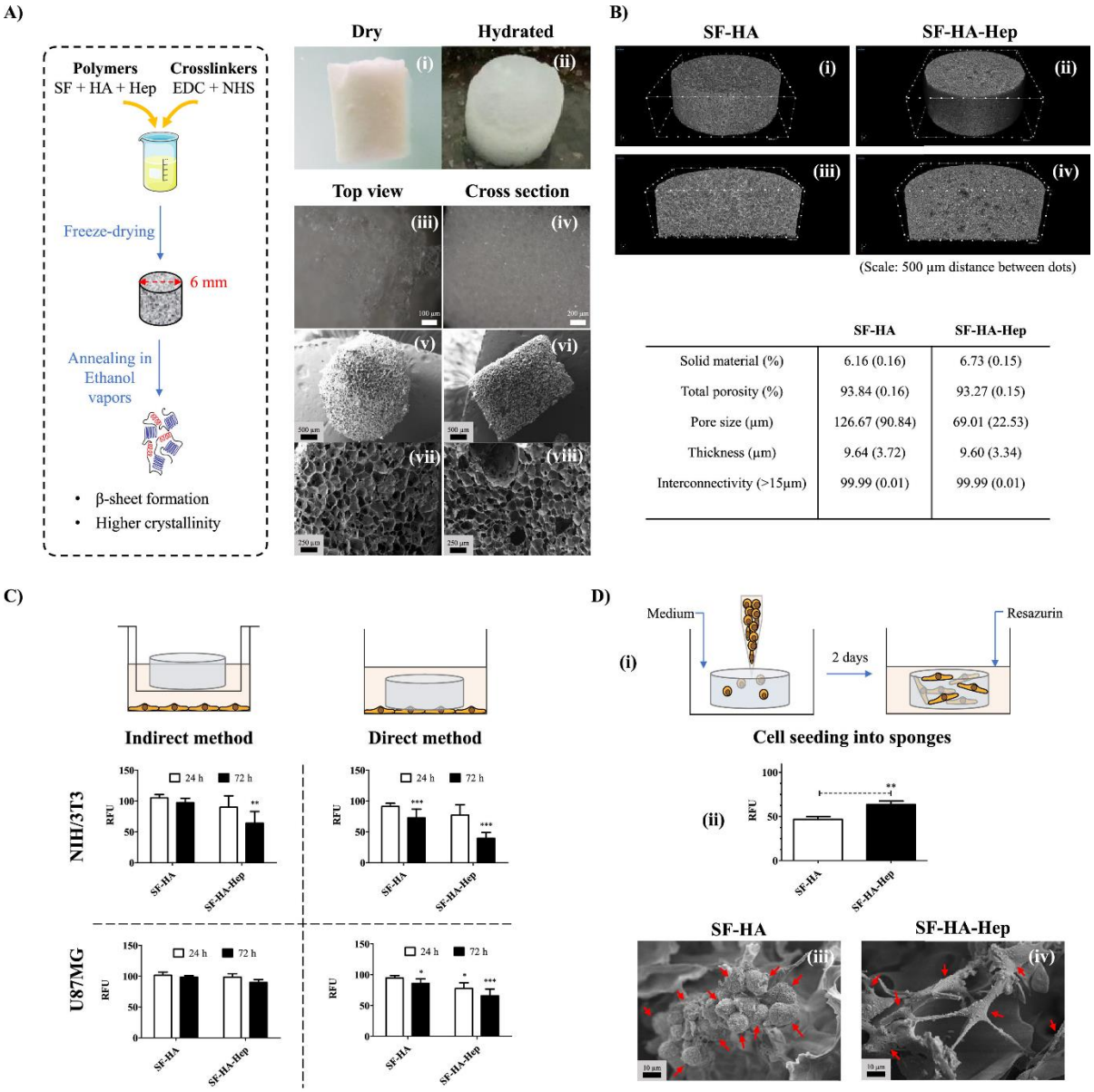

Fig. 2. Aerogel sponges, synthesis, structure, and cellular response. A) Synthesis and structure of the silk fibroin (SF), hyaluronic acid (HA), and heparin (Hep) sponges. Dry SF-HA-Hep sponges (i) rapidly absorb PBS and maintain their shape (ii). Stereomicroscopic images [(iii) and (iv)], and scanning electron micrographs [(v), (vi), (vii) and (viii)] showing the superficial and cross-sectional porous structure of SF-HA-Hep sponges. B) Microcomputed tomography (µCT) images for the evaluation of the porosity of sponges, the size and wall thickness of their pores, and the percentage of their connected pores with troughs > 15 µm. Depicted are representative µCT images of superficial [(i) and (ii)], and cross sections [(iii) and (iv)] of sponges without heparin (SF-HA) and with 1 % Heparin (SF-HA-Hep). C) The cell response of NIH/3T3 and U87MG cells after incubation with leachables from sponges (indirect method) and after direct contact of sponges with a cell monolayer (direct method) was evaluated using the resazurin assay. Depicted in the graphs are the percentages of the relative

fluorescent units (RFU) respective to control wells that contained no scaffolds (n = 3 replicates, with three repetitions). D) The response of cells directly seeded into scaffolds. U87MG cells were directly deposited into scaffolds. After 2 days, the cellular response in SF-HA and SF-HA-Hep scaffolds was evaluated by incubation with media containing resazurin (i). The produced fluorescence in the media was normalized to control wells with cells seeded on plastic and is expressed as the percentages of RFU (ii) (n = 5 replicates, with 2 repetitions). U87MG cells (red arrows) seen under scanning electron microscopy 3 days after seeding in SF-HA sponges (iii) and SF-HA-Hep sponges (iv). Levels of significance are: ∗: $p < 0.05$, ∗∗: $p < 0.01$, ∗∗∗: $p < 0.001$.

Different washing techniques were tested aiming to eliminate traces of crosslinkers to improve the cytocompatibility of SF-HA-Hep1% sponges. The first consisted in a 24-h wash in PBS under agitation, and the second in 5 x 30 s sonication cycles followed by agitation for 1 h in PBS. However, after 72-h of direct incubation of washed sponges with NIH/3T3 cells, no improvement was observed (**Fig. S1**). To determine whether EDC and NHS or Heparin were responsible for this cytotoxicity, two new sponges were produced. The first was composed of SF and HA crosslinked with the same concentration of crosslinkers as SF-HA-Hep (C_{EDC} = 15 mg/mL, C_{NHS} = 5.5 mg/mL) and was called SF-HA(+). The second was composed of SF, HA and Hep crosslinked with the same concentration of crosslinkers as SF-HA (C_{EDC} = 5 mg/mL, C_{NHS} = 1.8 mg/mL) and was called SF-HA-Hep(-). Because of the lower concentration of crosslinkers in the SF-HA-Hep(-) sponge, its shape was lost in the media.

Sponges with the same concentration of crosslinkers showed the same cytotoxicity, with a lower concentration of crosslinker leading to an increase in viability (**Fig. S1**). A tradeoff between stability and cytotoxicity had to be made, and therefore the original SF-HA-Hep1% sponge was kept for further studies. Additional evaluation of its 24-h cytotoxicity by the direct contact method on cells resemblant to resident cells of the normal brain parenchyma was performed. In this case, murine BV-2 and human HMC3 microglial cells showed a viability of 64.4 and 82.3%, respectively (**Fig. S2**).

3.4 The matrix of SF-HA-Hep sponges allowed a better U87MG GB cell response

To assess the response of cells in the scaffold's matrix, U87MG cells were directly deposited into the sponges as a cell suspension and cultured for 2 days. The cell response was evaluated by the resazurin assay **(Fig. 2D-i)**. Results showed that SF-HA-Hep sponges allowed a better response compared to SF-HA sponges **(Fig. 2D-ii)**. After 3 days of culture, SEM images showed cell aggregates in SF-HA sponges with no or little spreading of their soma **(Fig. 2D-iii)**, whereas cells in SF-HA-Hep1% sponges attached, spread, and formed large protrusions, suggesting a better interaction with GB cells **(Fig. 2D-iv)**.

3.5. SDF-1α-loaded sponges directionally attract U87MG-CXCR4+ cells *in vitro*

To evaluate the chemoattractant capacity *in vitro*, sponges loaded with SDF-1α (10 and/or 100 pmol) were added in the right well, contiguous to a well containing U87MG-CXCR4+ cells in an agarose gel **(Fig. 3)**. A well containing only PBS was also included to the left. After 3 days of culture with the addition of Aphidicolin as a proliferation inhibitor, results showed that there was a larger area of cells that migrated under the agarose towards the SDF-1α-loaded sponges as compared to controls located in the wells left to the cells. The migrated area depended on the dose of SDF-1α and the percentage of FBS used for cell seeding. Indeed, FBS was necessary for cells to adhere. This effect corresponded to a 3-fold increase of the invaded area for the 10 pmol loading and an 11.3-fold increase for the 100 pmol loading as compared to controls, in the case of 1% FBS seeded cells (**Fig. 3A-iii**). A larger area in both directions, towards the sponges and controls, was observed when cells were seeded with medium containing 10% FBS. However, increasing area ratios of 2.2-fold and 3-fold showed preferential migration of cells towards the sponges loaded with 10 and 100 pmol of SDF-1α, respectively (**Fig. 3A-iii**). To evaluate if the sponges alone were able to attract GB cells in vitro, the experiment was repeated with sponges containing only PBS compared to wells filled with only PBS (Fig. 3B-i). Results showed no significant difference in the areas of cell migration. When SDF-1α-loaded sponges were compared to sponges containing only PBS, only the former were able to show cell attraction (**Fig. 3B-iii)**, showing a similar pattern than agarose gels where only PBS was used as a negative control (**Fig. 3B-ii).**

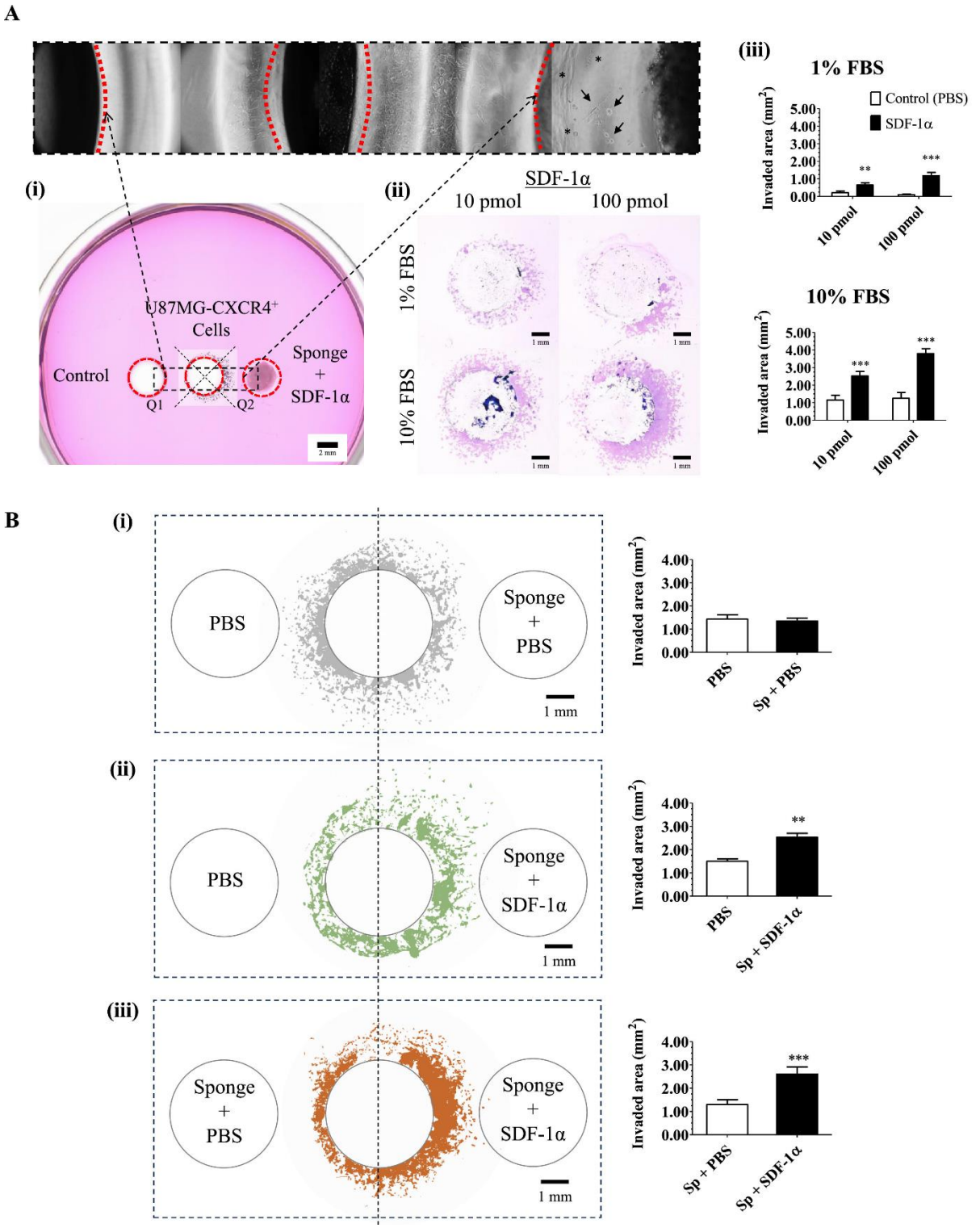

Fig. 3. *In vitro* cellular attraction. A) *In vitro* chemoattractant capacity of SDF-1α-loaded sponges: (i) agarose gel showing the disposition of cells (center well), sponges (right well), and control wells containing PBS (left well) to assess the induction of directional migration. Top panel: images (10x objective) of a representative experiment on day three after cell seeding. The assembled image shows the pattern of cell migration under the agarose gel. Some cells were detected near the sponges loaded with SDF-1α (100 pmol) (black arrows), with some cells undergoing cell death (asterisks). Of note is the "squeezed" shape of cells under the agarose,

whereas cells that invade the right agarose-gel-free well regain a “spindle-like” morphology. (ii) Giemsa staining of cells that migrated under the agarose after three days of incubation. Cells were seeded in media containing either 1 % or 10 % FBS and 5 µg/mL of Aphidicolin as a proliferation inhibitor. (iii) Quantification of the cell area of the binary images in the most proximal quarters (Q) to either control wells (Q1) or sponges (Q2) as depicted in the representative image in the center well of (i) (n = 3 replicates, with three repetitions). B) The effect of the sponges alone containing only PBS (i) or of sponges loaded with 100 pmol of SDF-1α (ii), as compared to wells loaded with only PBS (left wells). (iii) The effect of sponges containing 100 pmol of SDF-1α vs. sponges loaded with only PBS. (n = 3 replicates, with three repetitions). Levels of significance are: ∗: $p < 0.05$, ∗∗: $p < 0.01$, ∗∗∗: $p < 0.001$.

3.6. SDF-1α in SF-HA-Hep sponges enhanced their colonization *in vitro*

To assess the cell hosting capacity of sponges, single ~ 200-µm U87MG-CXCR4+ spheroids were cultured on top of SF-HA-Hep sponges that were loaded or not with 100 pmol of SDF-1α (**Fig. 4B**). Results showed that after 6 days of culture, there was a 1.4-fold larger area of glioma spheroids attachment on the surface of the sponges loaded with SDF-1α in relation to control sponges loaded with PBS (**Fig. 4B-iii**). In addition, a 1.6-fold larger infiltrated area and a 1.3-fold maximal infiltrated length in the sponges loaded with SDF-1α were observed compared to controls. However, cells remained within the contours of the glioma spheroids and did not spread out ubiquitously within the sponge in the 6-day time frame of the experiment.

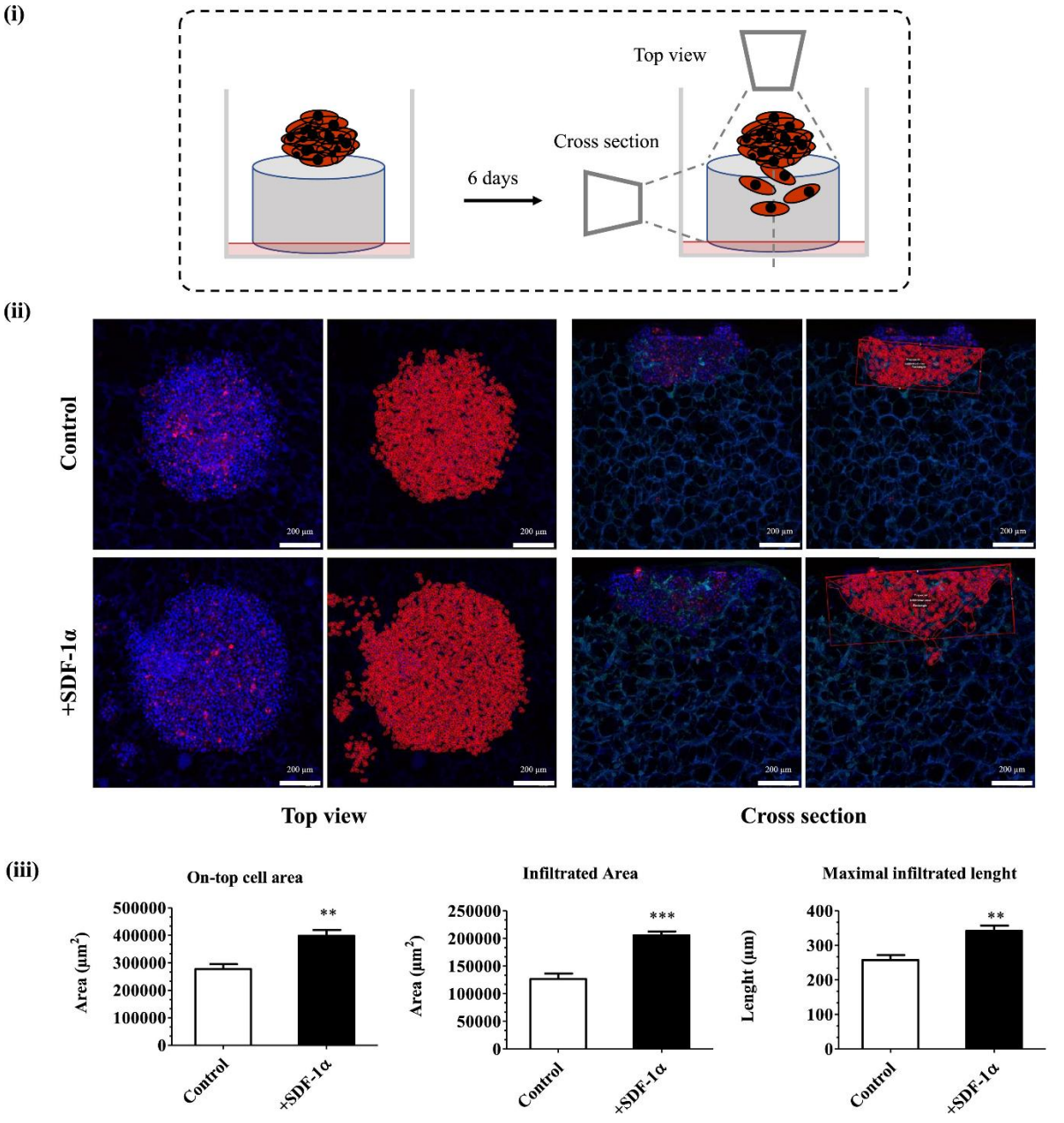

Fig. 4. ***In vitro*** **cellular colonization of sponges.** (i) Representation of the spheroid culture assay for the evaluation of the capacity of SF-HA-Hep sponges to be colonized by GB cells coming from GB spheroids. A single U87MG-CXCR4^{+} gliomaspheroid was deposited on top of a SF-HA-Hep sponge loaded or not with SDF-1α. After 6 days of culture, the on-top cell area, the infiltrated cross-sectional area, and the maximal infiltrated length were imaged (ii) and quantified (iii) (n = 3; 2 experimental repetitions). Levels of significance are: ∗: $p < 0.05$, ∗∗: $p < 0.01$, ∗∗∗: $p < 0.001$.

In vivo studies

3.7. Sponges are biocompatible and biodegradable *in vivo*

SF-HA and SF-HA-Hep sponges were implanted in the resection cavities of Fisher rats to evaluate the foreign body reaction in the brain as well as their biodegradability (**Fig. 5**). MRI images showed the presence of the sponges at D6 from implantation but completely degraded after 76 days as shown by the watery content in the cavities (**Fig. 5A**). SF-HA sponges were mostly absorbed after one week of implantation, which was confirmed by histological analysis (**Fig. 5B**). The cellular response was characteristic of a foreign body reaction with an acute inflammatory response at week one post-implantation, with the presence of polymorphonuclear (PMN) cells that was more important for SF-HA-Hep sponges compared to SF-HA sponges.

The presence of multinucleated giant cells was rare, but the concomitant presence of macrophages and lymphocytes showing up from the initial stages after implantation demonstrates a process of debridement and chronic inflammation that was prolonged to up to the third month post-implantation. The formation of new blood vessels was more evident on day 7 of evaluation for all groups suggesting that the brain damage caused by the surgical resection and the consequent signals induced this neoangiogenic response. On the third month of evaluation, the acute inflammation was resolved, and the chronic inflammation lessened. Interestingly, only the cavities of rats implanted with sponges kept some lymphocytes in the long term compared to cavity controls alone. The presence of hemosiderin-laden macrophages and calcification zones (mineralization) showed the late stages of cicatrization. Overall, the residual cavities were porencephalic, i.e., filled with resident cerebral cells but with the loss of brain matter, however no collagen deposition nor fibrotic tissue was observed in the implantation zone, suggesting a good reabsorption of the sponges without the formation of a scar. As SF-HA sponges were mostly degraded within the first week of implantation, SF-HA-Hep sponges were chosen for further experiments.

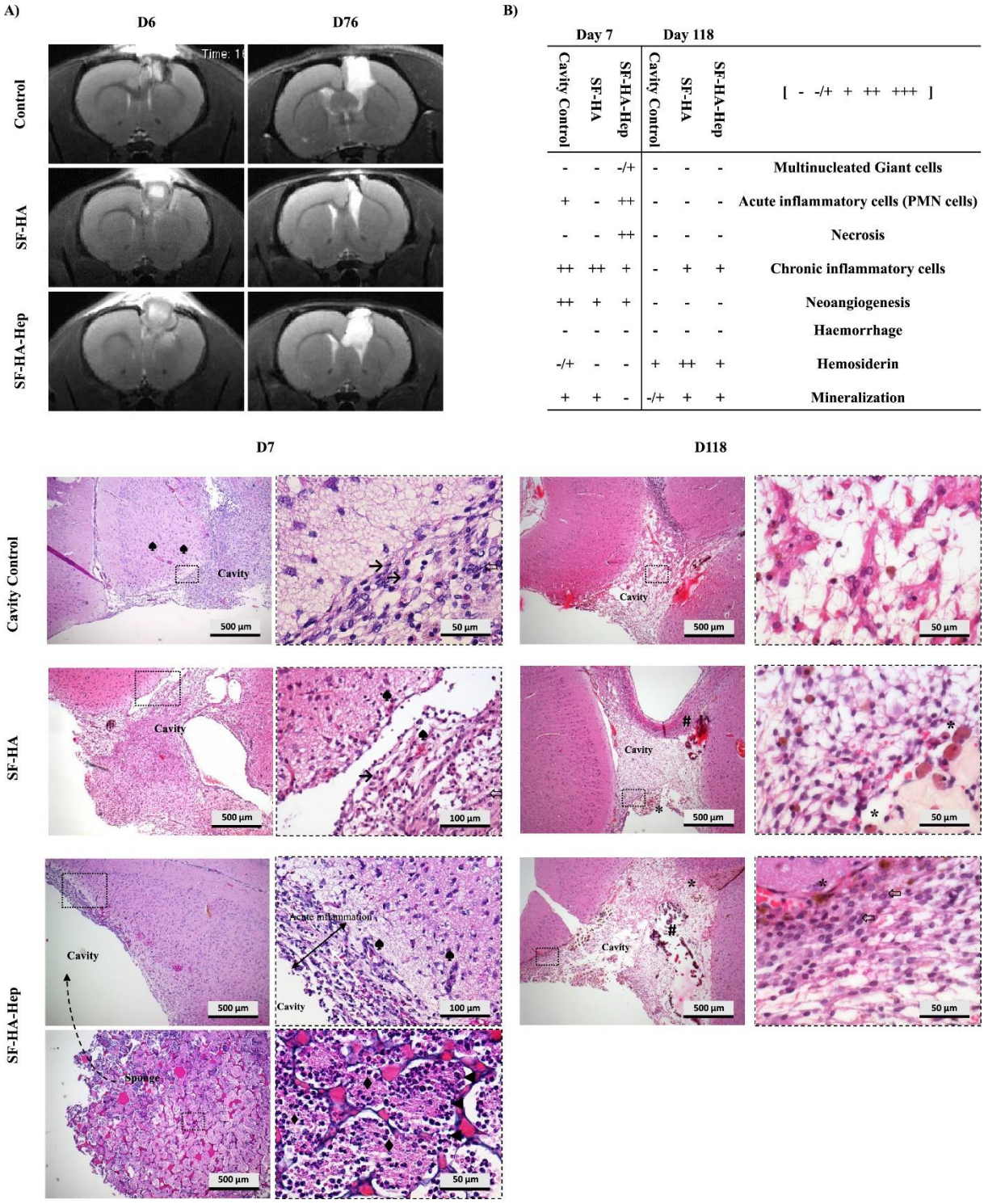

Fig. 5. *In vivo* biocompatibility and biodegradability of sponges. A) MRI scans of brains with implanted sponges. B) Characterization of the *in vivo* cellular response to implanted sponges in the rat brain cortex. Histological (H&E) staining (nuclei: blue/purple; cytoplasm: pink). SF-HA sponges were completely degraded after 7 days, while SF-HA-Hep sponges were still present. A representative image is shown of a SF-HA-Hep sponge that came out of the cavity during the slicing process (bottom left panel). Left panels: H&E representative images 7 days post-implantation showed an acute inflammatory response in rats implanted with SF-HA-Hep sponges. The acute response was less marked in the other groups. There was a local

chronic inflammatory response with the presence of lymphocytes that were more frequent in the cavity controls and in SF-HA implanted rats. At this 1-week time point, the formation of blood vessels (neoangiogenesis) was observed in all groups. Right panels: After 3 months, the acute inflammation was resolved, and the chronic inflammation lessened in the control cavity and SF-HA groups and remained in the SF-HA-Hep group. At this 3-month time point, mineralization and hemosiderin deposition were observed in all groups. Symbols are as follows: infiltrating polymorphonuclear (PMN) cells (◄), Necrosis (♦), macrophages (→), lymphocytes (⇦), neoangiogenesis (♠), hemosiderin (*), mineralization (#). Scores are as follows: (−) = nil, (-/+) = rare, (+) = mild, (++) = moderate, and (+++) = marked. Interrupted-line bordered images are magnifications of the smaller squares indicated in their respective left images.

3.8. SDF-1α was retained in SF-HA-Hep sponges *in vivo*

To evaluate the *in vivo* biodistribution of SDF-1α in the brain after the sponge's implantation, SF-HA-Hep sponges were loaded with 150 ng of AF-647 tagged SDF-1α and implanted in the resection cavities of Fisher rats. Results showed that 7 days post-implantation, AF647-SDF-1α was detected inside the sponges, and in the margins of the resection cavity as bulges detaching from the edges of the sponges that were undergoing degradation; but was not detected in the brain tissues beyond the resection limits (**Fig. 6A**). Interestingly, AF647-SDF-1α was distributed as droplets of about 10-100 µm diameter which corresponded to the internal structures observed in the sponges (**Fig. 6A-third panel**). Endogenous SDF-1α was stained indirectly with an antibody coupled with FITC and was distinguished from the exogenous SDF-1α that was loaded into the sponges, as the latter was not recognized by the primary antibody (**Fig. 6B**). Endogenous SDF-1α was found only scarcely expressed in small blood vessels surrounding the resection cavity. Interestingly, more nuclei were observed inside the sponges containing SDF-1α compared to the brain tissue. This correlates with the colonization of sponges by PMN cells as observed in **Fig.5B**.

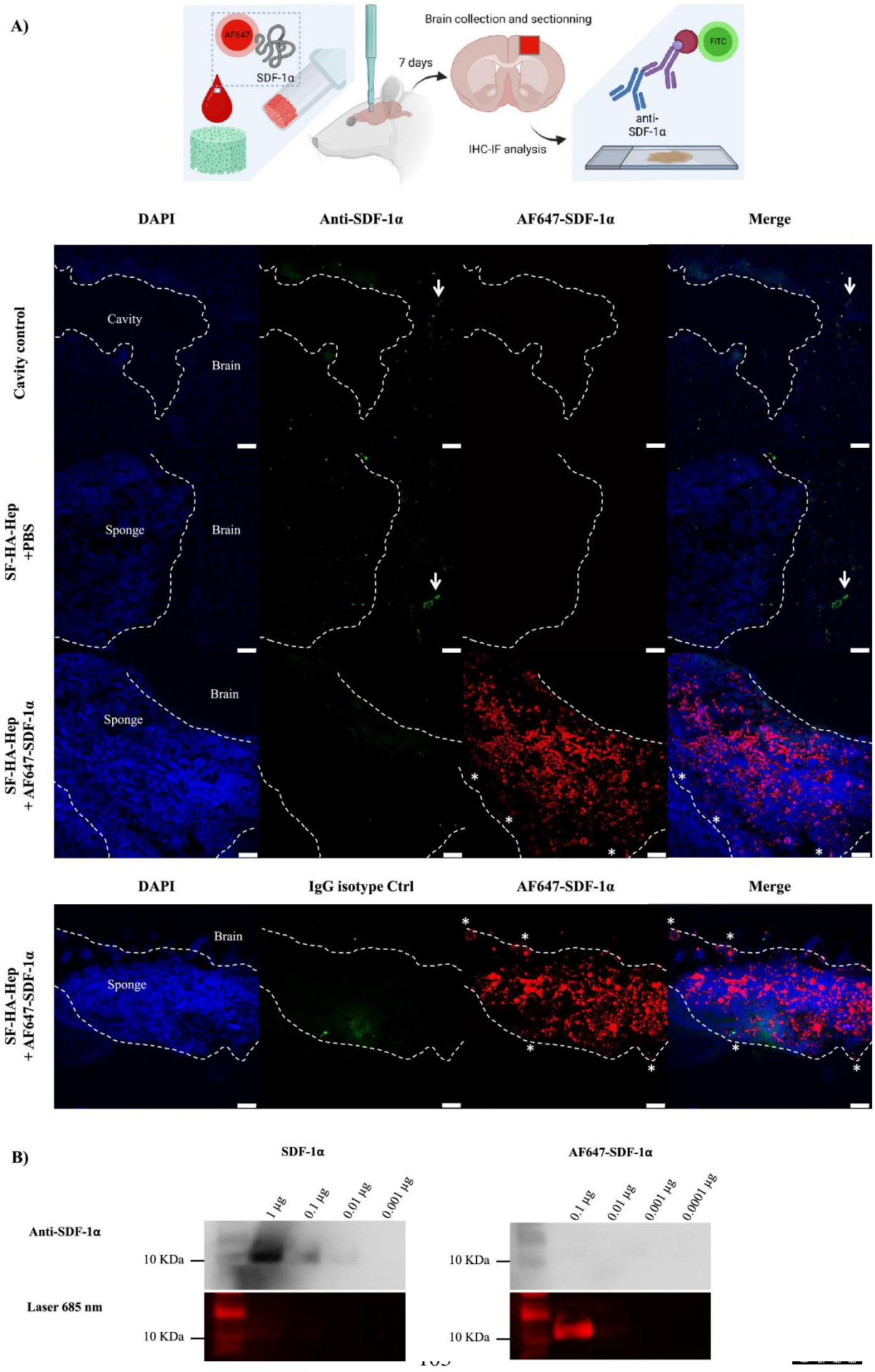
A)
AF647
SDF-1α
7 days
Brain collection and sectionning
IHC-IF analysis
FITC
anti-
SDF-1α
DAPI
Anti-SDF-1α
AF647-SDF-1α
Merge
Cavity control
Cavity
Brain
SF-HA-Hep
+PBS
Sponge
Brain
SF-HA-Hep
+ AF647-SDF-1α
Brain
Sponge
DAPI
IgG isotype Ctrl
AF647-SDF-1α
Merge
SF-HA-Hep
+ AF647-SDF-1α
Brain
Sponge
B)
SDF-1α
AF647-SDF-1α
1 µg
0.1 µg
0.01 µg
0.001 µg
0.1 µg
0.01 µg
0.001 µg
0.0001 µg
Anti-SDF-1α
10 KDa
Laser 685 nm
10 KDa
10 KDa
10 KDa

Fig. 6 (Previous page). *In vivo* distribution of SDF-1α. A) Implantation of SF-HA-Hep sponges containing SDF-1α tagged with AF-647, in the resection cavity in the frontal cortex of Fisher rats (Created with BioRender.com). Control sponges contained only PBS. Seven days after implantation, brains were collected and sliced. AF-647-SDF-1α was localized within the structure of the sponge (red channel, third column). Degradation of sponges was observed at their edges in contact with the borders of the resection cavity, and the detaching bulges containing AF-647-SDF-1α were located adjacent to the brain parenchyma (white asterisks). Further labeling with an anti-SDF-1α antibody and revelation by the Strep-FITC amplification method did not show the presence of AF-647-SDF-1α as the latter was not recognized by the anti-SDF-1α, see (B). The presence of small blood vessels positive for the anti-SDF-1α antibody was rarely observed in the margins of the resection (white arrows, second column, green channel). Scale bar = 100 µm. B) WB analysis for the immuno-detection of SDF-1α and AF-647-SDF-1α. The same anti-SDF-1α antibody recognized only the non-tagged SDF-1α but not the AF-647 tagged SDF-1α, which is however revealed by excitation with an IR laser.

3.9. CXCR4+ GB cells interacted with SDF-1α loaded sponges 7 days post-implantation

To assess the GB cell attractant capacity of sponges *in vivo*, two orthotopic models were tested in nude rats. In the first model, 5 x 10^3 U87MG-CXCR4+ cells were injected into the striatum. After 10 days of tumor development, a ~2-mm depth resection cavity was performed in the same vertical axis of cell injection, and SF-HA-Hep sponges were implanted loaded or not with SDF-1α. After 7 days, animals were euthanized, and brains were collected and analyzed by IHC-IF. Cell tracking by RFP, CXCR4 and Ki67 expression revealed colonization in only one implant loaded with SDF-1α (out of 3 animals) (**Fig. S3**). Although this experiment showed that SDF-1α-loaded sponges can be colonized by tumor cells after resection, the main complication found here was the lack of a reproducible resection. For instance, the tumor was completely removed in some cases and the distances between the tumors and scaffolds were not reproducible. To overcome this limitation, the second experimental set-up consisted in placing the implants and cells distanced from ~1 mm in the horizontal plane of the frontal brain cortex at the same time. First, SF-HA-Hep sponges with PBS or SDF-1α were implanted in the frontal cortex, followed by stereotactic injection of 2.5 x 10^4 U87MG-CXCR4+ cells 1 mm backward from the cavity edges (**Fig. 7**). Control rats were subjected to the same surgical and tumor cell injection procedures in the absence of sponges. After euthanasia, 7 days post-implantation, the brains were removed, snap-frozen and analyzed by IHC-IF. We observed a modification in the behavior of cells near the sponges compared to the cavity control alone. Cells constituting the anterior front of the tumor were able to interact with the surface of the sponges with a significant portion of CXCR4+ cells detaching from the main tumor mass towards the cavity containing the SDF-1α-loaded sponges or PBS-loaded sponges as compared to and cavity controls (**Fig. 7**). However, at this point, the interaction of cells with sponges was

only observed at the intermediate zone between the tumor leading edge and the edge of the sponges facing it.

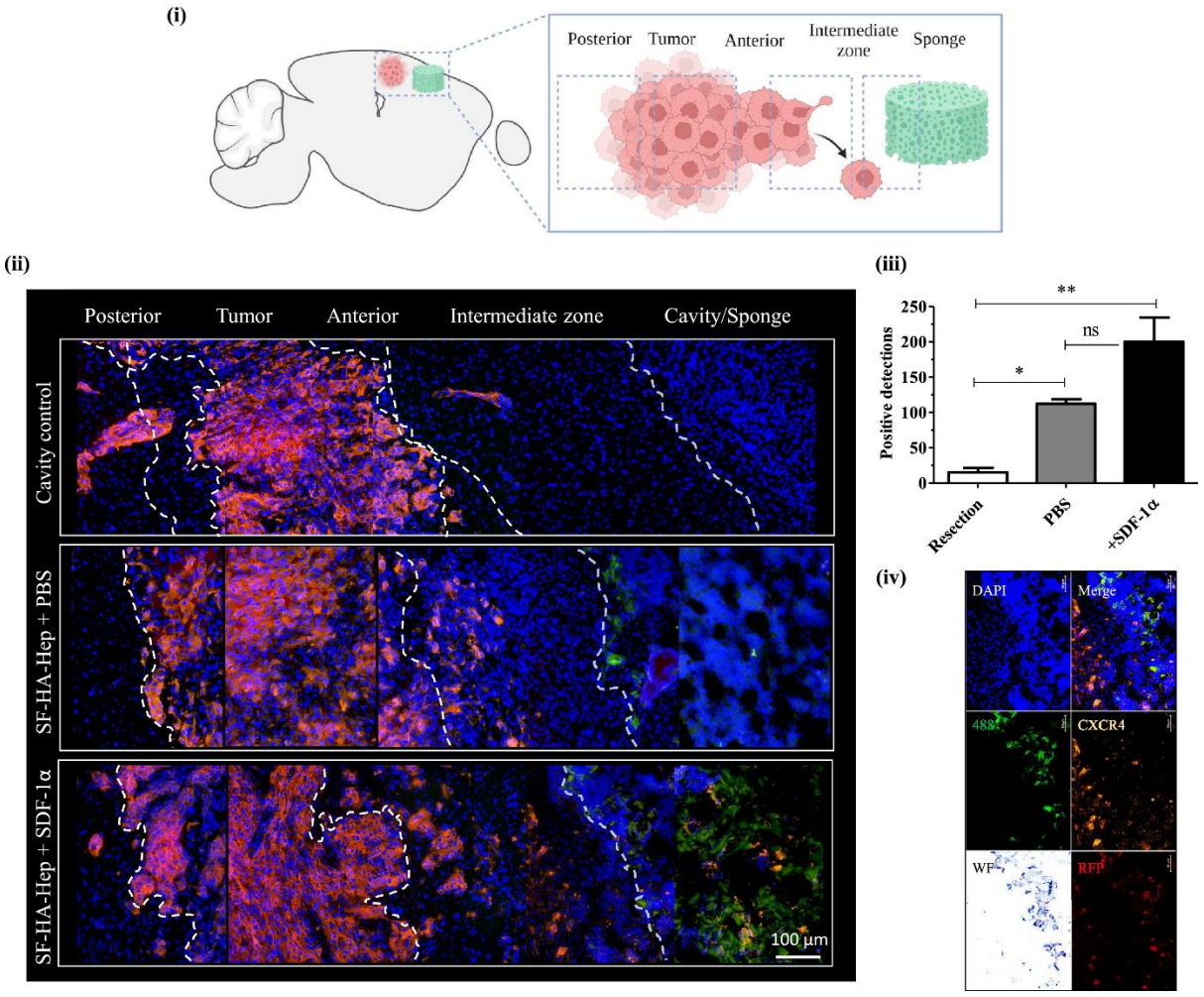

Fig. 7. *In vivo* response of GB cells to implantation of sponges. A model of the resection cavity in the brain cortex was developed in nude rats. U87MG-CXCR4$^+$ cells were injected near the sponges loaded or not with SDF-1α, or near the created cavity alone (i) (Created with BioRender.com). After seven days following implantation, cell detection was performed in cryosections by RFP expression and CXCR4 immunolabeling (yellow) (ii). Depicted are the composite images resulting from the merging of the different channels. An increased cell number of dissociated cells lying in the anterior/intermediate zone between the tumor and the sponges in rats bearing SF-HA-Hep sponges loaded with SDF-1α (SF-HA-Hep + SDF-1α) or sponges alone (SF-HA-Hep + PBS) was observed as compared to rats with the resection cavity alone with no implanted sponge (iii) ($n = 3$; $*$: $p < 0.05$, $**$: $p < 0.01$). The right panel shows an example of images from single channels as follows: WF (white field), RFP (red fluorescent protein), CXCR4 (yellow), DAPI (cell nuclei), 488 (green autofluorescence of sponges) (iv).

3.10. SF-HA-Hep sponges shaped the tumors and allowed their localized development

To assess the effect of sponges in the long term, the same orthotopic model used to evaluate the colonization of sponges was implemented, but this time 1 x 10^3 U87MG-CXCR4+ cells were injected. Animals were followed up until the defined endpoint, and tumor evolution was followed by MRI every week. All animals recovered within 2 hours after the procedure and did not show any signs of distress. Animals behaved normally and started to present symptoms from week 4 after surgery. Results showed that the survival of rats did not improve by sponge implantation in either case loaded or not with SDF-1α (**Fig. 8A**) compared to cavity controls. We observed that SDF-1α tended to reduce the median of survival to 27.5 days as compared to controls (31 days), though non-significant statistically (the fact that there is one animal from the SDF-1α group crossing the other survival curves makes this non-significant). This effect correlates with the average size of the tumor that tends to be larger (as a tendency as no statistical difference was observed) for rats implanted with SDF-1α-loaded as shown in **Fig. 8A right panel**. Therefore, SDF-1α contained within the sponges may be exerting an effect on tumor evolution favoring its development. This result can be explained by the fact that no killing signal was included in the study. However, we observed an effect of the sponges on the tumor shape and localization. Interestingly, the shape of the tumors fitted better to the projections' shape of the cross sections of the sponges in the three axes imaged and they were more rounded compared to the tumors where sponges were not present (**Fig. 8B**). Indeed, the reduced tumoral areas outside the projection of sponges, suggest that the tumor is better confined in the volume behold by the sponge's structure. This result highlights the relevance of the sponge implantation as a strategy to confine the tumor in a controllable area and confer a spherical shape that can facilitate their further treatment.

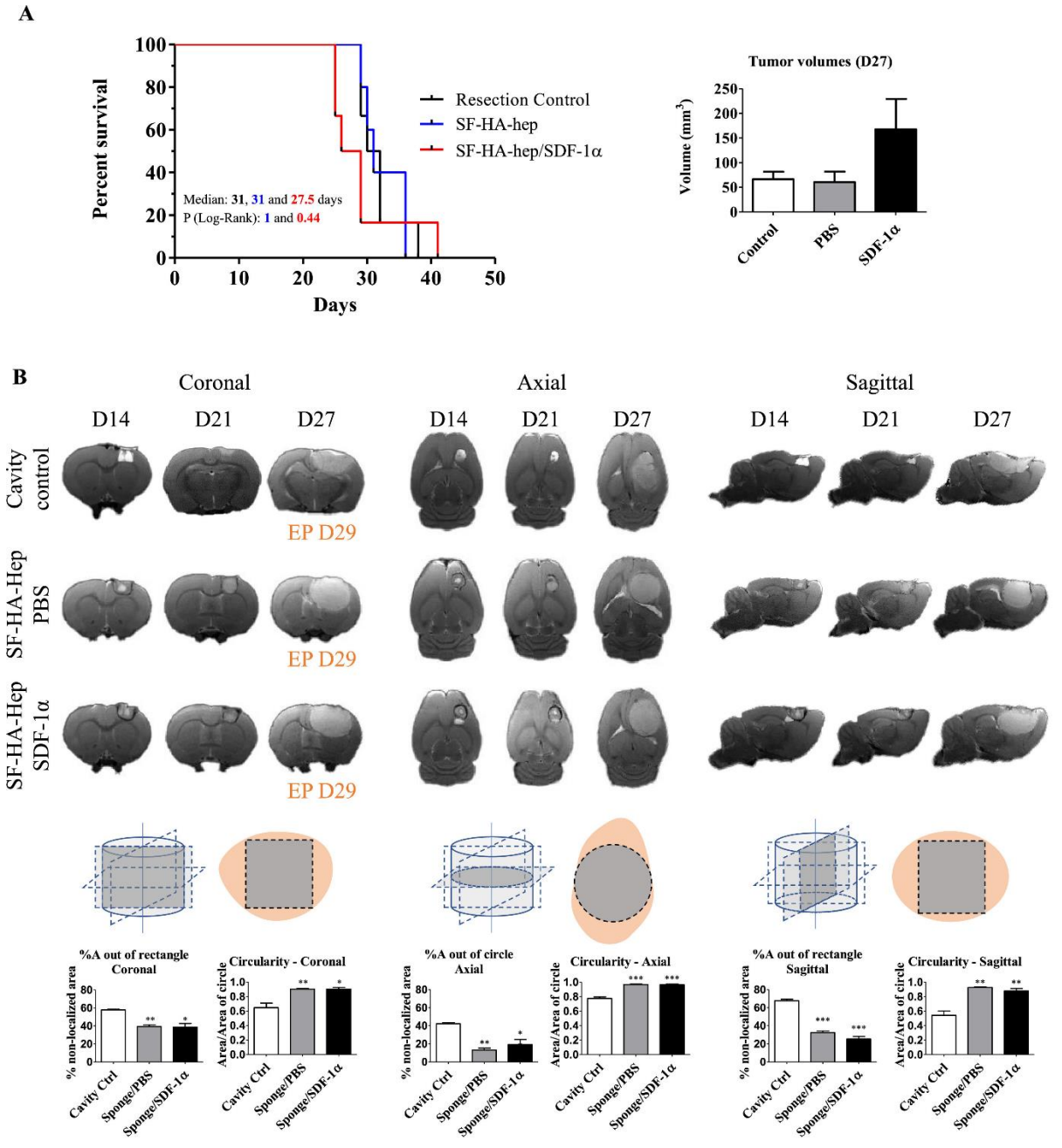

Fig. 8. Evolution of tumor growth and survival analysis of implanted rats vs cavity controls. A) Survival Analysis. Although no significant statistical difference is observed between groups, the calculated smaller median survival (27.5 d) for sponges loaded with SDF-1α correlates with a higher average tumor volume on day 27 (as a tendency as no statistical difference is observed, $P = 0.059$). B) The shape of the tumor is affected by the presence or absence of sponges. The area of the tumor out of the enclosed and shaped cross-sectional area projected from the sponge is depicted in the lower panels. The circularity is calculated as the area of the tumor cross-section divided by the area of the adjusted circle according to the tumor perimeter ($4\pi A/P^2$). Three slices were analyzed for each projection plane for each animal ($n = 3$ animals per group). Levels of significance are: ∗: $p < 0.05$, ∗∗: $p < 0.01$, ∗∗∗: $p < 0.001$.

4. Discussion

The main problem facing glioblastoma therapy is the infiltrative nature of GB cells remaining after standard treatment. cDNA expression analysis revealed that CXCR4 is overexpressed in 57% of primary glioblastoma (GB) tumors and in 88% of GB cell lines that were analyzed (Sehgal et al., 1998). CXCR4 expression is considered a prognostic marker in gliomas. Patients with CXCR4-positive GB had a reduced postoperative life expectancy (Chatterjee et al., 2014). CXCR4 was expressed in more than 50% of astrocytomas and 100% activated form (phosphorylated) in grades 2-4 astrocytomas and 76% in grade 1 astrocytomas (Woerner et al., 2005). Previously, it was shown that the CXCR4 receptor confers to GB cells increased infiltrative capacity into the brain parenchyma (Séhédic et al., 2017), and that the CXCR4/SDF-1α axis is related to the chemotaxis attraction of GB cells in vitro (Bian et al., 2007; Zhou et al., 2002) and of glioma stem cells (GSCs) to the tumor vasculature (Cheng et al., 2013). Here, a rupture concept was investigated, the strategy was to exploit CXCR4/SDF-1α axis to attract GB cells to a confining biodeposit consisting of a SF-HA-Hep sponge. This study aimed to investigate the preclinical feasibility and benefit of a new interventional approach using SDF-1α-loaded SF-HA-Hep aerogel sponges as implantable scaffolds into the brain resection cavity. Fischer rats were used to assess the in vivo biocompatibility of scaffolds to observe the complete foreign body reaction. However, to evaluate the in vivo performance of sponges, athymic nude rats were chosen because of the human cellular model that was used. The sponges are biodegradable. They were well tolerated for more than 3 months and reabsorbed after implantation into rat brains. The disappearance of the sponges is attributed to the inherent biodegradability of the scaffolds, primarily through hydrolysis and solubilization of the components. In vitro studies reported 85% degradation within 3 weeks (Najberg et al., 2020), under conditions mimicking in vivo enzyme presence. This gradual degradation can facilitate temporary accommodation of cancer cells within the cavity, minimizing the risk of long-term adverse reactions or the need for surgical removal. Their shape memory permitted fitting into the resection cavities and their highly interconnected pores supported cell infiltration and growth.

To assess the *in vivo* sponges' bioperformence, a cavity resection model was developed. Due to the difficulty of reproducibility of resected tumors by using a punch biopsy pen and an aspiration method, the developed rat model here shows that concomitant placement of implants and GB cells is feasible to investigate the functionality of interventional scaffolds in a model of the residual disease were infiltrating cells are situated adjacent to the cavities in the brain parenchyma. This strategy might be used to assess different scenarios including the distance between cells and scaffolds, and the number of injected cells. Here, by 1-mm distant placement of GB cells relative to resected zones, it was revealed that GB cells interacted with the sponges 7 days post-implantation. Serving as a chemokine reservoir in the tissue, SDF-1α remained within the sponges after 7 days of implantation.

In vitro, sponges loaded with SDF-1α directionally attracted U87MG-CXCR4+ GB cells and enhanced cell colonization within the scaffold. The function of SDF-1a is observed in the under-agarose assay in vitro from a distance that is 2-fold larger than the sponge implanted in vivo. The sponges alone did not show a difference relative to only wells containing PBS (**Figure 2B-i**). And sponges loaded with SDF-1a attracted cells vs sponges alone (**Fig. 2B-iii**). This means that the signaling provided by the released SDF-1α is necessary to attract GB cells distantly placed in a semi-confined site. In this case, the agarose gel provides a layer between the plastic and the gel that cells can invade. Moreover, the in vitro assay using tumor cells grown as spheroids demonstrated the importance of SDF-1α for improving the sponge colonization. In vivo, cells were injected approximately 1 mm away from sponges. This nearer placement of sponges as compared to the in vitro experiment, can influence the interaction of cells growing from the main tumor as observed in the intermediate zones and edges of the sponges facing the tumors in Figure 7. Interestingly, SF-HA-Hep sponges were able to shape and locate the tumors inside the cavities. The effect of shaping of the tumor by sponges alone (**Figure 8D**) can be explained by the attraction of cells by mechanisms yet undetermined and independent from SDF-1α. In vivo, on day 7 after cell injection, there was no significant difference between the positive detections of cells in the intermediate zone located between the tumor and sponges loaded with SDF-1α or sponges alone (**Figure 7**). This can be linked to the effect of sponges loaded or not with SDF-1α on tumor shaping. The MRI images provided on Figure 8B corresponding to day 27 suggest a displacement of the tumor towards the cavities that contained sponges. Results did not reflect a survival improvement, but this was in part expected as no killing signal was introduced. The tumor-shaping and -sitting effect occurred regardless of SDF-1α loading, suggesting it is associated with the properties of the SF-HA-Hep sponges.

4.1 SF-HA-Hep sponges as a tool for intervention: instructing the tumor ecosystem

The dynamic crosstalk between cancer cells and their environment might be interfered to instruct the GB ecosystem and potentially improve treatment. Cancer cell behavior and fate are strongly associated with non-cellular components, such as the ECM. Thus, the unique composition and architecture of the brain ECM can offer opportunities, being implemented as a target and as an instrument for various therapeutic strategies (Belousov et al., 2019; Mohiuddin and Wakimoto, 2021; Sood et al., 2019). GB cell morphology, migration and proliferation can be influenced by the composition of the biomaterial (Chen et al., 2018; Rao et al., 2013; Wang et al., 2014). And parameters such as porosity, permeability and the stiffness of the scaffold can be crucial in terms of cell ingrowth, cell growth, migration, and scaffold colonization (Bartoš et al., 2018).

Previously, the physicochemical and mechanical similarities between the brain ECM and SF-HA-Hep sponges were described (Najberg et al., 2020). Here, we demonstrated that the multiple interconnected 69µm-pore-channel networks of SF-HA-Hep sponges played a

significant role in GB cells' infiltration and spreading by providing adequate internal space and support for cell growth. Pore size is a fundamental factor implicated in the invasion and migration of GB cells (Saif Ur Rahman et al., 2023), which occur after matrix degradation when the cross-sectional area of the interfibrillar pore is less than 7 μm² (Wolf et al., 2013). Above this value, cells can undergo physical deformations to squeeze through the pores of the brain ECM and migrate (Polyak and Weinberg, 2009). The spatial arrangement of the matrix fibers near primary tumor sites can influence the motility of tumor cells, and aligned fibers offer tracks that are more conducive to migration (Paul et al., 2017; Provenzano et al., 2008). With this regard, Jain et al. (2014) demonstrated that aligned fibers can be used as guidance elements to direct brain resident GB cells toward an extracortical zone. In contrast, SF-HA-Hep sponges presented here did not feature any structural alignment (Jain et al., 2014). Other works using non-aligned porous scaffolds made use of an attracting signaling strategy, trying to imitate metastatic niches. For example, De la Fuente et al. (2015) used extracellular vesicles to demonstrate the luring capacity of ovarian cancer cells when loaded into the scaffold's matrix (de la Fuente et al., 2015). Moreover, Azarin et al. (2015) showed that the implantation of PLG microporous scaffolds in mice mammary fat pads induced the recruitment of immune cells by cytokines including CCL22, that in turn induced the recruitment of metastatic breast cancer cells (Azarin et al., 2015). In the context of glioblastoma, Giadel wafers used for carmustine delivery are FDA approved, but no other porous scaffolds like sponges have been used for the trapping of GB cells. This paper hence describes a new system. Porous SF-HA-Hep sponges offer the possibility of covering a larger space and taking advantage of the resection cavity after implantation. These sponges are biodegradable, so a second surgery to remove the device would not be necessary.

In the present work, we explored the effect of loading a chemoattractant into SF-HA-Hep sponges and found that SDF-1α -loaded sponges were able to attract GB cells *in vitro*. *In vivo*, clusters of tumor cells and individual cells were observed infiltrating the intermediate zone between the anterior tumor border and the sponges, which was promoted by the SDF-1α load compared to the cavity controls. However, we also found that tumor shaping and localization were favored to fit the resection cavities containing implants, and this occurred independently of SDF-1α loading. Interestingly, the shape of the tumors matched the shape of the cross-sectional projections of the sponges in the three MRI axes imaged, being more rounded when compared to the tumors where sponges were absent. This suggests that the implants exerted an attraction force from the site of cell injection toward the resection cavity. Indeed, the sponge structure was not seen anymore during the 4th week of MRI imaging. This can be explained by 1) the total colonization of the sponges by U87MG-CXCR4+ cells during the experiment, hindering the sponges' structure, 2) the complete sponge's degradation favored by the tumoral environment, and 3) the ejection of sponges by the tumor's center of mass displacement and further elimination of the sponges.

Despite not knowing the precise mechanism, the attraction of GB cells seen at the sponge-parenchyma intermediate zone after 7 days of implantation, even in the absence of SDF-1α,

suggests that sponges alone may modulate GB cell behavior. Cancer cells can be guided towards laminin and hyaluronan molecules in the ECM by internal integrins and CD44 receptors respectively, and via haptotaxis by chemokines and growth factors immobilized along tracks (Aznavoorian et al., 1990; Fan et al., 2014). In line with this, HA may have contributed to tumor cell presence inside SF-HA-Hep sponges, via CD44/HA axis (Wolf et al., 2020), as the majority of U87MG-CXCR4+ cells expressed the CD44 receptor (**Fig. S4**). In addition, in vitro U87MG cells responded better when directly seeded into SF-HA-Hep sponges as compared to SF-HA sponges (**Fig. 2D**), highlighting the effect of the matrix structure and composition. Heparin and other glycosaminoglycans (GAGs) can regulate glioma cell adhesion to ECM proteins leading to cell proliferation or cell migration, according to the ECM composition, thus modulating tumor cell properties (Mendes de Aguiar et al., 2005). Heparin can be safely used when it is modified or covalently incorporated into scaffolds for biomedical applications (Choi et al., 2017; Rodrigues et al., 2019; Zhao et al., 2019) offering cell contact sites by the recruitment of molecules promoting cell adhesion. Therefore, the enhanced in-vitro cell response observed here could be explained by the trapping of factors from the media containing FBS such as fibronectin and vitronectin, both of which harbor heparin binding sites (Hayman et al., 1985; Zhong et al., 2018).

Furthermore, the strong heparin-chemokine complex was responsible for SDF-1α retention in SF-HA-Hep sponges (Najberg et al., 2020; Seeger et al., 2012). As this chemokine can be rapidly turned over (Rusetska et al., 2022) and inactivated by nitration *in vivo* (Janssens et al., 2016), the SDF-1α immobilization in the sponges combined with their slow degradation rate can offer an advantage as a reservoir reinforcing its role in haptotaxis versus chemotaxis, here pivotal for directional cell migration and colonization of the sponge. SDF-1α linked to heparin-binding domains had similar activity to the free chemokine (Laguri et al., 2007). Here, fragments of SF-HA-Hep sponges as AF647-SDF-1α bulges were seen in the edges of the brain cavities containing a high number of cell nuclei. These bulges might have induced a haptotaxis response (Yamada and Sixt, 2019).

The recruitment of immune cells in the site of scaffold implantation has been described as having a role in the creation of premetastatic niches for the capture of breast cancer cells. Leukocytes can be recruited into scaffolds reorganizing as a site of pre-metastasis in a murine breast cancer model. This is due in part to the secretion of soluble factors from recruited Gr1hiCD11b+ cells that can attract cancer cells (Aguado et al., 2018; Azarin et al., 2015). SDF-1α is a cytokine that can be secreted by immune cells including neutrophils (Nakayama et al., 2011). Despite PMN cells were recruited into the sponges, endogenous SDF-1α in the site of implantation was not detected in both implanted and mock surgery resected rats. Besides, other soluble factors can attract cancer cells which do not exclude the possible effect of implantation of SF-HA-Hep sponges alone as a premetastatic niche. Further experiments need to consider the distant placement of sponges (> 1 mm) from the primary tumor site to assess their premetastatic potential.

Alternatively, the attraction driving force might have been physical. Cells were injected after scaffold implantation, so the sponge was most probably not exerting any absorption of liquid, as they were already equilibrated with the liquids inside the cavity. By exclusion, this effect may be related to sponge stiffness, as stiffness gradients can induce cell migration (Davies, 2013; Yamada et al., 2019). Considering this, the young modulus of SF-HA-Hep sponges (13 KPa) (Najberg et al., 2020) is larger than that of the human brain (1-10 KPa) (Nava et al., 2012; Singh and Chanda, 2021), but may better suit the tumor microenvironment, where the altered ECM presents enhanced matrix stiffness (11.4 to 33.1 KPa) (Peng et al., 2022). Thus, SF-HA-Hep sponges may confer to cells a suitable substrate with stronger mechanical forces than the brain ECM, allowing them to move up-gradient, in a durotaxis response.

The reverse effect of the ECM on cancer cells and the progression of tumors remains to be investigated (Belousov et al., 2019; Erickson et al., 2018; Saleh et al., 2019; Sood et al., 2019). Here, we showed that alteration of the tumor ecosystem can be done by the implantation of SF-HA-Hep sponges in the resection cavity. The exact underlying mechanisms of how SF-HA-Hep sponges helped to the resection cavity siting and shaping of the tumors remain to be completely determined. Further studies including scaffold-to-tumor distance variation, the measuring of mechano-sensing markers and the identification of immune cells can give more clarification in this matter. Overall, the biological and mechanical properties of SF-HA-Hep sponges may allow the concentration of remaining GB cells in a controllable area for further elimination.

4.2. Limits and perspectives

Incorporating dynamic biological information into scaffolds to match the *in vivo* environment of the native tissue has gained great appreciation (Litowczenko et al., 2021). However, this design can be a colossal challenge considering the complexity of the aberrant cues and signaling of cancer. The increasing understanding of the pre-metastatic niches and their roles in welcoming metastatic dissemination (Aguado et al., 2017; Bassi et al., 2020; D'Angelo et al., 2020) has inspired scientists to create different strategies to trap migrating cancer cells (de la Fuente et al., 2015; Huang et al., 2020; Oakes et al., 2020; Xiong et al., 2022). In our exploration of SDF-1α as a bait to attract GB cells, we have encountered several challenges.

4.2.1. Release and control of SDF-1α into the brain parenchyma

We were previously able to observe the capacity of SF-HA-Hep sponges to integrate SDF-1α into their structure according to the loading methods used by simple dropping (Najberg et al., 2020). The distribution profile of the protein inside the sponge was visualized using SDF-1α coupled to AlexaFluor 647 thus demonstrating a radial concentration gradient from the center (where the drop was deposited) toward the edges of the sponges (Najberg et al., 2020). The ability of heparin to bind SDF-1α in polymer matrices is a proven fact thus facilitating the loading of chemokine (Krieger et al., 2018; Prokoph et al., 2012). Here, the SDF-1α retention

capacity displayed by the SF-HA-Hep sponge correlates with the presence of AF 647-SDF-1α within the sponges in the brain parenchyma on day 7 of evaluation.

For strategies envisaging to attract cancer cells from a distant site, chemoattraction is an attractive strategy. The first challenge is related to the design of the scaffold to provide a releasing signal so that it creates a gradient, perdures and gets to the site of cancer cell residence. SF-HA-Hep sponges showed strong retention of SDF-1α. The initial burst of SDF-1α that occurred during the first day was about 4% of the total load, quickly reaching a 5% cumulative release plateau thereafter (Najberg et al., 2020). *In vitro*, this initial burst of SDF-1α was enough to chemoattract U87MG-CXCR4+ cells. Indeed, the calculated concentration in 30 µL of liquid within the well of the agarose gel (1070 ng/mL) was sufficient to create a gradient of SDF-1α. And, even if all the released SDF-1α were diffused within the 3-mL gel, the final concentration (10.7 ng/mL) would still be active (Zhou et al., 2002). Nevertheless, these remarks may not apply to the *in vivo* scenario. In this case, 32 ng of SDF-1α are released in a watery volume of ~20 µL corresponding to the resection cavity. Assuming a homogeneous distribution, the after-burst concentration of the soluble SDF-1α within the resection would be 1600 ng/mL. However, the surgical procedure involves leakage from drained liquids, including blood; therefore, it seems difficult that this concentration remains within the cavity. Moreover, if we consider SDF-1α degradation by enzymes and the inflammatory environment, the calculated SDF-1α initial concentration would be further reduced. In addition, SDF-1α being a small cytokine is rapidly dispersed in a water environment but the diffusion coefficient in the brain may be different.

Importantly, no AF647-SDF-1α was detected by fluorescence in the brain parenchyma, apart from the signal present in the detaching bulges from the edges of the sponges corresponding to the heparin complexed form of SDF-1α (**Fig. 6A**). Of note is that the levels of detection of the fluorescent protein by WB were only possible at 100 ng of protein concentrated in a band (**Fig. 6B).** Therefore, it is possible that lower levels of AF-647 were not detected in the brain parenchyma. Further studies need to consider different time points to evaluate the *in vivo* releasing profile of SDF-1α from the sponges using a radiolabeled protein. Discerning between chemotaxis and haptotaxis can be addressed by varying the placement of cells relative to sponges. Here, the effect of SDF-1α can be explained in part by a combination of chemotaxis and haptotaxis signaling as cells were injected beside the sponges. Under the premise that if SDF-1α is not released then chemoattraction can be limited, to improve the releasing profile of the chemokine, another strategy can be envisaged such as the incorporation of the protein into nanoparticles (Gascon et al., 2020; Molina-Peña et al., 2021) for further integration into the sponges.

The optimal concentration of SDF-1α for GB-cell attraction may depend on several factors such as the stage of the disease, the type of cells involved, and the presence of other factors that may influence the chemokine activity. The effects of SDF-1α on cancer cell behavior can be concentration-dependent. Low concentrations of SDF-1α can promote cancer cell migration

and invasion, while high concentrations can inhibit these processes by causing receptor internalization and desensitization (Tavor et al., 2004). Pasquier et al. (2015) showed that low concentrations of SDF-1α promote the migration of breast cancer cells through the activation of RhoA, while high concentrations increased adhesion through the activation of Rac1 (Pasquier et al., 2015). Therefore, the task involves the design of a releasing profile to reach a steady state biological concentration of the chemokine during the time required to reach the target, which implies further and in-depth knowledge of the system.

4.2.2 Pleiotropic effects of SDF-1a

The concept of tumor entrapment aims to confine and eliminate cancer cells within a controlled microenvironment. Two primary strategies involve synergy with locoregional irradiation and the use of compounds to counteract tumor cell growth and resistance. SDF-1α, a versatile signaling molecule, plays a pivotal role in various biological processes. Its initial advantages, such as chemoattraction and migration, can turn detrimental to inhibiting proliferation. Hence, the development of diverse SDF-1α analogs offers promise for selectively modulating its functions (Faber et al., 2007). Exploring distinct SDF-1 isoforms like SDF-1γ, with unique biomatrix binding properties, can further optimize the balance between beneficial chemotaxis and reduced proliferation (Migliorini et al., 2015).

The SDF-1α network is intrinsically connected with several genetic and molecular events in the tumor microenvironment (Henke et al., 2020), reflecting in tumor growth and cell invasion. CXCR4-mediated chemotaxis can be mediated by the activation of PI3 kinase (PI3K) by both Gβγ and Gα subunits of the activated G-protein coupled receptor. PI3K activation results in the phosphorylation of several focal adhesion components, paxillin among them (Teicher and Fricker, 2010). Tyr118, the main residue of paxillin phosphorylation by focal adhesion kinase (FAK) was found here in gradual phosphorylated levels according to the increasing time of exposure to SDF-1α, suggesting a gradual formation of focal adhesions (Hu et al., 2017). However, we also found activation of Akt and Erk. Independent activation of Akt and ERK1/2 by SDF-1α can support cell growth (Würth et al., 2014), and exert a positive effect on the survival of GB cells (Zhou et al., 2002).

Therefore, although the initial strategy of using SDF-1α as a chemoattractant was coherent with the observed gradual increase in p-paxillin and the strong chemotactic in-vitro response, the utilization of SDF-1α to attract infiltrative GB cells *in vivo* entails a risk of tumor progression and dissemination that must be evaluated. Indeed, we found that the effect of SDF-1α on migration was independent of cell proliferation *in vitro*. However, the reduced cell hallo observed in the ADC-treated agarose drops (proliferation inhibited), also suggests a positive effect of SDF-1α on survival and/or proliferation. Moreover, the *in vivo* observations about the larger average tumor size and reduced median survival suggest that SDF-1α contained within the sponges may favor the development of the tumors. Therefore, this may lead to an increase in tumor aggressiveness if not controlled.

A better understanding of SDF-1α pathways' activation after loading into SF-HA-Hep sponges might help to find an optimal condition. For instance, SDF-1α forms oligomers upon binding to free GAGs in brain ECM, which implies the regulation of chemokine function (Migliorini et al., 2015). Whether chemoattraction alone can be activated in the SDF1α /CXCR4 axis is not known. However, evidence exists that the SDF-1γ isoform did not induce robust cell motility unless it was bound to heparin (Janowski, 2009; Laguri et al., 2007). Then, a modification of the scaffold-chemokine interaction or the use of a different isoform might favor chemotaxis against proliferation or survival.

4.2.3. Tumor heterogeneity, the evolution of cancer cells and endogenous signals

SDF-1α has been shown to exert a chemoattractant effect *in vitro* on GB patient-derived cell lines expressing the CXCR4 receptor (Zhou et al., 2002). In addition, U87MG-CXCR4+ cells are infiltrative into the normal mouse brain parenchyma (Séhédic et al., 2017). However, cell lines may not represent completely GB as a heterogeneous tumor. Even if the cell of origin might be a common neural stem cell or progenitor cell (Alcantara Llaguno and Parada, 2016), the evolution of the tumoral cell content is dictated by the tumoral ecosystem, and different glioma stem cells with their progeny may be present (Kanu et al., 2009). Therefore, the expression of the CXCR4 receptor might be variable, reducing the targeting efficiency.

Furthermore, the expression of endogenous signals in the brain can represent competitional zones for cell attraction. For example, we observed SDF-1α expression in blood vessels, which are sites of GB cell migration. Macrophage migration inhibitory factor (MIF) can also bind to the CXCR4 receptor, and it is expressed by U87MG cells (**Fig. S5**), therefore the autologous/paracrine signaling from the tumor itself can also interfere with the efficiency of the chemoattraction strategy.

4.2.4. Cellular/tissue barriers to migration

Another consideration is related to the body's reaction to the material itself. Fibrotic capsules are often formed in materials recognized as strange bodies as implanted devices (Horejs, 2021). The cellular and tissue barriers formed around them, represent then an obstacle to cell colonization. For example, the M-Trap device showed increased mean survival of human ovarian cancer xenografted rats (de la Fuente et al., 2015), but has failed to demonstrate safety and efficacy in clinical trials. This was attributed to surgical complexity and the numerous intraperitoneal adhesions developed after implantation, preventing tumor cells from reaching the devices (Gil-Moreno et al., 2021). In the brain context, Autier et al. (2019), designed bacterial cellulose (BC) membranes for tumor bed implantation, as a system for trapping residual GB cells. *In vitro* assessments showed that F98 tumor cells were trapped and unable to move onto the surface of the membranes. However, a fibrous capsule was observed around the material after brain implantation, which may prevent or decrease cell access (Autier et al., 2019). This reaction was not observed for any of the implanted sponges as demonstrated by the

histological analysis in rats, however the host reaction might be different as observed in humans for the M-trap device.

4.2.5. Tumor microenvironment (TME)'s response

SF-HA-Hep sponges caused an acute and chronic inflammatory response that was characteristic of a foreign body reaction with the recruitment of PMN cells, macrophages and lymphocytes. The presence of diverse cell types within the GB TME can influence the progression of the disease. For instance, GB cells are thought to induce an immunosuppressive environment by secretion of different factors. Among them, M-CSF, TGFb-1 and IL-10 skew macrophages to the immunosuppressive M2 phenotype (Nduom et al., 2015). The presence of M2-stage macrophages is correlated with vessel dilation and malignancy in different human glioma samples (Mathivet et al., 2017). Furthermore, normal monocytes exposed to glioma cells acquire properties like those of myeloid-derived suppressor cells (MDSCs) (Rodrigues et al., 2010). Secretion of VEGF induces neoangiogenesis, inhibits maturation of dendritic cells, hinders infiltration of effector T-cells and activates antigen-specific regulatory T cells (Motz and Coukos, 2013). In addition, reactive astrogliosis produces growth factors, cytokines and metabolites that promote gliomagenesis (De Vleeschouwer, 2017). We observed the presence of PMN cells and chronic inflammatory cells in both SF-HA-Hep and control cavities without sponges. Although this observation was true in the immunocompetent Fischer rats, nude rats (with 70% Fischer background, Janvier Labs) may have a similar response due to the presence of most of these immune cells except for mature T-cells. In nude animals, SF-HA-Hep implantation alone did not influence survival as compared to cavities, therefore the discrimination of a positive effect of the inflammatory response on tumor progression cannot be discerned. To explore the effect of the whole immune system, the complete immunocompetent model would have to be used. Whether these immune reactions could be exploited for targeting cancer cells remains to be explored, i.e., the reversion into a positive factor for GB treatment.

Taken together, these listed factors should be considered in the design of a tumor cell trapping strategy, independently of the molecules used. Their adequate consideration may increase the efficacy of the cell trapping capacity.

4.3. The resection cavity as a part of the pathology and perspectives on sponges as "meeting rooms" to direct the GB ecosystem

In operable GB, the resection cavity is part of the pathology. After tumor surgical resection, the brain parenchyma is extremely fragile, and the cavities present unpredictable shapes and sizes. These aspects hinder the local administration of post-operative treatments, resulting in a high probability of recurrence (~90% of the cases) (Lemée et al., 2015). Mainly, tumor cells present in the peritumoral brain zone are responsible for that, and today it is impossible to image and target them using the maximum tolerated dose of radiotherapy after surgery (Autier

et al., 2019). However, the resection space can also offer an opportunity for the treatment of recurrent GB. The two main limitations contributing to the failure of conventional therapy are i) treatment resistance and ii) sub-optimal delivery of active principles. Different strategies have been investigated for the local and enhanced delivery of chemotherapeutic agents. Convection-enhanced delivery (CED) allows direct delivery of chemotherapeutics via a catheter in the tissue surrounding the GB resection cavity, but this method results in unpredictable brain diffusion and requires the use of several surgical procedures, leading to a high risk of infection or bleeding (Cruz Da Silva et al., 2021). Other strategies include the use of hydrogels and other implantable scaffolds (Bastiancich et al., 2016; Djoudi et al., 2022) for the sustained and local delivery of chemotherapeutics. However, only Gliadel wafers, consisting of an implantable copolymer that allows the controlled release of carmustine within the cavity, have reached the clinic. Recently, it was reported that adjuvant treatment with Gliadel may prolong the overall survival of malignant glioma patients (Iuchi et al., 2022), but their association with a high rate of complications is still controversial (Bregy et al., 2013; Buonerba et al., 2011; Yeini et al., 2021).

Alteration of the GB ecosystem may offer a new perspective for the targeting of the residual disease. Luring of GB cells is now being explored to concentrate GB cells for further elimination (Autier et al., 2019; Jain et al., 2014). For this purpose, the use of an implantable support as means of direct contact with the brain parenchyma is fundamental for the targeting of residual GB cells. In this line, shape-memory lasting SF-HA-Hep sponges may allow the brain parenchyma to have better structural support, preventing a collapse of this tissue after surgery and lasting long enough to permit cell infiltration.

However, the limitations presented and discussed for the tumor cell trapping strategy may still impede the complete eradication of infiltrative GB cells. Combined approaches, such as the use of chemoattractants and killing agents (Kasapidou et al., 2021), local radiotherapy (Séhédic et al., 2017), or the delivery of cellular components such as engineered tumoricidal neural stem cells (Sheets et al., 2020) may help a better outcome.

Switching the focus from the cancer cell alone to one that includes the normal host environment offers new perspectives (Belousov et al., 2019; De Boeck et al., 2020). SF-HA-Hep sponges and other implants (Autier et al., 2019; de la Fuente et al., 2015) caused a local inflammatory response. Moreover, the presence of CD11b/c-positive cells inside the sponges and GFAP-positive cells in the vicinity of the cavities seven days post-implantation (**Supp. Fig. 6**) indicate that various cell types can interact with the implant, regardless of whether it is loaded with SDF-1α or not. These interactions could potentially impact the TME. Integrin CD11b is primarily expressed in monocytes, macrophages, neutrophils, dendritic cells (DCs), NK cells, and a subset of B and T cells (absent in the case of nude rats). Conversely, CD11c is a widely used marker for defining DCs (Gallizioli et al., 2020) . The Glial fibrillary acidic protein (GFAP), on the other hand, is specifically found on the surfaces of cells belonging to the myeloid lineage, such as microglia (Yang and Wang, 2015). Ideally, implantable materials

should have a regenerating anti-inflammatory and neuro-regenerative effect after surgical resection of the tumor (Belousov et al., 2019; Newland et al., 2015). However, the inflammatory cells observed in the cavities might be reeducated for the tackling of tumor cells. GB is known to create an immunosuppressive environment (Pearson et al., 2020). This is due to the crosstalk between glioma and immune cells, which opens the possibility of the immunomodulation of the TME. Therefore, the presence of macrophages and lymphocytes after implantation of SF-HA-Hep sponges could be reverted in a positive factor to improve the immune response against the tumor by loading other chemokines and immunostimulatory molecules. Additionally, the chronic inflammatory cells can help to break down the ECM and increase blood flow to the tumor, improving drug penetration and increasing treatment efficacy (Huang et al., 2021). Further research is needed to fully understand the potential benefits of this approach as a "cell meeting room" implantable scaffold to remodel the GB ecosystem for better therapy outcomes.

5. Conclusion

The plethora of strategies investigated for GB treatment is impressive, but the reflection on patient survival is nowadays limited. This is due to the high infiltrative capacity of GB cells. Considering GB as an ecosystem disease may help in the designing of therapeutic strategies that explore the alteration of its elements such as migratory niches. Here, SF-HA-Hep sponges were able to attract GB cells from the parenchyma surrounding the created brain cavity in rats, and sited and shaped the tumors in the resection spaces. Besides, the sponges demonstrated to have characteristics compatible with an implantable biomaterial, adequate for the brain tissue. This work has shown this scaffold is a potential tool for GB treatment, although there are yet some limitations regarding the use of SDF-1α. The concentration of GB cells and the shaping of the tumor may improve cancer treatment by improving post-surgical outcomes, enhancing the effectiveness of chemotherapy and other targeted therapies, and improving the precision of radiation therapy. Still, limitations exist for the complete attraction of residual cells, therefore other combinatorial and immune-modulating approaches can be considered.

Acknowledgements

Authors would like to thank Romain Mallet, Florence Manero and Rodolphe Perrot from SCIAM (Common Service for Imaging and Microscopy Analysis, SFR ICAT 4208, Université d'Angers, France), Florence Franconi and Samuel Bonnet from PRISM (Imagerie et spectroscopie multi-modales, SFR ICAT 4208, Université d'Angers, France), Catherine Guillet, Jérôme Cayon and Lydie Bonneau from PACeM (Plateforme d'Analyses Cellules et Moléculaire, SFR ICAT 4208, Université d'Angers, France) Aurélia Rolland from IMAC (Imagerie Cellulaire, INRAE, Angers, France), and Laurence Sindji and Anne Clavreul for their useful comments.

Funding

This work was funded by the French National Research Agency (ANR) under the frame of EuroNanoMed III (project GLIOSILK “Silk-fibroin interventional nano-trap for the treatment of glioblastoma”) [grant ANR-19-ENM3-0003-01]. It was also supported by the Instituto de Salud Carlos III (ISCIII) [AC19/00067] Cofinanciado FEDER, Spain, by the Institut National de la Santé et de la Recherche Médicale (INSERM) and by the University of Angers (Angers, France). The work was in addition related to: (i) to the French ANR under the frame of the LabEx IRON (Innovative Radiopharmaceuticals in Oncology and Neurology) as part of the French government Investissements d’Avenir program (ANR-11-LABX-0018 to E.G.) ; (ii) the “Région Pays-de-la-Loire” under the frame of the Target’In project (Improvement of targeting radiopharmaceuticals for better diagnostic and therapy in nuclear medicine to E.G.) ; iii) the “Ligue Nationale contre le Cancer” and the “Comité Départemental de Maine-et-Loire de la Ligue contre le Cancer” (CD49) under the frame of the FusTarG project (Design and application of precision RNA oligonucleotides and aptamers for targeting gene fusion products in glioblastoma to E.G.) and iv) the "Tumour targeting, Imaging and radiotherapies network" of the “Cancéropôle Grand-Ouest” (France). RMP was a PhD fellow from the French “Ministère de l’Enseignement supérieur, de la recherche et de l’innovation” (MESRI). MN received a PhD fellowship from “La Région Pays-de-la-Loire” under the frame of the Erasmus Mundus Joint Doctorate program for Nanomedicine and Pharmaceutical Innovation (EMJD NanoFar).

Declaration of Competing Interests

The authors declare that they have no conflict of interest.

Data Availability

The data that support the findings of this study are available from the corresponding authors, upon reasonable request.

Supplementary Data

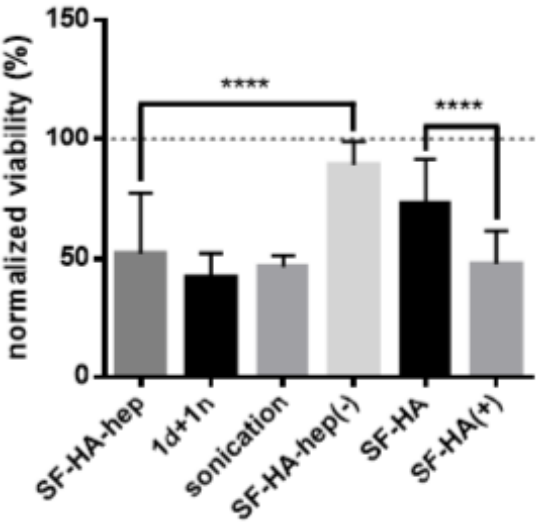

Supp. Fig. 1. Effect of the washing process and the concentration of crosslinkers on the cytotoxicity of cells. SF-HA-Hep = no additional washing, 1d+1n = 1 day agitation in PBS + 1 wash, sonication = 5 x 30 s sonication cycles followed by agitation for 1 h in PBS. SF-HA-Hep(-) = SF-HA-Hep sponge crosslinked with the same concentration as SF-HA, SF-HA(+) = SF-HA sponge crosslinked with the same concentration as SF-HA-Hep (n = 5-6 replicates).

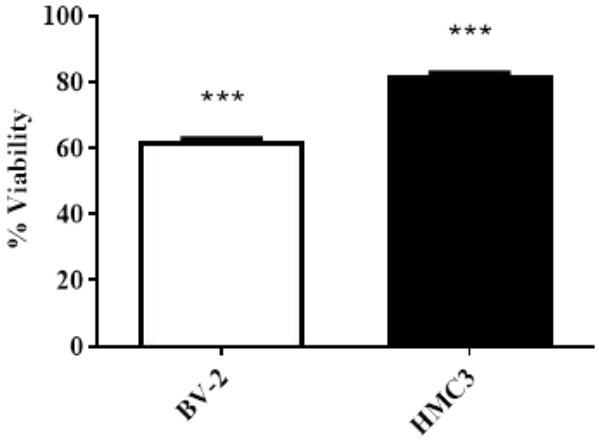

Supp. Fig. 2. Viability of murine BV-2 (A) and human HMC3 (B) microglial cells. Cells were incubated with sponges via the direct contact method for 24h (n = 6 replicates).

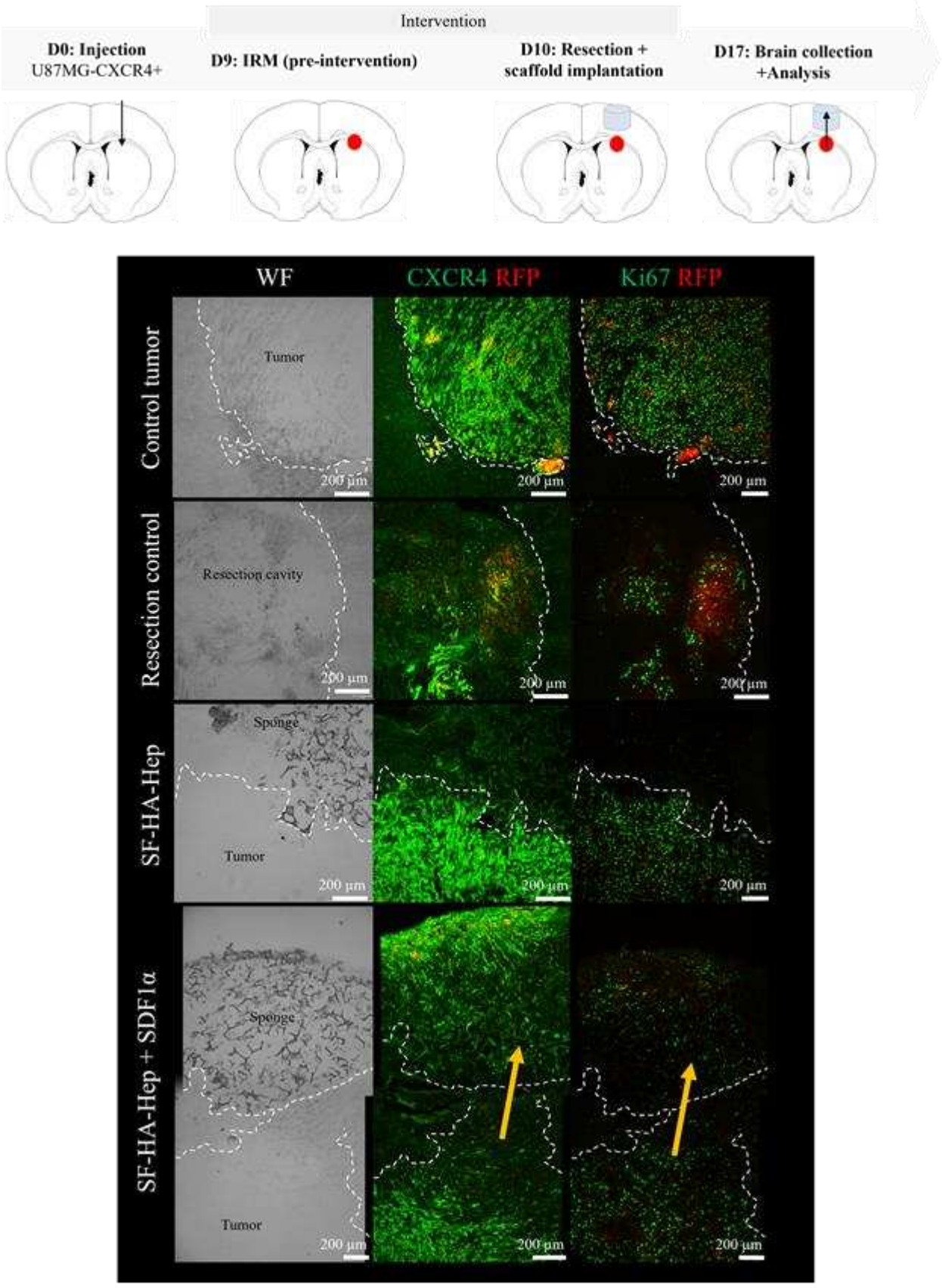

Supp. Fig. 3. In vivo colonization of sponges after resection and implantation near the tumor graft. 5 x 10^3 U87MG-CXCR4$^+$ cells were implanted in the striatum, just below the corpus callosum, in the brains of nude rats. After 9 days, detection of the tumor was performed

by MRI. On day 10, a brain cavity was performed in rats within the groups: resection control (second panel from top to bottom), SF-HA-Hep, and SF-HA-Hep + SDF1α. For the latter two groups, an SF-HA-Hep sponge either hydrated with PBS or loaded with SDF1α was implanted in the resection cavity, respectively. Controls correspond to rats bearing tumors without resection at D10. After 7 days from intervention animals were euthanized, and brains were collected and analyzed by IHC of CXCR4 and Ki67 (green channels) and tracking of red fluorescent protein (RFP) expressed by tumor cells.

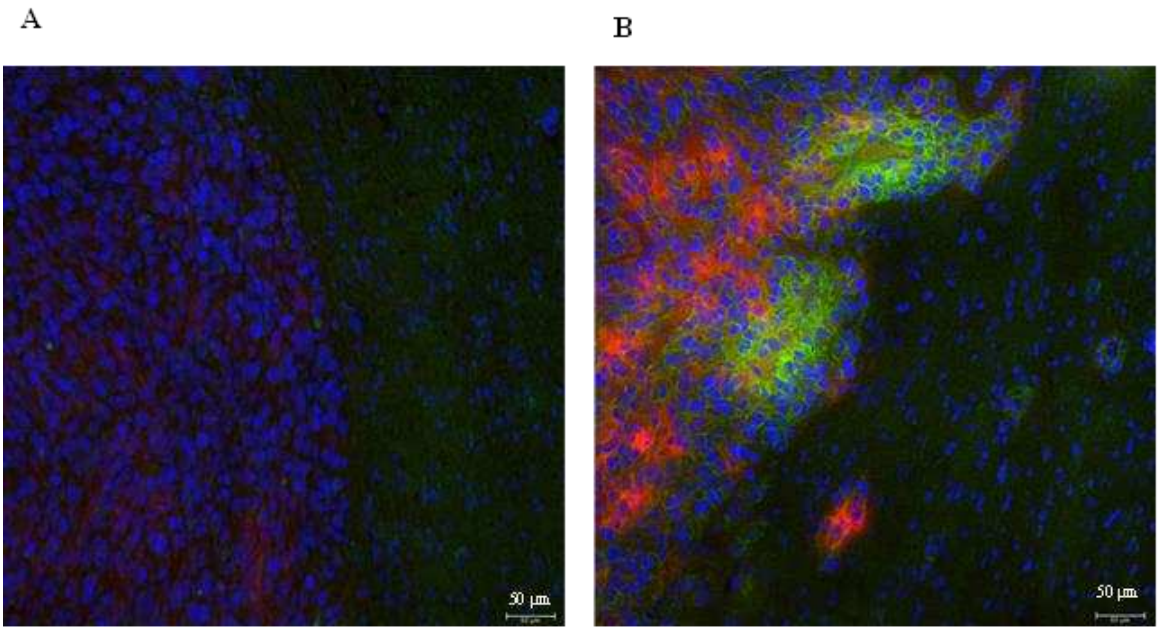

Supp. Fig. 4. CD44 expression in U87MG-CXCR4+ xenografts. 21-day tumors in nude rats. **A)** IgG1 isotype control and **B)** CD44 expression (green). Red = Red fluorescent protein.

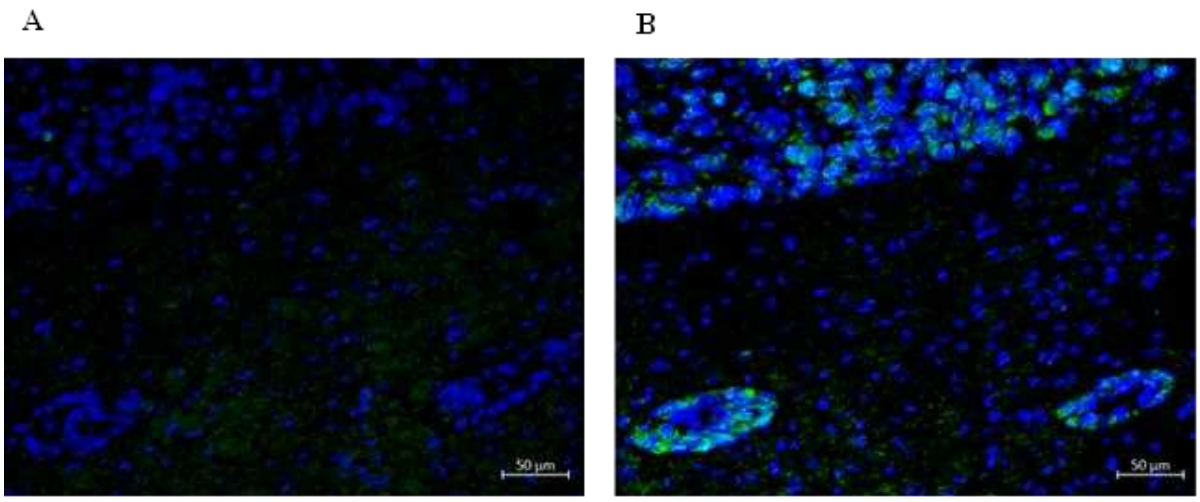

Supp. Fig. 5. MIF expression in U87MG-CXCR4+ xenografts. 21-day tumors in nude rats. A) DA1E isotype control and B) MIF expression (green). As PFA fixation was used, the RFP signal was lost.

Supp. Video 1. Shape Memory Behavior of Hydrated SF-HA-Hep Sponges.

(Uploaded as a separate file)

A

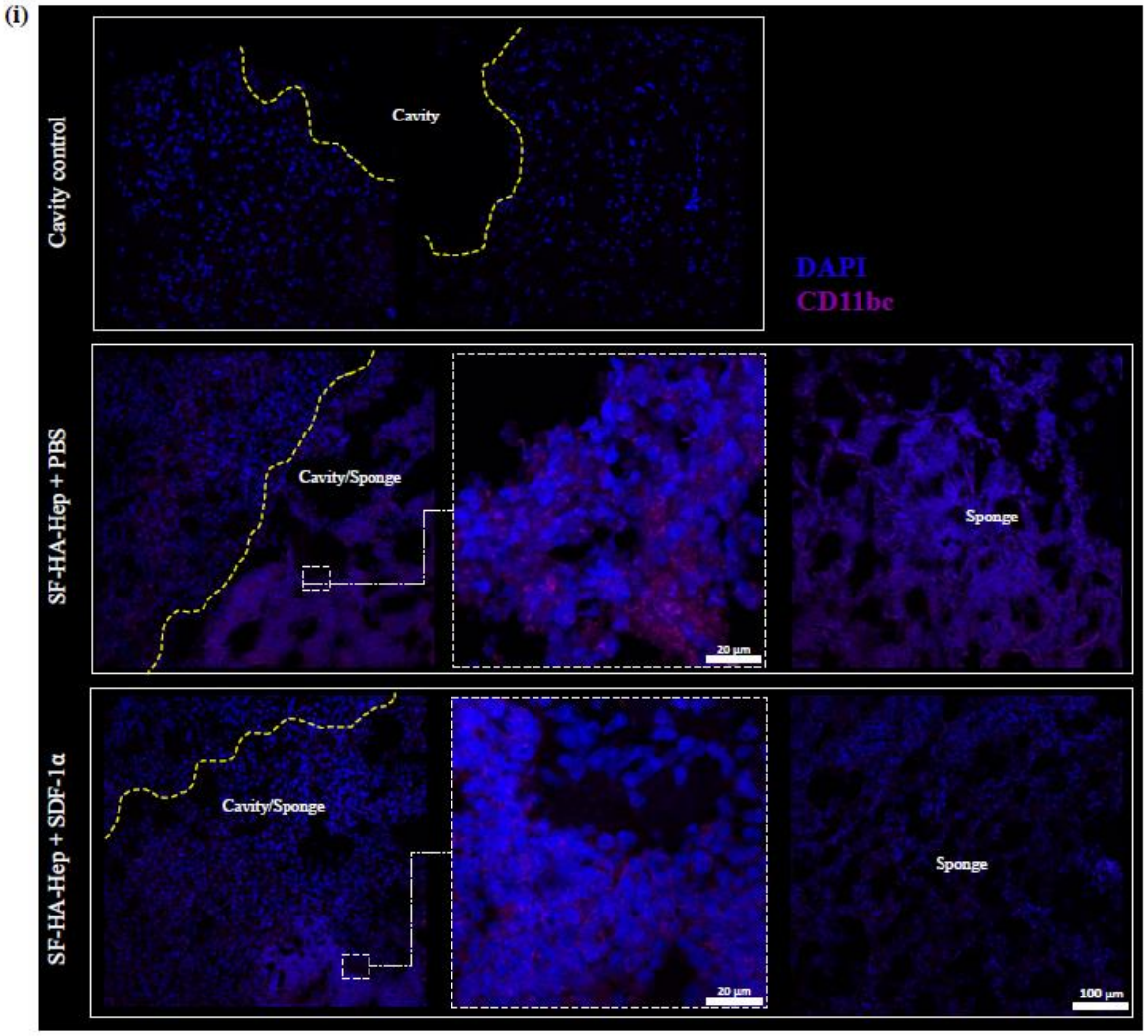
(i)
Cavity control
Cavity
DAPI
CD11bc
SF-HA-Hep + PBS
Cavity/Sponge
Sponge
20 µm
SF-HA-Hep + SDF-1α
Cavity/Sponge
Sponge
20 µm
100 µm
(ii)
Positive detections per frame
1500
1000
500
0
**
*
Cavity control
SF-HA-Hep + PBS
SF-HA-Hep + SDF-1α
(iii)
WE
Cavity/Sponge
Sponge
DAPI
IgGκK
Cavity/Sponge
Sponge

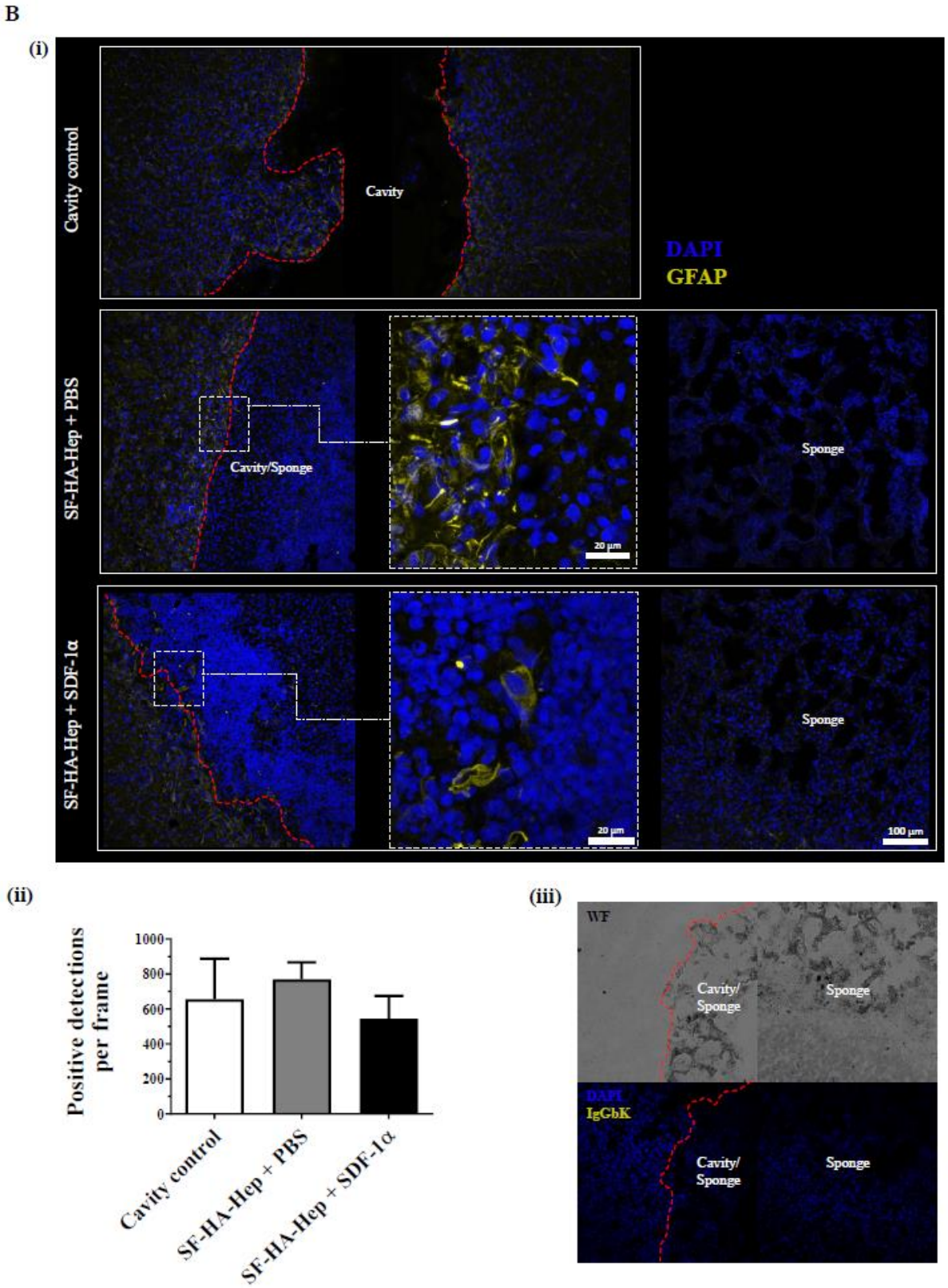

Supp. Fig. 6. In Vivo Cellular Response to Sponge Implantation. Cell detection in cryosections of the brain cortex resection cavity in nude rats using CD11b/c (**A**) and GFAP (**B**) immunolabeling (in purple and yellow, respectively). Composite images (**A-i**) show merged

channels. Increased CD11b/c-positive cell numbers were observed inside SF-HA-Hep sponges (with or without SDF-1α) compared to the cavity control group (**A-ii**). GFAP-positive cells were found around cavities in all groups without significant differences. Right panels show isotype control images (**A-iii**, IgGaK, and **B-iii**, IgGbK) and white field (WF) examples. (n = 3; ∗: $p < 0.05$, ∗∗: $p < 0.01$)

3.5. Unpublished results

3.5.1. F98 and RG2 rat GB cells are invasive toward an SDF-1α gradient

To assess if the other GB cells can be attracted to sites containing SDF-1α, an agarose spot assay adapted from (Wiggins and Rappoport, 2010) was used. Briefly, 0.51% w/v agarose solutions were prepared with or without SDF-1α (100 or 1000 nM) and 10 µL were deposited onto the right side of a well (12-well plate) for obtaining a single drop containing either 1 or 10 pmol of SDF-1α. Control drops containing only PBS were deposited left to the SDF-1α-containing drops. The agarose drops were left to solidify at 4°C for 5 min, and 1.9 x 10^5 F98 or RG2 cells in 1 mL of 1%-FBS-containing DMEM were deposited into the wells and dispersed by homogeneous shaking (before cell collection with acutase, cells were starved in 1%-FBS-DMEM for 24h). The plates were left incubated for 48 hours, wells fixed with 4% PFA, and images taken for analysis of cell migration under the agarose spots. Results showed an increased number of both F98 and RG2 cells in the agarose spots containing SDF-1α (**Fig. 3.2**). This suggests that both F98 and RG2 cells can invade areas using SDF-1α chemoattraction.

3.5.2. Assessment of the effect of sponge implantation at 3 mm from tumors.

To determine if there was a distal effect of sponges loaded or not with SDF-1α on cancer cell attraction, 1 x 10^5 U87MG-CXCR4+ GB cells were injected 3 mm away from the resection edges of the cavities containing sponges or not. After 7 days, brains were collected, and slices were stained for CXCR4 expression. The fluorescence of the left and right sides of the tumors was quantified to determine if there was a difference in the expression of CXCR4 that could be related to the effect of the implanted sponges, considering that the tumor edges might have been deformed due to the migration of cells. No significant difference was observed between groups (**Fig. 3.3**).

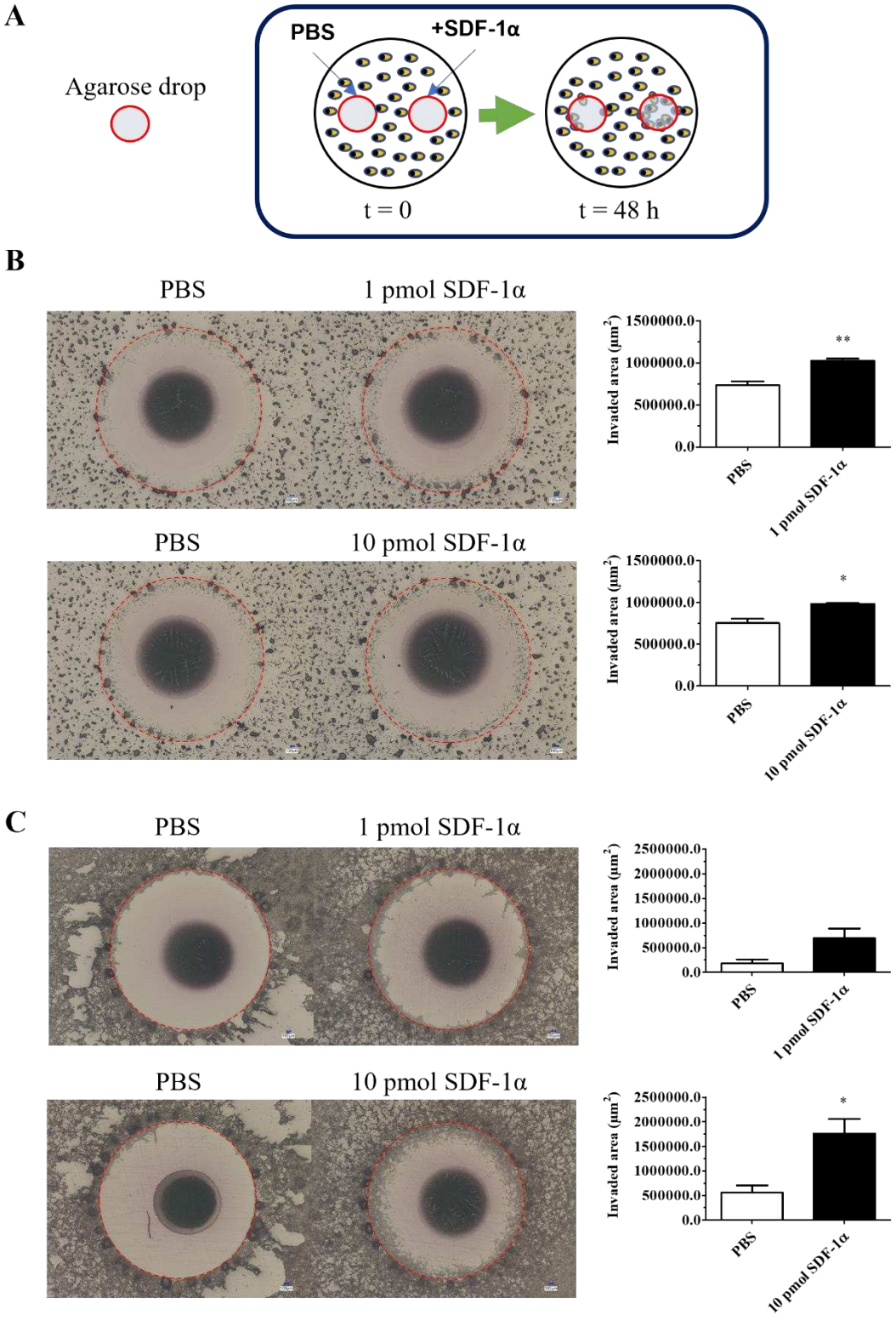

Figure 3.2. Chemoattraction of rat GB cells towards an SDF-1α gradient. A) Agarose spot assay: agarose spots (PBS controls (left) and +SDF-1α (right)) are deposited in a well. After solidification, cells are deposited and incubated to assess their response. B) Response of F98 GB cells. C) Response of RG2 GB cells. The borders of the agarose drops where cells were first in contact are depicted in red circles. The center black spots in the encircled area correspond to the dehydrated agarose after fixation.

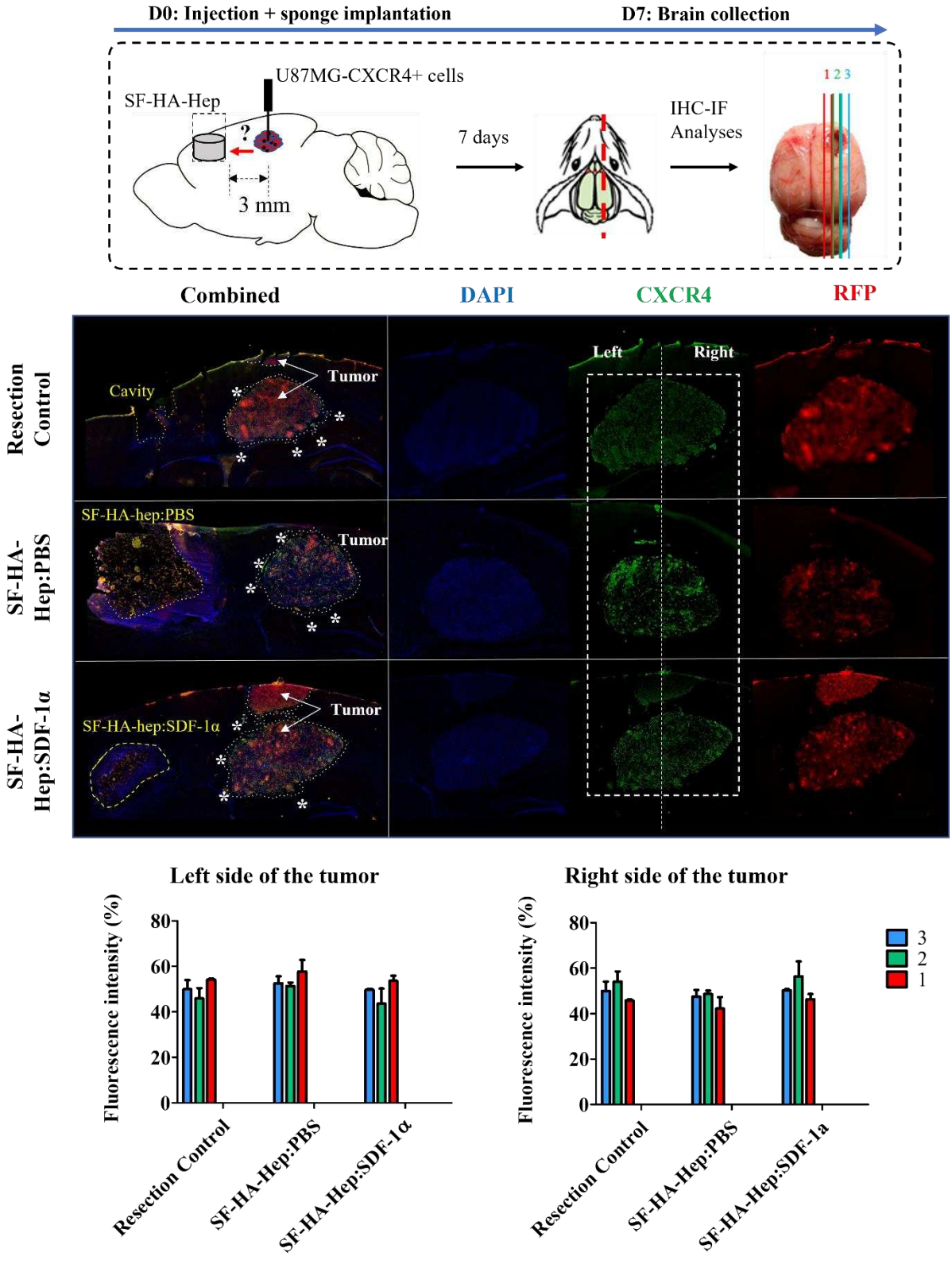

Figure 3.3. ***In-vivo*** **response of tumor cells injected concomitantly with sponge implantation.** Chemoattractant capacity of sponges from a distant site (3 mm from cell injection). Fluorescence intensity of anterior and posterior portions of the tumors is depicted as % relative to the total fluorescence (both sides); * indicates invasive foci.

3.6. Discussion of Chapter 3

The objective of this chapter was to address if an interventional bioimplant could be integrated to modify the behavior of the tumoral ecosystem and attract GB cells in a model of the resection cavity. In our strategy to demonstrate the proof of concept we adopted the use of transduced U87MG cells for the expression of CXCR4. Although these cells can be thought of artificially constructed cells, in general, the receptor expression on GB cells is part of the disease and is at the origin of tumor cell migration and expansion (Chatterjee et al., 2014; Zagzag et al., 2008). Therefore, by taking this approach, the stable expression of the CXCR4 receptor can guarantee a more reproducible behavior in terms of cell chemoattraction.

In the presented manuscript the effect of SDF-1α on CXCR4-expressing U87MG cells has been demonstrated and the profile of expression of the molecular effectors corresponded to early findings on patient-derived cell lines (Zhou et al., 2002). Despite the parental U87MG cell line did not express the CXCR4 receptor as assessed by flow cytometry, Zhou et al. (2002) found some but reduced expression (at the level of transcript expression) as compared to patient-derived cells (Zhou et al., 2002). Importantly, the diversification of the U87MG cell line has been reported in the literature (Allen et al., 2016). In the presented manuscript it was shown that U87MG-CXCR4+ cells were able to leave a confined area from an agarose drop upon SDF-1α incubation (gradient from the outside towards the center of the drops), whereas U87MG parental cells (CXCR4-) did not respond to this treatment (**Fig.1-D**). Moreover, the observation that the U87MG cell line shows a reduced infiltration into the brain parenchyma compared to diffuse gliomas (Séhédic et al., 2017; Toussaint et al., 2012), reinforces the choice of the use of the U87MG-CXCR4+ cell line in this study.

Another point for discussion is the choice of placing the cells near the resection cavity as a model of residual cells next to the resected area. This new model offers indeed the possibility of being more reproducible when the resection is not performed with the best methods resembling the clinical practice. In the latter case, this would involve the use of a fluorescent dye or fluorescent cells and microdissection techniques. However, even in this case, the tumors are not always similar and hence would introduce variability in the resection cavity. In terms of practicality, the developed model could be valuable to study not only the type of GB cells implanted near the resection borders but also the number of cells. This is because an individual cell, a small or large group of cells, or cells in the form of spheroids, are likely to behave differently due to the intrinsic autocrine/paracrine signaling and their hijacking potential of the elements of the brain parenchyma to create the tumor ecosystem.

The concomitant lateral implantation of the cells near the sponge resulted in a better reproducibility than inoculation of tumor cells into the striatum followed by resection with a biopsy punch in the cortex such that the sponge would be implanted just above (**Fig. Supp. 3**). Although this procedure offered the features of an established tumor from a relatively low cell seeding density (5000 cells) that grew to a size of ~ 0.8 (SD = 0.14) mm^2 (maximal observed area in the axial MRI projection) in 9 days, the surgical punching followed by vacuum

suctioning of the cut brain cortex did not permit a correct visualization of the aspiration of only the cortex tissue above the tumors, because the axis of manipulation was vertical to the rat brain (axial projection, relative to the rat body axis).

Notwithstanding these shortcomings, this latter model offers interesting opportunities concerning a developed tumor. Perhaps it can be implemented by utilizing the horizontal axis parallel to the rat's body. This is to induce the formation of a tumor in the cortex followed by a resection just beside the tumor in the horizontal axis instead of the vertical axis as previously discussed for the striatum tumors.

Another interesting approach would be to implant the sponges in the contralateral hemisphere in different conditions including 1) concomitant injection of cells, and at different densities and 2) implantation after a tumor has already been developed. This is to assess if the sponges can indeed exert a distal attraction of glioblastoma cells from a developing tumor and an already established tumor ecosystem. By doing so, one could take advantage of the aligned paths offered by the corpus callosum and perhaps imitate the pattern of migration of the butterfly glioblastoma (**Sections 1.5 and 1.6, Chapter 1**). This, always keeping in mind the aim to study the potential of luring distant cells that are the cause of recurrence.

Importantly, in the manuscript presented in this section, the used cell density was 25000 cells which are 5x more than what was used to develop tumors in the striatum implantation. This number seemed reasonable for a short-time evaluation (7 d) compared to other experiments where cell densities for the U87MG cell line ranged from 3 x 10^4 to 2 x 10^5 (Bianco et al., 2017; Kauer et al., 2011; Séhédic et al., 2017; Yin et al., 2013). However, a scenario might exist in which the paracrine signaling might overcome the luring signals provided by the trap. This is relevant since we and others have observed the production of SDF-1α in blood vessels, and the tumor induces increased angiogenesis (vascular niche) (Zagzag et al., 2008). Moreover, here, U87MG-CXCR4+ cells were able to produce MIF *in vivo* (**Supp. Fig. 5**), which is also a ligand for CXCR4. Whereas it is implicated in the migration of GB cells remains to be explored.

Another remark is that with the developed model the distance of cell injection relative to the sponge site can be varied in the sagittal axis in the same hemisphere. In the previous manuscript, ~1-mm cell placement was assessed from the edges of the resection. The observation of increased tumor shedding towards the sponges loaded with SDF-1α suggested the chemoattractant effect on U87MG-CXCR4 cells. However, due to the relative proximity to cells, other mechanisms including haptotaxis, the HA/CD44 axis, and durotaxis cannot be excluded.

An experiment where cells were implanted 3 mm away from the sponges showed no evidence of bulk cell attraction towards the sponges at 7-days-time of evaluation compared to non-loaded sponges and resection controls, as quantified by the total fluorescence in the anterior zone of the tumor mass facing the sponges (**Fig. 3.3**, unpublished results). C6 GB cells have been demonstrated to displace at an average rate of 24.7 µm/h (~590 µm/day) in an *ex-vivo* model

of GB (Farin et al., 2006). Here, U87MG-CXCR4+ cells displaced at an average rate of ~30 µm/h (2 mm in 3 days), *in vitro*. Considering this data, it might be expected that in a 7-day experiment, cells can displace ~4 mm at that average speed. However, the direction of the displacement can vary, and it has been demonstrated that it oscillates even in the reverse direction (Farin et al., 2006). Therefore, the "snapshot" taken at 7 days of this experiment might not represent the dynamic effect on attraction. Despite this, if GB cells decide to leave the main tumor mass and seed away from it, the formation of clusters (foci) should represent an estimation of the capacity of the scaffold to attract GB cells. Therefore, the quantification of foci and the shape of the tumors in this experiment should be performed, in addition to the already quantified fluorescence at the tumor sides (**Fig. 3.3**, unpublished results). Of note, this experiment differed however in that the number of injected cells was 4x respective to the 1-mm distance placement, therefore the effect on the paracrine signaling from the tumors might be stronger as discussed above. Finally, this result shows one possible shortcoming of this sponge system where the relatively low and short release of SDF-1α might be not enough to attract cells from a distant site *in vivo*. Considering the availability of free chemoattract, and also its degradation, the concentration of SDF-1α might not reach the target, or the SDF-1α signal is not enough sustained to induce its chemoattraction from distal sites.

Two additional remarks concerning the type of cells and models, and the type of chemoattractant might be applicable. The developed model might be applied using different cell lines. Particularly interesting would be to use the syngeneic rat models, using F98 and RG2 cell lines, which are more invasive towards a site containing SDF-1α as observed in the invaded areas under agarose spots containing SDF-1α (**Fig. 3.2** unpublished results). These cell lines are weak or non-immunogenic and have an invasive pattern of growth and uniform lethality (Kaur and Barth, 2009). The second point is the use of other chemoattractants, especially considering recent data showing reduced apoptosis of GB cells upon radiation (Yadav et al., 2016), and temozolomide treatment (Wang et al., 2020).

Despite this, the attraction and concentration of cells, and shaping of the tumors can be levered by combining a cell death signal. Therefore, an experiment will be performed in which treatment by external beam radiation therapy will be applied to observe the outcome on survival in groups of rats implanted with SDF-1α-loaded and non-loaded sponges. Importantly, the M-trap system that has shown efficacy in ovarian cancer cell trapping (de la Fuente et al., 2015), has also shown the capacity to concentrate GB cells *in vivo*, and will be evaluated in combination with radiation therapy within the Gliosilk consortium of which this project makes part.

3.7. Conclusion of Chapter 3

In this chapter, the main work on the selection of the cellular model, its validation as a GB cell model responsive to SDF-1α, and the capacity of SDF-1α-loaded sponges to attract GB cells *in vitro* and *in vivo* has been assessed positively. *In vitro,* the sponges were able to attract U87MG-CXCR4+ cells under agarose gels from a 2-mm distance. *In vivo*, the sponges were able to attract cells from 1 mm but not from a 3-mm distance. This might obey the nature of the sponges that complexed SDF-1α strongly, which might not allow a sustained release of the chemoattractant into the brain parenchyma, although a radiolabeling approach might be needed to confirm this. Despite this, it is demonstrated that the sponges can round-shape the tumors and localize them in the resection cavity when implanted just near cells. This offers an opportunity to perform a more localized treatment of the tumor. While the use of bioimplants in regenerative medicine is well exploited, few works have explored the use of biointeractive scaffolds as cancer cell traps. The resection cavity offers an opportunity to explore the use of such biointeractive deposits to test the hypothesis of GB cell attraction and concentration for further eradication. Here, our results showed a favorable proof of concept applied to glioblastoma that would be worth testing with a killing signal. Indeed, sponge implantation with external beam radiation as therapy will be evaluated next.

3.8. References

Aguado, B.A., Bushnell, G.G., Rao, S.S., Jeruss, J.S., Shea, L.D., 2017. Engineering the pre-metastatic niche. Nat Biomed Eng 1, 0077. https://doi.org/10.1038/s41551-017-0077

Aguado, B.A., Hartfield, R.M., Bushnell, G.G., Decker, J.T., Azarin, S.M., Nanavati, D., Schipma, M.J., Rao, S.S., Oakes, R.S., Zhang, Y., Jeruss, J.S., Shea, L.D., 2018. Biomaterial Scaffolds as Pre-metastatic Niche Mimics Systemically Alter the Primary Tumor and Tumor Microenvironment. Advanced Healthcare Materials 7, 1700903. https://doi.org/10.1002/adhm.201700903

Alcantara Llaguno, S.R., Parada, L.F., 2016. Cell of origin of glioma: biological and clinical implications. Br J Cancer 115, 1445–1450. https://doi.org/10.1038/bjc.2016.354

Allen, M., Bjerke, M., Edlund, H., Nelander, S., Westermark, B., 2016. Origin of the U87MG glioma cell line: Good news and bad news. Science Translational Medicine 8, 354re3-354re3. https://doi.org/10.1126/scitranslmed.aaf6853

Autier, L., Clavreul, A., Cacicedo, M.L., Franconi, F., Sindji, L., Rousseau, A., Perrot, R., Montero-Menei, C.N., Castro, G.R., Menei, P., 2019. A new glioblastoma cell trap for implantation after surgical resection. Acta Biomaterialia 84, 268–279. https://doi.org/10.1016/j.actbio.2018.11.027

Azarin, S.M., Yi, J., Gower, R.M., Aguado, B.A., Sullivan, M.E., Goodman, A.G., Jiang, E.J., Rao, S.S., Ren, Y., Tucker, S.L., Backman, V., Jeruss, J.S., Shea, L.D., 2015. In vivo capture and label-free detection of early metastatic cells. Nature Communications 6, 8094. https://doi.org/10.1038/ncomms9094

Aznavoorian, S., Stracke, M.L., Krutzsch, H., Schiffmann, E., Liotta, L.A., 1990. Signal transduction for chemotaxis and haptotaxis by matrix molecules in tumor cells. J Cell Biol 110, 1427–1438. https://doi.org/10.1083/jcb.110.4.1427

Bartoš, M., Suchý, T., Foltán, R., 2018. Note on the use of different approaches to determine the pore sizes of tissue engineering scaffolds: what do we measure? BioMedical Engineering OnLine 17, 110. https://doi.org/10.1186/s12938-018-0543-z

Bassi, G., Panseri, S., Dozio, S.M., Sandri, M., Campodoni, E., Dapporto, M., Sprio, S., Tampieri, A., Montesi, M., 2020. Scaffold-based 3D cellular models mimicking the heterogeneity of osteosarcoma stem cell niche. Sci Rep 10, 22294. https://doi.org/10.1038/s41598-020-79448-y

Bastiancich, C., Danhier, P., Préat, V., Danhier, F., 2016. Anticancer drug-loaded hydrogels as drug delivery systems for the local treatment of glioblastoma. Journal of Controlled Release 243, 29–42. https://doi.org/10.1016/j.jconrel.2016.09.034

Belousov, A., Titov, S., Shved, N., Garbuz, M., Malykin, G., Gulaia, V., Kagansky, A., Kumeiko, V., 2019. The Extracellular Matrix and Biocompatible Materials in Glioblastoma Treatment. Frontiers in Bioengineering and Biotechnology 7.

Bian, X., Yang, S., Chen, J., Ping, Y., Zhou, X., Wang, Q., Jiang, X., Gong, W., Xiao, H., Du, L., Chen, Z., Zhao, W., Shi, J., Wang, J.M., 2007. PREFERENTIAL EXPRESSION OF CHEMOKINE RECEPTOR CXCR4 BY HIGHLY MALIGNANT HUMAN GLIOMAS AND ITS ASSOCIATION WITH POOR PATIENT SURVIVAL. Neurosurgery 61, 570–579. https://doi.org/10.1227/01.NEU.0000290905.53685.A2

Bianco, J., Bastiancich, C., Joudiou, N., Gallez, B., des Rieux, A., Danhier, F., 2017. Novel model of orthotopic U-87 MG glioblastoma resection in athymic nude mice. Journal of Neuroscience Methods 284, 96–102. https://doi.org/10.1016/j.jneumeth.2017.04.019

Birzu, C., French, P., Caccese, M., Cerretti, G., Idbaih, A., Zagonel, V., Lombardi, G., 2021. Recurrent Glioblastoma: From Molecular Landscape to New Treatment Perspectives. Cancers 13, 47. https://doi.org/10.3390/cancers13010047

Bregy, A., Shah, A.H., Diaz, M.V., Pierce, H.E., Ames, P.L., Diaz, D., Komotar, R.J., 2013. The role of Gliadel wafers in the treatment of high-grade gliomas. Expert Review of Anticancer Therapy 13, 1453–1461. https://doi.org/10.1586/14737140.2013.840090

Buonerba, C., Di Lorenzo, G., Marinelli, A., Federico, P., Palmieri, G., Imbimbo, M., Conti, P., Peluso, G., De Placido, S., Sampson, J.H., 2011. A comprehensive outlook on intracerebral therapy of malignant gliomas. Crit Rev Oncol Hematol 80, 54–68. https://doi.org/10.1016/j.critrevonc.2010.09.001

Chatterjee, S., Behnam Azad, B., Nimmagadda, S., 2014. Chapter Two - The Intricate Role of CXCR4 in Cancer, in: Pomper, M.G., Fisher, P.B. (Eds.), Advances in Cancer Research, Emerging Applications of Molecular Imaging to Oncology. Academic Press, pp. 31–82. https://doi.org/10.1016/B978-0-12-411638-2.00002-1

Chen, J.-W.E., Pedron, S., Shyu, P., Hu, Y., Sarkaria, J.N., Harley, B.A.C., 2018. Influence of Hyaluronic Acid Transitions in Tumor Microenvironment on Glioblastoma Malignancy and Invasive Behavior. Frontiers in Materials 5.

Cheng, L., Huang, Z., Zhou, W., Wu, Q., Donnola, S., Liu, J.K., Fang, X., Sloan, A.E., Mao, Y., Lathia, J.D., Min, W., McLendon, R.E., Rich, J.N., Bao, S., 2013. Glioblastoma Stem Cells Generate Vascular Pericytes to Support Vessel Function and Tumor Growth. Cell 153, 139–152. https://doi.org/10.1016/j.cell.2013.02.021

Choi, W.I., Sahu, A., Vilos, C., Kamaly, N., Jo, S.-M., Lee, J.H., Tae, G., 2017. Bioinspired Heparin Nanosponge Prepared by Photo-crosslinking for Controlled Release of Growth Factors. Sci Rep 7, 14351. https://doi.org/10.1038/s41598-017-14040-5

Cruz Da Silva, E., Mercier, M.-C., Etienne-Selloum, N., Dontenwill, M., Choulier, L., 2021. A Systematic Review of Glioblastoma-Targeted Therapies in Phases II, III, IV Clinical Trials. Cancers 13, 1795. https://doi.org/10.3390/cancers13081795

D'Angelo, E., Natarajan, D., Sensi, F., Ajayi, O., Fassan, M., Mammano, E., Pilati, P., Pavan, P., Bresolin, S., Preziosi, M., Miquel, R., Zen, Y., Chokshi, S., Menon, K., Heaton, N., Spolverato, G., Piccoli, M., Williams, R., Urbani, L., Agostini, M., 2020. Patient-Derived Scaffolds of Colorectal Cancer Metastases as an Organotypic 3D Model of the Liver Metastatic Microenvironment. Cancers 12, 364. https://doi.org/10.3390/cancers12020364

Davies, J.A., 2013. Chapter 11 - Guidance by Contact, in: Davies, J.A. (Ed.), Mechanisms of Morphogenesis (Second Edition). Academic Press, Boston, pp. 129–145. https://doi.org/10.1016/B978-0-12-391062-2.00011-5

De Boeck, A., Ahn, B.Y., D'Mello, C., Lun, X., Menon, S.V., Alshehri, M.M., Szulzewsky, F., Shen, Y., Khan, L., Dang, N.H., Reichardt, E., Goring, K.-A., King, J., Grisdale, C.J., Grinshtein, N., Hambardzumyan, D., Reilly, K.M., Blough, M.D., Cairncross, J.G., Yong, V.W., Marra, M.A.,

Jones, S.J.M., Kaplan, D.R., McCoy, K.D., Holland, E.C., Bose, P., Chan, J.A., Robbins, S.M., Senger, D.L., 2020. Glioma-derived IL-33 orchestrates an inflammatory brain tumor microenvironment that accelerates glioma progression. Nat Commun 11, 4997. https://doi.org/10.1038/s41467-020-18569-4

de la Fuente, A., Alonso-Alconada, L., Costa, C., Cueva, J., Garcia-Caballero, T., Lopez-Lopez, R., Abal, M., 2015. M-Trap: Exosome-Based Capture of Tumor Cells as a New Technology in Peritoneal Metastasis. J Natl Cancer Inst 107. https://doi.org/10.1093/jnci/djv184

De Vleeschouwer, S. (Ed.), 2017. Glioblastoma. Codon Publications, Brisbane (AU).

Djoudi, A., Molina-Peña, R., Ferreira, N., Ottonelli, I., Tosi, G., Garcion, E., Boury, F., 2022. Hyaluronic Acid Scaffolds for Loco-Regional Therapy in Nervous System Related Disorders. International Journal of Molecular Sciences 23, 12174. https://doi.org/10.3390/ijms232012174

Ehtesham, M., Winston, J.A., Kabos, P., Thompson, R.C., 2006. CXCR4 expression mediates glioma cell invasiveness. Oncogene 25, 2801–2806. https://doi.org/10.1038/sj.onc.1209302

Erickson, A.E., Lan Levengood, S.K., Sun, J., Chang, F.-C., Zhang, M., 2018. Fabrication and Characterization of Chitosan–Hyaluronic Acid Scaffolds with Varying Stiffness for Glioblastoma Cell Culture. Advanced Healthcare Materials 7, 1800295. https://doi.org/10.1002/adhm.201800295

Faber, A., Roderburg, C., Wein, F., Saffrich, R., Seckinger, A., Horsch, K., Diehlmann, A., Wong, D., Bridger, G., Eckstein, V., Ho, A.D., Wagner, W., 2007. The many facets of SDF-1alpha, CXCR4 agonists and antagonists on hematopoietic progenitor cells. J Biomed Biotechnol 2007, 26065. https://doi.org/10.1155/2007/26065

Fan, Z., Zhang, F., Liu, T., Zuo, B.Q., 2014. Effect of hyaluronan molecular weight on structure and biocompatibility of silk fibroin/hyaluronan scaffolds. Int J Biol Macromol 65, 516–523. https://doi.org/10.1016/j.ijbiomac.2014.01.058

Farin, A., Suzuki, S.O., Weiker, M., Goldman, J.E., Bruce, J.N., Canoll, P., 2006. Transplanted glioma cells migrate and proliferate on host brain vasculature: a dynamic analysis. Glia 53, 799–808. https://doi.org/10.1002/glia.20334

Gallizioli, M., Miró-Mur, F., Otxoa-de-Amezaga, A., Cugota, R., Salas-Perdomo, A., Justicia, C., Brait, V.H., Ruiz-Jaén, F., Arbaizar-Rovirosa, M., Pedragosa, J., Bonfill-Teixidor, E., Gelderblom, M., Magnus, T., Cano, E., Del Fresno, C., Sancho, D., Planas, A.M., 2020. Dendritic Cells and Microglia Have Non-redundant Functions in the Inflamed Brain with Protective Effects of Type 1 cDCs. Cell Rep 33, 108291. https://doi.org/10.1016/j.celrep.2020.108291

Gascon, S., Giraldo Solano, A., El Kheir, W., Therriault, H., Berthelin, P., Cattier, B., Marcos, B., Virgilio, N., Paquette, B., Faucheux, N., Lauzon, M.-A., 2020. Characterization and Mathematical Modeling of Alginate/Chitosan-Based Nanoparticles Releasing the Chemokine CXCL12 to Attract Glioblastoma Cells. Pharmaceutics 12, 356. https://doi.org/10.3390/pharmaceutics12040356

Giese, A., Bjerkvig, R., Berens, M.E., Westphal, M., 2003. Cost of migration: invasion of malignant gliomas and implications for treatment. J Clin Oncol 21, 1624–1636. https://doi.org/10.1200/JCO.2003.05.063

Gil-Moreno, A., Alonso-Alconada, L., Díaz-Feijoo, B., Domingo, S., Vilar, A., Hernández, A., Gilabert, J., Llueca, A., Torné, A., de Santiago, J., Carbonell-Socias, M., Lago, V., Arias, E., Sampayo, V., Siegrist, J., Chipirliu, A., Sánchez-Iglesias, J.L., Pérez-Benavente, A., Padilla-Iserte, P., Santacana, M., Matias-Guiu, X., Abal, M., Lopez-Lopez, R., 2021. M-TRAP: Safety and performance of metastatic tumor cell trap device in advanced ovarian cancer patients. Gynecologic Oncology 161, 681–686. https://doi.org/10.1016/j.ygyno.2021.03.022

Hayman, E.G., Pierschbacher, M.D., Suzuki, S., Ruoslahti, E., 1985. Vitronectin--a major cell attachment-promoting protein in fetal bovine serum. Exp Cell Res 160, 245–258. https://doi.org/10.1016/0014-4827(85)90173-9

Heit, B., Kubes, P., 2003. Measuring Chemotaxis and Chemokinesis: The Under-Agarose Cell Migration Assay. Science's STKE 2003, pl5–pl5. https://doi.org/10.1126/stke.2003.170.pl5

Henke, E., Nandigama, R., Ergün, S., 2020. Extracellular Matrix in the Tumor Microenvironment and Its Impact on Cancer Therapy. Frontiers in Molecular Biosciences 6.

Hira, V.V.V., Verbovšek, U., Breznik, B., Srdič, M., Novinec, M., Kakar, H., Wormer, J., der Swaan, B.V., Lenarčič, B., Juliano, L., Mehta, S., Van Noorden, C.J.F., Lah, T.T., 2017. Cathepsin K

cleavage of SDF-1α inhibits its chemotactic activity towards glioblastoma stem-like cells. Biochim Biophys Acta Mol Cell Res 1864, 594–603. https://doi.org/10.1016/j.bbamcr.2016.12.021

Horejs, C., 2021. Preventing fibrotic encapsulation. Nat Rev Mater 6, 554–554. https://doi.org/10.1038/s41578-021-00338-4

Hu, Y., Lu, J., Xu, X., Lyu, J., Zhang, H., 2017. Regulation of focal adhesion turnover in SDF-1α-stimulated migration of mesenchymal stem cells in neural differentiation. Sci Rep 7, 10013. https://doi.org/10.1038/s41598-017-09736-7

Huang, J., Zhang, L., Wan, D., Zhou, L., Zheng, S., Lin, S., Qiao, Y., 2021. Extracellular matrix and its therapeutic potential for cancer treatment. Sig Transduct Target Ther 6, 1–24. https://doi.org/10.1038/s41392-021-00544-0

Huang, Y., Hakamivala, A., Li, S., Nair, A., Saxena, R., Hsieh, J.-T., Tang, L., 2020. Chemokine releasing particle implants for trapping circulating prostate cancer cells. Sci Rep 10, 4433. https://doi.org/10.1038/s41598-020-60696-x

Ishii, N., Maier, D., Merlo, A., Tada, M., Sawamura, Y., Diserens, A.-C., Van Meir, E.G., 1999. Frequent Co-Alterations of TP53, p16/CDKN2A, p14ARF, PTEN Tumor Suppressor Genes in Human Glioma Cell Lines. Brain Pathology 9, 469–479. https://doi.org/10.1111/j.1750-3639.1999.tb00536.x

Iuchi, T., Inoue, A., Hirose, Y., Morioka, M., Horiguchi, K., Natsume, A., Arakawa, Y., Iwasaki, K., Fujiki, M., Kumabe, T., Sakata, Y., 2022. Long-term effectiveness of Gliadel implant for malignant glioma and prognostic factors for survival: 3-year results of a postmarketing surveillance in Japan. Neuro-Oncology Advances 4, vdab189. https://doi.org/10.1093/noajnl/vdab189

Jain, A., Betancur, M., Patel, G.D., Valmikinathan, C.M., Mukhatyar, V.J., Vakharia, A., Pai, S.B., Brahma, B., MacDonald, T.J., Bellamkonda, R.V., 2014. Guiding intracortical brain tumour cells to an extracortical cytotoxic hydrogel using aligned polymeric nanofibres. Nature Mater 13, 308–316. https://doi.org/10.1038/nmat3878

Janowski, M., 2009. Functional diversity of SDF-1 splicing variants. Cell Adhesion & Migration 3, 243–249. https://doi.org/10.4161/cam.3.3.8260

Janssens, R., Mortier, A., Boff, D., Vanheule, V., Gouwy, M., Franck, C., Larsen, O., Rosenkilde, M.M., Damme, J.V., Amaral, F.A., Teixeira, M.M., Struyf, S., Proost, P., 2016. Natural nitration of CXCL12 reduces its signaling capacity and chemotactic activity in vitro and abrogates intra-articular lymphocyte recruitment in vivo. Oncotarget 7, 62439–62459. https://doi.org/10.18632/oncotarget.11516

Jensen, G., Holloway, J.L., Stabenfeldt, S.E., 2020. Hyaluronic Acid Biomaterials for Central Nervous System Regenerative Medicine. Cells 9, 2113. https://doi.org/10.3390/cells9092113

Kanu, O.O., Mehta, A., Di, C., Lin, N., Bortoff, K., Bigner, D.D., Yan, H., Adamson, D.C., 2009. Glioblastoma multiforme: a review of therapeutic targets. Expert Opinion on Therapeutic Targets 13, 701–718. https://doi.org/10.1517/14728220902942348

Kasapidou, P.M., Montullé, E.L. de, Dembélé, K.-P., Mutel, A., Desrues, L., Gubala, V., Castel, H., 2021. Hyaluronic acid-based hydrogels loaded with chemoattractant and anticancer drug – new formulation for attracting and tackling glioma cells. Soft Matter 17, 10846–10861. https://doi.org/10.1039/D1SM01003D

Kauer, T.M., Figueiredo, J.-L., Hingtgen, S., Shah, K., 2011. Encapsulated therapeutic stem cells implanted in the tumor resection cavity induce cell death in gliomas. Nat Neurosci 15, 197–204. https://doi.org/10.1038/nn.3019

Kaur, B., Barth, R.F., 2009. Rat Glioma Models for Preclinical Evaluation of Novel Therapeutic and Diagnostic Modalities, in: Meir, E.G. (Ed.), CNS Cancer: Models, Markers, Prognostic Factors, Targets, and Therapeutic Approaches, Cancer Drug Discovery and Development. Humana Press, Totowa, NJ, pp. 181–205. https://doi.org/10.1007/978-1-60327-553-8_10

Kim, H., Roh, H.S., Kim, J.E., Park, S.D., Park, W.H., Moon, J.-Y., 2016. Compound K attenuates stromal cell-derived growth factor 1 (SDF-1)-induced migration of C6 glioma cells. Nutr Res Pract 10, 259–264. https://doi.org/10.4162/nrp.2016.10.3.259

Krieger, M.S., Moreau, J.M., Zhang, H., Chien, M., Zehnder, J.L., Nowak, M.A., Craig, M., 2018. Novel cytokine interactions identified during perturbed hematopoiesis. https://doi.org/10.1101/484170

Laguri, C., Sadir, R., Rueda, P., Baleux, F., Gans, P., Arenzana-Seisdedos, F., Lortat-Jacob, H., 2007. The Novel CXCL12γ Isoform Encodes an Unstructured Cationic Domain Which Regulates Bioactivity and Interaction with Both Glycosaminoglycans and CXCR4. PLOS ONE 2, e1110. https://doi.org/10.1371/journal.pone.0001110

Lemée, J.-M., Clavreul, A., Menei, P., 2015. Intratumoral heterogeneity in glioblastoma: don't forget the peritumoral brain zone. Neuro-Oncology 17, 1322–1332. https://doi.org/10.1093/neuonc/nov119

Litowczenko, J., Woźniak-Budych, M.J., Staszak, K., Wieszczycka, K., Jurga, S., Tylkowski, B., 2021. Milestones and current achievements in development of multifunctional bioscaffolds for medical application. Bioactive Materials 6, 2412–2438. https://doi.org/10.1016/j.bioactmat.2021.01.007

Mathivet, T., Bouleti, C., Van Woensel, M., Stanchi, F., Verschuere, T., Phng, L.-K., Dejaegher, J., Balcer, M., Matsumoto, K., Georgieva, P.B., Belmans, J., Sciot, R., Stockmann, C., Mazzone, M., De Vleeschouwer, S., Gerhardt, H., 2017. Dynamic stroma reorganization drives blood vessel dysmorphia during glioma growth. EMBO Molecular Medicine 9, 1629–1645. https://doi.org/10.15252/emmm.201607445

Mendes de Aguiar, C.B.N., Lobão-Soares, B., Alvarez-Silva, M., Trentin, A.G., 2005. Glycosaminoglycans modulate C6 glioma cell adhesion to extracellular matrix components and alter cell proliferation and cell migration. BMC Cell Biology 6, 31. https://doi.org/10.1186/1471-2121-6-31

Migliorini, E., Thakar, D., Kühnle, J., Sadir, R., Dyer, D.P., Li, Y., Sun, C., Volkman, B.F., Handel, T.M., Coche-Guerente, L., Fernig, D.G., Lortat-Jacob, H., Richter, R.P., 2015. Cytokines and growth factors cross-link heparan sulfate. Open Biol. 5, 150046. https://doi.org/10.1098/rsob.150046

Milner, R., Edwards, G., Streuli, C., Ffrench-Constant, C., 1996. A role in migration for the alpha V beta 1 integrin expressed on oligodendrocyte precursors. J Neurosci 16, 7240–7252.

Mohiuddin, E., Wakimoto, H., 2021. Extracellular matrix in glioblastoma: opportunities for emerging therapeutic approaches. Am J Cancer Res 11, 3742–3754.

Molina-Peña, R., Haji Mansor, M., Najberg, M., Thomassin, J.-M., Gueza, B., Alvarez-Lorenzo, C., Garcion, E., Jérôme, C., Boury, F., 2021. Nanoparticle-containing electrospun nanofibrous scaffolds for sustained release of SDF-1α. Int J Pharm 610, 121205. https://doi.org/10.1016/j.ijpharm.2021.121205

Motz, G.T., Coukos, G., 2013. Deciphering and Reversing Tumor Immune Suppression. Immunity 39, 61–73. https://doi.org/10.1016/j.immuni.2013.07.005

Najberg, M., Haji Mansor, M., Boury, F., Alvarez-Lorenzo, C., Garcion, E., 2019. Reversing the Tumor Target: Establishment of a Tumor Trap. Frontiers in Pharmacology 10, 887. https://doi.org/10.3389/fphar.2019.00887

Najberg, M., Haji Mansor, M., Taillé, T., Bouré, C., Molina-Peña, R., Boury, F., Cenis, J.L., Garcion, E., Alvarez-Lorenzo, C., 2020. Aerogel sponges of silk fibroin, hyaluronic acid and heparin for soft tissue engineering: Composition-properties relationship. Carbohydrate Polymers 237, 116107. https://doi.org/10.1016/j.carbpol.2020.116107

Nakayama, E., Shiratsuchi, Y., Kobayashi, Y., Nagata, K., 2011. The importance of infiltrating neutrophils in SDF-1 production leading to regeneration of the thymus after whole-body X-irradiation. Cellular Immunology 268, 24–28. https://doi.org/10.1016/j.cellimm.2011.01.006

Nava, M.M., Raimondi, M.T., Pietrabissa, R., 2012. Controlling Self-Renewal and Differentiation of Stem Cells via Mechanical Cues. BioMed Research International 2012, e797410. https://doi.org/10.1155/2012/797410

Nduom, E.K., Weller, M., Heimberger, A.B., 2015. Immunosuppressive mechanisms in glioblastoma. Neuro Oncol 17 Suppl 7, vii9–vii14. https://doi.org/10.1093/neuonc/nov151

Newland, B., Welzel, P.B., Newland, H., Renneberg, C., Kolar, P., Tsurkan, M., Rosser, A., Freudenberg, U., Werner, C., 2015. Tackling Cell Transplantation Anoikis: An Injectable,

Shape Memory Cryogel Microcarrier Platform Material for Stem Cell and Neuronal Cell Growth. Small 11, 5047–5053. https://doi.org/10.1002/smll.201500898

Nicolas, J., Magli, S., Rabbachin, L., Sampaolesi, S., Nicotra, F., Russo, L., 2020. 3D Extracellular Matrix Mimics: Fundamental Concepts and Role of Materials Chemistry to Influence Stem Cell Fate. Biomacromolecules 21, 1968–1994. https://doi.org/10.1021/acs.biomac.0c00045

Oakes, R.S., Bushnell, G.G., Orbach, S.M., Kandagatla, P., Zhang, Y., Morris, A.H., Hall, M.S., LaFaire, P., Decker, J.T., Hartfield, R.M., Brooks, M.D., Wicha, M.S., Jeruss, J.S., Shea, L.D., 2020. Metastatic Conditioning of Myeloid Cells at a Subcutaneous Synthetic Niche Reflects Disease Progression and Predicts Therapeutic Outcomes. Cancer Research 80, 602–612. https://doi.org/10.1158/0008-5472.CAN-19-1932

Pasquier, J., Abu-Kaoud, N., Abdesselem, H., Madani, A., Hoarau-Véchot, J., Thawadi, H.Al., Vidal, F., Couderc, B., Favre, G., Rafii, A., 2015. SDF-1alpha concentration dependent modulation of RhoA and Rac1 modifies breast cancer and stromal cells interaction. BMC Cancer 15, 569. https://doi.org/10.1186/s12885-015-1556-7

Paul, C.D., Mistriotis, P., Konstantopoulos, K., 2017. Cancer cell motility: lessons from migration in confined spaces. Nat Rev Cancer 17, 131–140. https://doi.org/10.1038/nrc.2016.123

Pearson, J.R.D., Cuzzubbo, S., McArthur, S., Durrant, L.G., Adhikaree, J., Tinsley, C.J., Pockley, A.G., McArdle, S.E.B., 2020. Immune Escape in Glioblastoma Multiforme and the Adaptation of Immunotherapies for Treatment. Frontiers in Immunology 11.

Peng, Y., Chen, Z., He, Y., Li, P., Chen, Y., Chen, X., Jiang, Y., Qin, X., Li, S., Li, T., Wu, C., Yang, H., You, F., Liu, Y., 2022. Non-muscle myosin II isoforms orchestrate substrate stiffness sensing to promote cancer cell contractility and migration. Cancer Letters 524, 245–258. https://doi.org/10.1016/j.canlet.2021.10.030

Polyak, K., Weinberg, R.A., 2009. Transitions between epithelial and mesenchymal states: acquisition of malignant and stem cell traits. Nat Rev Cancer 9, 265–273. https://doi.org/10.1038/nrc2620

Prokoph, S., Chavakis, E., Levental, K.R., Zieris, A., Freudenberg, U., Dimmeler, S., Werner, C., 2012. Sustained delivery of SDF-1α from heparin-based hydrogels to attract circulating pro-angiogenic cells. Biomaterials 33, 4792–4800. https://doi.org/10.1016/j.biomaterials.2012.03.039

Provenzano, P.P., Inman, D.R., Eliceiri, K.W., Trier, S.M., Keely, P.J., 2008. Contact guidance mediated three-dimensional cell migration is regulated by Rho/ROCK-dependent matrix reorganization. Biophys J 95, 5374–5384. https://doi.org/10.1529/biophysj.108.133116

Rao, S.S., DeJesus, J., Short, A.R., Otero, J.J., Sarkar, A., Winter, J.O., 2013. Glioblastoma Behaviors in Three-Dimensional Collagen-Hyaluronan Composite Hydrogels. ACS Appl. Mater. Interfaces 5, 9276–9284. https://doi.org/10.1021/am402097j

Rodrigues, E.M., Cornélio, A.L.G., Godoi, P.H., da Costa, P.I., Rossa-Junior, C., Faria, G., Guerreiro Tanomaru, J.M., Tanomaru-Filho, M., 2019. Heparin is biocompatible and can induce differentiation of human dental pulp cells. Int Endod J 52, 829–837. https://doi.org/10.1111/iej.13061

Rodrigues, J.C., Gonzalez, G.C., Zhang, L., Ibrahim, G., Kelly, J.J., Gustafson, M.P., Lin, Y., Dietz, A.B., Forsyth, P.A., Yong, V.W., Parney, I.F., 2010. Normal human monocytes exposed to glioma cells acquire myeloid-derived suppressor cell-like properties. Neuro-Oncology 12, 351–365. https://doi.org/10.1093/neuonc/nop023

Rusetska, N., Kowalski, K., Zalewski, K., Zięba, S., Bidziński, M., Goryca, K., Kotowicz, B., Fuksiewicz, M., Kopczynski, J., Bakuła-Zalewska, E., Kowalik, A., Kowalewska, M., 2022. CXCR4/ACKR3/CXCL12 axis in the lymphatic metastasis of vulvar squamous cell carcinoma. Journal of Clinical Pathology 75, 324–332. https://doi.org/10.1136/jclinpath-2020-206917

Saif Ur Rahman, M., Wu, J., Chen, H., Sun, C., Liu, Y., Xu, S., 2023. Matrix mechanophysical factor: pore size governs the cell behavior in cancer. Advances in Physics: X 8, 2153624. https://doi.org/10.1080/23746149.2022.2153624

Saleh, A., Marhuenda, E., Fabre, C., Hassani, Z., Weille, J. de, Boukhaddaoui, H., Guelfi, S., Maldonado, I.L., Hugnot, J.-P., Duffau, H., Bauchet, L., Cornu, D., Bakalara, N., 2019. A novel 3D nanofibre scaffold conserves the plasticity of glioblastoma stem cell invasion by regulating galectin-3 and integrin-β1 expression. Sci Rep 9, 14612. https://doi.org/10.1038/s41598-019-51108-w

Seeger, F.H., Rasper, T., Fischer, A., Muhly-Reinholz, M., Hergenreider, E., Leistner, D.M., Sommer, K., Manavski, Y., Henschler, R., Chavakis, E., Assmus, B., Zeiher, A.M., Dimmeler, S., 2012. Heparin Disrupts the CXCR4/SDF-1 Axis and Impairs the Functional Capacity of Bone Marrow–Derived Mononuclear Cells Used for Cardiovascular Repair. Circulation Research 111, 854–862. https://doi.org/10.1161/CIRCRESAHA.112.265678

Séhédic, D., Chourpa, I., Tétaud, C., Griveau, A., Loussouarn, C., Avril, S., Legendre, C., Lepareur, N., Wion, D., Hindré, F., Davodeau, F., Garcion, E., 2017. Locoregional Confinement and Major Clinical Benefit of 188Re-Loaded CXCR4-Targeted Nanocarriers in an Orthotopic Human to Mouse Model of Glioblastoma. Theranostics 7, 4517–4536. https://doi.org/10.7150/thno.19403

Sehgal, A., Keener, C., Boynton, A.L., Warrick, J., Murphy, G.P., 1998. CXCR-4, a chemokine receptor, is overexpressed in and required for proliferation of glioblastoma tumor cells. J Surg Oncol 69, 99–104. https://doi.org/10.1002/(sici)1096-9098(199810)69:2<99::aid-jso10>3.0.co;2-m

Sheets, K.T., Ewend, M.G., Mohiti-Asli, M., Tuin, S.A., Loboa, E.G., Aboody, K.S., Hingtgen, S.D., 2020. Developing Implantable Scaffolds to Enhance Neural Stem Cell Therapy for Post-Operative Glioblastoma. Molecular Therapy 28, 1056–1067. https://doi.org/10.1016/j.ymthe.2020.02.008

Singh, G., Chanda, A., 2021. Mechanical properties of whole-body soft human tissues: a review. Biomed Mater 16. https://doi.org/10.1088/1748-605X/ac2b7a

Sood, A., Gupta, A., Agrawal, G., 2021. Recent advances in polysaccharides based biomaterials for drug delivery and tissue engineering applications. Carbohydrate Polymer Technologies and Applications 2, 100067. https://doi.org/10.1016/j.carpta.2021.100067

Sood, D., Tang-Schomer, M., Pouli, D., Mizzoni, C., Raia, N., Tai, A., Arkun, K., Wu, J., Black, L.D., Scheffler, B., Georgakoudi, I., Steindler, D.A., Kaplan, D.L., 2019. 3D extracellular matrix microenvironment in bioengineered tissue models of primary pediatric and adult brain tumors. Nat Commun 10, 4529. https://doi.org/10.1038/s41467-019-12420-1

Tavor, S., Petit, I., Porozov, S., Avigdor, A., Dar, A., Leider-Trejo, L., Shemtov, N., Deutsch, V., Naparstek, E., Nagler, A., Lapidot, T., 2004. CXCR4 Regulates Migration and Development of Human Acute Myelogenous Leukemia Stem Cells in Transplanted NOD/SCID Mice. Cancer Research 64, 2817–2824. https://doi.org/10.1158/0008-5472.CAN-03-3693

Teicher, B.A., Fricker, S.P., 2010. CXCL12 (SDF-1)/CXCR4 Pathway in Cancer. Clinical Cancer Research 16, 2927–2931. https://doi.org/10.1158/1078-0432.CCR-09-2329

Toussaint, L.G., Nilson, A.E., Goble, J.M., Ballman, K.V., James, C.D., Lefranc, F., Kiss, R., Uhm, J.H., 2012. Galectin-1, a gene preferentially expressed at the tumor margin, promotes glioblastoma cell invasion. Molecular Cancer 11, 32. https://doi.org/10.1186/1476-4598-11-32

Van Der Sanden, B., Appaix, F., Berger, F., Selek, L., Issartel, J.-P., Wion, D., 2013. Translation of the ecological trap concept to glioma therapy: the cancer cell trap concept. Future Oncol 817–824. https://doi.org/10.2217/fon.13.30

Wang, C., Tong, X., Yang, F., 2014. Bioengineered 3D Brain Tumor Model To Elucidate the Effects of Matrix Stiffness on Glioblastoma Cell Behavior Using PEG-Based Hydrogels. Mol. Pharmaceutics 11, 2115–2125. https://doi.org/10.1021/mp5000828

Wang, S., Chen, C., Li, J., Xu, X., Chen, W., Li, F., 2020. The CXCL12/CXCR4 axis confers temozolomide resistance to human glioblastoma cells via up-regulation of FOXM1. Journal of the Neurological Sciences 414, 116837. https://doi.org/10.1016/j.jns.2020.116837

Wiggins, H., Rappoport, J., 2010. An agarose spot assay for chemotactic invasion. Biotechniques 48, 121–124. https://doi.org/10.2144/000113353

Woerner, B.M., Warrington, N.M., Kung, A.L., Perry, A., Rubin, J.B., 2005. Widespread CXCR4 Activation in Astrocytomas Revealed by Phospho-CXCR4-Specific Antibodies. Cancer Research 65, 11392–11399. https://doi.org/10.1158/0008-5472.CAN-05-0847

Wolf, K., Te Lindert, M., Krause, M., Alexander, S., Te Riet, J., Willis, A.L., Hoffman, R.M., Figdor, C.G., Weiss, S.J., Friedl, P., 2013. Physical limits of cell migration: control by ECM space and nuclear deformation and tuning by proteolysis and traction force. J Cell Biol 201, 1069–1084. https://doi.org/10.1083/jcb.201210152

Wolf, K.J., Shukla, P., Springer, K., Lee, S., Coombes, J.D., Choy, C.J., Kenny, S.J., Xu, K., Kumar, S., 2020. A mode of cell adhesion and migration facilitated by CD44-dependent microtentacles. Proceedings of the National Academy of Sciences 117, 11432–11443. https://doi.org/10.1073/pnas.1914294117

Würth, R., Bajetto, A., Harrison, J.K., Barbieri, F., Florio, T., 2014. CXCL12 modulation of CXCR4 and CXCR7 activity in human glioblastoma stem-like cells and regulation of the tumor microenvironment. Front Cell Neurosci 8, 144. https://doi.org/10.3389/fncel.2014.00144

Xiong, Q., Zhang, N., Zhang, M., Wang, M., Wang, L., Fan, Y., Lin, C.-Y., 2022. Engineer a pre-metastatic niched microenvironment to attract breast cancer cells by utilizing a 3D printed polycaprolactone/nano-hydroxyapatite osteogenic scaffold – An in vitro model system for proof of concept. Journal of Biomedical Materials Research Part B: Applied Biomaterials 110, 1604–1614. https://doi.org/10.1002/jbm.b.35021

Xu, Y., Chen, C., Hellwarth, P.B., Bao, X., 2019. Biomaterials for stem cell engineering and biomanufacturing. Bioactive Materials 4, 366–379. https://doi.org/10.1016/j.bioactmat.2019.11.002

Yadav, V.N., Zamler, D., Baker, G.J., Kadiyala, P., Erdreich-Epstein, A., DeCarvalho, A.C., Mikkelsen, T., Castro, M.G., Lowenstein, P.R., 2016. CXCR4 increases in-vivo glioma perivascular invasion, and reduces radiation induced apoptosis: A genetic knockdown study. Oncotarget 7, 83701–83719. https://doi.org/10.18632/oncotarget.13295

Yamada, K.M., Collins, J.W., Cruz Walma, D.A., Doyle, A.D., Morales, S.G., Lu, J., Matsumoto, K., Nazari, S.S., Sekiguchi, R., Shinsato, Y., Wang, S., 2019. Extracellular matrix dynamics in cell migration, invasion and tissue morphogenesis. International Journal of Experimental Pathology 100, 144–152. https://doi.org/10.1111/iep.12329

Yamada, K.M., Sixt, M., 2019. Mechanisms of 3D cell migration. Nat Rev Mol Cell Biol 20, 738–752. https://doi.org/10.1038/s41580-019-0172-9

Yamahara, T., Numa, Y., Oishi, T., Kawaguchi, T., Seno, T., Asai, A., Kawamoto, K., 2010. Morphological and flow cytometric analysis of cell infiltration in glioblastoma: a comparison of autopsy brain and neuroimaging. Brain Tumor Pathol 27, 81–87. https://doi.org/10.1007/s10014-010-0275-7

Yang, Z., Wang, K.K.W., 2015. Glial fibrillary acidic protein: from intermediate filament assembly and gliosis to neurobiomarker. Trends Neurosci 38, 364–374. https://doi.org/10.1016/j.tins.2015.04.003

Yeini, E., Ofek, P., Albeck, N., Rodriguez Ajamil, D., Neufeld, L., Eldar-Boock, A., Kleiner, R., Vaskovich, D., Koshrovski-Michael, S., Dangoor, S.I., Krivitsky, A., Burgos Luna, C., Shenbach-Koltin, G., Goldenfeld, M., Hadad, O., Tiram, G., Satchi-Fainaro, R., 2021. Targeting Glioblastoma: Advances in Drug Delivery and Novel Therapeutic Approaches. Advanced Therapeutics 4, 2000124. https://doi.org/10.1002/adtp.202000124

Yin, D., Zhai, Y., Gruber, H.E., Ibanez, C.E., Robbins, J.M., Kells, A.P., Kasahara, N., Forsayeth, J., Jolly, D.J., Bankiewicz, K.S., 2013. Convection-enhanced delivery improves distribution and efficacy of tumor-selective retroviral replicating vectors in a rodent brain tumor model. Cancer Gene Ther 20, 336–341. https://doi.org/10.1038/cgt.2013.25

Zagzag, D., Esencay, M., Mendez, O., Yee, H., Smirnova, I., Huang, Y., Chiriboga, L., Lukyanov, E., Liu, M., Newcomb, E.W., 2008. Hypoxia- and vascular endothelial growth factor-induced stromal cell-derived factor-1alpha/CXCR4 expression in glioblastomas: one plausible explanation of Scherer's structures. Am J Pathol 173, 545–560. https://doi.org/10.2353/ajpath.2008.071197

Zhao, B., Zhao, Z., Ma, J., Ma, X., 2019. Modulation of angiogenic potential of tissue-engineered peripheral nerve by covalent incorporation of heparin and loading with vascular endothelial growth factor. Neurosci Lett 705, 259–264. https://doi.org/10.1016/j.neulet.2019.01.017

Zhong, X., Arnolds, O., Krenczyk, O., Gajewski, J., Pütz, S., Herrmann, C., Stoll, R., 2018. The Structure in Solution of Fibronectin Type III Domain 14 Reveals Its Synergistic Heparin Binding Site. Biochemistry 57, 6045–6049. https://doi.org/10.1021/acs.biochem.8b00771

Zhou, Y., Larsen, P.H., Hao, C., Yong, V.W., 2002. CXCR4 is a major chemokine receptor on glioma cells and mediates their survival. J Biol Chem 277, 49481–49487. https://doi.org/10.1074/jbc.M206222200

Chapter 4:

Development and evaluation of chitosan electrospun fiber mats

4. Development and evaluation of chitosan electrospun fiber mats

4.1. Introduction

This chapter concerns the synthesis and evaluation of electrospun chitosan fibers as an implantable device for the trapping of glioblastoma cells. The process of synthesis was part of the subject of the thesis by Haji Mansor et al. in collaboration with Dr. Christine Jerôme at the University of Liège (Haji Mansor, 2019). In summary, the process involves the nanoprecipitation of SDF-1α and incorporation into PLGA nanoparticles (NPs). Then, the NPs are incorporated into a chitosan solution for electrospinning. The resulting fibers are collected as films, also called mats, that contain nonwoven nanofibers with the incorporated SDF-1α-loaded nanoparticles (NPs). These fiber mats can be manipulated to form rolls as a system to be implanted in the resection cavities. In this thesis, the *in vitro* evaluation and *in vivo* biocompatibility and biodegradability are completed resulting in the following publication (Molina-Peña et al., 2021). The same cell line that was used for the evaluation of SF-HA-Hep sponges, U87MG-CXCR4+ cells, is also employed for the assessment of the bioactivity of the released SDF-1α from electrospun mats on cell migration by using an agarose drop assay. The evaluation of the *in vivo* biodegradability and biocompatibility was performed using blank NPs incorporated into the nanofibers. Unpublished results are also included and concern: a) a digital method to estimate the pore size and porosity of the fiber mats, b) the long-term biodegradability and biocompatibility *in vivo* evaluation, and c) observations regarding the behavior of U87MG-CXCR4+ cells seeded on modified surfaces containing aligned tracks. Finally, a succinct general discussion and conclusion of the chapter are presented.

4.2. Results

4.2.1. Manuscript published in the International Journal of Pharmaceutics

Nanoparticle-containing Electrospun Nanofibrous Scaffolds for Sustained Release of SDF-1α

Rodolfo Molina-Peña[a,1], Muhammad Haji Mansor[a,b,1], Mathie Najberg[a,c], Jean-Michel Thomassin[b], Baya Gueza[a], Carmen Alvarez-Lorenzo[c], Emmanuel Garcion[a], Christine Jérôme[b], Frank Boury[a,*]

[a]*Univ Angers, Université de Nantes, Inserm, CRCINA, SFR ICAT, F-49000 Angers, France*

[b]*Center for Education and Research on Macromolecules (CERM), CESAM-UR, University of Liège, B-4000 Liège, Belgium*

[c]*Departamento de Farmacología, Farmacia y Tecnología Farmacéutica, I+D Farma (GI-1645), Facultad de Farmacia, and Health Research Institute of Santiago de Compostela (IDIS), Universidade de Santiago de Compostela, 15782 Santiago de Compostela, Spain*

[1]*equal contribution*

[*] Corresponding author.

E-mail address: frank.boury@univ-angers.fr

Tel: +33 (0)2 44 68 85 28

Postal address:

Cancer and Immunology Research Centre Nantes-Angers (CRCINA)

INSERM U1232, Team GLIAD

Université d'Angers

IBS - CHU Angers

4 rue Larrey

49933 ANGERS CEDEX 9, France

Highlights

- Novel chitosan nanofibrous scaffold containing PLGA nanoparticles
- Electrospun nanofibers with SDF-1α-loaded nanoparticles for sustained release
- High cytocompatibility *in vitro* and *in vivo* and slow degradation profile
- Mat structure with good cell attachment of glioblastoma cells
- Bioimplant Intended as a sink for the trapping of CXCR4-expressing tumor cells

Abstract

Chemokines such as stromal cell-derived factor-1α (SDF-1α) regulate the migration of cancer cells that can spread from their primary tumor site by migrating up an SDF-1α concentration gradient, facilitating their local invasion and metastasis. Therefore, the implantation of SDF-1α-releasing scaffolds can be a useful strategy to trap cancer cells expressing the CXCR4 receptor. In this work, SDF-1α was encapsulated into poly(lactic-co-glycolic acid) (PLGA)-based nanoparticles and subsequently electrospun with chitosan to produce nanofibrous scaffolds of average fiber diameter of 261 ± 45 nm, intended for trapping glioblastoma (GBM) cells. The encapsulated SDF-1α maintained its biological activity after the electrospinning process as assessed by its capacity to induce the migration of cancer cells. The scaffolds could also provide sustained release of SDF-1α for at least 5 weeks. Using NIH3T3 mouse fibroblasts, human Thp-1 macrophages, and rat primary astrocytes we showed that the scaffolds possessed high cytocompatibility *in vitro*. Furthermore, a 7-day follow-up of Fischer rats bearing implanted scaffolds demonstrated the absence of adverse effects *in vivo*. In addition, the nanofibrous structure of the scaffolds provided excellent anchoring sites to support the adhesion of human GBM cells by extension of their pseudopodia. The scaffolds also demonstrated slow degradation kinetics, which may be useful in maximizing the time window for trapping GBM cells. As surgical resection does not permit a complete removal of GBM tumors, our results support the future implantation of these scaffolds into the walls of the resection cavity to evaluate their capacity to attract and trap the residual GBM cells in the brain.

Keywords

Stromal cell-derived factor-1α (SDF-1α), Poly(lactic-co-glycolic acid) (PLGA), Sustained release, Electrospinning, Chitosan nanofibrous scaffold, Glioblastoma (GBM).

Graphical Abstract

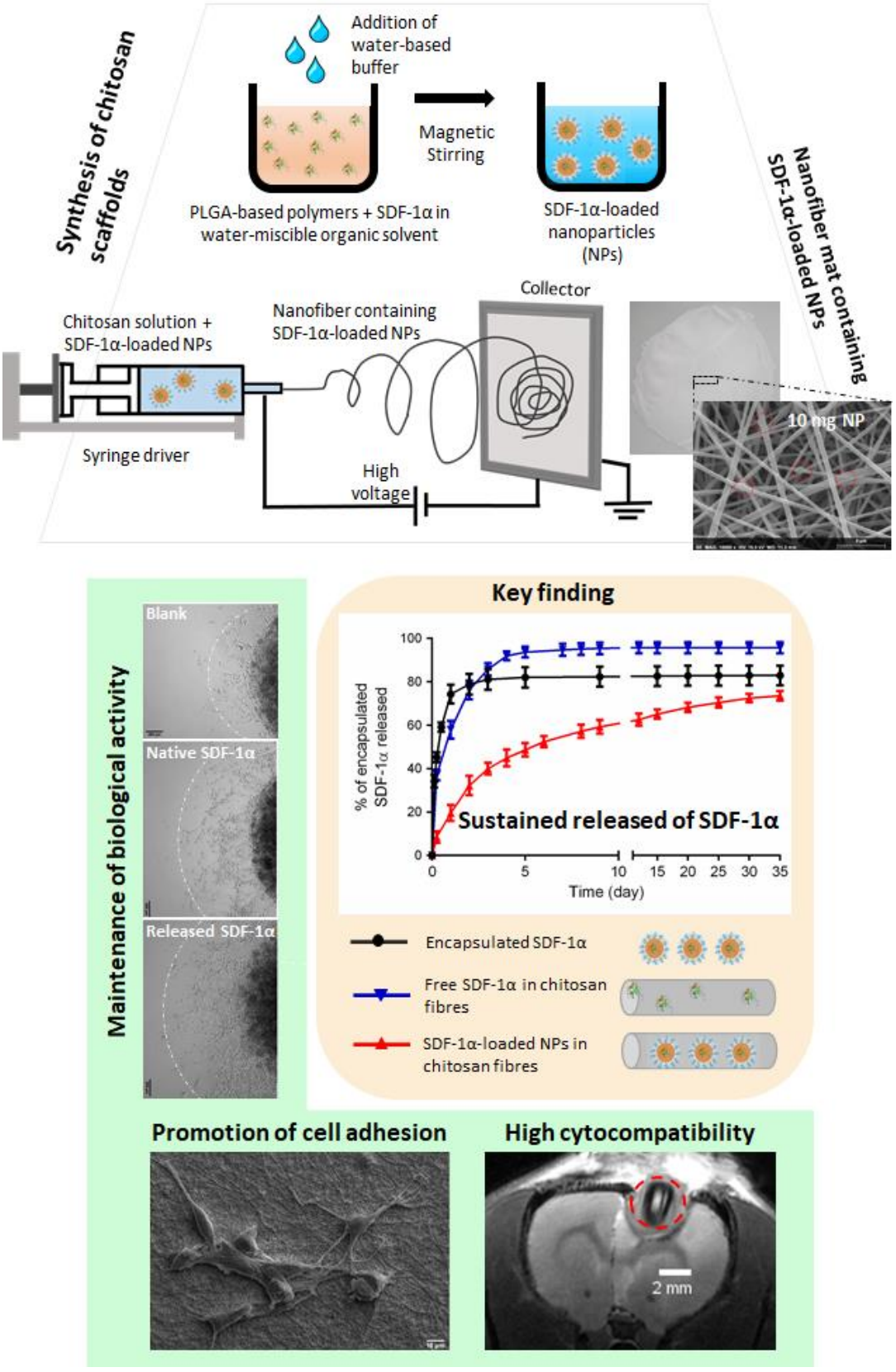

Introduction

Stromal cell-derived factor-1α (SDF-1α) is a 68-amino-acid chemokine (De La Luz Sierra et al., 2004) with a strong binding affinity to the C-X-C chemokine receptor type 4 (CXCR4) (Kofuku et al., 2009). One of its prominent physiological functions is to induce the migration of CXCR4-expressing stem and progenitor cells from the bone marrow towards a site of injury to initiate the process of tissue repair and recovery (Ratajczak et al., 2004). The directed migration is an effect of an elevated SDF-1α expression at the injury site (Deng et al., 2011; Kitaori et al., 2009; Knerlich-Lukoschus et al., 2010) and the simultaneous increase in SDF-1α degradation in the bone marrow (Jin et al., 2008; Marquez-Curtis et al., 2008) that creates a positive SDF-1α concentration gradient towards the site needing repair. In addition to its role in tissue regeneration, SDF-1α-induced chemotaxis also mediates the spreading of cancer cells that escaped their respective primary tumor sites. CXCR4-expressing cancer cells have been shown to penetrate the blood or lymphatic circulation and subsequently be chemoattracted to SDF-1α-secreting organs such as the liver (Kim et al., 2006), bone marrow (Roccaro et al., 2014) and lymph nodes (Katsura et al., 2018) for future metastatic colonization. Even in non-metastasizing cancers, the chemotactic effect of SDF-1α can support tumor progression by facilitating the invasion of cancer cells into proximal healthy tissues (Zagzag et al., 2008). The significant influence of SDF-1α on the migration of cancer cells has motivated the design of implants capable of releasing this chemokine to create a local concentration gradient that may attract CXCR4-expressing cancer cells relevant to many types of cancers including glioblastoma (GBM) (Carmo et al., 2010), melanoma (O'Boyle et al., 2013) and breast cancer (Sobolik et al., 2014).

Like other peptides and proteins, SDF-1α is water-soluble and thus can move rapidly through a physiological fluid compartment (Pardridge, 2011). Therefore, to establish and maintain a local concentration gradient of SDF-1α, sustained delivery of this chemokine from a fixed source is necessary. In this regard, encapsulation into nanocarriers composed of biodegradable polymers is a reasonable strategy to achieve gradual release of active molecules at the intended site of delivery (Almouazen et al., 2012; Hamoudeh et al., 2007; Nicolas et al., 2018). We have previously encapsulated SDF-1α into poly-(lactic-co-glycolic acid) (PLGA) nanoparticles (NPs) (Haji Mansor et al., 2018). However, we showed that the duration of SDF-1α release resulting from this approach was relatively brief. The release profile showed a steep initial release curve that leveled out shortly afterwards and that is characteristic of this kind of NPs with a two phase process where the first phase of "burst release" from locations near the NP's surface is followed by a second phase of prolonged release from the core compartment (Martínez Rivas et al., 2017). In addition, NPs tend to spread away from the initial site of application, making it difficult to establish a concentration gradient of the released drug molecules. Considering these shortcomings, we postulate that the SDF-1α-loaded NPs should be embedded within a suitable scaffold to slow down the SDF-1α release process and to prevent them from moving away from the initial site of administration.

Currently, there are multiple types of scaffolds within which drug-loaded carriers can be confined. These structures can provide an additional barrier to the drug diffusion process and may subsequently contribute to a longer duration of drug release from the primary carrier into the local environment. These include physically and chemically cross-linked hydrogels (Lee et al., 2018; Ono et al., 2017; Zhang et al., 2016), scaffolds prepared by the freeze-drying process (Gentile et al., 2015; Najberg et al., 2020; Pulavendran and Thiyagarajan, 2011) and those derived from a direct compression of the drug-loaded carriers (Du et al., 2017). However, these confining matrices usually lack the nanofibrous structures typically found in native human extracellular matrices (ECM). In relation to our objective, it is important to develop scaffolds with structures mirroring those of the ECM in order to promote the adhesion and retention of cancer cells. In this regard, nanofibrous scaffolds can be prepared using electrospinning (Huang et al., 2003; Pham et al., 2006). Many natural and synthetic materials can be used to produce electrospun ECM-mimetic nanofibrous scaffolds. Among these, chitosan has been an outstanding material for making electrospun scaffolds to be used in a variety of biomedical applications due to its excellent biocompatibility (Frohbergh et al., 2012; Ma et al., 2011; Xie et al., 2013). Nevertheless, the electrospinning of chitosan and many other materials involves challenging conditions, including the use of high voltage to draw fibers from the material solution, which may compromise the structural integrity of protein molecules pre-incorporated into the solubilized material (Bekard and Dunstan, 2013; Toschi et al., 2009; Wang et al., 2014; Zhao and Yang, 2010, 2009). Therefore, we hypothesize that by pre-encapsulating SDF-1α molecules into PLGA-based NPs, their denaturation during processing may be minimized.

In the present study, SDF-1α was encapsulated into NPs composed of PLGA and a polyethylene glycol (PEG)-PLGA co-polymer. The SDF-1α-loaded NPs were then dispersed in a chitosan solution in the presence of the fiber-forming additive polyethylene oxide (PEO) and subsequently electrospun to produce NP-containing nanofibrous scaffolds. After electrospinning, the charged chitosan amino groups within the nanofibers were deprotonated to improve the scaffold stability in physiological media. Following this, the *in vitro* release patterns of the model protein lysozyme as well as of SDF-1α from the scaffolds were studied. The bioactivity of the released SDF-1α was subsequently evaluated by assessing its capacity to induce the migration of CXCR4-expressing human GBM cells (U87-MG). Finally, after studying their degradation profiles, the scaffolds' ability to retain U87-MG cells as well as their cytocompatibility was assessed *in vitro* and *in vivo* to evaluate the appropriateness of their use in future *in vivo* studies.

Materials and Methods

2.1. Materials

Ester-capped PLGA (Mn = 5.5 kDa) and PEG-PLGA copolymer (Mn_{PEG} = 5 kDa, Mn_{PLGA} = 25.7 kDa) were synthesized using a ring-opening polymerization method as described

elsewhere (Haji Mansor et al., 2018). Glycofurol (Tetraglycol BioXtra®), isosorbide dimethyl ether, poloxamer 188 (Lutrol® F68), sodium chloride, lysozyme from hen egg white, glycine, 10 M sodium hydroxide, dimethyl sulfoxide, Tris base (Trizma®), 37% hydrochloric acid, *Micrococcus lysodeikticus,* low gelling point agarose and PEO (average Mv ~2 MDa) were obtained from Sigma-Aldrich (Saint Quentin Fallavier, France). Human SDF-1α (research grade) was purchased from Miltenyi Biotech (Paris, France), chitosan with a degree of deacetylation of ~80% and molecular weight ~ 10 – 50 kDa (Chitoceuticals®) from Heppe Medical Chitosan GmbH (Halle, Germany), 1X Dulbecco's phosphate-buffered saline (Biowhittaker®) from Lonza (Verviers, Belgium), bovine serum albumin fraction V from Roche Diagnostics GmbH (Mannheim, Germany) and high glucose Dulbecco's Modified Eagle's Medium (Gibco®) from Thermo Fisher Scientific (Villebon sur Yvette, France). Deionized water supply was obtained from a Milli-Q® Advantage A10 system (Millipore, Paris, France).

2.2. Preparation and characterization of protein-loaded nanoparticles

2.2.1. Preparation of protein-loaded nanoparticles

Protein-loaded NPs were prepared as described previously (Haji Mansor et al., 2018). Briefly, the lyophilized model protein lysozyme and SDF-1α as provided by their respective manufacturers were separately dissolved in 0.15 M sodium chloride (NaCl) solution containing 20% w/v poloxamer 188 at a concentration of 10 and 1.33 mg/mL, respectively. After that, 975 µL of glycofurol was added to 25 µL of the lysozyme solution, and 185 µL of glycofurol to 15 µL of the SDF-1α solution. A smaller volumetric ratio of glycofurol to SDF-1α solution was used for convenience and worked well as SDF-1α is less soluble than lysozyme in aqueous solutions. The mixtures were subsequently incubated in ice for 30 min to induce the formation of protein precipitates. Then, 100 µL of the protein precipitate dispersion containing either 25 µg lysozyme or 10 µg SDF-1α was mixed with 100 µL of a 12% w/v PEG-PLGA solution and 200 µL of a 12% w/v PLGA solution in isosorbide dimethyl ether (total volume after mixing was 400 µL). Using Equation (1), the theoretical drug loadings (DL) for lysozyme and SDF-1α were calculated to be 0.07% and 0.03% respectively. For the synthesis of unloaded NPs, the 100 µL protein precipitate dispersion was replaced with an equal volume of glycofurol alone. Then, 2.1 mL of 0.05 M glycine-sodium hydroxide buffer solution was added gradually under magnetic stirring to initiate the formation of NPs that encapsulated the protein load. As the solubilities of lysozyme and SDF-1α were reduced as the pH of their respective solutions reached their protein isoelectric points (pI) (pI lysozyme = 11.35; pI SDF-1α = 10.5), a greater encapsulation efficiency was achieved. Therefore, the pH of the buffer solution was set to 11.35 and 10.40 for the encapsulation of lysozyme and SDF-1α, respectively. The formed nanoparticle (NP) dispersion was subsequently diluted with excess deionized water and agitated under slow magnetic stirring for 1 h to wash out solvents and unencapsulated proteins.

The suspended NPs were then centrifuged for 30 min at 10,000 x g, and the supernatant was discarded and replaced with an equal volume of deionized water. The centrifugation was repeated once and after subsequent removal of the supernatant, the purified NP dispersion was stored at a concentration of approximately 40 mg/mL in 0.5 mL volume in deionized water at 4 °C until use.

$$DL\ (\%) = \frac{Initial\ mass\ of\ protein\ used\ as\ a\ starting\ material}{Total\ mass\ of\ PLGA\ and\ PEG{-}PLGA}\ x\ 100 \qquad \text{Equation (1)}$$

2.2.2. Characterization of protein-loaded nanoparticles

The morphology of the NPs was visualized using scanning electron microscopy (SEM) (JSM 6310F, JEOL, Paris, France). The purified NP dispersion was initially diluted 200-fold with deionized water to a concentration of approximately 200 µg/mL. Then, 2 µL of the dispersion was added onto a glass slide and left overnight to dry at room temperature. Prior to observation, a gold coating of 5 nm thickness was deposited onto the NP sample.

The size distribution of the NPs was determined using a dynamic light scattering (DLS) method whereas zeta-potentials were derived from the electrophoretic mobility values using the Smoluchowski's approximation in a Nanosizer® ZS (Malvern, Worcestershire, UK). Initially, the purified NP dispersion was diluted with either deionized water or 0.01 M NaCl solution (pH was adjusted to 7 prior to measurement) for size and zeta-potential measurements, respectively, to obtain optimal NP concentrations for analyses such that the attenuator values were in the range of 5–7. Each sample was measured three times, with one measurement representing the average value of at least 10 runs. All measurements were conducted at 25 °C under the automatic mode. In addition to the average particle size, the DLS protocol of Nanosizer® ZS generated a polydispersity index (PDI) ranging from 0 to 1 that estimates the width of the size distribution.

For the assessment of protein encapsulation efficiencies, the protein-loaded NPs were initially lyophilized for 16 h alongside the unloaded NPs that served as a control. Then, the NPs were dissolved in 1 mL of dimethyl sulfoxide. After 1 h, 3 mL of 0.01 M hydrochloric acid (HCl) was added to extract the protein load from the polymeric components of the NPs. The samples were then diluted appropriately prior to assessment using the protein quantification assays described in Section 2.6. The encapsulation efficiency (EE) was calculated using Equation (2).

$$EE\ (\%) = \frac{Mass\ of\ protein\ recovered\ from\ dissolved\ nanoparticles}{Initial\ mass\ of\ protein\ used\ as\ a\ starting\ material}\ x\ 100 \qquad \text{Equation (2)}$$

2.3. Preparation and characterization of nanoparticle-containing nanofibrous scaffolds

2.3.1. Preparation of nanoparticle-containing nanofibrous scaffolds

To prepare nanofibrous scaffolds containing protein-loaded NPs, 11 mg of PEO was initially added to 0.5 mL of NP dispersion in deionized water. The NP concentration was varied between 10 and 40 mg/mL to determine the maximum mass of NPs that can be loaded into the nanofibrous scaffolds. After that, the NPs/PEO mixture was added to 1.7 mL of 6.5% w/v chitosan solution in 1 M acetic acid. Based on this, the theoretical NP load in the nanofibrous scaffold to be synthesized ranged from 4.0 – 14.2% w/w (5 – 20 mg NPs per 110 mg chitosan and 11 mg PEO). The materials were then mixed at room temperature using a laboratory magnetic stirrer set to 100 rpm for 2 h. For the preparation of nanofibrous scaffolds carrying unencapsulated protein molecules, the PEO was dissolved in 0.5 mL deionized water containing either 25 µg lysozyme or 10 µg SDF-1α to match the protein load in the NPs prior to mixing with the 6.5% w/v chitosan solution. The homogenized materials were subsequently transferred into a 10 mL HSW SOFT-JECT® disposable plastic syringe (Henke-Sass, Wolf GmbH, Tuttlingen, Germany) with a luer slip tip that was fixed with a 21 G x 1½ in blunt-ended needle. The syringe was then left to stand for another 2 h for degassing.

For the electrospinning step, the syringe containing the protein-loaded NPs, PEO and chitosan was carefully mounted onto a syringe driver (KD Scientific, Holliston, MA, USA) with the tip of the needle positioned 17 cm away from the collector plate. The syringe driver was used to control the flow rate of the materials at 0.78 mL/h. To produce nanofibers, a Spellman SL10® high voltage generator (Spellman High Voltage Electronics Corp., Hauppauge, NY, USA) was used to apply a potential difference of 30 kV between the needle and the collector plate for 165 min. The nanofibers were deposited onto a piece of aluminum foil covering the collector plate to facilitate the subsequent retrieval of the electrospun scaffold.

2.3.2. Characterization of nanoparticle-containing nanofibrous scaffolds

The thickness of the nanofibrous scaffolds were measured using a Kaefer Dial Gauge (Kaefer Messuhrenfabrik GmbH, Villingen-Schwenningen, Germany).

The composition of the nanofibrous scaffolds was determined using attenuated total reflectance-Fourier transform infrared (ATR-FTIR) spectroscopy. ATR-FTIR spectra were recorded using a Nicolet iS5® spectrometer (Thermo Fisher Scientific) with a spectral resolution of 4 cm^{-1}.

The morphology of the nanofibrous scaffolds was observed using scanning electron microscopy (SEM) (JSM 840A, JEOL) and transmission electron microscopy (TEM) (JEM 1400, JEOL). For SEM, the nanofibrous scaffolds were coated with a 5 nm platinum layer prior to observation. Fiber diameter measurements were then performed using the ImageJ software

(NIH, USA) on 30 randomly selected fibers in a SEM image. Three SEM images were analyzed for each sample. For TEM, nanofibers were collected on a copper grid (Gilder Grids, Grantham, UK) placed in front of the collector plate for about 3 s during the electrospinning process and observed without any coating.

To investigate whether the electrospinning process contributes to any protein denaturation, 2 mL of 1 M acetic acid solution was added to the nanofibrous scaffolds to dissolve the nanofibers and subsequently release the protein-loaded NPs. After 1 h, 4 mL of a 1 M NaOH solution was added gradually to increase the basicity of the mixture (to pH > 13) to induce the precipitation of the chitosan molecules as well as the dissolution of the NPs. After another 1-h incubation, the mixture was centrifuged at 9,500 x g for 30 min to spin down the chitosan precipitates. 2 mL of the supernatant was kept for use in the protein quantification assays described in Section 2.6.

2.4. Stabilization of the nanofibrous scaffolds

To reduce the solubility of the nanofibrous scaffolds in physiological media, the charged amino groups of chitosan in the nanofibers were deprotonated (He et al., 2011; Tchemtchoua et al., 2011). To achieve this, the nanofibrous scaffolds were treated sequentially with absolute ethanol for 5 min and then 0.1 M NaOH for 30 s, followed by three times washing with 0.1X phosphate-buffered saline (PBS) (pH 7.4). The scaffolds were then dried under reduced pressure for 16 h.

2.5. *In vitro* protein release study

The *in vitro* protein release study was conducted on the protein-loaded NPs, nanofibrous scaffolds loaded with unencapsulated protein molecules and protein-loaded NPs incorporated into nanofibrous scaffolds. Protein-free NPs and nanofibrous scaffolds were used as controls. All nanofibrous scaffolds were stabilized prior to use as described in section 2.4. NPs and whole scaffolds were incubated separately at 37 °C in 2 mL of 0.05 M Tris-HCl buffer solution (pH 7.4) supplemented with 0.15 M NaCl and 1 mg/mL bovine serum albumin (BSA) as a protein stabilizer. At each pre-defined time point, 1.5 mL of the buffer solution was collected and replaced with fresh buffer. For the NP samples, the dispersion was centrifuged at 9,500 x g for 30 min to spin down the NPs and 1.5 mL of the supernatant was subsequently collected and replaced with fresh buffer. The quantification of protein molecules in the collected samples was conducted as described in Section 2.6.

2.6. Protein quantification

2.6.1. Quantification of lysozyme

Lysozyme was quantified using the turbidity reduction assay as described by Hassani and colleagues (Hassani et al., 2013). Briefly, 100 µL of lysozyme-containing sample was added to 2.9 mL of 0.015% w/v *Micrococcus lysodeikticus* suspension in 0.05 M Tris-HCl buffer solution (pH 7.4). The assay mixture was then incubated at 37 °C to allow the lysozyme molecules to lyse the *M. lysodeikticus* cell walls. After 4 h, the absorbance at 450 nm was measured (Multiskan Ascent, Labsystems, Les Ulis, France). To construct a standard curve, lysozyme solutions of concentration ranging from 100 to 1000 ng/mL were also assayed. Each sample was diluted with 0.05 M Tris-HCl buffer solution (pH 7.4) by several dilution factors to obtain absorbance readings that were within the standard curve range.

2.6.2. Quantification of SDF-1α

SDF-1α was quantified using an enzyme-linked immunosorbent assay (ELISA) as per supplier's instructions (R&D Systems, Lille, France). Briefly, a Nunc Maxisorp® 96-well microplate (Thermo Fisher Scientific) was incubated overnight with SDF-1α capture antibody solution to coat the wells. The plate was then washed with 0.05% w/v Tween® 20 in 1X PBS (pH 7.4). To prevent any non-specific protein binding during the sample incubation stage, the plate was subsequently incubated with 10 mg/mL BSA solution in 1X PBS (pH 7.4) for 1 h. After washing, SDF-1α-containing samples and the provided SDF-1α standard pre-diluted with 10 mg/mL BSA solution in 1X PBS (pH 7.4) were added to the wells for a 2-h incubation. Following another wash, the wells were incubated with detection antibody solution for 2 h. The plate was washed again prior to a 20-min incubation with streptavidin-horseradish peroxidase solution. The final washing step was carried out and the plate was then incubated with the substrate solution for another 20 min. The enzymatic reaction was subsequently terminated by adding 1 M sulfuric acid solution and the absorbance at 450 nm was immediately measured (Multiskan Ascent, Labsystems, Les Ulis, France). All incubations were done at room temperature.

2.7. Assessment of SDF-1α bioactivity

SDF-1α bioactivity was assessed using an agarose drop migration assay (Milner et al., 1996). Initially, constitutively CXCR4-expressing U87-MG cells, as produced by Séhédic and colleagues (Séhédic et al., 2017), were seeded into a 24-well flat-bottomed culture plate (Nunc, Strasbourg, France) at a density of 1 x 10^5 cells per well and incubated with Dulbecco's Modified Eagle's Medium (DMEM) supplemented with 10% fetal bovine serum (FBS) and 1% penicillin/streptomycin. To enhance cell adhesion, each well was previously treated with 500 µL of 10 µg/mL poly-D-lysine hydrobromide (Sigma-Aldrich) solution for 15 min and

subsequently washed with 1X PBS three times. After 72 h of incubation, the medium was replaced with deionized water to lyse the cells. The wells were washed with 1X PBS after 20 min and the thin cell-derived matrices coating the well surfaces were left to air-dry under laminar flow. Next, 2 µL of 1% w/v solution of low gelling point agarose containing 1 x 10^5 CXCR4-expressing U87-MG cells was deposited onto the center of each well and the plate was kept at 4 °C for 15 min for the gelation step. Then, the cell-loaded agarose drop was covered with 400 µL of DMEM (FBS-free, 1% penicillin/streptomycin) with or without 40 ng/mL of native SDF-1α as controls; or with DMEM containing SDF-1α extractables from scaffolds after electrospinning or leached SDF-1α from the releasing studies. Three drops were assayed for each medium condition in each experiment. After 72 h, the plan view of each well was captured using an optical microscope and a built-in camera (AxioCam® ICm 1, Zeiss, Jena, Germany). The cell migration distance was estimated by measuring the distance between the edge of the drop and the cell front on four distinct sides of the drop using the ImageJ software. The measurements were subsequently averaged to obtain a representative migration distance in each well. All incubations were done at 37 °C and 5% CO_2.

2.8. *In vitro* scaffold degradation study

Stabilized nanofibrous scaffolds were cut into quarters of approximately 25 mg in mass. The scaffold pieces were then incubated separately in 2 mL of 0.05 M Tris-HCl buffer solution (pH 7.4) supplemented with 0.15 M NaCl, 20 µg/mL lysozyme and 1 mg/mL BSA at 37 °C. At each pre-defined time point, three scaffold pieces were removed from their respective buffer solution using sterile tweezers, the excess liquid was blotted up using KIMTEC wipers, and the scaffolds were then dried in a desiccator under reduced pressure for 16 h. The dried scaffold pieces were then weighed, and the % of scaffold mass degraded throughout the incubation period was calculated using Equation (3).

$$\%\ of\ scaffold\ mass\ degraded = \frac{mass\ before\ incubation - mass\ after\ incubation}{mass\ before\ incubation}\ x\ 100\% \quad \text{Equation (3)}$$

2.9. *In vitro* cytocompatibility and cell adhesion assays

To exclude any potential proliferative effect of the protein load that may reduce the reliability of the study results, only the nanofibrous scaffold loaded with blank NPs and the unloaded nanofibrous scaffold were evaluated in these assays. Two *in vitro* methods were used to evaluate the scaffold cytocompatibility: (a) a 24-h incubation of cells with scaffold leachables, and (b) a more realistic scenario in which cells were incubated with scaffolds for 24 and 72 h. All incubations were done at 37 °C and 5% CO_2 and the medium used was always supplemented with 10% FBS and 1% penicillin/streptomycin.

2.9.1. *In vitro* cytocompatibility assay

2.9.1.a. Indirect method

The *in vitro* cytocompatibility of the nanofibrous scaffolds by the indirect test was assessed using the "scaffold extract" method adapted from Wang and colleagues (Wang et al., 2013). The nanofibrous scaffolds were cut into circular pieces of 10 mm in diameter and approximately 0.6 mg in mass to promote ease of handling. Five scaffold pieces were placed together in a well of a 24-well flat-bottomed culture plate (Nunc) containing 400 µL of DMEM and incubated for 24 h to produce the scaffold extract. Simultaneously, NIH3T3 mouse fibroblasts cells (CRL-1658™, ATCC, Rockville, Maryland, USA) were seeded in a 96-well flat-bottomed culture plate (Nunc) at a density of 5500 cells/well in 100 µL of DMEM and incubated for 24 h. Then, the medium on the cells was replaced with 100 µL of the scaffold extract and the cells were incubated for another 24 h. As a positive control, 100 µL of fresh medium was used in place of the scaffold extract. 10 µL of WST-1 reagent (Sigma-Aldrich) were subsequently added into each well. After 2 h of incubation, the number of viable cells was estimated from the absorbance of the cleaved product of the tetrazolium salts in the WST-1 reagent, called formazan, which was measured at 450 nm using a ClarioStar® microplate reader (BMG Labtech GmbH, Ortenberg, Germany). To estimate the background absorbance, the WST-1 reagent was also added to wells containing either the scaffold extract or fresh medium alone without any cells. All background-corrected absorbance values were normalized to those of the positive control.

2.9.1.b. Direct contact method

Contact-induced cytotoxicity of the nanofibrous scaffolds was assessed using NIH3T3 mouse fibroblasts, human Thp-1 macrophages, and rat primary astrocytes. Assays were conducted in 24-well cell culture plates (well diameter = 15.6 mm). All incubations were done at 37 °C and 5% CO_2 and DMEM supplemented with 10% FBS and 1% penicillin/streptomycin was used throughout the assay unless stated otherwise.

Cells were prepared accordingly prior to the 24 or 72-h period of incubation with the scaffolds. NIH3T3 cells were seeded at a density of 40 x 10^3 and 10 x 10^3 cells/well for the 24 and 72-h assays respectively and incubated in 500 µL medium 24 h before use. To obtain Thp-1 macrophages, Thp-1 monocytes (TIB-202™, ATCC) were seeded at a density of 200 x 10^3 cells and 50 x 10^3 cells/well for the 24 and 72-h assays, respectively. The Thp-1 monocytes were incubated in 500 µL complete Roswell Park Memorial Institute (RPMI) 1640 medium (Sigma-Aldrich) supplemented with 80 nM phorbol 12-myristate 13-acetate (PMA) (Sigma-Aldrich) for 24 h to induce their differentiation into macrophages. Following this, the PMA-containing medium was replaced with fresh complete RPMI medium (without PMA) and the cells were incubated for another 24 h before use. Purified cultures of newborn rat primary astrocytes were prepared from extracts of cerebral cortex using the mechanical dissociation

method as originally described (McCarthy and de Vellis, 1980). Brain extract was homogenized, lyophilized and reconstituted in cell culture medium before being added to the 24-well plate. The medium was refreshed twice weekly for two weeks to obtain highly pure cultures of primary astrocytes.

Prior to incubation with the cells, the nanofibrous scaffolds were cut into circular pieces of 10 or 14 mm in diameter, which correlated to a 2-fold difference in surface areas (79 vs. 154 mm^2, respectively). The scaffold pieces were washed with 1X PBS three times and incubated in the cell culture medium for 15 min before being deposited onto the cell monolayer prepared in the 24-well plate. Wells without scaffolds acted as control. After 24 or 72 h of incubation, the medium in each well was replaced with 500 µL fresh medium containing 44 µM resazurin. To estimate the background fluorescence, the resazurin-containing medium was also added into three empty wells of the assay plate (without any cells). The plate was incubated for another 2 h.

Cell viability was estimated from the fluorescence intensity of the reduced product of resazurin, called resorufin, which was measured using a ClarioStar microplate fluorometer (BMG Labtech GmbH, Ortenberg, Germany) at 545 nm excitation and 600 nm emission. All background-corrected fluorescence intensity values were normalized to those obtained with the control wells.

2.9.2. *In vitro* cell adhesion assay

The cell adhesion capacity of the nanofibrous scaffolds was studied using U87-MG cells (HTB-14™, ATCC). Initially, 25 µL of DMEM containing 10,000 cells was deposited on the top of a scaffold piece placed in a well of a 48-well flat-bottomed culture plate (Nunc). As a positive control, the same number of cells was added to a well without any scaffold. After 1 h of incubation, another 275 µL of medium was added into the wells and the plate was incubated for another 3 h to allow the cells to adhere to the scaffold or well surfaces. Then, the wells were washed with 1X PBS three times to remove any loosely attached cells. After another 24 h of incubation in 300 µL of fresh medium, the cell viability on the scaffold was evaluated using WST-1 reagent as described in Section 2.9.1.a. To ensure that the cells that reacted with the WST-1 reagent were those that were attached to the scaffolds and not of any colonies that formed on the well surface underneath, the scaffolds were transferred into new wells containing 300 µL of fresh medium before adding 30 µL of WST-1 reagent. To determine the background absorbance, the reagent was also added to cell-free wells containing DMEM with or without a scaffold piece. For the absorbance measurement, 100 µL of medium was transferred from each well to a 96-well plate 2 h after the addition of WST-1 reagent.

For the SEM analysis, the scaffolds were washed three times with PBS and equilibrated in DMEM. Then a 25 µL drop containing 2 x 10^4 cells was deposited on top of the scaffolds. After 1 h incubation at 37 °C, 275 µL of DMEM was added and the scaffolds incubated during 72 h. The scaffolds were then fixed in a 0.1 M phosphate buffer containing glutaraldehyde at

2.5 % for 2 h. The scaffolds were then rinsed with PBS and distilled water and incubated in a 1% osmium tetroxide aqueous solution for 1 h at room temperature. Dehydration in increasing concentration of ethanol solutions was performed, followed by desiccation in hexamethyldisilazane. A coating of platinum was performed before analysis in a Zeiss EVO LS10 microscope.

2.10. *In vivo* biocompatibility study

In vivo studies were also conducted by implanting the scaffolds into the brain of healthy rats to assess the potential toxicity of the scaffolds as well as their tendency to degrade in the brain environment. After implantation, brains were imaged by Magnetic Resonance Imaging (MRI) in order to obtain the volume of scaffolds at the beginning and end of the follow-up period.

2.10.1. *In vivo* implantation of nanofibrous scaffolds into rat brain cortex

Fischer female rats aged 8-10 weeks were obtained from Janvier Labs (Le Genest-Saint-Isle, France). The protocol was approved by the Ethical Committee for Animal Experimentation of Pays de la Loire, France. Animals were anesthetized by intraperitoneal injection of a mixture of ketamine (100 mg/kg) and xylazine (13 mg/kg) and positioned in a Kopf stereotaxic instrument. A 10 mm-long incision was made along the midline to create access to the surface of the skull. Following this, a burr hole was drilled into the skull using a high-speed drill to expose the brain tissues underneath. A portion of the brain cortex was then cut using a biopsy punch device and subsequently removed using vacuum suction to create a cavity that was approximately 3 mm wide and 2 mm deep.

To facilitate the scaffold implantation process, the nanofibrous scaffolds (containing 10 mg blank NPs) were rolled and cut into cylinders of 2 mm wide and 2 mm tall. Following the implantation of the scaffold into the cavity, the wound was sutured, and the rats were allowed to awake without any further intervention. All rats became fully conscious and active between 1 and 2 h after surgery and did not display any sign of distress. In control rats, the same surgical procedure was also performed, but no scaffold was implanted. The study consisted of 6 rats, 3 implanted with scaffolds and 3 controls, and was intended for a short-term follow-up of 7 days.

2.10.2. *In vivo* MRI

MRI analysis was performed on days 1 and 7 with a Bruker Biospec 70/20 system operating at 7 T, under isoflurane (0.5% 1 L/min O2) anesthesia, with the monitoring of respiratory parameters. T2-weighted images were acquired with a multispin echo sequence [FOV = 35 x 35 mm, 7 axial 0.8 mm slices (gap = 0.3 mm), matrix 256 x 256, TR = 2 s, 25 TE = 8, 16, 24... 200 ms, one average]. The volume of the scaffolds was measured by manually drawing the region of interest on the generated T2 maps.

2.11. Statistical analysis

All data were expressed as the mean ± standard deviation of at least three experiments ($n \geq 3$). When applicable, one-way ANOVA with Dunnet's post-hoc test with a significance level of P equal to 0.05 was employed to detect any statistically significant difference existing between multiple data groups. In the figures, * indicates $P \leq 0.05$, ** indicates $P \leq 0.01$, *** indicates $P \leq 0.001$ and **** indicates $P \leq 0.0001$.

Results

3.1. Characterization of protein-loaded nanoparticles

Nanoparticles (NPs) were produced from PLGA and PEG-PLGA using a phase separation process to encapsulate the protein of interest. The synthesized NPs were mostly spherical (Figure 1) and uniform in size, as indicated by the low PDI values of the NP formulations (Table 1), regardless of the type of protein encapsulated. The slightly negative zeta-potential values can be explained by the presence of the hydrophilic PEG layer on the surface of the NPs that shields the negatively charged carboxyl groups carried by the hydrophobic PLGA forming the NP core (Haji Mansor et al., 2018). The NPs were also highly efficient in encapsulating lysozyme and SDF-1α (Table 1).

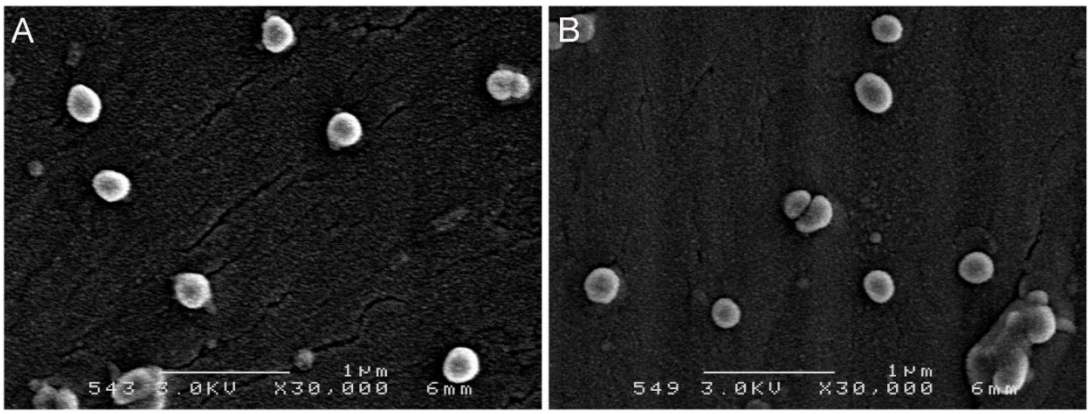

Figure 1. Scanning electron microscopy of (A) lysozyme-loaded and (B) SDF-1α-loaded nanoparticles.

Table 1. Average size, polydispersity index (PDI), zeta-potential (ZP) and encapsulation efficiencies of lysozyme-loaded and SDF-1α-loaded nanoparticle formulations.

Encapsulated protein	Average size (nm)[a]	Average PDI[a]	Average ZP (mV)[b]	Encapsulation efficiency (%)
Lysozyme	244 ± 11	0.14 ± 0.01	- 4.1 ± 0.7	96 ± 5
SDF-1α	238 ± 8	0.12 ± 0.01	- 3.5 ± 0.6	87 ± 5

[a] Purified nanoparticle dispersion was diluted to 100 µg/mL in deionized water prior to measurement

[b] Purified nanoparticle dispersion was diluted to 100 µg/mL in 0.01 M NaCl solution, and the pH was adjusted to pH 7 prior to measurement

3.2. Characterization of nanoparticle-containing nanofibrous scaffolds

3.2.1. Co-electrospinning of chitosan and protein-loaded nanoparticles

The electrospinning process produced flat scaffolds of approximately 40 µm thick after 165 min (Figure 2A). The presence of NPs in the scaffolds was initially confirmed using ATR-FTIR spectroscopy. ATR-FTIR spectra of scaffolds loaded with different concentrations of NPs revealed the presence of a peak at 1758 cm-1 (Figure 2B), which is characteristic of the ester bonds present in the PLGA component of the NP. In addition, as the NP load in the scaffolds was increased, the height of this peak increased proportionately (Figure 2B).

To gain an insight into the effect of different NP loads on the morphology of the electrospun nanofibers, SEM and TEM images of the scaffolds were recorded. SEM images revealed the presence of the NPs within the nanofibers as “bulges” that were visible along their lengths (Figure 2C), and these features became increasingly apparent as the NP load was increased from 4.0% w/w (5 mg of NPs) to 14.2% w/w (20 mg of NPs). Further observation using TEM confirmed the presence of spherical NPs within these “bulges” (Figure 2D). Interestingly, at the highest NP load tested (14.2% w/w), the nanofibers were found to be thinner (Table 2) and cut at random points (Figure 2 C&D, 20 mg NPs). Therefore, the maximum load of protein-loaded NPs in the nanofibrous scaffolds for further experiments was limited to 7.6% w/w (10 mg NPs per 121 mg chitosan-PEO mixture) to preserve good co-electrospinnability.

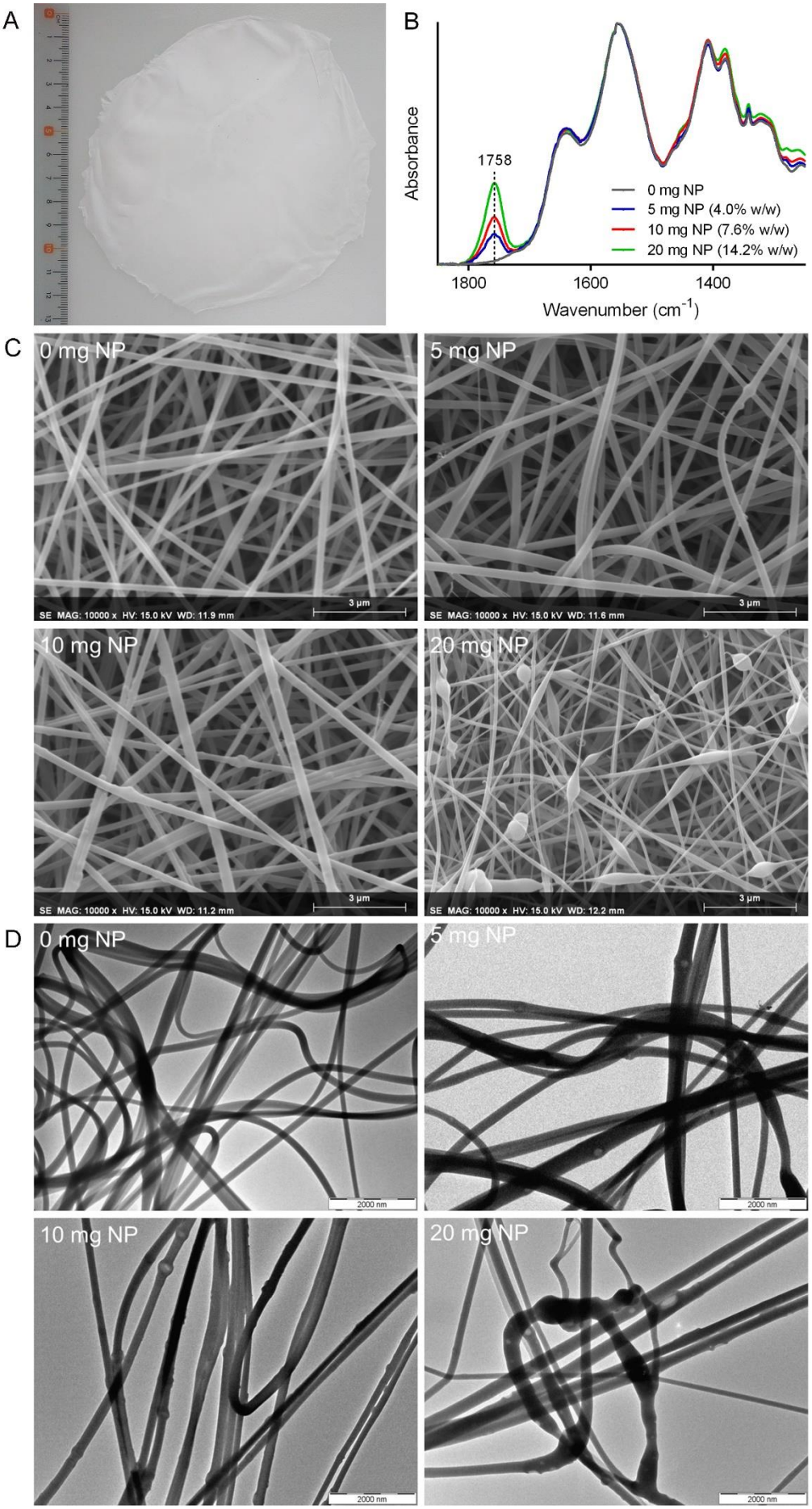
A
B
Absorbance
1758
0 mg NP
5 mg NP (4.0% w/w)
10 mg NP (7.6% w/w)
20 mg NP (14.2% w/w)
1800
1600
1400
Wavenumber (cm-1)
C
0 mg NP
5 mg NP
10 mg NP
20 mg NP
SE MAG: 10000 x HV: 15.0 kV WD: 11.9 mm
SE MAG: 10000 x HV: 15.0 kV WD: 11.6 mm
SE MAG: 10000 x HV: 15.0 kV WD: 11.2 mm
SE MAG: 10000 x HV: 15.0 kV WD: 12.2 mm
3 µm
D
0 mg NP
5 mg NP
10 mg NP
20 mg NP
2000 nm

Figure 2. Characterization of nanofibrous scaffolds (previous page). (A) An example of nanofibrous scaffolds produced from the electrospinning process. The scale placed on the left displayed length in centimeters. (B) ATR-FTIR spectra of nanofibrous scaffolds with different nanoparticle loads. For each spectrum, the absorbance values were normalized to their corresponding highest absorbance value, which was recorded at 1557 cm^{-1}, to permit height comparison of the peak at 1758 cm^{-1}. (C) SEM and (D) TEM micrographs of nanofibrous scaffolds with different nanoparticle loads.

Table 2. Fiber diameter of nanofibrous scaffolds with different nanoparticle loads.

Nanoparticle load	Fiber diameter before stabilization (nm)[a]	Fiber diameter after stabilization (nm)[a]
0 mg	249 ± 49	263 ± 42
5 mg (4.0% w/w)	244 ± 52	-
10 mg (7.6% w/w)	251 ± 46	261 ± 45
20 mg (14.0% w/w)	150 ± 43	-

[a] Only the parts of the nanofibers that were free of the "bulges" were measured

3.2.2. Stabilization of nanoparticle-containing nanofibrous scaffolds

To reduce the solubility of the developed electrospun scaffolds, a stabilization step was implemented. The changes in the composition of the NP-containing nanofibrous scaffolds after the stabilization step were investigated using ATR-FTIR spectroscopy (Figure 3A). The procedure successfully deprotonated the chitosan amino groups as evidenced by the appearance of a peak at 1592 cm^{-1}, which correlated to the N-H stretching of the NH_2 groups. The neutralization of the chitosan amino groups was accompanied by the disappearance of the peaks at 1557 and 1406 cm^{-1} originating from the asymmetric and symmetric stretching of the carboxylate component of acetate ions. In addition, the neutralization procedure increased the visibility of several chitosan characteristic peaks that were partially masked by the presence of the acetate ions. These include the trio of peaks at 1420, 1377 and 1322 cm^{-1} that represented CH_2 bending, CH_3 deformation and CH bending/CH_2 wagging respectively (Dong et al., 2001; Noriega and Subramanian, 2011). However, the peak at 1758 cm^{-1} that is characteristic of an ester bond as mentioned earlier remained visible after the stabilization procedure, suggesting that the PLGA/PEG-PLGA NPs were not significantly degraded by the 0.1 M NaOH neutralizing solution.

Using SEM, some degree of swelling can be observed in the stabilized nanofibers; however, the scaffold retained its overall nanofibrous morphology (Figure 3B).

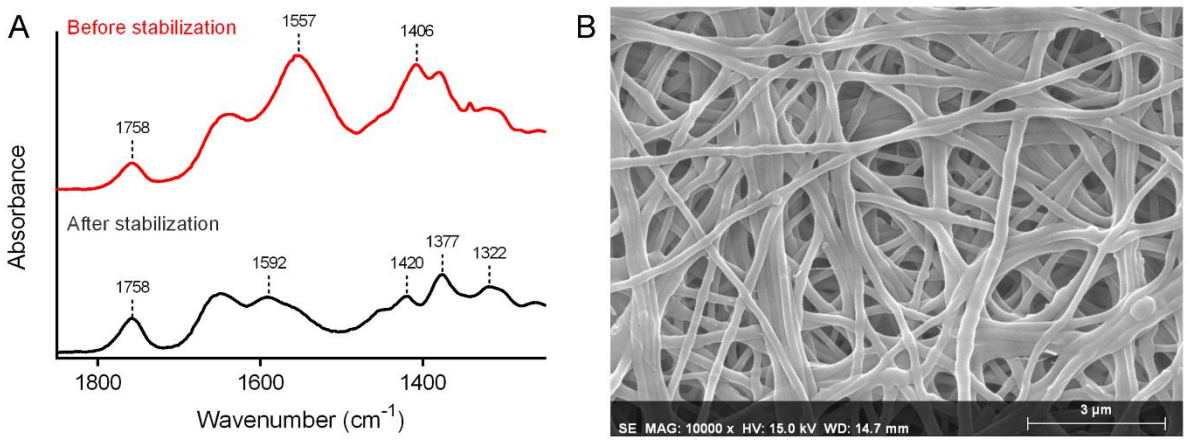

Figure 3. Scaffold stabilization. (A) ATR-FTIR spectra of a nanofibrous scaffold containing 10 mg NP load (7.6% w/w) before and after stabilization. (B) SEM micrograph of the stabilized NP-containing nanofibrous scaffold.

3.3. *In vitro* protein release study

3.3.1. *In vitro* lysozyme release

The release of lysozyme from (i) the lysozyme-loaded NPs, (ii) the nanofibrous scaffold loaded with unencapsulated lysozyme molecules and (iii) the lysozyme-loaded NPs incorporated into a nanofibrous scaffold is shown in Figure 4A. Consistent with our previous finding (Haji Mansor et al., 2018), a steep initial release curve that plateaued after 3 days was obtained in the first case (Figure 4A, black line). A similar release profile was also observed in the second case, indicating that a direct dispersion of lysozyme molecules within the nanofibrous scaffold did not prevent the huge initial burst release (Figure 4A, blue line). After only 6 h, 39% of the bioactive unencapsulated lysozyme load was released. Then, the release tailed off drastically between 6 and 120 h and became negligible thereafter. Interestingly, in the third case, a more sustained release profile was observed (Figure 4A, red line). The scaffold prepared with lysozyme-loaded NPs released only 11% of its bioactive encapsulated lysozyme load after 6 h. This was followed by a gradual release that persisted up to day 35, the last time point of evaluation.

3.3.2. *In vitro* SDF-1α release

SDF-1α release profiles were very similar to those observed with the model molecule lysozyme. The SDF-1α-loaded NPs and the nanofibrous scaffold loaded with unencapsulated SDF-1α (Figure 4B, black and blue lines, respectively) released most of their load steeply during the first three days of incubation and then leveled off with a negligible release after 5 days. In contrast, the nanofibrous scaffolds containing SDF-1α-loaded NPs provided a sustained release up to the last time point of evaluation, day 35 (Figure 4B, red line).

Having proved that a sustained release of the protein of interest was achieved, we then evaluated the biological activity of the released SDF-1α molecules using the agarose drop assay that we present next.

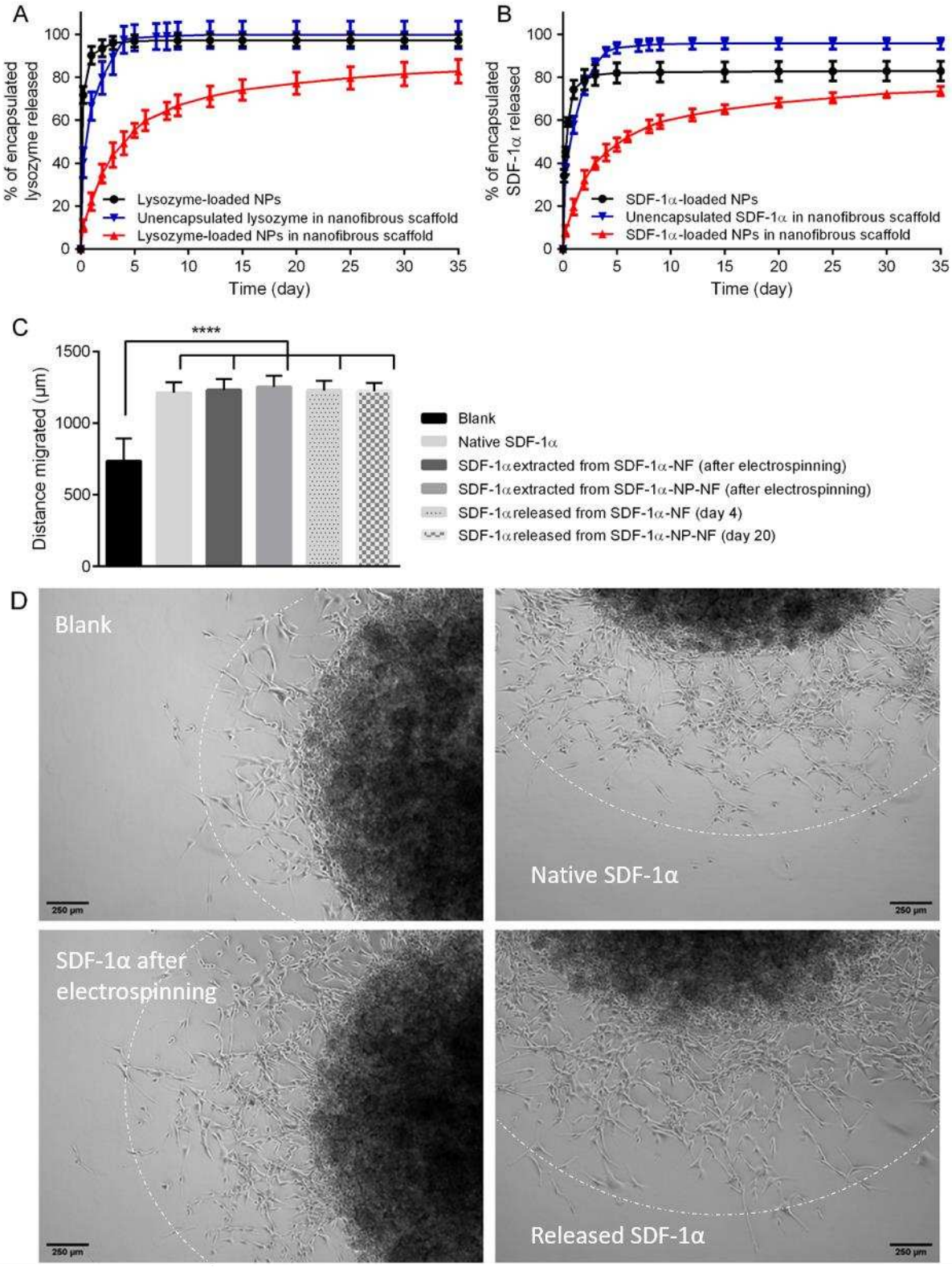

Figure 4. *In vitro* protein release study and evaluation of SDF-1α bioactivity. (A) Cumulative release of lysozyme with respect to the amount of bioactive lysozyme retrievable

from each sample (as quantified using the turbidity reduction assay). (B) Cumulative release of SDF-1α with respect to the amount of SDF-1α retrievable from each sample (as quantified using ELISA). (C) The distance of migration of CXCR4-expressing U87-MG cells induced by the SDF-1α-free medium (Blank), and medium supplemented with 40 ng/mL SDF-1α (native SDF-1α or those extracted just after electrospinning or released from nanofibrous scaffolds carrying either unencapsulated SDF-1α molecules (SDF-1α-NF) or SDF-1α-loaded nanoparticles (SDF-1α-NP-NF)). Statistical analysis was conducted to detect any significant difference ($P \leq 0.05$) between the multiple data groups; **** indicates $P \leq 0.0001$. (D) Representative images of CXCR4-expressing U87-MG cell-loaded agarose drops after 72-h incubation with SDF-1α-free medium (top left) or medium containing 40 ng/mL native SDF-1α (top right) or SDF-1α extracted after electrospinning (bottom left)/released (bottom right) from the nanofibrous scaffold containing SDF-1α-loaded NPs (day 20).

3.4. Evaluation of the biological activity of electrospun and released protein molecules

In order to differentiate the effect of the scaffold fabrication process that involves high voltage conditions and the possible protein denaturation during the incubation times in the protein release studies, the biological activity of the model protein lysozyme and of SDF-1α both extracted just after the electrospinning step was assessed concomitant with the SDF-1α molecules obtained from the release studies from nanofibrous scaffolds carrying either i) unencapsulated SDF-1α molecules or ii) SDF-1α-loaded NPs.

3.4.1. Effect of electrospinning on the biological activity of protein molecules

Using the turbidity reduction assay, 93 ± 6% of the lysozyme molecules extracted from the nanofibrous scaffolds containing lysozyme-loaded NPs remained biologically active. This fraction decreased to 58 ± 4% when the lysozyme molecules were directly mixed with chitosan prior to electrospinning, highlighting the importance of lysozyme encapsulation into the NPs on the preservation of its bioactivity. It was also confirmed that the denaturation of the unencapsulated lysozyme molecules occurred mainly during the electrospinning process and not during their extraction from the nanofibrous scaffold, as there was negligible loss in their biological activity after successive incubations in 1 M acetic acid solution, which was used to dissolve the chitosan/PEO nanofibers, and 1 M NaOH solution, which was the solvent for the PLGA/PEG-PLGA NPs.

To investigate whether SDF-1α was also susceptible to electrospinning-induced denaturation, nanofibrous scaffolds containing either unencapsulated SDF-1α molecules or SDF-1α-loaded NPs were prepared. Using ELISA, there was no difference in the percentage recovery of SDF-1α from both types of scaffolds (94 ± 5% and 92 ± 4% from scaffolds loaded with unencapsulated SDF-1α molecules and those containing SDF-1α-loaded NPs, respectively). When the biological activity of the recovered SDF-1α molecules were assessed using the agarose drop migration assay, the distance of migration of CXCR4-expressing U87-MG cells

induced by the SDF-1α molecules that were electrospun unencapsulated was similar to that induced by their encapsulated counterpart (Figure 4 C&D). In addition, no statistical difference was found as compared to the control drops incubated with native SDF-1α. These results suggest that SDF-1α was more resistant to electrospinning-induced denaturation than lysozyme.

3.4.2. Evaluation of the biological activity of the released SDF-1α

The bioactivity of the SDF-1α molecules released from the nanofibrous scaffolds was also assessed using the agarose drop migration assay. Release samples on day 4 from the nanofibrous scaffold loaded with unencapsulated SDF-1α molecules and on day 20 from the nanofibrous scaffold containing SDF-1α-loaded NPs were tested. These time points were chosen because the decrease in the release rate and the periodic refreshment of the release medium caused the amount of SDF-1α collected after these time points to be insufficient to achieve the optimal working concentration for the migration assay. SDF-1α molecules released from both scaffolds induced similar radial distances of CXCR4-expressing U87-MG cell migration compared to their pristine counterpart, and on average, a 1.8-fold increase in the radial cell migration distance relative to the negative control (Figure 4 C&D). This increase in radial distance corresponds to approximately $(R_2/R_1)^2 = 1.8^2 = 3.24$-fold increase in the area of cell migration compared to control drops, assuming circular areas. These results suggest that the biological activity of SDF-1α molecules was retained during the release process regardless of whether they were encapsulated into NPs or not.

3.5. Scaffold degradation study

The degradation of the nanofibrous scaffolds was assessed by monitoring the loss of scaffold mass throughout incubation in a buffer solution supplemented with chitosan-degrading lysozyme. The degradation profiles were similar regardless of whether the scaffolds were loaded with blank NPs or not (Figure 5A, red and blue lines, respectively). Despite losing over 10% of their original mass after 5 weeks of incubation (Figure 5A), the scaffolds retained their nanofibrous structure as observed under SEM (Figure 5B).

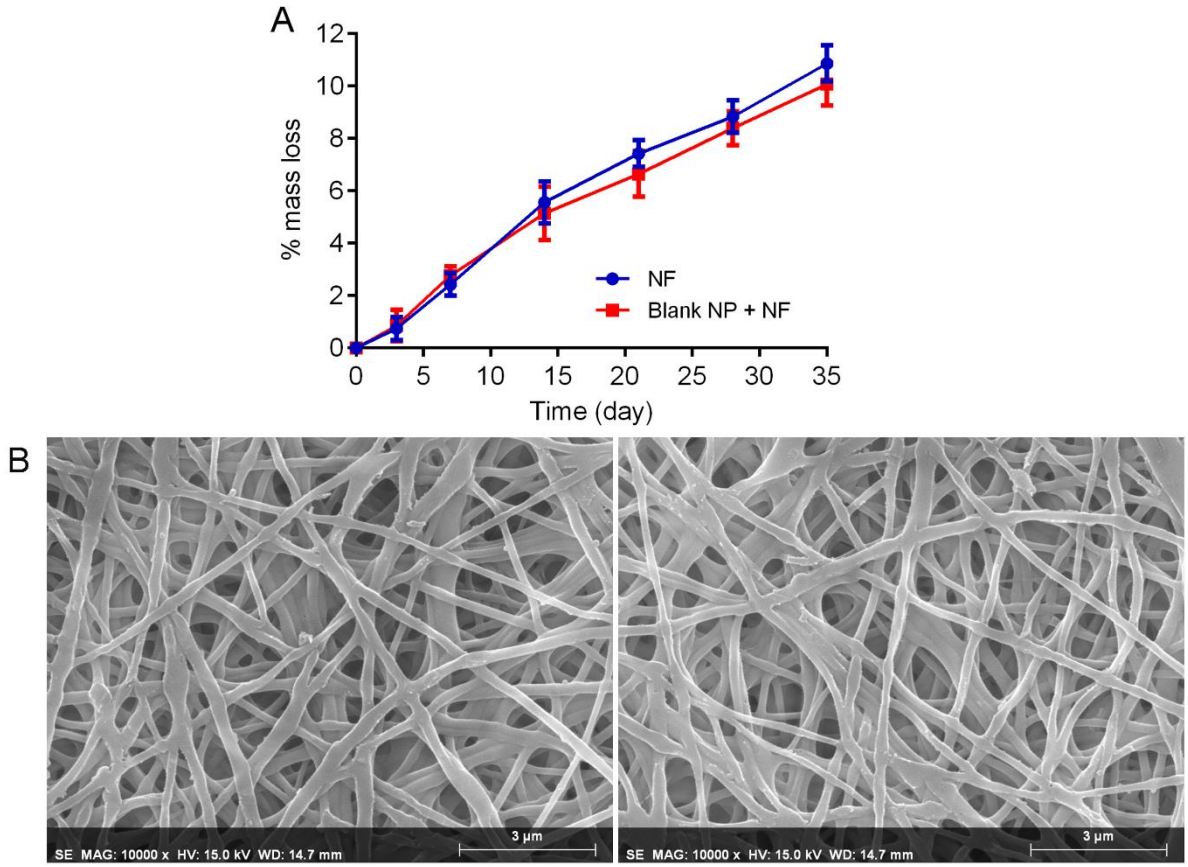

Figure 5. Degradability of scaffolds. (A) Percentage of original scaffold mass degraded with time of incubation in 0.05 M Tris-HCl buffer solution (pH 7.4) supplemented with 20 µg/mL lysozyme for the unloaded nanofibrous scaffolds (NF) and those loaded with 10 mg blank nanoparticles (Blank NP + NF). (B) SEM images of the unloaded nanofibrous scaffold (left) and the one loaded with 10 mg blank NP (right) after 5 weeks of incubation.

3.6. *In vitro* cytocompatibility and cell adhesion study

In order to evaluate the cytocompatibility of the nanofibrous scaffolds NIH3T3 mouse fibroblast cells were incubated with conditioned medium that contained leached products from nanofibrous scaffolds loaded with blank NPs or not, released after a 24-h incubation period. Results show that after a 24-h treatment of NIH3T3 cells with this conditioned medium, no cytotoxicity was observed (Figure 6A), indicating that the leached compounds from both scaffold types were well-tolerated, in the short term, by the NIH3T3 cells.

To further extend the evaluation of the scaffold cytocompatibility, different cell lines comprising NIH3T3 mouse fibroblasts, Thp-1 macrophages, and primary astrocytes were directly incubated with scaffold circular punches of 10 and 14 mm in diameter; the latter corresponding to the double area of the former. Regardless of the surface area, both types of nanofibrous scaffolds, loaded with blank NPs or not, presented a light effect on the viability of cells in the short 24-h incubation time. This effect on viability was decreasing on average as follows: NIH3T3 mouse fibroblasts (83%) < Thp-1 macrophages (89%) < primary astrocytes

(97%), for the nanofibers alone (NF, Figure 6B, 24 h); and, in the same cell order, 89% = 89% < 99%, for the nanofibers loaded with blank NPs (Blank NP + NF, Figure 6B, 24 h).

A similar trend was observed for the longer 72-h incubation period with results showing an average viability as follows: NIH3T3 mouse fibroblasts (74%) < Thp-1 macrophages (84%) < primary astrocytes (100%), for the nanofibers alone (NF, Figure 6B, 72 h); and, in the same cell order, 77% < 84% < 100%, for the nanofibers loaded with blank NPs (Blank NP + NF, Figure 6B, 72 h).

Finally, we evaluated the adhesion capacity of U87-MG cells on the nanofibrous scaffolds by depositing cells on top of scaffold sections for 4 h, followed by rinsing with PBS and incubation with routine culture medium for 24 h. Results showed that an average of 57 % of the cells adhered to both types of scaffolds, unloaded and NP loaded, relative to the control wells containing cells that adhered to the cell culture plastic surface (Figure 6C). Interestingly, the cells that attached to the scaffolds developed and extended their pseudopodia as observed in the SEM images in Figure 6D.

Figure 6. *In vitro* cytocompatibility and cell adhesion capacity of scaffolds (next page). (A) Indirect cytotoxicity: % viability of NIH3T3 cells treated for 24 h with conditioned medium containing leachables resulting from incubation with either unloaded nanofibrous scaffolds (NF) or those loaded with 10 mg blank nanoparticles (Blank NP + NF) normalized to the viability of cells treated with fresh medium (control). (B) Direct induced cytotoxicity: % viability of three different cell types including NIH3T3 mouse fibroblasts, Thp-1 macrophages and primary astrocytes that were cultivated in direct contact with scaffolds. Cells were incubated with either 79 or 154 mm^2 circular sections of unloaded nanofibrous scaffolds (NF) or those loaded with 10 mg blank nanoparticles (Blank NP + NF) for either 24 h or 72 h. % viability is relative to the control wells. (C) Absorbance at 450 nm proportional to the number of U87-MG cells attached to the control surface of the cell culture plate (CCP), NF and Blank NP + NF. Statistical analysis was conducted to detect any significant difference ($P \leq 0.05$) between the multiple data groups. * indicates $P \leq 0.05$. (D) SEM images showing the morphology of U87-MG cells attached to the surface of NF (left) and Blank NP + NF (right).

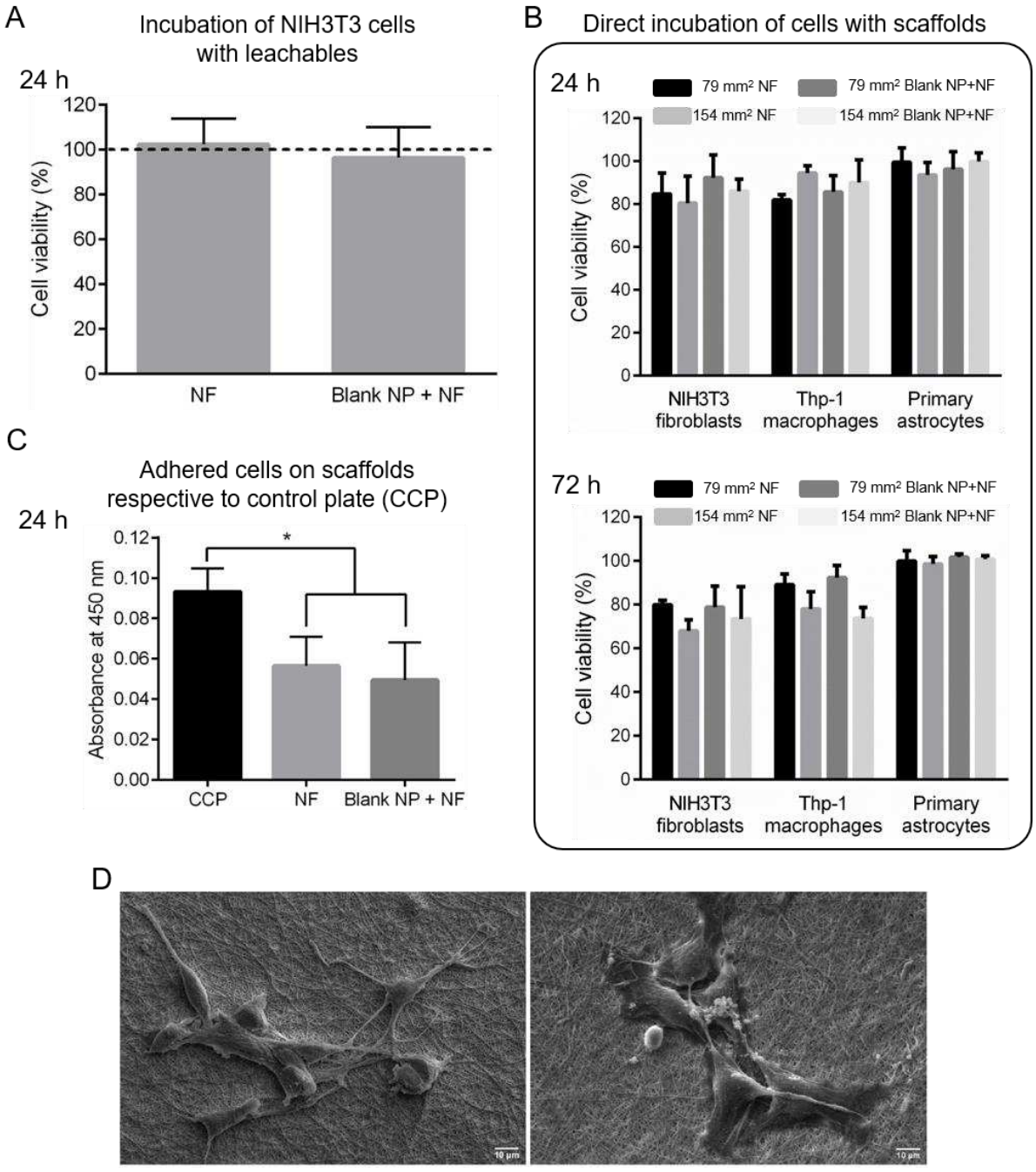

3.6. *In vivo* study

In order to assess the biocompatibility of the blank-NP-loaded nanofibrous scaffolds *in vivo*, they were implanted as compacted rolls in the brain of healthy Fischer rats as described in section 2.10.1 and Figure 7. All animals, those carrying implants and controls bearing only the resection cavities, did not show any signs of distress, just after recovering from the surgery, and afterwards, during the course of the 7-day study. In addition, by assessing the implant volume by IRM at 1 day and 7 days after implantation no difference was observed in the

calculated figures (Figure 7D). These results suggest an excellent biocompatibility and low degradation of scaffolds during the first week of treatment.

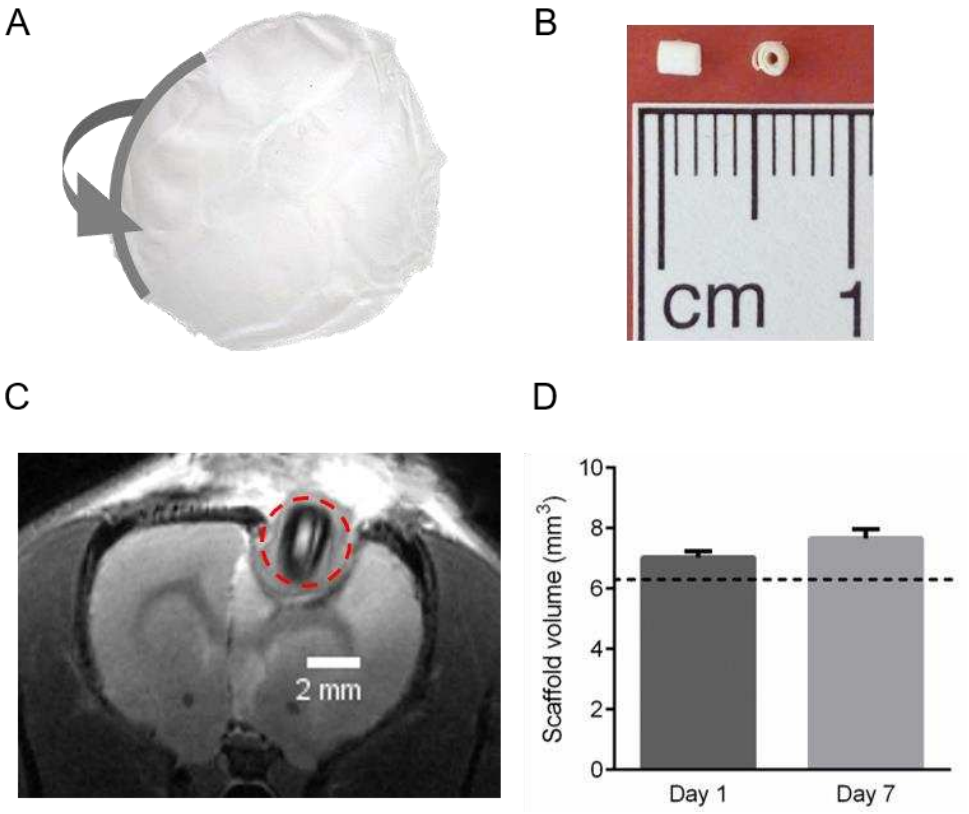

Figure 7. *In vivo* biocompatibility study. Nanofibrous scaffolds were rolled (A) and cut into compact cylinders of approximately 2 mm of height and 2 mm of diameter (B). Those rolled sections were then implanted in the resection cavity of healthy Fischer rats. The implanted scaffolds (C) were monitored by IRM 1 day and 7 days after implantation (only a representative MRI slice is shown). (D) Changes in the scaffold volume against the duration of implantation. The dotted line indicates the calculated dry volume of the scaffolds (6.3 mm^3). Paired t-test revealed no significant difference between the mean scaffold volume at day 1 and day 7 ($p = 0.10$).

Discussion

Chemokines such as SDF-1α can mobilize cancer cells from their respective primary tumor locations towards proximal or distant colonizable sites by making them migrate up the chemokine concentration gradient (Carmo et al., 2010; Katsura et al., 2018; Kim et al., 2006; Roccaro et al., 2014; Zagzag et al., 2008). The implantation of SDF-1α-secreting scaffolds therefore opens the possibility of trapping these cells for subsequent selective killing procedures. This approach is highly relevant for treating cancers capable of metastasis, as the SDF-1α-secreting scaffolds may divert the cancer cells away from their conventional metastatic niches and disrupt the natural cancer progression.

More importantly, for cancers with high rates of local relapse due to an incomplete primary tumor removal such as glioblastoma, the trapping strategy could be used to eradicate the residual cancer cells and therefore prevent tumor recurrence. Recently, it was reported that a chemoattractant-loaded membrane could attract glioblastoma cells *in vitro*, despite the presence of several limitations that might have impaired the trapping capacity of the device, including short duration of chemoattractant release (Autier et al., 2018). In the present work, we developed scaffolds capable of providing sustained release of SDF-1α in its bioactive form with excellent cytocompatibility and capacity to interact with human glioblastoma cells, which are intended for future implantation into the tumor resection cavity in the brain.

To achieve sustained SDF-1α release, the chemokine was encapsulated into biodegradable PLGA/PEG-PLGA nanoparticles (NPs), which were subsequently incorporated into nanofibrous scaffolds by electrospinning. Regarding the first step, the straightforward phase separation technique employed in this study yielded particles of mostly uniform shape and size that favored their incorporation into the nanofibrous scaffolds. For the subsequent electrospinning process, chitosan was the material of choice for synthesizing the nanofibrous scaffolds due to its unique physicochemical properties. As it is a weakly-basic polysaccharide, chitosan is insoluble in aqueous solutions of physiological pH. However, in dilute acid solutions such as 1 M acetic acid, the amino groups of chitosan are protonated, making the chitosan macromolecules soluble and thus feasible for electrospinning (Croisier and Jérôme, 2013; Rinaudo et al., 1999). In addition, the positively charged amino groups may have facilitated the interaction between the chitosan molecules and the negatively-charged SDF-1α-loaded NPs to ensure a successful co-electrospinning process. Nevertheless, the use of chitosan alone would not have permitted the generation of defect-free nanofibers under mild conditions (Dilamian et al., 2013; Geng et al., 2005; Kriegel et al., 2009; Ziani et al., 2011). Studies have shown that the strong electrostatic repulsion between positively-charged chitosan molecules prevents sufficient chain entanglement that is necessary for nanofiber formation (Min et al., 2004). Therefore, a small amount of high molecular weight PEO was added to the chitosan solution to promote chain entanglement by virtue of the formation of hydrogen bonds between the ether oxygen of PEO and the amino hydrogen of chitosan (Pakravan et al., 2011).

Up to a NP load of 10 mg (7.6% w/w), uniform nanofibers can be obtained at room temperature in the presence of PEO at a concentration of approximately 8.8% of the total PEO/chitosan mass in the electrospinning mixture (Figure 2). The requirement for such a low concentration of the biologically-inert PEO ensures that the electrospun scaffolds were predominantly characterized by the useful biological properties of chitosan, including excellent cancer cell adhesion (Dhiman et al., 2004) and slow biodegradation (Cunha-Reis et al., 2007), which was subsequently proven in our *in vitro* and *in vivo* studies. However, when the NP load was increased to 20 mg, beaded nanofibers of smaller diameter were produced (Figure 2 & Table 2). It was likely that the large number of negatively-charged NPs interacting with the positively-charged chitosan molecules reduced the hydrogen bond interactions and chain entanglement between the chitosan and PEO molecules, leading to the formation of thin fibers

with beaded morphology as reported in the literature (Kriegel et al., 2009). Despite this, we have shown that our electrospinning setup can ensure uniform incorporation of up to 10 mg of NPs into a nanofibrous scaffold made of 110 mg of chitosan and 11 mg of PEO. As long as this NP loading limit is not exceeded, the developed method can also produce uniform nanofibers capable of providing a robust anchoring platform that is suitable for the adhesion of glioblastoma cells.

After neutralizing the charged amino groups in the nanofibrous scaffolds to improve their stability in physiological media, we observed that scaffolds containing SDF-1α-loaded NPs can sustain the release of SDF-1α for a longer duration than SDF-1α-loaded NPs alone and scaffolds containing unencapsulated SDF-1α molecules (Figure 4B). This may be explained by a two-stepped process involved in the release of SDF-1α from the scaffolds containing SDF-1α-loaded NPs. SDF-1α molecules will have to first diffuse out of the NPs into the nanofibers before they could be released into the surrounding medium. The first stage of the diffusion process is likely to be rate-limiting as the positively-charged SDF-1α molecules will have to overcome their electrostatic interactions with the negatively-charged carboxyl groups of PLGA in the NPs (Balmert et al., 2015). These interactions can be disrupted by cations such as Na^+ (Pakulska et al., 2016) that were present at a physiologically-relevant concentration in the release medium on the condition that they first have to diffuse through the nanofiber to make contact with the NPs. Based on this assumption, it was not expected that SDF-1α release could be observed immediately after incubation in the release medium. A potential explanation for this observation is that some large NPs that were not completely embedded in the nanofibers, as visualized under SEM and TEM, were releasing part of their SDF-1α load immediately upon direct contact with the release medium. This stage of minimal burst release was then followed by the two-staged diffusion of SDF-1α from the NPs that were better embedded in the nanofibers as discussed above, contributing to gradual SDF-1α release.

As described earlier, the electrospinning step involves the use of high voltage to generate nanofibers. A strong electric field is needed to induce a repulsive force between the charged particles in a polymer solution to overcome the surface tension of the liquid that is necessary for the Taylor cone formation and subsequent fiber deposition on the collector plate (Ramakrishna et al., 2006). This harsh processing condition presents a significant barrier to the incorporation of protein molecules into electrospun scaffolds. Indeed, using lysozyme as a model protein, we observed that high voltage can denature more than 40% of the protein molecules that were electrospun directly without any prior encapsulation step. In contrast, the electrospinning process inflicted negligible loss of biological activity on lysozyme molecules that were pre-encapsulated into NPs. The protective effect of protein encapsulation may be explained by the immobilization of the protein molecules within the polymeric matrix of the NPs. In an electric field, dipole moments arising from individual domains within a protein molecule will be forced to align themselves along the applied field (Martin et al., 2018; Ojeda-May and Garcia, 2010; Ripoll et al., 2005). The movement of the polarized domains can alter the overall protein structure that may result in a loss of biological activity (Toschi et al., 2009;

Wang et al., 2014; Zhao and Yang, 2009), particularly for enzymes such as lysozyme with a sensitive substrate binding site (Bekard and Dunstan, 2013; Zhao and Yang, 2010). Differently, encapsulated lysozyme molecules have limited conformational mobility due to their steric and electrostatic interactions with the polymeric constituents of the NP, preventing them from undergoing structural changes that can compromise their enzymatic activity. However, we also observed that SDF-1α retained its biological activity after the electrospinning process regardless of whether it was encapsulated or not. Although it was not possible to accurately quantify the proportion of bioactive SDF-1α due to the semi-quantitative nature of the agarose drop migration assay, it is probable that SDF-1α is more resistant to electrospinning-induced denaturation than lysozyme. This could be due to the difference in the secondary structure of these two proteins. Based on the information from Protein Data Bank (PDB 1DPX; PDB 2KEE), lysozyme possesses seven helices as opposed to two of SDF-1α. Helical domains are characterized by large net dipole moments due to their unidirectionally-aligned peptide dipoles (Hol, 1985; Wada, 1976), making them very reactive to an external electric field. In fact, lysozyme has been reported to unfold irreversibly upon exposure to an electric field of a strength as low as 300 V m^{-1} (Bekard and Dunstan, 2013). Considering the much stronger electric field applied in this study, it is plausible that lysozyme unfolded more extensively than SDF-1α when these proteins were electrospun non encapsulated.

Having proved that the protein of interest remained active just after the electrospinning process, we evaluated the bioactivity of SDF-1α after releasing into a medium resembling physiological characteristic, using an agarose drop assay. As stated before, the evaluated media corresponded to samples collected at day 4 and day 20 for the unencapsulated-SDF-1α-loaded scaffolds and the SDF-1α-loaded NP-containing scaffolds, respectively. After those points, SDF-1α was too diluted to obtain adequate working concentrations of the chemoattractant as the media was refreshed periodically at the defined time points. Interestingly, in spite of 20 days of incubation at 37 °C for the scaffolds containing SDF-1α-loaded NPs, the chemoattractant capacity of SDF-1α remained unaltered as observed over the effect on the cell-migrated radial distances and areas (1.8-fold and 3.24-fold increase, respectively) relative to controls without chemoattractant (Figure 4 C&D). Based on these observations, the sustained release profile during the studied 5-week SDF-1α release period, together with the maintenance of the bioactivity of the released SDF-1α, are likely to provide a longer time window for glioblastoma cell trapping compared to the 2-day protein release duration achieved with the chemoattractant-loadable membranes developed by Autier and colleagues for a similar purpose (Autier et al., 2018).

To study the degradation of the nanofibrous scaffolds, lysozyme was the enzyme of choice as chitosan is hydrolyzed *in vivo* mainly via the action of this enzyme (Vårum et al., 1997). However, despite the exposure to lysozyme at a concentration comparable to the cerebrospinal fluid lysozyme levels of 1 – 14 µg/mL (Constantopoulos et al., 1976; Newman et al., 1974), the nanofibrous scaffolds remained mostly intact at the end of the degradation study (Figure 5). The slow degradation rate can be explained by the high degree of deacetylation (~80%) of

the chitosan used to prepare the scaffolds. As lysozyme degrades chitosan by targeting its acetylated residues (Sashiwa et al., 1990), the degradation rate generally decreases with an increasing degree of chitosan deacetylation (Freier et al., 2005; Ren et al., 2005). This slow degradation rate was also confirmed in the 7-day *in vivo* study, where the scaffolds volumes as assessed by MRI remained equal after 1 day and 7 days post-implantation. It is expected that the high stability of the scaffolds will be beneficial for holding the SDF-1α-loaded NPs in place during the gradual SDF-1α release process to permit the establishment of a local SDF-1α concentration gradient that is necessary for the chemotactic attraction of glioblastoma cells.

In addition, the scaffolds' nanofibrous feature was observed to be unaffected by their slow degradation rates (Figure 5B). It has been reported that surface structure significantly influences the extent of cell adhesion, and scaffolds with three-dimensional nanofibrous topography retain cancer cells to a greater degree than two-dimensional flat films (Du et al., 2011). As such, the robust nanofibrous structure suggests that our scaffolds can provide a cell-anchoring platform to retain the attracted glioblastoma cells until the subsequent killing step.

In our cell adhesion assay, U87-MG cells could spread well on the scaffold surface by extending their pseudopodia to maximize cell-scaffold interactions (Figure 6 C&D). However, there was minimal cell infiltration into the scaffolds due to the compact arrangement of the nanofibers. This dense structure resulted from the deposition of nanofibers over an aluminum sheet used as collector in the electrospinning process. This aspect may limit the GBM cell trapping capacity of the used electrospun scaffolds as cell migration requires matrix remodeling in pores of less than 7 μm^2 in size (Wolf et al., 2013). Indeed, cancer cells including gliomas (Hagemann et al., 2012) or other cell types within the tumor microenvironment (Kessenbrock et al., 2010) often express high levels of matrix metalloproteinases to digest ECM components such as collagen, fibronectin and laminin to facilitate their invasion into surrounding healthy tissues. Considering that chitosan is not a native constituent of the ECM, it is unlikely that cancer cells such as those of GBM can enzymatically degrade chitosan-based scaffolds to infiltrate these constructs. In spite of this, our results suggest strong adhesion of cells as they remained attached on the scaffolds following 3 PBS washes after only 4 h passed from cell seeding. Should it become necessary to increase cell infiltration into the scaffolds to ameliorate their cell trapping capacity, the electrospinning technique can be improved to decrease the fiber density, by using for example custom-made collectors (Blakeney et al., 2011) and/or post-electrospinning treatments (Lee et al., 2005; Wu and Hong, 2016).

Finally, we evaluated the cytocompatibility of the scaffolds *in vitro* and *in vivo*. The implemented direct contact method provides a more realistic *in vitro* scenario. For that case, regardless of the surface area, both types of nanofibrous scaffolds (with and without blank NPs) were not highly toxic on any of the three cell lines tested (Figure 6B). This result was not surprising considering the well-reported biocompatibility of chitosan-based constructs (Mayerberger et al., 2018; Saravanan et al., 2018; Toullec et al., 2021; Tyliszczak et al., 2017; Wang et al., 2018). At the 24-h limit, the lowest percentage viability recorded was 80% and

this value decreased to 68% at the 72-h limit. These figures were recorded when the larger-sized (154 mm^2) NP-free scaffolds were put into contact with NIH3T3 fibroblasts, which are known to be highly sensitive to chemical-induced toxicities (Xia et al., 2008). It is worth mentioning that among the three cell lines tested, the brain-resident primary astrocytes appeared to be the most resistant against any toxic effects of the scaffolds, with an average percentage viability of 99%. This observation provides early evidence for the safe use of the nanofibrous scaffolds in the brain.

Furthermore, slow-degrading chitosan scaffolds have also been reported to be more biocompatible than their fast-degrading counterparts due to the slower production of pro-inflammatory degradation products (Tomihata and Ikada, 1997). Therefore, the developed slow-degrading nanofiber scaffolds, coupled with the absence of cytotoxic leached compounds from the scaffolds observed in our cytocompatibility study (Figure 6A), may help to diminish the risk of an unfavorable immune or toxicological response during the several weeks of implantation period that will be necessary for maximizing the trapping of glioblastoma cells.

Lastly, we evaluated the biocompatibility of nanofibrous scaffolds *in vivo*. Flat electrospun chitosan scaffolds were rolled into cylinders before being implanted into the brain cortex. This approach increased the surface area for cell contact as cells may access the interior of the scaffolds by migrating from either the top or bottom of the construct. The absence of adverse effects on implanted rats during the 7-day evaluation period together with the slow biodegradability of scaffolds, encourage their use for their long-term evaluation. Overall, based on our results, the developed scaffolds may support prolonged duration of GBM cell trapping by acting as a stable reservoir for gradual SDF-1α release as well as by serving as a durable matrix to retain the recruited cells. The latter contribution is especially important as premature scaffold degradation may increase the risk of GBM cells being released back into the brain after their recruitment, which reduces the purpose of the scaffold to merely a “relay site”, instead of a trap, for the GBM cells.

Conclusion

This study reports on the successful development of a novel chitosan-based nanofibrous scaffolds containing SDF-1α-loaded PLGA-based NPs to achieve sustained release of SDF-1α while keeping stable for at least 5 weeks *in vitro*. The scaffolds were also stable for at least 1 week *in vivo*. The usability of such a composite polymeric vehicle for local delivery of protein molecules of similar physicochemical characteristics to SDF-1α should be explored. More importantly, as the scaffolds demonstrated excellent *in vitro* and *in vivo* cytocompatibility and capacity to support the adhesion of glioblastoma cells *in vitro*, it is justifiable to proceed to the *in vivo* assessment of their bioperformace as a tumor cell trap for residual glioblastoma cells.

Acknowledgements

Authors would like to thank R. Mallet and R. Perrot of the SCIAM (Common Service for Imaging and Microscopy Analysis, Angers, France) as well as V. Pitrebois and M. Dejeneffe of CERM for SEM and TEM analyses.

Disclosures

Authors have no conflict of interest to declare.

Funding

This work was supported by the "Institut National de la Santé et de la Recherche Médicale" (INSERM), the University of Angers, France; MINECO [SAF2017-83118-R], Agencia Estatal de Investigación (AEI) and Instituto de Salud Carlos III (ISCIII) [AC19/00067] Cofinanciado FEDER, Spain; and FEDER (FMF - Prostem) for the University of Liege (Liege, Belgium). It is also related to the regional programs Bioimplants for Bone Regeneration (BILBO) part of the BIOREGATE Research-Training-Innovation consortium (RFI), and NanoFar+ both supported by the French Région Pays-de-la-Loire; LabEx IRON "Innovative Radiopharmaceuticals in Oncology and Neurology" as part of the French government "Investissements d'Avenir" program; the INCa (Institut National du Cancer) MARENGO consortium "MicroRNA agonist and antagonist Nanomedicines for Glioblastoma treatment: from molecular programmation to preclinical validation" [Grant PL-BIO 2014-2020]; the MuMoFRaT project "Multi-scale Modeling & simulation of the response to hypo-Fractionated Radiotherapy or repeated molecular radiation Therapies" supported by La Région Pays-de-la-Loire and the Cancéropôle Grand-Ouest; and the French National Research Agency (ANR) under the frame of EuroNanoMed III (project GLIOSILK "Silk-fibroin interventional nano-trap for the treatment of glioblastoma") [grant ANR-19-ENM3-0003-01]. Muhammad Haji Mansor and Mathie Najberg were Ph.D. students involved in the EMJD (Erasmus Mundus Joint Doctorate) NanoFar program funded by the European Education and Culture Executive Agency (EACEA). Muhammad Haji Mansor and Rodolfo Molina-Pena were PhD fellows from the French "Ministère de l'Enseignement supérieur, de la Recherche et de l'Innovation" (MESRI), while Mathie Najberg received a fellowship from La Région Pays-de-la-Loire.

4.3. Unpublished results

4.3.1. Assessment of the pore diameter and porosity of electrospun fiber mats

The effect of nanoparticle load in the pore size distribution of the nanofibrous scaffolds was evaluated with DiameterJ by digital segmentation algorithms embedded in the plugin for ImageJ as described elsewhere (Hotaling et al., 2015). Briefly, 10 SEM images were taken for each of the conditions and batched for analysis. The best segmentations according to the standardized method were selected and the binary images were analyzed. Results were combined and histograms were plotted.

The mean pore area ranged from 0.20 to 0.38 μm^2, with the lowest mean pore size corresponding to the highest nanoparticle load. However, no linear correlation can be established between the mean pore area and the nanoparticle load of scaffolds (**Table 4.1**). By using violin plots, it can be observed that the pore area data for the different particle loads followed similar frequency distributions with most data points lying within the first two quartiles corresponding to pore areas < 0.5 μm^2 (**Fig. 4.1**). The average estimated porosity was 46% in the 2D image projections of the SEM images and was independent of the loading NPs concentration (**Table 4.1**).

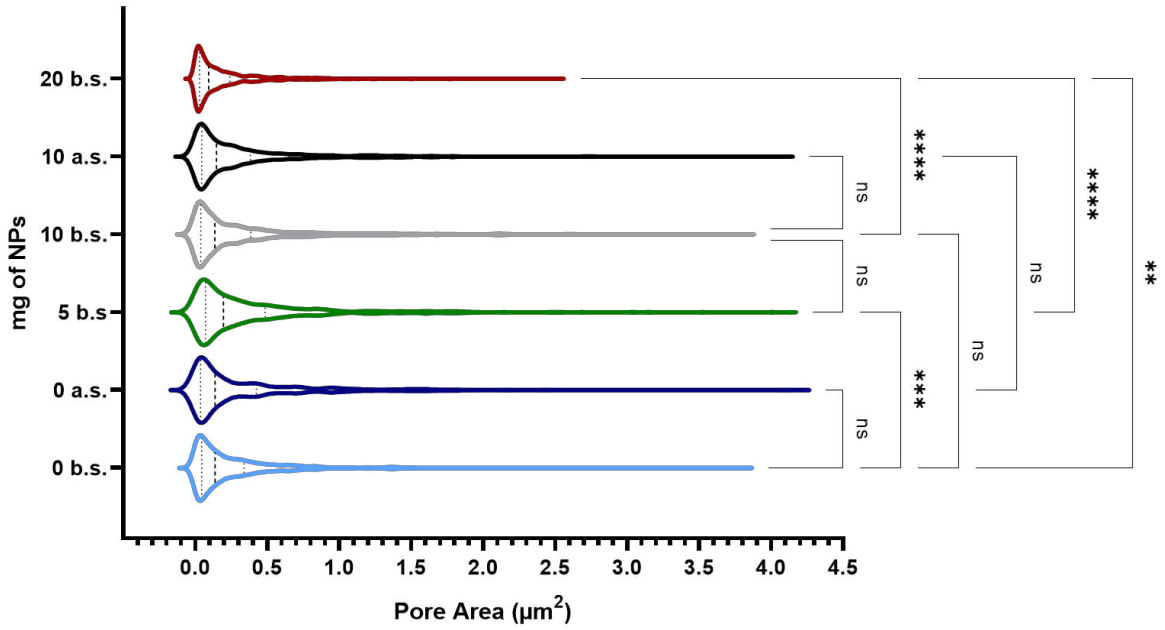

Figure 4.1. Pore Area of NP-loaded fibers before (b.s.) or after (a.s.) stabilization. Violin plots show the approximate distribution of the pore area data for the different nanoparticle (NP) loads. The middle vertical interrupted line on each plot represents the median, whereas the extreme vertical interrupted lines represent the limits of the two first quartiles. Only 0 and 10 mg of NP loads were evaluated after the stabilization step.

Table 4.1. Mean pore area and porosity of nanofibrous scaffolds with different nanoparticle loads.

Nanoparticle load	Before stabilization		After stabilization	
	Pore area $(\mu m)^2$	Porosity (%)	Pore area $(\mu m)^2$	Porosity (%)
0 mg	0.27 ± 0.40	48 ± 3.0	0.33 ± 0.49	45 ± 3.0
5 mg (4.0% w/w)	0.38 ± 0.53	47 ± 5.0		
10 mg (7.6% w/w)	0.32 ± 0.48	48 ± 2.0	0.33 ± 0.48	43 ± 3.0
20 mg (14.0% w/w)	0.20 ± 0.29	47 ± 4.0		

[a] The statistical analysis is shown in Figure 4.1.

[b] Non-significant difference between the mean porosities of all conditions.

The dispersion corresponds to the SD.

4.3.2. *In vivo* scaffold's biodegradability and histological analysis

The stability of chitosan scaffolds was evaluated *in vivo* by the implantation of scaffolds in the resection cavities as described in materials and methods (Section 4.2.1). The scaffolds remained in the same place at 5, 75, and 110 days of evaluation (**Fig. 4.2-A**), with no apparent alteration of the volume. Moreover, the structure of the rolled mats was maintained after 7 (**Fig. 4.2-B**) and 118 days of implantation (**Fig. 4.2-C**). No cell infiltration was observed in the zones where the rolled scaffolds were tightly compacted leaving not enough space for cells to navigate through these zones (**Fig. 4.2-C-i**). Although no scoring was performed, the histological pictures show an acute inflammatory reaction on day 7, as observed by the numerous polymorphonuclear (PMN) cells and macrophages recruited within the scaffold's walls, the cavity space, and the resection cavity borders (**Fig. 4.2-B**). The acute foreign body reaction was lessened to chronic inflammation with reduced presence of PMN cells and macrophages (**Fig. 4.2-C**). The inflammation was more marked at the resection edges and the zones of direct contact with the implant. However, the contralateral hemispheres showed a normal appearance, equal to control resections without scaffold implantation (data not shown). The presence of scar tissue was observed on day 118 with fibroblasts lying on the collagen fibers as observed in **Fig. 4-2-C-ii**.

Figure 4.2 (next page). *In vivo* biocompatibility and biodegradability of chitosan scaffolds.

A) MRI scans of brains with implanted scaffolds containing blank nanoparticles (NPs). B) and C) Characterization of the *in vivo* cellular response to implanted scaffolds containing blank NPs in the rat brain cortex after 7 and 118 days after implantation, respectively. B) Histological hematoxylin, phloxin, and saffron (HPS) staining (nuclei: violet/purple; cytoplasm: pink, scaffold: red) 7 days post-implantation. B-i) In this image, the implanted scaffold appears rolled with open spaces allowing cell infiltration. There was an acute inflammatory response with the presence of abundant polymorphonuclear cells (PMNC) in the three zones including the resection cavity border (B-ii), the cavity space (B-iii), and within the walls of the rolled scaffold (B-iv). Macrophages can be observed in the interrupted-line frame in (ii). C) Histological hematoxylin, phloxin, and saffron (HPS) staining (nuclei: violet/purple; cytoplasm: pink, scaffold: red, collagen: light pink) 118 days post-implantation. C-i) The scaffold came out of the cavity during slicing and is shown separated from the corresponding implanted brain zone in (C-iii). There was a local chronic inflammatory response with the presence of a scar with fibrotic tissue containing fibroblasts surrounding the scaffold (*) as shown in (C-ii). The right panels are a magnification of the contoured regions.

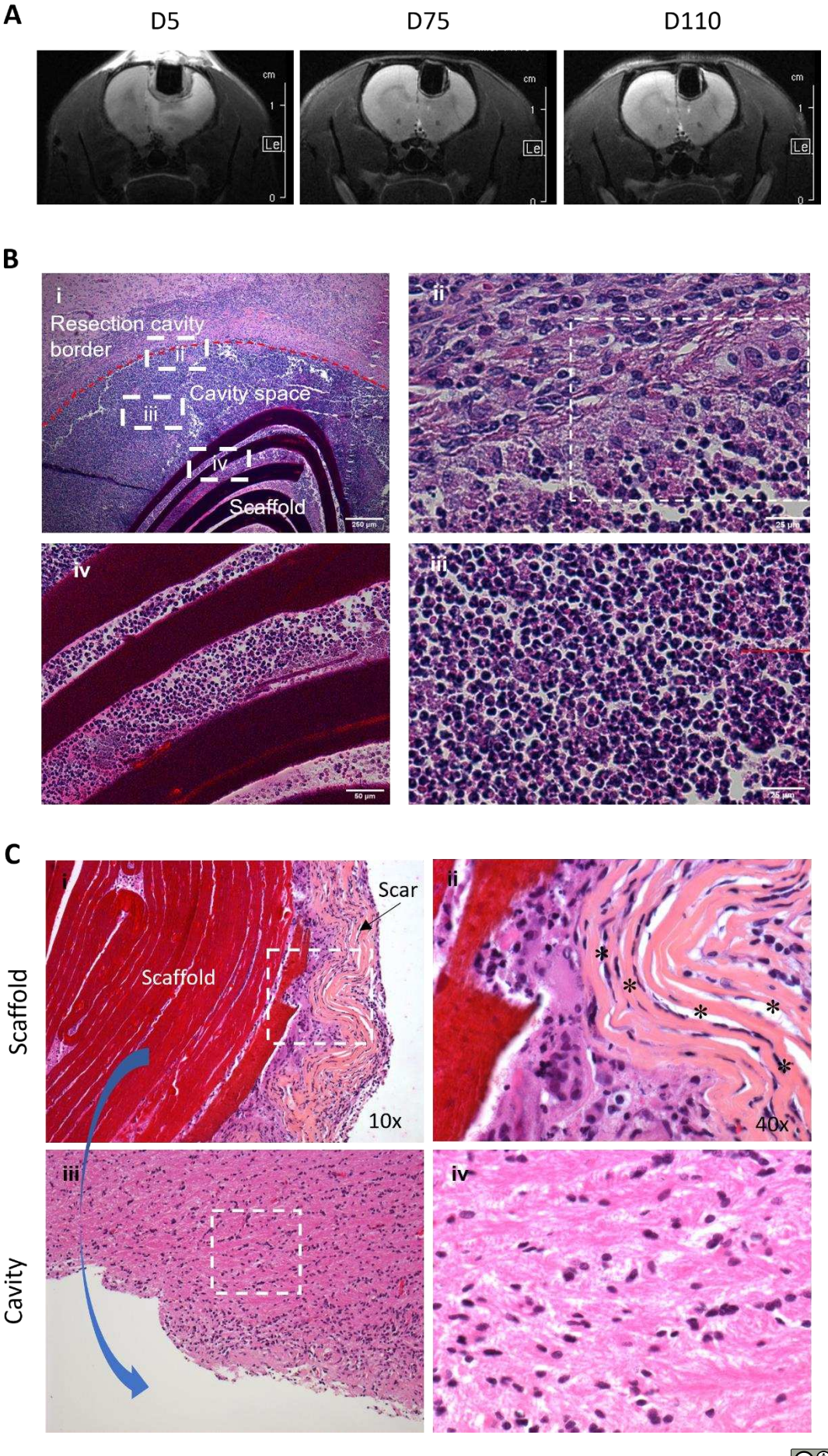
A
D5
D75
D110
B
i
Resection cavity border
ii
Cavity space
iii
iv
Scaffold
ii
iv
iii
C
Scaffold
Cavity
i
Scar
Scaffold
10x
ii
40x
iii
iv

4.3.3. Qualitative observations of U87MG-CXCR4+ cell alignment

To observe the behavior of the used model cell line U87MG-CXCR4+, cells were plated in different surfaces that were modified physically either by scratching with a pipette tip or by grooving with a scalpel, or by coating with collagen that was deposited in an aligned fashion by a one-directional movement with a cell scrapper. Empirical results showed that U87MG-CXCR4+ cells preferred aligned paths in the used culture conditions with reduced serum medium (**Fig. 4.2**).

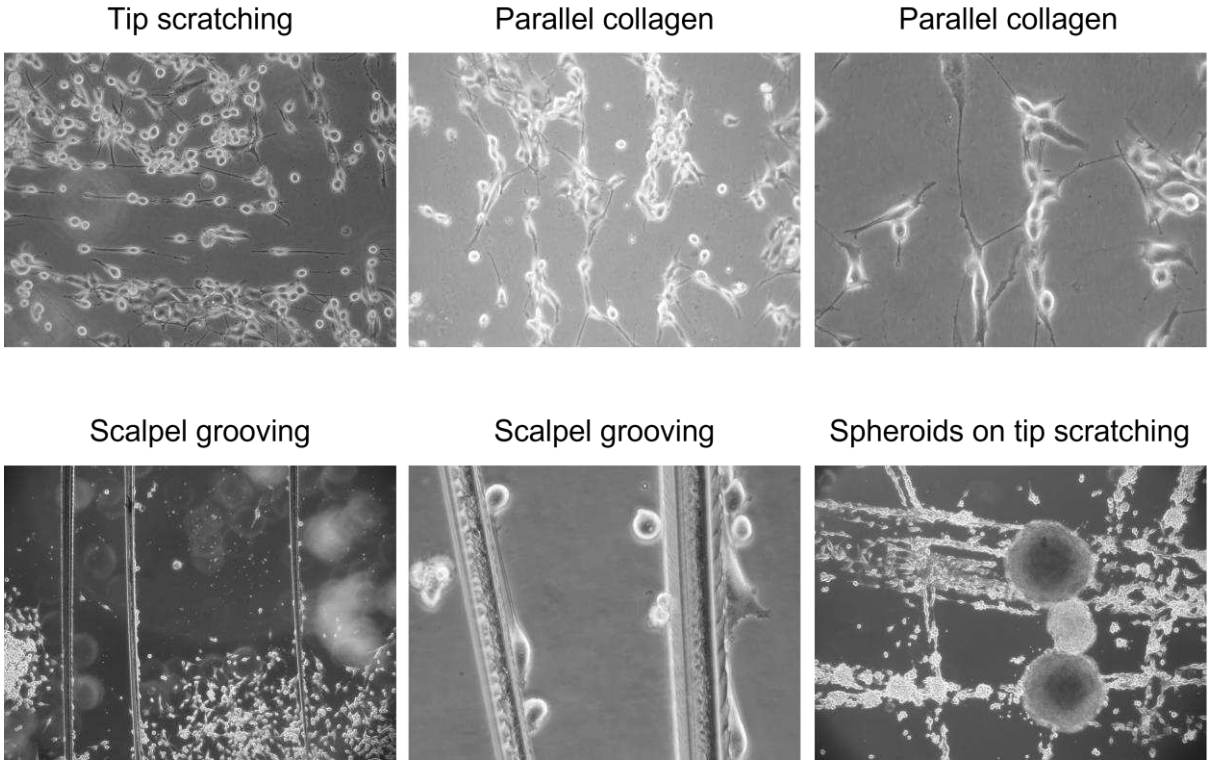

Figure 4.3. Effect of surface modification on the pattern of cell attachment and migration of U87MG-CXCR4+ cells. Tip scratching: cells were left in culture up to 80% confluence, followed by scratching using a 200 µL-pipette tip and culturing in serum-free medium for 24 h. Parallel collagen: a collagen solution in PBS was dispersed with one-direction forward movement using a cell scrapper, followed by drying and seeding of cells. A higher magnification image is shown to the right. Scalpel grooving: the culture plate was grooved using a scalpel, followed by deposition of a drop of a concentrated cell suspension in one extreme of the seeding surface, cells were left to adhere for 2 h, followed by deposition of 1%-FBS DMEM, and incubated for 48h. A higher magnification image is shown to the right. Spheroids on tip scratching: U87MG-CXCR4+ spheroids were induced for 7 days in a spheroid-defined medium, after this they were cultured on a tip-scratched culture surface for 48h in 1%-FBS DMEM.

4.4. Discussion of Chapter 4

In this chapter, the physicochemical characterization, *in vitro* evaluation in terms of cytocompatibility, cell adhesion capacity, and the activity of the released SDF-1α have been performed. The main findings highlight that the *in vitro* releasing profile was improved by the incorporation of SDF-1α-loaded NPs into electrospun fibers and that the released SDF-1α was bioactive as assessed by using an agarose drop assay. Importantly, the sustained release of SDF-1α was maintained for around a month, which might offer opportunities in the *in vivo* context to maintain a chemoattractant gradient. *In vivo*, the assessment of biocompatibility and biodegradability was done by the implantation of fiber mats as rolled pieces that were inserted into the resection cavities of Fisher rats. The scaffolds remained intact after up to 4 months of implantation. This structural stability can potentially make available a cell adhesion surface for cells within the resection cavity, as demonstrated by the good *in-vitro* adherence capacity of GB cells. However, the formation of scar tissue as evaluated on day 118, may create a barrier for cell migration and recruitment from the periphery, and the performance of the scaffold as a tumor cell trap could be reduced. This kind of tissue reaction has been observed in non-degradable matrices as reported by Autier et al. in the context of a cellulose matrix as a glioblastoma cell trap (Autier et al., 2018). On the other hand, Alonso-Alconada et al. determined that the foreign body reaction, which also induced collagen deposition, contributed to the formation of a premetastatic niche to trap ovarian cancer cells in a murine model of metastatic ovarian cancer implanted with the non-absorbable M-Trap device (Alonso-Alconada et al., 2020). Therefore, a trade-off may exist that suggests further exploration of chitosan scaffolds.

Although the method used for the determination of the pore size and porosity is an estimate based on 2D images, it was evident that the pore size was in the order of the submicron scale, as can be observed in **Fig. 6D** of the published manuscript, in which cells and mats can be seen growing on the fibrous mats. Therefore, such films may offer a surface but not a 3D environment to home cancer cells. Despite this, the interspaces in rolled films may serve as sites for cancer cell deposits. However, from the *in vivo* histological analysis, it was shown that if the spaces between the walls of the rolled mats were too tight, this resulted in reduced, or no infiltration of immune and resident cells as shown in **Fig. 4.2** of the unpublished results. Moreover, the formation of the contouring fibrotic tissue may reduce the ability of the scaffold to recruit cancer cells. The time point of evaluation might be critical considering that the scar is gradually formed. Therefore, different time points should be included when the assessment of the trapping capacity is performed.

The bioperformance evaluation of the developed chitosan fiber mats as cancer cell traps has not been accomplished here. Although these scaffolds in the present form do not offer an adequate pore size and interconnected pore network, their function as a chemokine reservoir with sustained release would be interesting to evaluate, first *in vitro* using the under-agarose assay and *in vivo* using our developed model with the placement of cells at different distances.

Interestingly, Jain et al. (2014) developed aligned PCL fibers as films that were placed orthogonal to GB tumors by using gel support (Jain et al., 2014). This type of conduit guided GB cells extra-cortically, which highlights that GB cells are likely to follow aligned paths. This was observed here for the case of U87MG-CXCR4+ cells, that migrated and grew preferentially in aligned paths as shown in **Fig. 4.3** (unpublished results). Therefore, it would be interesting to reproduce such experiments using aligned fibers with a gradient of SDF-1α-loaded NPs.

In addition, the scaffolds, as durable as they were, and providing a sustained release of therapeutics, could be used as a platform for other strategies such as immunomodulation, differentiation of glioma stem cells, radio-sensitization, and chemotherapy. From the point of view of medical devices, the safety of this scaffold could be an asset as it is composed of approved biomaterials, and more importantly, the fate of NPs can be controlled as they are embedded within the nanofibers.

4.5. Conclusion of Chapter 4

Electrospun chitosan fibers containing SDF-1α-loaded NPs are an excellent biocompatible device for sustained release of the active chemokine. However, their bioperformance evaluation as a cancer cell trap remains to be explored. The formation of fibrotic tissue may reduce or hamper its bioperformance. Opportunities might exist by adapting this system with aligned fibers, therefore, offering a double function as a chemoattract releasing device and structural guidance scaffold. The release of other molecules such as immunomodulators, radio-sensitizers, and differentiation and chemotherapeutics agents might also be explored.

4.6. References

Almouazen, E., Bourgeois, S., Boussaïd, A., Valot, P., Malleval, C., Fessi, H., Nataf, S., Briançon, S., 2012. Development of a nanoparticle-based system for the delivery of retinoic acid into macrophages. International Journal of Pharmaceutics 430, 207–215. https://doi.org/10.1016/j.ijpharm.2012.03.025

Alonso-Alconada, L., de la Fuente, A., Santacana, M., Ferreiros, A., Lopez-Lopez, R., Matias-Guiu, X., Abal, M., 2020. Biomimetic device and foreign body reaction cooperate for efficient tumour cell capture in murine advanced ovarian cancer. Dis Model Mech 13, dmm043653. https://doi.org/10.1242/dmm.043653

Autier, L., Clavreul, A., Cacicedo, M.L., Franconi, F., Sindji, L., Rousseau, A., Perrot, R., Montero-Menei, C.N., Castro, G.R., Menei, P., 2018. A new glioblastoma cell trap for implantation after surgical resection. Acta Biomaterialia 84, 268–279. https://doi.org/10.1016/j.actbio.2018.11.027

Balmert, S.C., Zmolek, A.C., Glowacki, A.J., Knab, T.D., Rothstein, S.N., Wokpetah, J.M., Fedorchak, M. V., Little, S.R., 2015. Positive charge of "sticky" peptides and proteins impedes release from negatively charged PLGA matrices. Journal of Materials Chemistry B 3, 4723–4734. https://doi.org/10.1039/c5tb00515a

Bekard, I., Dunstan, D.E., 2013. Electric field induced changes in protein conformation. Soft Matter 10, 431–437. https://doi.org/10.1039/C3SM52653D

Blakeney, B.A., Tambralli, A., Anderson, J.M., Andukuri, A., Lim, D.-J., Dean, D.R., Jun, H.-W., 2011. Cell infiltration and growth in a low density, uncompressed three-dimensional electrospun

nanofibrous scaffold. Biomaterials 32, 1583–1590. https://doi.org/10.1016/j.biomaterials.2010.10.056

Carmo, A. do, Patricio, I., Cruz, M.T., Carvalheiro, H., Oliveira, C.R., Lopes, M.C., 2010. CXCL12/CXCR4 promotes motility and proliferation of glioma cells. Cancer Biology & Therapy 9, 56–65. https://doi.org/10.4161/cbt.9.1.10342

Constantopoulos, A., Antonakakis, K., Matsaniotis, N., Kapsalakis, Z., 1976. Spinal Fluid Lysozyme in the Diagnosis of Central Nervous System Tumours. Neurochirurgia 19, 169–171. https://doi.org/10.1055/s-0028-1090407

Croisier, F., Jérôme, C., 2013. Chitosan-based biomaterials for tissue engineering. European Polymer Journal, Biobased Polymers and Related Materials 49, 780–792. https://doi.org/10.1016/j.eurpolymj.2012.12.009

Cunha-Reis, C., Tuzlakoglu, K., Baas, E., Yang, Y., Haj, A. El, Reis, R.L., 2007. Influence of porosity and fibre diameter on the degradation of chitosan fibre-mesh scaffolds and cell adhesion. Journal of Materials Science: Materials in Medicine 18, 195–200. https://doi.org/10.1007/s10856-006-0681-x

De La Luz Sierra, M., Yang, F., Narazaki, M., Salvucci, O., Davis, D., Yarchoan, R., Zhang, H.H., Fales, H., Tosato, G., 2004. Differential processing of stromal-derived factor-1alpha and stromal-derived factor-1beta explains functional diversity. Blood 103, 2452–2459. https://doi.org/10.1182/blood-2003-08-2857

Deng, J., Zou, Z.M., Zhou, T.L., Su, Y.P., Ai, G.P., Wang, J.P., Xu, H., Dong, S.W., 2011. Bone marrow mesenchymal stem cells can be mobilized into peripheral blood by G-CSF in vivo and integrate into traumatically injured cerebral tissue. Neurological Sciences 32, 641–651. https://doi.org/10.1007/s10072-011-0608-2

Dhiman, H.K., Ray, A.R., Panda, A.K., 2004. Characterization and evaluation of chitosan matrix for in vitro growth of MCF-7 breast cancer cell lines. Biomaterials 25, 5147–5154. https://doi.org/10.1016/j.biomaterials.2003.12.025

Dilamian, M., Montazer, M., Masoumi, J., 2013. Antimicrobial electrospun membranes of chitosan / poly (ethylene oxide) incorporating poly (hexamethylene biguanide) hydrochloride. Carbohydrate Polymers 94, 364–371. https://doi.org/10.1016/j.carbpol.2013.01.059

Dong, Y., Xu, C., Wang, J., Wang, M., Wu, Y., Ruan, Y., 2001. Determination of degree of substitution for N-acylated chitosan using IR spectra. Science in China, Series B: Chemistry 44, 216–224. https://doi.org/10.1007/BF02879541

Du, J., Che, P.L., Wang, Z.Y., Aich, U., Yarema, K.J., 2011. Designing a binding interface for control of cancer cell adhesion via 3D topography and metabolic oligosaccharide engineering. Biomaterials 32, 5427–5437. https://doi.org/10.1016/j.biomaterials.2011.04.005

Du, L., Yang, S., Li, W., Li, H., Feng, S., Zeng, R., Yu, B., Xiao, L., Nie, H.Y., Tu, M., 2017. Scaffold composed of porous vancomycin-loaded poly(lactide-co-glycolide) microspheres: A controlled-release drug delivery system with shape-memory effect. Materials Science and Engineering C 78, 1172–1178. https://doi.org/10.1016/j.msec.2017.04.099

Freier, T., Koh, H.S., Kazazian, K., Shoichet, M.S., 2005. Controlling cell adhesion and degradation of chitosan films by N-acetylation. Biomaterials 26, 5872–5878. https://doi.org/10.1016/j.biomaterials.2005.02.033

Frohbergh, M.E., Katsman, A., Botta, G.P., Lazarovici, P., Schauer, C.L., Wegst, U.G.K., Lelkes, P.I., 2012. Electrospun hydroxyapatite-containing chitosan nanofibers crosslinked with genipin for bone tissue engineering. Biomaterials 33, 9167–9178. https://doi.org/10.1016/j.biomaterials.2012.09.009

Geng, X., Kwon, O.H., Jang, J., 2005. Electrospinning of chitosan dissolved in concentrated acetic acid solution. Biomaterials 26, 5427–5432. https://doi.org/10.1016/j.biomaterials.2005.01.066

Gentile, P., Nandagiri, V.K., Pabari, R., Daly, J., Tonda-Turo, C., Ciardelli, G., Ramtoola, Z., 2015. Influence of parathyroid hormone-loaded plga nanoparticles in porous scaffolds for bone regeneration. International Journal of Molecular Sciences 16, 20492–20510. https://doi.org/10.3390/ijms160920492

Hagemann, C., Anacker, J., Ernestus, R.-I., Vince, G.H., 2012. A complete compilation of matrix metalloproteinase expression in human malignant gliomas. World J Clin Oncol 3, 67–79. https://doi.org/10.5306/wjco.v3.i5.67

Haji Mansor, M., 2019. Functionalized polymer implants for the trapping of glioblastoma cells (Doctoral Thesis). Univerité d'Angers.

Haji Mansor, M., Najberg, M., Contini, A., Alvarez-Lorenzo, C., Garcion, E., Jérôme, C., Boury, F., 2018. Development of a Non-toxic and Non-denaturing Formulation Process for Encapsulation of SDF-1α into PLGA/PEG-PLGA Nanoparticles to Achieve Sustained Release. European Journal of Pharmaceutics and Biopharmaceutics 125, 38–50. https://doi.org/10.1016/j.ejpb.2017.12.020

Hamoudeh, M., Salim, H., Barbos, D., Paunoiu, C., Fessi, H., 2007. Preparation and characterization of radioactive dirhenium decacarbonyl-loaded PLLA nanoparticles for radionuclide intra-tumoral therapy. European Journal of Pharmaceutics and Biopharmaceutics 67, 597–611. https://doi.org/10.1016/j.ejpb.2007.04.003

Hassani, L.N., Hindré, F., Beuvier, T., Calvignac, B., Lautram, N., Gibaud, A., Boury, F., 2013. Lysozyme encapsulation into nanostructured CaCO3 microparticles using a supercritical CO2 process and comparison with the normal route. Journal of Materials Chemistry B 1, 4011–4019. https://doi.org/10.1039/c3tb20467g

He, Q., Ao, Q., Gong, Y., Zhang, X., 2011. Preparation of chitosan films using different neutralizing solutions to improve endothelial cell compatibility. Journal of Materials Science: Materials in Medicine 22, 2791–2802. https://doi.org/10.1007/s10856-011-4444-y

Hol, W.G.J., 1985. The role of the α-helix dipole in protein function and structure. Progress in Biophysics and Molecular Biology 45, 149–195. https://doi.org/10.1016/0079-6107(85)90001-X

Hotaling, N.A., Bharti, K., Kriel, H., Simon, C.G., 2015. DiameterJ: A validated open source nanofiber diameter measurement tool. Biomaterials 61, 327–338. https://doi.org/10.1016/j.biomaterials.2015.05.015

Huang, Z.M., Zhang, Y.Z., Kotaki, M., Ramakrishna, S., 2003. A review on polymer nanofibers by electrospinning and their applications in nanocomposites. Composites Science and Technology 63, 2223–2253. https://doi.org/10.1016/S0266-3538(03)00178-7

Jain, A., Betancur, M., Patel, G.D., Valmikinathan, C.M., Mukhatyar, V.J., Vakharia, A., Pai, S.B., Brahma, B., MacDonald, T.J., Bellamkonda, R.V., 2014. Guiding intracortical brain tumour cells to an extracortical cytotoxic hydrogel using aligned polymeric nanofibres. Nature Mater 13, 308–316. https://doi.org/10.1038/nmat3878

Jin, F., Zhai, Q., Qiu, L., Meng, H., Zou, D., Wang, Y., Li, Q., Yu, Z., Han, J., Li, Q., Zhou, B., 2008. Degradation of BM SDF-1 by MMP-9: The role in G-CSF-induced hematopoietic stem/progenitor cell mobilization. Bone Marrow Transplantation 42, 581–588. https://doi.org/10.1038/bmt.2008.222

Katsura, M., Shoji, F., Okamoto, T., Shimamatsu, S., Hirai, F., Toyokawa, G., Morodomi, Y., Tagawa, T., Oda, Y., Maehara, Y., 2018. Correlation between CXCR4/CXCR7/CXCL12 chemokine axis expression and prognosis in lymph-node-positive lung cancer patients. Cancer Science 109, 154–165. https://doi.org/10.1111/cas.13422

Kessenbrock, K., Plaks, V., Werb, Z., 2010. Matrix Metalloproteinases: Regulators of the Tumor Microenvironment. Cell 141, 52–67. https://doi.org/10.1016/j.cell.2010.03.015

Kim, J., Mori, T., Chen, S.L., Amersi, F.F., Martinez, S.R., Kuo, C., Turner, R.R., Ye, X., Bilchik, A.J., Morton, D.L., Hoon, D.S.B., 2006. Chemokine receptor CXCR4 expression in patients with melanoma and colorectal cancer liver metastases and the association with disease outcome. Annals of Surgery 244, 113–120. https://doi.org/10.1097/01.sla.0000217690.65909.9c

Kitaori, T., Ito, H., Schwarz, E.M., Tsutsumi, R., Yoshitomi, H., Oishi, S., Nakano, M., Fujii, N., Nagasawa, T., Nakamura, T., 2009. Stromal cell-derived factor 1/CXCR4 signaling is critical for the recruitment of mesenchymal stem cells to the fracture site during skeletal repair in a mouse model. Arthritis and Rheumatism 60, 813–823. https://doi.org/10.1002/art.24330

Knerlich-Lukoschus, F., Von Der Ropp-Brenner, B., Lucius, R., Mehdorn, H.M., Held-Feindt, J., 2010. Chemokine expression in the white matter spinal cord precursor niche after force-defined spinal cord contusion injuries in adult rats. Glia 58, 916–931. https://doi.org/10.1002/glia.20974

Kofuku, Y., Yoshiura, C., Ueda, T., Terasawa, H., Hirai, T., Tominaga, S., Hirose, M., Maeda, Y., Takahashi, H., Terashima, Y., Matsushima, K., Shimada, I., 2009. Structural basis of the interaction between chemokine stromal cell-derived factor-1/CXCL12 and its G-protein-

coupled receptor CXCR4. Journal of Biological Chemistry 284, 35240–35250. https://doi.org/10.1074/jbc.M109.024851

Kriegel, C., Kit, K.M., Mcclements, D.J., Weiss, J., 2009. Electrospinning of chitosan – poly (ethylene oxide) blend nanofibers in the presence of micellar surfactant solutions. Polymer 50, 189–200. https://doi.org/10.1016/j.polymer.2008.09.041

Lee, A.L.Z., Voo, Z.X., Chin, W., Ono, R.J., Yang, C., Gao, S., Hedrick, J.L., Yang, Y.Y., 2018. Injectable Coacervate Hydrogel for Delivery of Anticancer Drug-Loaded Nanoparticles in vivo. ACS Applied Materials and Interfaces 10, 13274–13282. https://doi.org/10.1021/acsami.7b14319

Lee, Y.H., Lee, J.H., An, I.-G., Kim, C., Lee, D.S., Lee, Y.K., Nam, J.-D., 2005. Electrospun dual-porosity structure and biodegradation morphology of Montmorillonite reinforced PLLA nanocomposite scaffolds. Biomaterials 26, 3165–3172. https://doi.org/10.1016/j.biomaterials.2004.08.018

Ma, G., Liu, Y., Peng, C., Fang, D., He, B., Nie, J., 2011. Paclitaxel loaded electrospun porous nanofibers as mat potential application for chemotherapy against prostate cancer. Carbohydrate Polymers 86, 505–512. https://doi.org/10.1016/j.carbpol.2011.04.082

Marquez-Curtis, L., Jalili, A., Deiteren, K., Shirvaikar, N., Lambeir, A.-M., Janowska-Wieczorek, A., 2008. Carboxypeptidase M Expressed by Human Bone Marrow Cells Cleaves the C-Terminal Lysine of Stromal Cell-Derived Factor-1α: Another Player in Hematopoietic Stem/Progenitor Cell Mobilization? Stem Cells 26, 1211–1220. https://doi.org/10.1634/stemcells.2007-0725

Martin, L.J., Akhavan, B., Bilek, M.M.M., 2018. Electric fields control the orientation of peptides irreversibly immobilized on radical-functionalized surfaces. Nature Communications 9, 357–367. https://doi.org/10.1038/s41467-017-02545-6

Martínez Rivas, C.J., Tarhini, M., Badri, W., Miladi, K., Greige-Gerges, H., Nazari, Q.A., Galindo Rodríguez, S.A., Román, R.Á., Fessi, H., Elaissari, A., 2017. Nanoprecipitation process: From encapsulation to drug delivery. International Journal of Pharmaceutics 532, 66–81. https://doi.org/10.1016/j.ijpharm.2017.08.064

Mayerberger, E.A., Street, R.M., McDaniel, R.M., Barsoum, M.W., Schauer, C.L., 2018. Antibacterial properties of electrospun Ti3C2Tz (MXene)/chitosan nanofibers. RSC Adv. 8, 35386–35394. https://doi.org/10.1039/C8RA06274A

McCarthy, K.D., de Vellis, J., 1980. Preparation of separate astroglial and oligodendroglial cell cultures from rat cerebral tissue. J Cell Biol 85, 890–902. https://doi.org/10.1083/jcb.85.3.890

Milner, R., Edwards, G., Streuli, C., Ffrench-Constant, C., 1996. A role in migration for the alpha V beta 1 integrin expressed on oligodendrocyte precursors. The Journal of neuroscience : the official journal of the Society for Neuroscience 16, 7240–7252. https://doi.org/10.1523/JNEUROSCI.16-22-07240.1996

Min, B.M., Lee, S.W., Lim, J.N., You, Y., Lee, T.S., Kang, P.H., Park, W.H., 2004. Chitin and chitosan nanofibers: Electrospinning of chitin and deacetylation of chitin nanofibers. Polymer 45, 7137–7142. https://doi.org/10.1016/j.polymer.2004.08.048

Molina-Peña, R., Haji Mansor, M., Najberg, M., Thomassin, J.-M., Gueza, B., Alvarez-Lorenzo, C., Garcion, E., Jérôme, C., Boury, F., 2021. Nanoparticle-containing electrospun nanofibrous scaffolds for sustained release of SDF-1α. Int J Pharm 610, 121205. https://doi.org/10.1016/j.ijpharm.2021.121205

Najberg, M., Haji Mansor, M., Taillé, T., Bouré, C., Molina-Peña, R., Boury, F., Cenis, J.L., Garcion, E., Alvarez-Lorenzo, C., 2020. Aerogel sponges of silk fibroin, hyaluronic acid and heparin for soft tissue engineering: Composition-properties relationship. Carbohydrate Polymers 237, 116107. https://doi.org/10.1016/j.carbpol.2020.116107

Newman, J., Josephson, A.S., Cacatian, A., Tsang, A., 1974. Spinal-fluid lysozyme in the diagnosis of central-nervous-system tumors. The Lancet 304, 756–757. https://doi.org/10.1016/S0140-6736(74)90946-5

Nicolas, S., Bolzinger, M.-A., Jordheim, L.P., Chevalier, Y., Fessi, H., Almouazen, E., 2018. Polymeric nanocapsules as drug carriers for sustained anticancer activity of calcitriol in breast cancer cells. International Journal of Pharmaceutics 550, 170–179. https://doi.org/10.1016/j.ijpharm.2018.08.022

Noriega, S.E., Subramanian, A., 2011. Consequences of Neutralization on the Proliferation and Cytoskeletal Organization of Chondrocytes on Chitosan-Based Matrices. International Journal of Carbohydrate Chemistry 2011, 1–13. https://doi.org/10.1155/2011/809743

O'Boyle, G., Swidenbank, I., Marshall, H., Barker, C.E., Armstrong, J., White, S.A., Fricker, S.P., Plummer, R., Wright, M., Lovat, P.E., 2013. Inhibition of CXCR4-CXCL12 chemotaxis in melanoma by AMD11070. British Journal of Cancer 108, 1634–1640. https://doi.org/10.1038/bjc.2013.124

Ojeda-May, P., Garcia, M.E., 2010. Electric field-driven disruption of a native β-sheet protein conformation and generation of a helix-structure. Biophysical Journal 99, 595–599. https://doi.org/10.1016/j.bpj.2010.04.040

Ono, R.J., Lee, A.L.Z., Voo, Z.X., Venkataraman, S., Koh, B.W., Yang, Y.Y., Hedrick, J.L., 2017. Biodegradable Strain-Promoted Click Hydrogels for Encapsulation of Drug-Loaded Nanoparticles and Sustained Release of Therapeutics. Biomacromolecules 18, 2277–2285. https://doi.org/10.1021/acs.biomac.7b00377

Pakravan, M., Heuzey, M., Ajji, A., 2011. A fundamental study of chitosan / PEO electrospinning. Polymer 52, 4813–4824. https://doi.org/10.1016/j.polymer.2011.08.034

Pakulska, M.M., Elliott Donaghue, I., Obermeyer, J.M., Tuladhar, A., McLaughlin, C.K., Shendruk, T.N., Shoichet, M.S., 2016. Encapsulation-free controlled release: Electrostatic adsorption eliminates the need for protein encapsulation in PLGA nanoparticles. Science Advances 2, e1600519–e1600528. https://doi.org/10.1126/sciadv.1600519

Pardridge, W.M., 2011. Drug transport in brain via the cerebrospinal fluid. Fluids and Barriers of the CNS 8, 7–10. https://doi.org/10.1186/2045-8118-8-7

Pham, Q.P., Sharma, U., Mikos, A.G., 2006. Electrospinning of polymeric nanofibers for tissue engineering applications: a review. Tissue engineering 12, 1197–211. https://doi.org/10.1089/ten.2006.12.1197

Pulavendran, S., Thiyagarajan, G., 2011. Three-dimensional scaffold containing EGF incorporated biodegradable polymeric nanoparticles for stem cell based tissue engineering applications. Biotechnology and Bioprocess Engineering 16, 393–399. https://doi.org/10.1007/s12257-009-3155-4

Ramakrishna, S., Fujihara, K., Teo, W.E., Yong, T., Ma, Z., Ramaseshan, R., 2006. Electrospun nanofibers: Solving global issues. Materials Today 9, 40–50. https://doi.org/10.1016/S1369-7021(06)71389-X

Ratajczak, M.Z., Kucia, M., Reca, R., Majka, M., Janowska-Wieczorek, A., Ratajczak, J., 2004. Stem cell plasticity revisited: CXCR4-positive cells expressing mRNA for early muscle, liver and neural cells "hide out" in the bone marrow. Leukemia 18, 29–40. https://doi.org/10.1038/sj.leu.2403184

Ren, D., Yi, H., Wang, W., Ma, X., 2005. The enzymatic degradation and swelling properties of chitosan matrices with different degrees of N-acetylation. Carbohydrate Research 340, 2403–2410. https://doi.org/10.1016/j.carres.2005.07.022

Rinaudo, M., Pavlov, G., Desbrières, J., 1999. Influence of acetic acid concentration on the solubilization of chitosan. Polymer 40, 7029–7032. https://doi.org/10.1016/S0032-3861(99)00056-7

Ripoll, D.R., Vila, J.A., Scheraga, H.A., 2005. On the orientation of the backbone dipoles in native folds. Proceedings of the National Academy of Sciences 102, 7559–7564. https://doi.org/10.1073/pnas.0502754102

Roccaro, A.M., Sacco, A., Purschke, W.G., Moschetta, M., Buchner, K., Maasch, C., Zboralski, D., Zöllner, S., Vonhoff, S., Mishima, Y., Maiso, P., Reagan, M.R., Lonardi, S., Ungari, M., Facchetti, F., Eulberg, D., Kruschinski, A., Vater, A., Rossi, G., Klussmann, S., Ghobrial, I.M., 2014. SDF-1 inhibition targets the bone marrow niche for cancer therapy. Cell Reports 9, 118–128. https://doi.org/10.1016/j.celrep.2014.08.042

Saravanan, S., Sareen, N., Abu-El-Rub, E., Ashour, H., Sequiera, G.L., Ammar, H.I., Gopinath, V., Shamaa, A.A., Sayed, S.S.E., Moudgil, M., Vadivelu, J., Dhingra, S., 2018. Graphene Oxide-Gold Nanosheets Containing Chitosan Scaffold Improves Ventricular Contractility and Function After Implantation into Infarcted Heart. Scientific Reports 8, 15069. https://doi.org/10.1038/s41598-018-33144-0

Sashiwa, H., Saimoto, H., Shigemasa, Y., Ogawa, R., Tokura, S., 1990. Lysozyme susceptibility of partially deacetylated chitin. International Journal of Biological Macromolecules 12, 295–296. https://doi.org/10.1016/0141-8130(90)90016-4

Séhédic, D., Chourpa, I., Tétaud, C., Griveau, A., Loussouarn, C., Avril, S., Legendre, C., Lepareur, N., Wion, D., Hindré, F., Davodeau, F., Garcion, E., 2017. Locoregional Confinement and Major Clinical Benefit of ^{188} Re-Loaded CXCR4-Targeted Nanocarriers in an Orthotopic Human to Mouse Model of Glioblastoma. Theranostics 7, 4517–4536. https://doi.org/10.7150/thno.19403

Sobolik, T., Su, Y. -j., Wells, S., Ayers, G.D., Cook, R.S., Richmond, A., 2014. CXCR4 drives the metastatic phenotype in breast cancer through induction of CXCR2 and activation of MEK and PI3K pathways. Molecular Biology of the Cell 25, 566–582. https://doi.org/10.1091/mbc.E13-07-0360

Tchemtchoua, V.T., Atanasova, G., Aqil, A., Filée, P., Garbacki, N., Vanhooteghem, O., Deroanne, C., Noël, A., Jérome, C., Nusgens, B., Poumay, Y., Colige, A., 2011. Development of a Chitosan Nanofibrillar Scaffold for Skin Repair and Regeneration. Biomacromolecules 12, 3194–3204. https://doi.org/10.1021/bm200680q

Tomihata, K., Ikada, Y., 1997. In vitro and in vivo degradation of films of chitin and its deacetylated derivatives. Biomaterials 18, 567–575. https://doi.org/10.1016/S0142-9612(96)00167-6

Toschi, F., Lugli, F., Biscarini, F., Zerbetto, F., 2009. Effects of Electric Field Stress on a β-Amyloid Peptide. J. Phys. Chem. B 113, 369–376. https://doi.org/10.1021/jp807896g

Toullec, C., Le Bideau, J., Geoffroy, V., Halgand, B., Buchtova, N., Molina-Peña, R., Garcion, E., Avril, S., Sindji, L., Dube, A., Boury, F., Jérôme, C., 2021. Curdlan–Chitosan Electrospun Fibers as Potential Scaffolds for Bone Regeneration. Polymers 13, 526. https://doi.org/10.3390/polym13040526

Tyliszczak, B., Drabczyk, A., Kudłacik-Kramarczyk, S., Bialik-Wąs, K., Sobczak-Kupiec, A., 2017. In vitro cytotoxicity of hydrogels based on chitosan and modified with gold nanoparticles. J Polym Res 24, 153. https://doi.org/10.1007/s10965-017-1315-3

Vårum, K.M., Myhr, M.M., Hjerde, R.J.N., Smidsrød, O., 1997. In vitro degradation rates of partially N-acetylated chitosans in human serum. Carbohydrate Research 299, 99–101. https://doi.org/10.1016/S0008-6215(96)00332-1

Wada, A., 1976. The alpha-helix as an electric macro-dipole. Advances in Biophysics 9, 1–63.

Wang, M.O., Etheridge, J.M., Thompson, J.A., Vorwald, C.E., Dean, D., Fisher, J.P., 2013. Evaluation of the In Vitro Cytotoxicity of Cross-Linked Biomaterial. Biomacromolecules 14, 1321–1329. https://doi.org/10.1021/bm301962f

Wang, X., Guan, J., Zhuang, X., Li, Z., Huang, S., Yang, J., Liu, C., Li, F., Tian, F., Wu, J., Shu, Z., 2018. Exploration of Blood Coagulation of N-Alkyl Chitosan Nanofiber Membrane in Vitro. Biomacromolecules 19, 731–739. https://doi.org/10.1021/acs.biomac.7b01492

Wang, X., Li, Y., He, X., Chen, S., Zhang, J.Z.H., 2014. Effect of strong electric field on the conformational integrity of insulin. J Phys Chem A 118, 8942–8952. https://doi.org/10.1021/jp501051r

Wolf, K., Te Lindert, M., Krause, M., Alexander, S., Te Riet, J., Willis, A.L., Hoffman, R.M., Figdor, C.G., Weiss, S.J., Friedl, P., 2013. Physical limits of cell migration: control by ECM space and nuclear deformation and tuning by proteolysis and traction force. J Cell Biol 201, 1069–1084. https://doi.org/10.1083/jcb.201210152

Wu, J., Hong, Y., 2016. Enhancing cell infiltration of electrospun fibrous scaffolds in tissue regeneration. Bioactive Materials 1, 56–64. https://doi.org/10.1016/j.bioactmat.2016.07.001

Xia, M., Huang, R., Witt, K.L., Southall, N., Fostel, J., Cho, M.-H., Jadhav, A., Smith, C.S., Inglese, J., Portier, C.J., Tice, R.R., Austin, C.P., 2008. Compound Cytotoxicity Profiling Using Quantitative High-Throughput Screening. Environ Health Perspect 116, 284–291. https://doi.org/10.1289/ehp.10727

Xie, Z., Paras, C.B., Weng, H., Punnakitikashem, P., Su, L.C., Vu, K., Tang, L., Yang, J., Nguyen, K.T., 2013. Dual growth factor releasing multi-functional nanofibers for wound healing. Acta Biomaterialia 9, 9351–9359. https://doi.org/10.1016/j.actbio.2013.07.030

Zagzag, D., Esencay, M., Mendez, O., Yee, H., Smirnova, I., Huang, Y., Chiriboga, L., Lukyanov, E., Liu, M., Newcomb, E.W., 2008. Hypoxia- and Vascular Endothelial Growth Factor-Induced

Stromal Cell-Derived Factor-1α/CXCR4 Expression in Glioblastomas. The American Journal of Pathology 173, 545–560. https://doi.org/10.2353/ajpath.2008.071197

Zhang, H., Tian, Y., Zhu, Z., Xu, H., Li, X., Zheng, D., Sun, W., 2016. Efficient antitumor effect of co-drug-loaded nanoparticles with gelatin hydrogel by local implantation. Scientific Reports 6, 1–14. https://doi.org/10.1038/srep26546

Zhao, W., Yang, R., 2010. Experimental Study on Conformational Changes of Lysozyme in Solution Induced by Pulsed Electric Field and Thermal Stresses. J. Phys. Chem. B 114, 503–510. https://doi.org/10.1021/jp9081189

Zhao, W., Yang, R., 2009. Effect of high-intensity pulsed electric fields on the activity, conformation and self-aggregation of pepsin. Food Chemistry 114, 777–781. https://doi.org/10.1016/j.foodchem.2008.10.016

Ziani, K., Henrist, C., Jérôme, C., Aqil, A., Maté, J.I., Cloots, R., 2011. Effect of nonionic surfactant and acidity on chitosan nanofibers with different molecular weights. Carbohydrate Polymers 83, 470–476. https://doi.org/10.1016/j.carbpol.2010.08.002

Chapter 5:

General discussion, conclusion, and perspectives

5. General discussion, conclusion, and perspectives

5.1 The GB challenges

Efforts are continuously being attempted to improve the outcome of GB patients. In the last 40 years, there has been a large number of tested therapies ranging from combinations of classical chemotherapies and radiotherapies, antiangiogenic and its combination therapies, to new targeted therapies, some of which have shown promising preclinical results; however, at this point, glioblastoma is mostly recurrent (Birzu et al., 2021; Reifenberger et al., 2017). This supports the continuous search for innovative therapies. Tumor-treating fields (TTFields) showing a survival benefit are now considered a standard of care (SOC) (Lukas et al., 2019). Two recent phase-3 clinical trials have shown an improvement over SOC temozolomide/radiotherapy. One involves the combination of lomustine with temozolomide in addition to radiotherapy (Herrlinger et al., 2019), and the other is the use of a patient-lysate-derived pulsed dendritic cell vaccine in combination with the SOC (Liau et al., 2023). Unfortunately, these improvements concern an extended median overall survival of a few months relative to the SOC Stupp protocol (**Section 1.6**).

Many factors can play a role in defining the success of the developed therapies. Among them:

Clinical factors concerning the intrinsic variability of the population, the patient's age, medical condition, and Karnofsky performance status (KPS) (Kanu et al., 2009; Reifenberger et al., 2017).

The pharmacodynamics and pharmacokinetics limitations that have to do with the active pharmaceutical ingredient's (API) biodistribution, the natural filter imposed by the blood-brain barrier (BBB), the medicament's efficacity, and the dose-limiting toxicity of the API (Le Rhun et al., 2023).

Cell heterogeneity, resistance, and plasticity. Resistance is associated with the complex heterogeneity of GB, mosaicism of genomic alterations, the clonal selection and the tumor evolution induced by the treatment, the intrinsic capacity of cells to repair and survive, the cellular scape from treatment zones, and the capacity of cells to hide in protective niches. A hierarchical model reproduces the cancer cell heterogeneity of GB. Chemotherapy enriches glioma stem cells (GSCs) (Lan et al., 2017). GSCs have been reported to be more resistant to therapies (Olivier et al., 2021). More primitive slow-cycling GSCs can give rise to rapidly dividing progenitors and more differentiated cells (Lan et al., 2017). However, they also can differentiate into pericytes (Cheng et al., 2013), which reflects the plasticity of GB cells. The existence of different populations of GSCs has been proposed (Kanu et al., 2009). This heterogeneity can arise from the plasticity of all GB cells instructed by the tumor microenvironment (Dirkse et al., 2019). This warns against the use of therapies directed only against GSCs (Molina-Peña et al., 2020). In addition, although directed targeted and immunotherapies have shown efficacy in preclinical studies, antigen-loss variants are often

observed, undermining the effectiveness of such kind of monotargeted therapies in a clinical setting (Vyas et al., 2017).

The GB ecosystem is immunosuppressive. The GB ecosystem presents a reduced immunogenic activity due to the regulation of immune effectors by other ecosystem elements such as M2 macrophages and myeloid-derived suppressor cells (MDSCs) (Nduom et al., 2015). In addition, infiltrating reactive astrocytes produce inflammatory molecules promoting gliomagenesis (De Vleeschouwer and Bergers, 2017; Nduom et al., 2015).

The hypoxic environment promotes angiogenesis and unfavorable prognosis. Necrosis and microvascular proliferation are associated with pseudo-palisading cells in hypoxic regions with the secretion of HIF-1α, VEGF, and IL-8, and are a sign of unfavorable prognosis (Rong et al., 2006). In this case, different combinatorial examples using anti-angiogenesis therapeutics have failed to prove efficacy (**Section 1.5**). This might indicate that a feedback loop is established because the depletion of signals for new vessel formation might induce the ecosystem to compensate for them, giving rise to a redundant cycle or other compensatory mechanisms.

GB cell infiltration into the normal parenchyma is a major problem because tracking and reaching all of them is nowadays impossible.

Suboptimal delivery of therapeutics. Although different strategies have been investigated to enhance and optimize the delivery of therapeutics to GB tumors, GB cells have been found to invade beyond 2 cm of the resection cavity, farther than 4 cm (**Section 1.5**) (Gaspar et al., 1992; Silbergeld and Chicoine, 1997; Yamahara et al., 2010). Therefore, the probability of not reaching those cells is in part reflected in the frequent recurrences (> 90% of cases) (Lemée et al., 2015). Convection-enhanced delivery (CED), hydrogels, and scaffolds for loco-regional drug delivery have shown that the principle can be translated to the clinic (**Sections 1.10.2 and 1.11**), however, the eradication of all GB cells remains a challenge. Unfortunately, Gliadel® wafers designed for local delivery of carmustine did not show a benefit compared to SOC, and related post-operative complications have been observed (**Section 1.6**). The use of targeted therapies such as homogeneous ADCs (Anami et al., 2022) and ADCs administered by CED (Porath et al., 2022), and vectorized internal radiotherapy (Bailly et al., 2019; Séhédic et al., 2017), are promising strategies, but still, the outcome will depend on how effective such molecules and their killing principle can reach the target.

Preclinical success, but frequent clinical trial failure. Despite the success of various innovative treatments evaluated in preclinical murine and rat models, the translation is unfortunately often stopped at different phases of clinical evaluation. One of the reasons is the pharmacological issues as stated before. However, it also suggests the lack of use of an adequate animal model that reproduces key parameters of human GB (Liu et al., 2020). Many works during the 90s-2000s devoted to gene therapy of GB are examples of such cases (Holland, 2000). The use of immunocompromised animals is useful to assess human-derived cells or tissues, however, the response of the host is limited, and the contribution of the host to 1) the tumor ecosystem establishment and 2) tumor cell combating might not reproduce completely the natural history

of a GB. Syngeneic and transgenic models might represent a more representative approach. Liu et al. (2020) showed that in comparison to the GL261 mouse model, the CT2A model exhibited immunologic features consistent with human GB including reduced anti-PD-L1 sensitivity and hypofunctional tumor-infiltrating lymphocytes (TILs) (Liu et al., 2020). Syngeneic rat models include the RG2 and F98 models, which are diffusive and weak or non-immunogenic with uniform lethality (Kaur and Barth, 2009).

5.2 Novel synergic and system-based strategies

A few synergic strategies have shown impressive results at the preclinical evaluation level. Two recent cases include the use of the immunostimulatory (multivalent vaccine) effect combined with an immunomodulatory (anti-PD-L1) effect (Liu et al., 2020), and the use of a synergistic strategy by blocking the SDF-1α/CXCR4 pathway combined with radiotherapy (Alghamri et al., 2022). Another interesting approach is the use of targeted radio-immunotherapies, especially using radioisotopes that can have a high lethality in a short range of activities such as alpha-particle and Auger-electron emitters (Kunikowska et al., 2022; Pirovano et al., 2020). Such therapies can provide a double effect, cell-lethal radiation, and other radiation-related mechanisms; and bystander (transmission of lethal signals), and abscopal effects related to the exposure of neoantigens and DAMPS to the immune cells present within the system, and secretion of inflammatory cytokines, conferring activation of the immune response to tackle cancer cells (Awada et al., 2023; Pouget and Constanzo, 2021).

Substantial improvements in the understanding of the GB microenvironment, including the molecular interactions and composition of their niches that include the hypoxic, vascular, and invasive niches, as well as the physical environment, including the extracellular matrix of the tumor and normal brain parenchyma, and the matter and energy flux, sustain GB as an ecosystem (the “whole system” as coined by Sir Arthur Tansley in 1935) (Rich, 1988).

This remark can be supported by observing the natural history of GB. For example, it has been suggested that necrotic zones make GB cells migrate away from them forming pseudo-palisades, which shows a “scaping cell” arrangement due to a natural modification of the environment (**Section 1.5**). Secondly, the migration patterns of GB cells using brain structures are also an aspect that shows the cellular interactions with the biophysical-chemical components. Under this concept, modifying aspects of the GB ecosystem might help to tackle cancer cells. By luring them toward a confined location by using a suitable biodeposit or “cancer cell trap” it might become possible to concentrate diffusive GB cells for further elimination.

5.3 Thesis accomplishments and perspectives

The present thesis aimed at testing two different systems as GB cell traps. One was SF-HA-Hep sponges and the other was electrospun chitosan-nanofiber mats containing PLGA-PEG NPs. Both systems were designed for the local delivery of SDF-1α, as implantable systems in

the resection cavity of GB tumors, taking advantage of the loco-regional space, to induce the attraction of CXCR4+ GB cells. Most of the objectives have been addressed, including the *in vitro* and *in vivo* bioperformance evaluation of sponges as GB cell traps, except for the corresponding evaluation of chitosan mats. The proof of concept has been demonstrated by the attraction of GB cells *in vitro* using an under-agarose assay and *in vivo* by direct placement of SF-HA-Hep sponges near U87MG-CXCR4+ cells, in a developed model of residual cells contiguous to the resection cavity in rats. Interestingly, the results showed a modification of the tumor shape being more rounded and localized to resection sites thanks to the sponge's implantation. These results open the possibility to combine a cell-killing signal such as localized chemotherapy and radiotherapy. An experiment using external beam radiation will be performed to test whether these effects on tumor shaping and localization improve the efficacy of the treatment. Despite chitosan mats being not evaluated functionally as cancer cell traps, i.e., the attraction and trapping of cancer cells, important findings were still observed such as their good cell adhesion capacity and their good biocompatibility *in vivo*. Moreover, the innovative composition of the biomaterial with SDF-1α encapsulated into NPs that were further embedded into chitosan nanofibers offered an excellent chemokine-releasing profile that was durable in time, and which can offer an unprecedented advantage to deliver therapeutics in the central nervous system. While not all rubrics can be filled, some comparisons between the two systems, sponges and chitosan mats, might be pertinent and are presented in **Table 5.1**.

Table 5.1. Comparison of the two scaffolds as GB traps

	SF-HA-Hep sponges	**Chitosan nanofibers**
Porosity	> 90%	~ 46 %
Pore size	69 µm	< 1 µm
Interconnectivity	~ 99 % with pore openings > 15 µm in dried form	Nondetermined
Young modulus	13 KPa	Nondetermined
Structural alignment	Nonaligned pores or conduits	Nonaligned fibers
Wall/fiber thickness	Δx = 20 µm	Δx = 261 nm
Tridimensional structure	3D sponge	Films (Thickness ~ 40 µm)
Placement -*in vivo*	Hydrated form	Rolled films
Interconnectivity after placement	Retained for 7 days, most probably the network structure is lost by 3-4 weeks after placement.	Open spaces between the walls of rolled films depend on the tightening of the rolling.
Shape memory	Yes, upon hydration	Nondetermined
Cell infiltration -*in vitro*	Good	Non
Cell infiltration -*in vivo*	Good	Depending on the space provided by the open spaces between the walls of rolled films
Cell adhesion -*in vitro*	Good	Good
***In vitro* cytotoxicity**	Low to moderate	Very low

Table 5.1. (Continued) Comparison of the two scaffolds as GB traps

	SF-HA-Hep sponges	**Chitosan nanofibers**
***In vitro* biodegradability**	85% in 3 weeks	10% in 5 weeks
***In vivo* biodegradability**	~ 3 weeks	Nondegraded up to ~ 4 months
***In vivo* biocompatibility**	Low chronic inflammation was present, but not influencing the feeding and sleeping of animals	Low chronic inflammation was present, but not influencing the feeding and sleeping of animals
Scar tissue	Non detected	Fibrous tissue observed on the 4th month
Expected performance as a GB cell trap	Depends on if 3-4 weeks is enough to attract and home GB cells	Lasting duration as a platform providing surfaces for GB cell attachment. Fibrotic tissue may diminish its performance
SDF-1α loading	Drop deposition	NP containing the chemokine embedded in chitosan nanofibers
Mechanism of SDF-1α retention	Adsorption via heparin-binding domains + electrostatic interactions	Entrapping of SDF-1α molecules within NPs + electrostatic interactions with PLGA
SDF-1α release -*in vitro*	3% burst in 1 day reaching a 5% plateau in 7 days	20% release in 1 day with sustained release for up to 5 weeks (75%)
Mechanism of SDF-1α release	Diffusion of weekly adsorbed SDF-1α molecules	Two-step diffusion process (from NPs and across nanofibers)
SDF-1α release -*in vivo*	SDF-1α retained within the sponge on day 7 of the evaluation	Non assessed

5.3.1 Improving biomaterials' design

Sponges

Results showed that sponges were able to attract GB cells *in vitro* from 2 mm, and *in vivo* from a short distance (1 mm), but not from a longer distance (3 mm) in the timeframe evaluated of 7 days. This reduced effect observed over long distances might be related to the short release of SDF-1α from the sponges as discussed in **Chapter 3**. However, a more robust detection method using radiolabeled SDF-1α to track the chemokine's fate is needed to observe the SDF-1α release *in-vivo* profile. Therefore, some improvements in the scaffold's design can be envisaged. The first corresponds to reducing the amount of heparin. The strong retention of SDF-1α was due to mostly electrostatic interactions. SDF-1α holding a positive charge, and heparin and HA negative charges in physiological conditions (Fermas et al., 2008), can explain the strong retention of the chemokine and the release of only ~ 5% in a week. However, heparin provided enhanced cell adhesion of GB cells compared to scaffolds without heparin. Therefore, a tradeoff of reducing the heparin content could be of interest.

Heparin and heparan sulfate (HS) GAGs bind SDF-1α via interaction with sulfate groups and induce the formation of dimers via a crevice containing amino acids of a positive charge (Sadir et al., 2001). HS GAGs have been found necessary for SDF-1α/CXCR4 interaction in the cell surface, by promoting increased local concentration of the ligand and its dimerization (Monneau et al., 2016). However, the incubation of SDF-1α with soluble heparin and HS reduces its chemotactic effect *in vitro* (Murphy et al., 2007), and impedes the recruitment of bone-marrow-derived mononuclear cells *in vivo* (Seeger et al., 2012). These results can be explained by the diminution of the capacity of the SDF-1α/heparin and SDF-1α/HS complexes to interact with the CXCR4 receptor, and additionally, *in vivo*, by the competition of administered GAGs with naturally present cell surface GAGs (Murphy et al., 2007; Seeger et al., 2012). Therefore, although heparin was initially intended to be used as an SDF-1α-containing reservoir and for its SDF-1α's protection from degradation/inactivation (Monneau et al., 2016; Sadir et al., 2004), if SDF-1α is not dissociated from heparin, this may entail a caveat by interrupting the internalization of the SDF-1α/CXCR4 complex and further signaling, (Seeger et al., 2012). However, there are HS-regulated haptotaxis gradients in physiological conditions and it is suggested that the naturally occurring variety of HS GAGs can modulate the activity of SDF-1α depending on the physiological context (Fermas et al., 2008). It should be noted that heparin occurs naturally but only intracellularly in mast cells to sequester different proteases (Monneau et al., 2016). Furthermore, it has been shown that stabilized heparin/SDF-1α in collagen scaffolds induced the recruitment of progenitor cells and CD11b+ and CD11c+ cells *in vivo* (Bladergroen et al., 2009). There was a 50% burst of SDF-1α in 24 h followed by an asymptotical increase of 10% release during the following 5 days. The complete washout of SDF-1α from the scaffolds did not induce the recruitment of cells (Bladergroen et al., 2009). Similarly, PLGA-PCL electrospun fiber vascular grafts were covalently coated with heparin for further functionalization with SDF-1α. The SDF-1α/heparin complex provided a better

stabilization of the chemokine under fluidic conditions with a 70% burst in 24 h followed by 10% cumulative release in 6 days. SDF-1α effectively recruited endothelial progenitor cells (EDP) to the luminal surface of the grafts and also increased the recruitment of smooth muscle progenitor cells into the grafts (Yu et al., 2012). In addition, CD34+ cells recruited to the middle portion of the grafts were also positive for CXCR7, suggesting that these progenitor cells were specifically recruited by SDF-1α (Yu et al., 2012). Whether cell infiltration was thanks to the possible haptotaxis signals was not addressed. However, their results suggest that complexed SDF-1α to heparin may have helped in cell infiltration. In the present thesis, enhanced penetration of U87MG-CXCR4+ neurospheroids was observed for sponges containing SDF-1α, and placement of sponges near cells *in vivo* allowed an enhanced attraction of cells after 7 days. Whether this effect was due to the burst release of SDF-1α or a putative haptotaxis response remains to be determined.

The use of HS instead of heparin can be also envisaged provided that the dissociation constant for heparin is half for HS (93 and 200 nM, respectively) (Laguri et al., 2007). However, the effectiveness/cost ratio needs to be evaluated. Another approach would be the use of tunable scaffolds that can be enzymatically degraded (Tsurkan et al., 2010). And more in line with the observed results for electrospun chitosan fibers, encapsulation of the chemokine into NPs for further incorporation into the SF-HA walls, with perhaps a minimal amount of heparin. Regarding the structure of the scaffolds, one could envisage using aligned pores and conduits as it is used for the fabrication of nerve conduits replacement (Semmler et al., 2023) and taking into account that GB cells can follow aligned paths (See **Fig. 4.3** in **Chapter 4** and reference (Jain et al., 2014)). However, the present results using SDF-1α-loaded sponges (**Fig. 3B Chapter 3**) and preliminary results culturing GB neuro-spheroids on top of the M-Trap device (**Fig. 5.1, Chapter 5**) showed that GB cells can indeed penetrate nonaligned but interconnected porous scaffolds. In the case of the M-Trap device, cells adhered to the walls and follow the surface structure of the collagen-coated walls, whereas, in the same time frame, gliomaspheroids cultured on sponges infiltrate as an invasive frontal mass. Of note is that the walls of the M-trap device are rather rigid (as observed empirically), and the connected walls provide a marked path to follow. Therefore, this strategy may be better than designing a solid scaffold that uses aligned conduits, in terms of optimizing the use of the resection space. Finally, SF-HA-Hep sponges were rather biodegradable in a time-lapse of 3-4 weeks (See (Najberg et al., 2020)). To improve the sponge's stability, optimization of the crosslinking strategy with EDC/NHS can be envisaged by 1) using a buffer that does not contain COOH and/or NH elements (to eliminate other competition sites for crosslinking), 2) the crosslinker activation of HA or SF chains of the biomaterials before mixing (Staros et al., 1986), and 3) increasing the time of cross-linkage. Another strategy is to increase the content of β-sheets (See **Fig.1.13** in **Section 1.10.1**) within the structure by augmenting the exposure of sponges to ethanol vapors (Fan et al., 2014), or using water vapors instead (Hu et al., 2011). In addition, the uniformity of the blend can be increased by diminishing the viscosity of the slurry by

heating, using HA of lower molecular weight, or using a lower amount of HA. This would increase more uniform interactions of the biomaterials' molecules with the crosslinker.

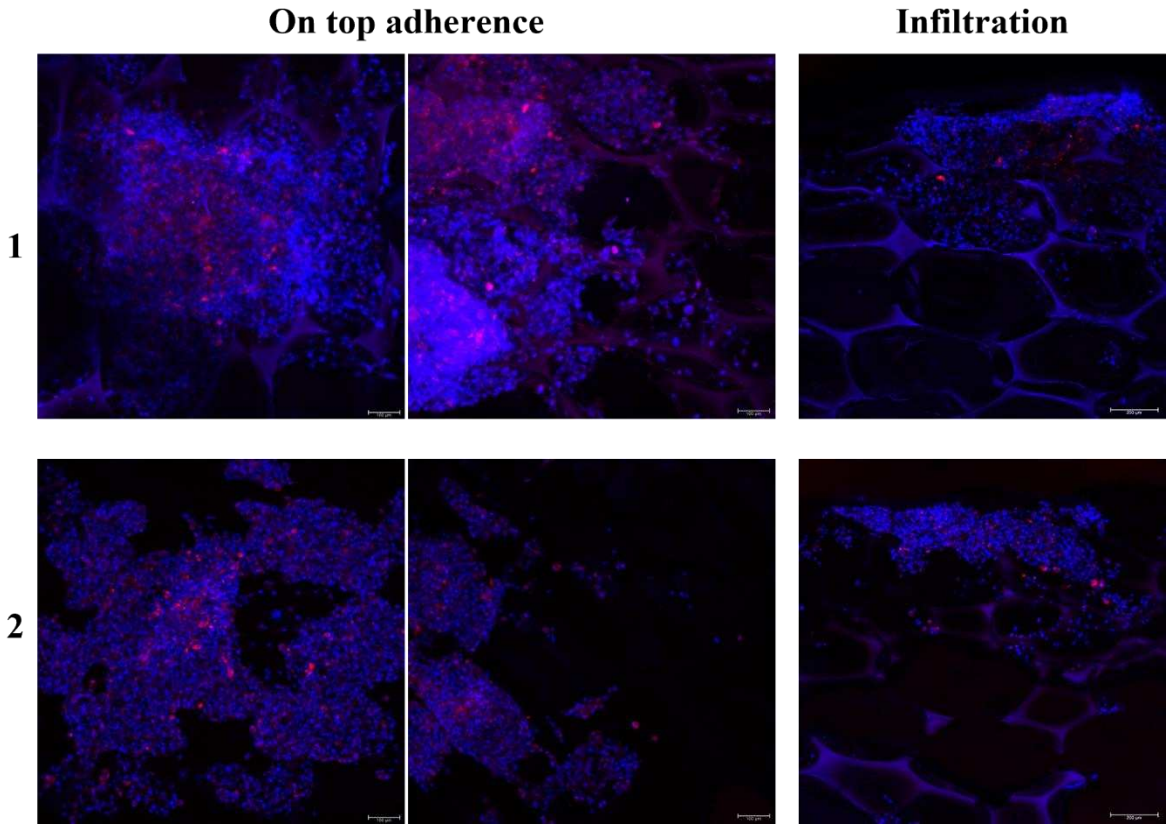

Figure 5.1. U87MG-CXCR4+ spheroids cultured on the M-Trap. Pictures were taken after 6 days of culture of a single spheroid on top of the device in 1%-FBS DMEM. It can be observed that the spheroid disintegrated, and cells attached to the walls and dispersed onto the external surface (left: on top) and internally into the walls (right: cross-section).

Chitosan fibrous scaffolds

Despite the chitosan fiber mats were not evaluated for their bioperformance as cancer cell traps, one of the most visible shortcomings is the reduced porosity and submicron pore size. Although fiber mats have been used in the GB context, they were aligned and put in contact perpendicular to the tumor with the aid of a hydrogel, resembling a conduit with a film of aligned paths in the center (Jain et al., 2014). During this thesis work, it was observed that U87MG-CXCR4+ cells indeed aligned and followed defined tracks as shown in **Fig. 4.3** (**Chapter 4**). Therefore, this observation gives a clue for the use of electrospinning to create a scaffold with a printable volume to be implanted with a defined pattern for cells to infiltrate, for example the sprouting-like fibers of the *Mimosa pudica* flower (**Fig. 5.2**), and which deposition would have to be adjustable to fit the resection cavity. Else, the design could imply the use of 3D-aligned fibers orthogonal to the resection walls within a hydrogel. Although both approaches might be difficult to translate into the clinic. Another strategy is to use a cylinder collector in the electrospinning setup instead of a plate to increase the porosity and thickness of the mat (Yu et

al., 2012). This would allow the creation of a network of fibrous pores with enough size for cell infiltration. Although the limitation of the 3D architecture to fit the cavity would still be present, the excellent adhesion and anti-bacterial properties of chitosan can be an advantage for the deposition of chitosan films on the resection cavity walls. Another advantage of chitosan is that it showed excellent *in vitro* cytocompatibility, and although chronic inflammation was observed *in vivo*, this corresponded to a foreign body reaction similar to what was observed for SF-HA-Hep sponges. The rolled scaffolds were not degradable during the 4-month time of evaluation *in vivo*. This structural stability could confer scaffolds lasting long enough, and given a proper structural design, provide mechanical and guiding cues for cells to migrate. However, the foreign body reaction also entailed the deposition of collagen and the formation of a fibrotic tissue surrounding the scaffold that could hamper its colonization by GB cells. This kind of tissue reaction has been observed in implantable devices that are not biodegradable (Alonso-Alconada et al., 2020; Autier et al., 2019). While Alonso-Alconada et al. found that the inflammation including collagen deposition helped to set a premetastatic niche to recruit ovarian cancer cells in a murine model (Alonso-Alconada et al., 2020), the M-trap efficiency was not optimal in a clinical trial, being the encapsulation of the M-trap by fibrotic tissue a plausible explanation of the failure of cancer cell recruitment (Gil-Moreno et al., 2021). Despite this, the evaluation of chitosan scaffolds as a GB cell trap should be performed to elucidate the different mechanisms that may be set.

Especially interesting is that the innovative process of embedding NPs within the fibers provided a steady and sustained release profile of the chemokine for up to 5 weeks *in vitro*, surpassing the profile observed in the SDF-1α loaded sponges. Moreover, the chemokine was active at the 3rd week of release as assessed by its capacity to induce the migration of GB cells from a confined spot (**Chapter 4**). Combining this gradient with the alignment of the fibers in a 3D scaffold might be a suitable approach to only using chitosan mats, as one important feature to profit from is the space and maximal contact with the resection edges.

Figure 5.2. ***Mimosa pudica*** **flower**

Another remark on the scaffolds' design is that it may be pertinent to explore mono-component devices. This is for example, using a single constituent like silk-fibroin or chitosan alone, but perhaps with different structural elements such as in the case of NP-containing fibers or walls for sustained delivery. This considering that simplification and optimization of the design may allow a different path towards clinical evaluation. In this regard, collagen is another biomaterial that would be of interest. As a coating present in the M-trap, it allowed cell adherence and infiltration (**Fig. 5.1**). It might therefore be used as a sponge, hydrogel, or electrospun scaffold. The selection of the best option would imply the evaluation of the cell guidance, cell attraction, and cell trapping capacities.

5.3.2. Selection of the chemoattractant/luring strategy

The involvement of the CXCR4/SDF-1α axis in brain cancers has been demonstrated in several studies. cDNA expression analysis revealed that CXCR4 is overexpressed in 57% of primary glioblastoma (GB) tumors and in 88% of GB cell lines that were analyzed (Sehgal et al., 1998). CXCR4 expression is considered a prognostic marker in gliomas. Patients with CXCR4-positive GB had a reduced postoperative life expectancy (Chatterjee et al., 2014). CXCR4 was expressed in more than 50% of astrocytomas and 100% activated form (phosphorylated) in grades 2-4 astrocytomas and 76% in grade 1 astrocytomas (Woerner et al., 2005). CXCR4 expression is upregulated by HIF-1α and HGF (Esencay et al., 2010; Zagzag et al., 2008). The CXCR4/SDF-1α axis is related to the chemotaxis attraction of GB cells *in vitro* (Bian et al., 2007; Zhou et al., 2002) and GSCs to the tumor vasculature (Cheng et al., 2013). CXCR4 is overexpressed in the invading regions of tumors and satellite tumors. And SDF-1α is expressed in neurons, blood vessels, subpial regions, and white matter tracks (Zagzag et al., 2008). The CXCR4/SDF-1α axis is also implicated in GB cell lines survival (Zhou et al., 2002) and *in vivo* resistance to temozolomide (Wang et al., 2020) by reducing apoptosis. It is also involved in GB cell proliferation (Sehgal et al., 1998). In addition, the CXCR7 receptor is also upregulated in GB (Bianco et al., 2015; Calatozzolo et al., 2011). It is found in pseudo-palisade cells and the tumor endothelium (Bianco et al., 2015). CXCR7 is involved in cell survival to temozolomide and proliferation upon SDF-1α treatment (Hattermann et al., 2012, 2010). Moreover, the crosstalk with EGFR (Salazar et al., 2014), which was associated with increased proliferation, and with TGFβR (Wu et al., 2016), which was associated with increased invasion and cancer stem cell formation, have been reported. Therefore, strategies to disrupt the CXCR4/CXCR7/SDF-1α axis by blocking the signaling cascade at the level of the receptor have been explored (Domanska et al., 2013; Santagata et al., 2021).

Here, a rupture concept was investigated, the strategy was to exploit CXCR4/SDF-1α axis to attract GB cells to a confining biodeposit consisting of a SF-HA-Hep sponge. It was observed that GB cells could be attracted toward the scaffolds both *in vitro* and *in vivo*. And the scaffolds as a form of porous sponges helped to sit and shape the tumors in the resection cavities. However, the concern of activation of survival and proliferation cascades makes to think of

different questions: 1) what is the time window to attract cells without enhancing their proliferation? 2) If survival is also enhanced, can it be turned off once cells are concentrated to apply a cell death signal? 3) Can the effect of CXCR4 be modulated to induce only cell migration? To address these questions *in vitro* approaches can be envisaged, for example, 1) the use of standard colony formation cell survival experiments upon radiation exposure, 2) the use of the gliomaspheroid colonization experiment deposited on sponges followed by assessment of cell viability after radiation, and more directly, 3) the effect of radiation focalized on the resection cavities on survival when scaffolds are present. Whether activation of chemotaxis alone is possible by modulation of the CXCR4/CXCR7/SDF-1α pathway is not known. But there is evidence that HS can modulate the response and different isoforms of SDF-1 are modulated differently (Laguri et al., 2007; Monneau et al., 2016).

Other molecules that have also been screened in GB tumors include CXCL10, semaphorins, netrins, and urotensin (UII) peptide ligand, and have been found to induce the chemoattraction of GB cells (**Table 5.2**). However, each of them is involved in signaling networks inducing other effects such as survival, proliferation, and angiogenesis. Therefore, its utilization can also entrain a risk that should be evaluated. On the other hand, apart from chemotaxis, structural guidance (Jain et al., 2014), haptotaxis (Monneau et al., 2016), and durotaxis (Staneva et al., 2018) might represent novel strategies for capturing residual GB cells near the resection cavity. Interestingly, the proteome analysis of laser micro-dissected invasion regions of GB tumor sections showed the overexpression of proteolipid protein 1 (PLP1), the predominant component of myelin, in the matrix of the invading front (Daubon et al., 2019). Addressing the question of whether the invasive tumor cells induced this expression or rather, they followed intrinsic signals embedded in those PLP1-expressing regions could give additional clues on the guidance of migratory GB cells. With this regard, the use of scaffolds made of ECM proteins might offer guidance clues, combined with the structural design of scaffolds as aligned fibers, for GB cells neighboring the resection and in direct contact with such scaffolds. However, long-distance infiltrated GB cells might not be attracted unless a biochemical signal reaches them. This has been observed, as previously discussed, in a PLGA-PCL-based electrospun graft to which SDF-1α was adsorbed, showing recruitment of circulating CXCR4+ cells and enhanced endothelization as compared to the scaffold without the chemokine (Yu et al., 2012). Thus, as suggested in the previous section, a combination of optimal chemokine release, and optimal structural design giving guidance cues may enhance the performance of the scaffolds as GB cell traps.

Another point that has to be addressed is if the scaffold alone can serve to attract cancer cells. This, as observed by Azarin et al. (2015) in breast cancer (Azarin et al., 2015), is due to the immunomodulation of the microenvironment recruiting immune cells that in turn secrete factors attracting cancer cells (**Figure 1.11 Section 1.9.2**). In the present sponge's evaluation, we observed the recruitment of immune cells in Fischer rats in the biocompatibility analysis. We also showed that SDF-1α-loaded sponges and sponges alone can locate the tumors in the resection cavity. However, if colonization of scaffolds was complete in the 3-4 weeks of the

survival experiment was not demonstrated. Therefore, the sectioning and evaluation of those samples should be performed. This additional information could help address the questions on the mechanisms of cell attraction.

Table. 5.2. Other molecules that can induce the attraction of GB cells.

Ligand	Receptor(s)	Expression	Effect	References
CXCL10	CXCR3	Varied in different cell lines. Increased membrane expression in the invasive front of human GB xenografted spheroids. Regulation by LRP1.	Survival and invasion of GB cells.	(Boyé et al., 2017)
Semaphorins	Neuropilin-1, neuropilin-2 and PlexinA1	Varied in different GB and patient-derived cell lines.	Chemoattraction or repulsion depending on complex regulation.	(Kerhervé et al., 2022; Nakayama et al., 2018; Nasarre et al., 2009)
Netrin-1	Neogenin and UNC5B	Varied expression in different GB cell lines.	Chemoattraction and increased angiogenesis.	(Akino et al., 2014; Shimizu et al., 2013)
Urotensin (UII) peptide ligand	GPCR UT receptor	Wide expression in cell lines, and GB patient tissues.	Chemoattraction and increased angiogenesis.	(Kasapidou et al., 2021; Lecointre et al., 2015)

5.3.3. Luring strategies: from antagonistic pleiotropy to ecosystem-based traps

Even in the case of enhanced chemoattraction combined with other types of cell guidance, the probability of attraction and confinement of all cells might not be 100%. This is because of the inherent heterogeneity of GB, the varying decisions on directional migration depending on the ECM and other signals, and the possible escape of cells from the biodeposit. With this regard, combinatory approaches are needed to tackle cancer cells. This might be addressed by loading a chemotherapeutic agent within the scaffold. Whereas the attractant capacity and killing sink can readily function concomitantly in the resection cavity remains to be explored. Here, it was observed that SF-HA-Hep sponges served as scaffolds to sit the tumors in the resection cavities and round-shaped them. Therefore, this suggests that a more localized treatment of tumors by radiation compared to more diffuse control tumors, might be put in place, which may help the elimination of concentrated cells. In the current clinical therapeutical setting, in which after resection concomitant radio/chemotherapy is applied, there is a time frame of 3-6 weeks after initiation of the postresection treatment (Lukas et al., 2019), in which implantation of the sponges might help concentrate some of the cells. What would be the optimal time to initiate treatment remains to be explored. This is to address what is the time to allow a more comprehensive GB cell recruitment before their killing by radio/chemotherapy is initiated.

Another perspective is including the use of the scaffolds as an immunomodulatory component. As previously discussed, scaffolds recruiting immune cells served as premetastatic niches by conditioning the microenvironment with early colonizing cells before cancer cell arrival (Azarin et al., 2015). But beyond this scope, it may be thought of scaffolds as a site of encounter with immune cells. It was shown that sponges alone could attract macrophages and lymphocytes in the short and long term (**Fig. 4 Section 3.4**). This is an aspect that can be taken into consideration to find strategies to re-educate those cells to redirect the immunosuppressive GB environment to tackle GB cells. More like a lymphoid organ works. This might be accomplished by enhancing the frequency of immune effector cells crossing with GB cells, with the synergistic effect of immune checkpoint inhibitors that could be loaded into the scaffold. Therefore, those meeting rooms might have a dual effect and more durable effect by modification of the GB ecosystem.

Intraperitoneal implantation of a PLG scaffold attracted leukocytes secreting CCL22, which in turn attracted Gr-1^{+}CD11b^{+} myeloid-derived suppressor cells (MDSC) which promoted the recruitment of breast cancer cells within the scaffold (Azarin et al., 2015). This process resembles the premetastatic cascade of breast cancer in organs such as the lung (Aguado et al., 2018). In another example, but this time in tissue regeneration, collagen-heparin/SDF-1α scaffolds recruited low numbers of HSCs/progenitors in 1 week that populated the scaffold within 5 weeks, with increased numbers of CD11b+ and CD11c+ cells which comprise granulocytes, monocytes and macrophages, fibroblasts, and CD31+ endothelial cells (Bladergroen et al., 2009). B and T cells were observed rarely, although their attraction and regulation by the SDF-1α/CXCR4 axis have been reported (Bleul et al., 1996; Cinamon et al.,

2001; Nagasawa, 2006; Tokoyoda et al., 2004). In another tissue engineering approach, anastomosis of a PLGA/PCL electrospun porous microfiber vascular graft coated with heparin for SDF-1α complexation showed the recruitment of CD34+ endothelial progenitor cells (EPC) and smooth muscle progenitor cells (SMPC) that allowed the regeneration of the vessel. However, CD68+ macrophages, CD11b+ inflammatory cells, and CD3+ T cells were rare (Yu et al., 2012). In the present thesis, implantation of non-SDF-1α loaded SF-HA-Hep sponges in Fisher rats entrained an acute immune response that lessened to a chronic inflammation after 4 months, with the presence of PMN cells, lymphocytes, and macrophages. A similar response was observed for chitosan scaffolds. However, the nature of the macrophages and lymphocytes was not determined. This assessment was not performed in the context of the SDF-1α loaded sponges during their evaluation as GB traps. Although in the latter case, nude rats were used, they still have a 70% Fischer background, with the absence of T cells (Janvier Labs). Thus, it would be interesting to elucidate what immune cells are attracted to compared to non-SDF-1α-loaded scaffolds. This is because the interplay between immune elements might be crucial to 1) knowing if the scaffolds alone can serve as premetastatic niches, and 2) determining the status of the GB ecosystem, in terms of immunosuppression. As discussed before, GB cells are thought to induce an immunosuppressive environment by secretion of different factors. Among them, M-CSF, TGFβ-1, and IL-10 skew macrophages to the immunosuppressive M2 phenotype (Nduom et al., 2015). The presence of M2-stage macrophages is correlated with vessel dilation and malignancy in different human glioma samples (Mathivet et al., 2017). Furthermore, normal monocytes exposed to glioma cells acquire properties like those of MDSCs (Rodrigues et al., 2010). Secretion of VEGF induces neoangiogenesis, inhibits maturation of dendritic cells, hinders infiltration of effector T-cells, and activates antigen-specific regulatory T-cells (Motz and Coukos, 2013). In addition, reactive astrogliosis produces growth factors, cytokines, and metabolites that promote gliomagenesis (De Vleeschouwer, 2017).

T cell effector cells are activated in GB mouse models. Recently, a synergistic effect was observed by using vaccination combined with anti-PD-L1. The strategy allowed for long-term survival compared with either strategy alone (Liu et al., 2020). In another synergistic strategy, blocking of the CXCR4/SDF-1α axis combined with radiation allowed the reduction of the tumor infiltration of CXCR4+ MDSCs, and the induction of immunogenic cell death by priming of T cells by delivered DAMPs from dying tumor cells (Alghamri et al., 2022). This strategy provided long-term immunoprotection as shown in rechallenged mice. These latter results pose the question of whether using the CXCR4/SDF-1α axis to attract GB cells would portray a benefit over the potential threats including enhanced survival, proliferation, and invasion of GB cells, and infiltration of immunosuppressive CXCR4+ MDSCs.

Here, although the tendency of the median survival was slightly reduced using SDF-1α (but not significantly compared to controls), the effect of the sponges on the developed tumors suggests that an improvement by a more localized treatment may be achieved. The luring of GB cells at the expense of the risks of using SDF-1α may allow a better eradication after

conferring some advantages, but this needs to be tested in conjunction with a killing signal such as focalized radiation therapy. The principle is of relevance, because despite the concerns about using SDF-1α, other approaches may be used to concentrate GB cells as discussed in the previous section.

In the latter study from (Alghamri et al., 2022), ~ 60% of mice had no detectable tumors at 100 days. Interestingly, in the multivalent vaccination plus anti-PD-L1 administration study, also 60% of mice were still surviving at day 50, whereas reduced survival was observed for the controls (Liu et al., 2020). These encouraging results highlight the relevance of synergistic and systems approaches. Still, in both studies, 40% of mice died at the time the studies were stopped, which reflects the resistance or scaped residual cells within the parenchyma. Therefore, the incorporation of a GB cell trap to concentrate cells, combined with radiation therapy and immunomodulation of the GB ecosystem represents an interesting approach that may be worth testing.

From a global perspective, different axes of the tumoral ecosystem might be targeted comprising the migration of GB cells, the tumor vasculature, the immune microenvironment, modulation of tumoral metabolism, and the primitive status (GSC content) of the tumor (**Fig. 5.3**). One view is to tackle those axes from an individual perspective. The other is from an evolutionary trapping perspective. For example, one might think of a scaffold that could attract GSCs and induce their differentiation; an immune trap that could enhance cancer cell encounters and prime immune cells to target cancer cells, either by attracting immune cells or by loading, for instance, engineered chimeric antigen receptor (CAR) T cells; a metabolic trap that could sensitize tumoral cells to radiation; and a vascular lure to induce normalization and exit of the tumor from its hypoxic condition and promoting a better distribution of therapeutic agents.

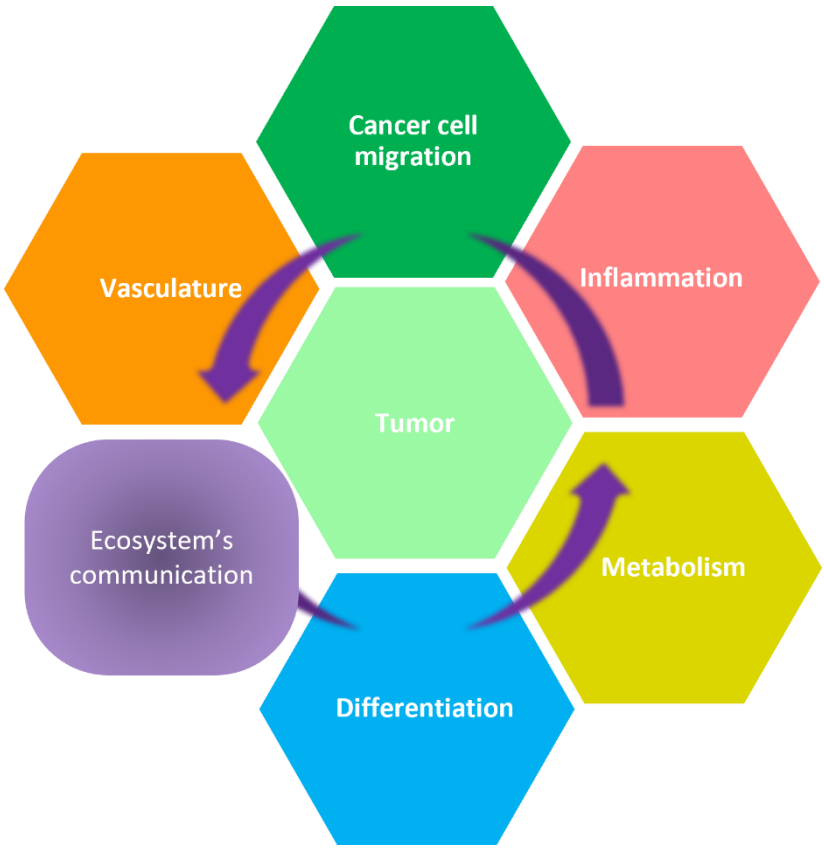

Figure 5.3. Ecosystem axes that can be targeted for tumor luring.

Finally, from a molecular perspective, evolutionary traps can be designed by antagonistic pleiotropy. This is observed with the induced selection of cellular tumoral components that are resistant to therapy. For example, by luring with an initial treatment the tumor becomes more prone to cell death with a second treatment, a chemotherapy-induced evolutionary trap (Lin et al., 2020). Unifying these concepts may help propose new system-based strategies to combat GB.

5.3.4. Past, present, and future of the surgical management of glioblastoma

This project was focused on the case of operable GB. Gross total resection rates have been reported between 14 to 46% in low-grade gliomas, and 33 to 76% in high-grade gliomas (Sanai, 2012). Indeed, tumor resection depends on the location of the tumor and the assessment of the patient's suitability for undergoing surgery (Ferroli et al., 2013). Historically, surgery improved the survival of operable patients over biopsy alone (Holland, 2000), and better surgical techniques, for instance including the use of the dye 5-ALA, have been related to improved survival based on the better safe extent of primary tumor removal (Stummer et al., 2006) (See **Section 1.6**). However, the preservation of cerebral function is a major challenge in surgical resection (Ferroli et al., 2013). While it might be thought that removing additional tissue from the limits of the main tumor, including an additional 2 cm from the edges, could

improve the outcome by eliminating residual GB cells as much as possible, postoperative morbidity can also contribute to a poor outcome (Ahmed et al., 2014). Therefore, keeping the functionality of the organ is also considered (Alexander and Cloughesy, 2017). Today, the use of awake craniotomy, in which the surgeon assesses the regions that should be preserved for the patient's maintenance of functions, limits the operable regions of the brain tissue where the tumoral cells may have invaded. Much more interest has increased in brain white matter fiber connectivity, for example, in the frontal aslant tracts which are involved in symmetric and asymmetric functions of the brain (Gallet et al., 2022). In the measure that more brain connectivity functions are elucidated, the threshold for surgery within the brain zones is prone to evolve to obtain an "onco-functional balance" (i.e., the best tradeoff between the extent of resection and functional preservation) (Gallet et al., 2022). With this regard, the application of scaffolds for locoregional therapy may also have to evolve to meet such challenges. An example of applicable hydrogel systems for the case of nonresectable tumors is intratumoral delivery of hydrogel liquid components for in situ gelation triggered by applying photoirradiation (See **Fig. 1.19-B** in **Section 1.11**).

Tumor resection has always been a critical part of clinical management since the advent of neurosurgery (Ahmed et al., 2014). The Stupp protocol implemented since 2005 included the use of adjuvant temozolomide concomitant with radiotherapy (Stupp et al., 2005). Even before the addition of chemo-radiotherapy, residual GB cells after resection were known to be the cause of recurrences. The potential of using loco-regional treatments to take advantage of the resection cavity to overcome the BBB was seen early for example with the development of Gliadel wafers to deliver carmustine. However, this treatment did not perform better than the Stupp protocol evaluated independently around the same time (See **Box 2, Section 1.6**). No other such systems have been included in the management of GB up to date. However, in parallel with the development of scaffolds for regenerative medicine and tissue engineering during the last 20 years, larger interest in such systems including hydrogels, porous scaffolds, and fiber mats has awakened interest in the potential application in the resected GB context and other solid tumors (Anderson and Segura, 2020; Cavo et al., 2020; Djoudi et al., 2022). In the current schedule for the management of glioblastoma (**Fig. 5.4**), after diagnosis, the surgeon undergoes resection in operable GB and takes a biopsy to confirm GB. After this, there is a timeframe of around 1 month and up to 6-7 weeks in which diagnosis of GB, and the patient's recovery from surgery is awaited before chemo-irradiation is started (Lukas et al., 2019). This timeframe, as evoked previously, offers the opportunity to act by using interventional bioimplants that could modify the GB microenvironment in the different axes shown in **Fig. 5.3**. While resection is still used, the application of loco-regional scaffolds would profit from the surgical intervention, and therefore would not require additional surgery in the current setting, apart from the additional time spent for the correct placement inside the cavity. One of the bottlenecks of this strategy is that because there is a waiting time for biopsy confirmation to decide on the post-surgical treatment, the bioimplants with associated therapeutical compounds should be active over different types of gliomas. Additionally, a promising avenue

is the companion molecular diagnostics before the intervention, for example, if a liquid biopsy or molecular imaging of brain tumors can determine the tumor entity before the intervention, then more specific interventional bio-traps/implants could be implemented. This strategy thus could offer an optimization of the management time applicable to the current setting, would benefit from the resected space, and has the advantage to overcome the BBB with the potential to modify the microenvironment to tackle GB by evolutionary luring.

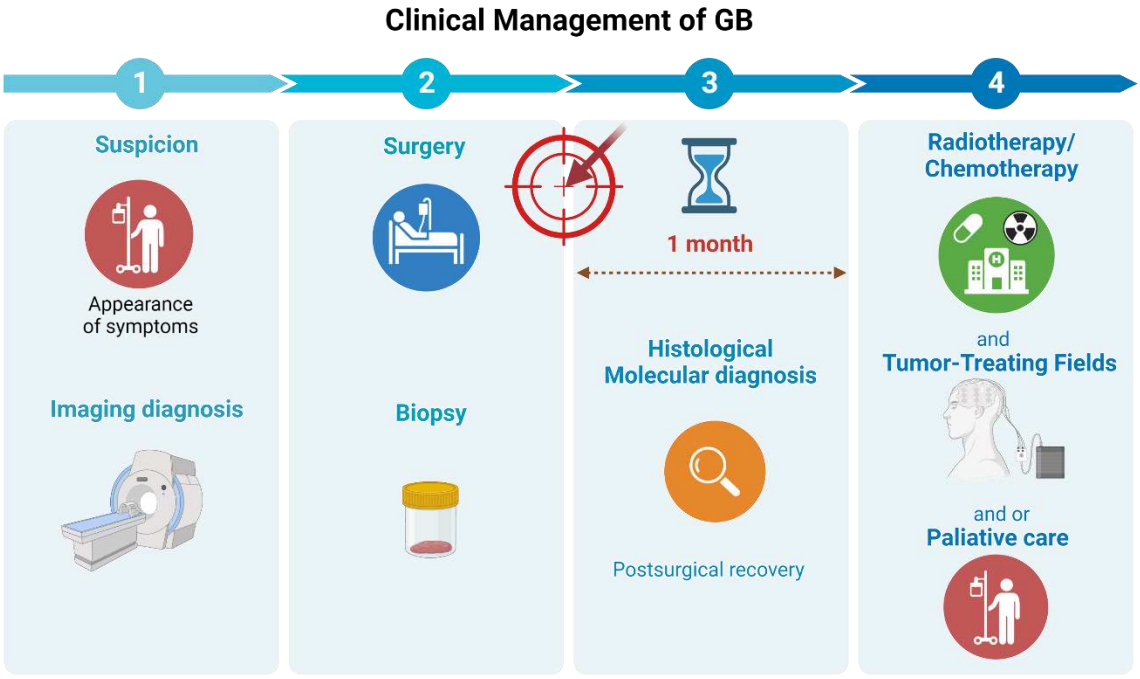

Figure 5.4. Current clinical management of GB. Patients with suspicion of GB go through 4 stages in the current clinical setting: 1) clinical diagnosis by MRI, 2) surgery accompanied by a biopsy to determine the type and grade of glioma, 3) a waiting time to confirm the diagnosis and the allow the patient for post-surgical recovery, and 4) treatment by the standard of care. The timeframe of around 1 month after surgery for therapeutical intervention by bio-implants/traps is depicted with an interrupted line. Created with Biorender.

5.4. Conclusion

In the present thesis, a GB cell trap based on an SF-HA-Hep sponge has demonstrated the capacity to attract GB cells *in vitro* and *in vivo* from a 1-mm distance. Releasing of SDF-1α and structural stability to biodegradation can be improved. The chitosan fibers were not evaluated as a trap but offered an excellent releasing profile of SDF-1α, which would be worth assessing *in vivo*. While slow-degradable chitosan scaffolds induced the formation of fibrotic tissue *in vivo*, SF-HA-Hep sponges did not and were biodegradable. The SDF-1α/CXCR4 axis being a hallmark of GB cell migration, U87MG cells transduced for CXCR4 stable expression were used as a model for addressing the proof of concept, but other cell lines and patient-derived cells/xenografts can be further explored. The fact that the implantation of sponges near cells helped sit and shape the tumors was not an expected result. This effect could enhance the effectiveness of more localized therapies including combinatorial chemo/radiotherapy. An experiment will be performed next to assess the effect on survival of external beam radiation therapy in rats implanted with SF-HA-Hep sponges (loaded or not with SDF-1α). Still, concerns exist about the use of SDF-1α due to its capacity to enhance GB cell survival, proliferation, and invasiveness, and attract immunosuppressive MDSCs. However, the benefit of the induced cell concentration concomitant with a cell-killing signal should be evaluated to get definitive conclusions on the ratio benefits/disadvantages. Other molecules such as netrins, semaphorins, and urotensin (UII) peptide ligand might be tested but they also entail a risk that must be evaluated. Here, the proof of concept has been assessed positively, and the developed *in vitro* and *in vivo* tools offer opportunities to explore other structural and mono-component designs based on single biomaterials such as silk fibroin, chitosan, and collagen alone. For example, in such a way as to provide cells guiding cues including structural guidance. Incorporation of SDF-1α into NPs followed by NP embedding into nanofibers improved the releasing profile of SDF-1α from chitosan scaffolds. This also helped in the preservation of the stability and activity of the chemokine. In addition, this embedding strategy might help control the fate of NPs in the brain, which is a point to be considered for the safety evaluation before clinical translation. Therefore, a similar approach might be tested in SF sponges. The presented scaffolds could be a platform for testing different luring strategies, for example, immune modulation of the microenvironment, inducing the differentiation of GSCs, and tackling the metabolism for on-purpose sensitization to sequential treatments. The use of such platforms could be an asset to the standard of care, taking advantage of the resected cavity, the waiting time after surgery to initiate radiotherapy, and the possibility to effectuate a loco-regional therapy overcoming the blood-brain barrier. Finally, the GB ecosystem might be tackled from an evolutionary trapping perspective given its complexity that is reflected in frequent recurrences.

5.5 References

Aguado, B.A., Hartfield, R.M., Bushnell, G.G., Decker, J.T., Azarin, S.M., Nanavati, D., Schipma, M.J., Rao, S.S., Oakes, R.S., Zhang, Y., Jeruss, J.S., Shea, L.D., 2018. Biomaterial Scaffolds as Pre-metastatic Niche Mimics Systemically Alter the Primary Tumor and Tumor Microenvironment. Advanced Healthcare Materials 7, 1700903. https://doi.org/10.1002/adhm.201700903

Ahmed, R., Oborski, M.J., Hwang, M., Lieberman, F.S., Mountz, J.M., 2014. Malignant gliomas: current perspectives in diagnosis, treatment, and early response assessment using advanced quantitative imaging methods. Cancer Manag Res 6, 149–170. https://doi.org/10.2147/CMAR.S54726

Akino, T., Han, X., Nakayama, H., McNeish, B., Zurakowski, D., Mammoto, A., Klagsbrun, M., Smith, E., 2014. Netrin-1 Promotes Medulloblastoma Cell Invasiveness and Angiogenesis, and Demonstrates Elevated Expression in Tumor Tissue and Urine of Patients with Pediatric Medulloblastoma. Cancer Research 74, 3716–3726. https://doi.org/10.1158/0008-5472.CAN-13-3116

Alexander, B.M., Cloughesy, T.F., 2017. Adult Glioblastoma. Journal of Clinical Oncology. https://doi.org/10.1200/JCO.2017.73.0119

Alghamri, M.S., Banerjee, K., Mujeeb, A.A., Mauser, A., Taher, A., Thalla, R., McClellan, B.L., Varela, M.L., Stamatovic, S.M., Martinez-Revollar, G., Andjelkovic, A.V., Gregory, J.V., Kadiyala, P., Calinescu, A., Jiménez, J.A., Apfelbaum, A.A., Lawlor, E.R., Carney, S., Comba, A., Faisal, S.M., Barissi, M., Edwards, M.B., Appelman, H., Sun, Y., Gan, J., Ackermann, R., Schwendeman, A., Candolfi, M., Olin, M.R., Lahann, J., Lowenstein, P.R., Castro, M.G., 2022. Systemic Delivery of an Adjuvant CXCR4–CXCL12 Signaling Inhibitor Encapsulated in Synthetic Protein Nanoparticles for Glioma Immunotherapy. ACS Nano 16, 8729–8750. https://doi.org/10.1021/acsnano.1c07492

Alonso-Alconada, L., de la Fuente, A., Santacana, M., Ferreiros, A., Lopez-Lopez, R., Matias-Guiu, X., Abal, M., 2020. Biomimetic device and foreign body reaction cooperate for efficient tumour cell capture in murine advanced ovarian cancer. Dis Model Mech 13, dmm043653. https://doi.org/10.1242/dmm.043653

Anami, Y., Otani, Y., Xiong, W., Ha, S.Y.Y., Yamaguchi, A., Rivera-Caraballo, K.A., Zhang, N., An, Z., Kaur, B., Tsuchikama, K., 2022. Homogeneity of antibody-drug conjugates critically impacts the therapeutic efficacy in brain tumors. Cell Reports 39, 110839. https://doi.org/10.1016/j.celrep.2022.110839

Anderson, A.R., Segura, T., 2020. Injectable biomaterials for treatment of glioblastoma. Adv Mater Interfaces 7, 2001055. https://doi.org/10.1002/admi.202001055

Autier, L., Clavreul, A., Cacicedo, M.L., Franconi, F., Sindji, L., Rousseau, A., Perrot, R., Montero-Menei, C.N., Castro, G.R., Menei, P., 2019. A new glioblastoma cell trap for implantation after surgical resection. Acta Biomaterialia 84, 268–279. https://doi.org/10.1016/j.actbio.2018.11.027

Awada, H., Paris, F., Pecqueur, C., 2023. Exploiting radiation immunostimulatory effects to improve glioblastoma outcome. Neuro-Oncology 25, 433–446. https://doi.org/10.1093/neuonc/noac239

Azarin, S.M., Yi, J., Gower, R.M., Aguado, B.A., Sullivan, M.E., Goodman, A.G., Jiang, E.J., Rao, S.S., Ren, Y., Tucker, S.L., Backman, V., Jeruss, J.S., Shea, L.D., 2015. In vivo capture and label-free detection of early metastatic cells. Nature Communications 6, 8094. https://doi.org/10.1038/ncomms9094

Bailly, C., Vidal, A., Bonnemaire, C., Kraeber-Bodéré, F., Chérel, M., Pallardy, A., Rousseau, C., Garcion, E., Lacoeuille, F., Hindré, F., Valable, S., Bernaudin, M., Bodet-Milin, C., Bourgeois, M., 2019. Potential for Nuclear Medicine Therapy for Glioblastoma Treatment. Front Pharmacol 10, 772. https://doi.org/10.3389/fphar.2019.00772

Bian, X., Yang, S., Chen, J., Ping, Y., Zhou, X., Wang, Q., Jiang, X., Gong, W., Xiao, H., Du, L., Chen, Z., Zhao, W., Shi, J., Wang, J.M., 2007. PREFERENTIAL EXPRESSION OF CHEMOKINE RECEPTOR CXCR4 BY HIGHLY MALIGNANT HUMAN GLIOMAS AND ITS ASSOCIATION WITH POOR PATIENT SURVIVAL. Neurosurgery 61, 570–579. https://doi.org/10.1227/01.NEU.0000290905.53685.A2

Bianco, A.M., Uno, M., Oba-Shinjo, S.M., Clara, C.A., de Almeida Galatro, T.F., Rosemberg, S., Teixeira, M.J., Nagahashi Marie, S.K., 2015. CXCR7 and CXCR4 Expressions in Infiltrative Astrocytomas and Their Interactions with HIF1α Expression and IDH1 Mutation. Pathol. Oncol. Res. 21, 229–240. https://doi.org/10.1007/s12253-014-9813-7

Birzu, C., French, P., Caccese, M., Cerretti, G., Idbaih, A., Zagonel, V., Lombardi, G., 2021. Recurrent Glioblastoma: From Molecular Landscape to New Treatment Perspectives. Cancers 13, 47. https://doi.org/10.3390/cancers13010047

Bladergroen, B.A., Siebum, B., Siebers-Vermeulen, K.G.C., Van Kuppevelt, T.H., Poot, A.A., Feijen, J., Figdor, C.G., Torensma, R., 2009. In vivo recruitment of hematopoietic cells using stromal cell-derived factor 1 alpha-loaded heparinized three-dimensional collagen scaffolds. Tissue Eng Part A 15, 1591–1599. https://doi.org/10.1089/ten.tea.2008.0348

Bleul, C.C., Fuhlbrigge, R.C., Casasnovas, J.M., Aiuti, A., Springer, T.A., 1996. A highly efficacious lymphocyte chemoattractant, stromal cell-derived factor 1 (SDF-1). Journal of Experimental Medicine 184, 1101–1109. https://doi.org/10.1084/jem.184.3.1101

Boyé, K., Pujol, N., D Alves, I., Chen, Y.-P., Daubon, T., Lee, Y.-Z., Dedieu, S., Constantin, M., Bello, L., Rossi, M., Bjerkvig, R., Sue, S.-C., Bikfalvi, A., Billottet, C., 2017. The role of CXCR3/LRP1 cross-talk in the invasion of primary brain tumors. Nat Commun 8, 1571. https://doi.org/10.1038/s41467-017-01686-y

Calatozzolo, C., Canazza, A., Pollo, B., Di Pierro, E., Ciusani, E., Maderna, E., Salce, E., Sponza, V., Frigerio, S., Di Meco, F., Schinelli, S., Salmaggi, A., 2011. Expression of the new CXCL12 receptor, CXCR7, in gliomas. Cancer Biology & Therapy 11, 242–253. https://doi.org/10.4161/cbt.11.2.13951

Cavo, M., Serio, F., Kale, N.R., D'Amone, E., Gigli, G., Mercato, L.L. del, 2020. Electrospun nanofibers in cancer research: from engineering of in vitro 3D cancer models to therapy. Biomater. Sci. 8, 4887–4905. https://doi.org/10.1039/D0BM00390E

Chatterjee, S., Behnam Azad, B., Nimmagadda, S., 2014. Chapter Two - The Intricate Role of CXCR4 in Cancer, in: Pomper, M.G., Fisher, P.B. (Eds.), Advances in Cancer Research, Emerging Applications of Molecular Imaging to Oncology. Academic Press, pp. 31–82. https://doi.org/10.1016/B978-0-12-411638-2.00002-1

Cheng, L., Huang, Z., Zhou, W., Wu, Q., Donnola, S., Liu, J.K., Fang, X., Sloan, A.E., Mao, Y., Lathia, J.D., Min, W., McLendon, R.E., Rich, J.N., Bao, S., 2013. Glioblastoma Stem Cells Generate Vascular Pericytes to Support Vessel Function and Tumor Growth. Cell 153, 139–152. https://doi.org/10.1016/j.cell.2013.02.021

Cinamon, G., Shinder, V., Alon, R., 2001. Shear forces promote lymphocyte migration across vascular endothelium bearing apical chemokines. Nat Immunol 2, 515–522. https://doi.org/10.1038/88710

Daubon, T., Guyon, J., Raymond, A.-A., Dartigues, B., Rudewicz, J., Ezzoukhry, Z., Dupuy, J.-W., Herbert, J.M.J., Saltel, F., Bjerkvig, R., Nikolski, M., Bikfalvi, A., 2019. The invasive proteome of glioblastoma revealed by laser-capture microdissection. Neuro-Oncology Advances 1, vdz029. https://doi.org/10.1093/noajnl/vdz029

De Vleeschouwer, S. (Ed.), 2017. Glioblastoma. Codon Publications, Brisbane (AU).

De Vleeschouwer, S., Bergers, G., 2017. Glioblastoma: To Target the Tumor Cell or the Microenvironment?, in: De Vleeschouwer, S. (Ed.), Glioblastoma. Codon Publications, Brisbane (AU).

Dirkse, A., Golebiewska, A., Buder, T., Nazarov, P.V., Muller, A., Poovathingal, S., Brons, N.H.C., Leite, S., Sauvageot, N., Sarkisjan, D., Seyfrid, M., Fritah, S., Stieber, D., Michelucci, A., Hertel, F., Herold-Mende, C., Azuaje, F., Skupin, A., Bjerkvig, R., Deutsch, A., Voss-Böhme, A., Niclou, S.P., 2019. Stem cell-associated heterogeneity in Glioblastoma results from intrinsic tumor plasticity shaped by the microenvironment. Nat Commun 10, 1–16. https://doi.org/10.1038/s41467-019-09853-z

Djoudi, A., Molina-Peña, R., Ferreira, N., Ottonelli, I., Tosi, G., Garcion, E., Boury, F., 2022. Hyaluronic Acid Scaffolds for Loco-Regional Therapy in Nervous System Related Disorders. International Journal of Molecular Sciences 23, 12174. https://doi.org/10.3390/ijms232012174

Domanska, U.M., Kruizinga, R.C., Nagengast, W.B., Timmer-Bosscha, H., Huls, G., de Vries, E.G.E., Walenkamp, A.M.E., 2013. A review on CXCR4/CXCL12 axis in oncology: No place to hide. European Journal of Cancer 49, 219–230. https://doi.org/10.1016/j.ejca.2012.05.005

Esencay, M., Newcomb, E.W., Zagzag, D., 2010. HGF upregulates CXCR4 expression in gliomas via NF-κB: Implications for glioma cell migration. J Neurooncol 99, 33–40. https://doi.org/10.1007/s11060-010-0111-2

Fan, Z., Zhang, F., Liu, T., Zuo, B.Q., 2014. Effect of hyaluronan molecular weight on structure and biocompatibility of silk fibroin/hyaluronan scaffolds. Int J Biol Macromol 65, 516–523. https://doi.org/10.1016/j.ijbiomac.2014.01.058

Fermas, S., Gonnet, F., Sutton, A., Charnaux, N., Mulloy, B., Du, Y., Baleux, F., Daniel, R., 2008. Sulfated oligosaccharides (heparin and fucoidan) binding and dimerization of stromal cell-derived factor-1 (SDF-1/CXCL 12) are coupled as evidenced by affinity CE-MS analysis. Glycobiology 18, 1054–1064. https://doi.org/10.1093/glycob/cwn088

Ferroli, P., Schiariti, M., Finocchiaro, G., Salmaggi, A., Castiglione, M., Acerbi, F., Tringali, G., Farinotti, M., Broggi, M., Roberto, C., Maccagnano, E., Broggi, G., 2013. Operability of glioblastomas: "sins of action" versus "sins of non-action." Neurol Sci 34, 2107–2116. https://doi.org/10.1007/s10072-013-1345-5

Gallet, C., Clavreul, A., Bernard, F., Menei, P., Lemée, J.-M., 2022. Frontal aslant tract in the non-dominant hemisphere: A systematic review of anatomy, functions, and surgical applications. Frontiers in Neuroanatomy 16.

Gaspar, L.E., Fisher, B.J., Macdonald, D.R., Leber, D.V., Halperin, E.C., Schold, S.C., Cairncross, J.G., 1992. Supratentorial malignant glioma: Patterns of recurrence and implications for external beam local treatment. International Journal of Radiation Oncology*Biology*Physics 24, 55–57. https://doi.org/10.1016/0360-3016(92)91021-E

Gil-Moreno, A., Alonso-Alconada, L., Díaz-Feijoo, B., Domingo, S., Vilar, A., Hernández, A., Gilabert, J., Llueca, A., Torné, A., de Santiago, J., Carbonell-Socias, M., Lago, V., Arias, E., Sampayo, V., Siegrist, J., Chipirliu, A., Sánchez-Iglesias, J.L., Pérez-Benavente, A., Padilla-Iserte, P., Santacana, M., Matias-Guiu, X., Abal, M., Lopez-Lopez, R., 2021. M-TRAP: Safety and performance of metastatic tumor cell trap device in advanced ovarian cancer patients. Gynecologic Oncology 161, 681–686. https://doi.org/10.1016/j.ygyno.2021.03.022

Hattermann, K., Held-Feindt, J., Lucius, R., Müerköster, S.S., Penfold, M.E.T., Schall, T.J., Mentlein, R., 2010. The Chemokine Receptor CXCR7 Is Highly Expressed in Human Glioma Cells and Mediates Antiapoptotic Effects. Cancer Research 70, 3299–3308. https://doi.org/10.1158/0008-5472.CAN-09-3642

Hattermann, K., Mentlein, R., Held-Feindt, J., 2012. CXCL12 mediates apoptosis resistance in rat C6 glioma cells. Oncology Reports 27, 1348–1352. https://doi.org/10.3892/or.2012.1674

Herrlinger, U., Tzaridis, T., Mack, F., Steinbach, J.P., Schlegel, U., Sabel, M., Hau, P., Kortmann, R.-D., Krex, D., Grauer, O., Goldbrunner, R., Schnell, O., Bähr, O., Uhl, M., Seidel, C., Tabatabai, G., Kowalski, T., Ringel, F., Schmidt-Graf, F., Suchorska, B., Brehmer, S., Weyerbrock, A., Renovanz, M., Bullinger, L., Galldiks, N., Vajkoczy, P., Misch, M., Vatter, H., Stuplich, M., Schäfer, N., Kebir, S., Weller, J., Schaub, C., Stummer, W., Tonn, J.-C., Simon, M., Keil, V.C., Nelles, M., Urbach, H., Coenen, M., Wick, W., Weller, M., Fimmers, R., Schmid, M., Hattingen, E., Pietsch, T., Coch, C., Glas, M., 2019. Lomustine-temozolomide combination therapy versus standard temozolomide therapy in patients with newly diagnosed glioblastoma with methylated MGMT promoter (CeTeG/NOA–09): a randomised, open-label, phase 3 trial. The Lancet 393, 678–688. https://doi.org/10.1016/S0140-6736(18)31791-4

Holland, E.C., 2000. Glioblastoma multiforme: The terminator. Proc Natl Acad Sci U S A 97, 6242–6244.

Hu, X., Shmelev, K., Sun, L., Gil, E.-S., Park, S.-H., Cebe, P., Kaplan, D.L., 2011. Regulation of Silk Material Structure by Temperature-Controlled Water Vapor Annealing. Biomacromolecules 12, 1686–1696. https://doi.org/10.1021/bm200062a

Jain, A., Betancur, M., Patel, G.D., Valmikinathan, C.M., Mukhatyar, V.J., Vakharia, A., Pai, S.B., Brahma, B., MacDonald, T.J., Bellamkonda, R.V., 2014. Guiding intracortical brain tumour cells to an extracortical cytotoxic hydrogel using aligned polymeric nanofibres. Nature Mater 13, 308–316. https://doi.org/10.1038/nmat3878

Kanu, O.O., Mehta, A., Di, C., Lin, N., Bortoff, K., Bigner, D.D., Yan, H., Adamson, D.C., 2009. Glioblastoma multiforme: a review of therapeutic targets. Expert Opinion on Therapeutic Targets 13, 701–718. https://doi.org/10.1517/14728220902942348

Kasapidou, P.M., Montullé, E.L. de, Dembélé, K.-P., Mutel, A., Desrues, L., Gubala, V., Castel, H., 2021. Hyaluronic acid-based hydrogels loaded with chemoattractant and anticancer drug – new formulation for attracting and tackling glioma cells. Soft Matter 17, 10846–10861. https://doi.org/10.1039/D1SM01003D

Kaur, B., Barth, R.F., 2009. Rat Glioma Models for Preclinical Evaluation of Novel Therapeutic and Diagnostic Modalities, in: Meir, E.G. (Ed.), CNS Cancer: Models, Markers, Prognostic Factors, Targets, and Therapeutic Approaches, Cancer Drug Discovery and Development. Humana Press, Totowa, NJ, pp. 181–205. https://doi.org/10.1007/978-1-60327-553-8_10

Kerhervé, M., Rosińska, S., Trillet, K., Zeinaty, A., Feyeux, M., Nedellec, S., Gavard, J., 2022. Neuropilin-1 modulates the 3D invasive properties of glioblastoma stem-like cells. Frontiers in Cell and Developmental Biology 10.

Kunikowska, J., Morgenstern, A., Pełka, K., Bruchertseifer, F., Królicki, L., 2022. Targeted alpha therapy for glioblastoma. Frontiers in Medicine 9.

Laguri, C., Sadir, R., Rueda, P., Baleux, F., Gans, P., Arenzana-Seisdedos, F., Lortat-Jacob, H., 2007. The Novel CXCL12γ Isoform Encodes an Unstructured Cationic Domain Which Regulates Bioactivity and Interaction with Both Glycosaminoglycans and CXCR4. PLOS ONE 2, e1110. https://doi.org/10.1371/journal.pone.0001110

Lan, X., Jörg, D.J., Cavalli, F.M.G., Richards, L.M., Nguyen, L.V., Vanner, R.J., Guilhamon, P., Lee, L., Kushida, M.M., Pellacani, D., Park, N.I., Coutinho, F.J., Whetstone, H., Selvadurai, H.J., Che, C., Luu, B., Carles, A., Moksa, M., Rastegar, N., Head, R., Dolma, S., Prinos, P., Cusimano, M.D., Das, S., Bernstein, M., Arrowsmith, C.H., Mungall, A.J., Moore, R.A., Ma, Y., Gallo, M., Lupien, M., Pugh, T.J., Taylor, M.D., Hirst, M., Eaves, C.J., Simons, B.D., Dirks, P.B., 2017. Fate mapping of human glioblastoma reveals an invariant stem cell hierarchy. Nature 549, 227–232. https://doi.org/10.1038/nature23666

Le Rhun, E., Oppong, F.B., van den Bent, M., Wick, W., Brandes, A.A., Taphoorn, M.JB., Platten, M., Idbaih, A., Clement, P.M., Preusser, M., Golfinopoulos, V., Gorlia, T., Weller, M., 2023. Thrombocytopenia limits the feasibility of salvage lomustine chemotherapy in recurrent glioblastoma: a secondary analysis of EORTC 26101. European Journal of Cancer 178, 13–22. https://doi.org/10.1016/j.ejca.2022.10.006

Lecointre, C., Desrues, L., Joubert, J.E., Perzo, N., Guichet, P.-O., Le Joncour, V., Brulé, C., Chabbert, M., Leduc, R., Prézeau, L., Laquerrière, A., Proust, F., Gandolfo, P., Morin, F., Castel, H., 2015. Signaling switch of the urotensin II vasosactive peptide GPCR: prototypic chemotaxic mechanism in glioma. Oncogene 34, 5080–5094. https://doi.org/10.1038/onc.2014.433

Lemée, J.-M., Clavreul, A., Menei, P., 2015. Intratumoral heterogeneity in glioblastoma: don't forget the peritumoral brain zone. Neuro-Oncology 17, 1322–1332. https://doi.org/10.1093/neuonc/nov119

Liau, L.M., Ashkan, K., Brem, S., Campian, J.L., Trusheim, J.E., Iwamoto, F.M., Tran, D.D., Ansstas, G., Cobbs, C.S., Heth, J.A., Salacz, M.E., D'Andre, S., Aiken, R.D., Moshel, Y.A., Nam, J.Y., Pillainayagam, C.P., Wagner, S.A., Walter, K.A., Chaudhary, R., Goldlust, S.A., Lee, I.Y., Bota, D.A., Elinzano, H., Grewal, J., Lillehei, K., Mikkelsen, T., Walbert, T., Abram, S., Brenner, A.J., Ewend, M.G., Khagi, S., Lovick, D.S., Portnow, J., Kim, L., Loudon, W.G., Martinez, N.L., Thompson, R.C., Avigan, D.E., Fink, K.L., Geoffroy, F.J., Giglio, P., Gligich, O., Krex, D., Lindhorst, S.M., Lutzky, J., Meisel, H.-J., Nadji-Ohl, M., Sanchin, L., Sloan, A., Taylor, L.P., Wu, J.K., Dunbar, E.M., Etame, A.B., Kesari, S., Mathieu, D., Piccioni, D.E., Baskin, D.S., Lacroix, M., May, S.-A., New, P.Z., Pluard, T.J., Toms, S.A., Tse, V., Peak, S., Villano, J.L., Battiste, J.D., Mulholland, P.J., Pearlman, M.L., Petrecca, K., Schulder, M., Prins, R.M., Boynton, A.L., Bosch, M.L., 2023. Association of Autologous Tumor Lysate-Loaded Dendritic Cell Vaccination With Extension of Survival Among Patients With Newly Diagnosed and Recurrent Glioblastoma: A Phase 3 Prospective Externally Controlled Cohort Trial. JAMA Oncology 9, 112–121. https://doi.org/10.1001/jamaoncol.2022.5370

Lin, K.H., Rutter, J.C., Xie, A., Pardieu, B., Winn, E.T., Bello, R.D., Forget, A., Itzykson, R., Ahn, Y.-R., Dai, Z., Sobhan, R.T., Anderson, G.R., Singleton, K.R., Decker, A.E., Winter, P.S.,

Locasale, J.W., Crawford, L., Puissant, A., Wood, K.C., 2020. Using antagonistic pleiotropy to design a chemotherapy-induced evolutionary trap to target drug resistance in cancer. Nature Genetics 52, 408–417. https://doi.org/10.1038/s41588-020-0590-9

Liu, C.J., Schaettler, M., Blaha, D.T., Bowman-Kirigin, J.A., Kobayashi, D.K., Livingstone, A.J., Bender, D., Miller, C.A., Kranz, D.M., Johanns, T.M., Dunn, G.P., 2020. Treatment of an aggressive orthotopic murine glioblastoma model with combination checkpoint blockade and a multivalent neoantigen vaccine. Neuro-Oncology 22, 1276–1288. https://doi.org/10.1093/neuonc/noaa050

Lukas, R.V., Wainwright, D.A., Ladomersky, E., Sachdev, S., Sonabend, A.M., Stupp, R., 2019. Newly Diagnosed Glioblastoma: A Review on Clinical Management. Oncology (Williston Park) 33, 91–100.

Mathivet, T., Bouleti, C., Van Woensel, M., Stanchi, F., Verschuere, T., Phng, L.-K., Dejaegher, J., Balcer, M., Matsumoto, K., Georgieva, P.B., Belmans, J., Sciot, R., Stockmann, C., Mazzone, M., De Vleeschouwer, S., Gerhardt, H., 2017. Dynamic stroma reorganization drives blood vessel dysmorphia during glioma growth. EMBO Molecular Medicine 9, 1629–1645. https://doi.org/10.15252/emmm.201607445

Molina-Peña, R., Tudon-Martinez, J.C., Aquines-Gutiérrez, O., 2020. A Mathematical Model of Average Dynamics in a Stem Cell Hierarchy Suggests the Combinatorial Targeting of Cancer Stem Cells and Progenitor Cells as a Potential Strategy against Tumor Growth. Cancers 12, 2590. https://doi.org/10.3390/cancers12092590

Monneau, Y., Arenzana-Seisdedos, F., Lortat-Jacob, H., 2016. The sweet spot: how GAGs help chemokines guide migrating cells. Journal of Leukocyte Biology 99, 935–953. https://doi.org/10.1189/jlb.3MR0915-440R

Motz, G.T., Coukos, G., 2013. Deciphering and Reversing Tumor Immune Suppression. Immunity 39, 61–73. https://doi.org/10.1016/j.immuni.2013.07.005

Murphy, J.W., Cho, Y., Sachpatzidis, A., Fan, C., Hodsdon, M.E., Lolis, E., 2007. Structural and Functional Basis of CXCL12 (Stromal Cell-derived Factor-1α) Binding to Heparin*. Journal of Biological Chemistry 282, 10018–10027. https://doi.org/10.1074/jbc.M608796200

Nagasawa, T., 2006. Microenvironmental niches in the bone marrow required for B-cell development. Nat Rev Immunol 6, 107–116. https://doi.org/10.1038/nri1780

Najberg, M., Haji Mansor, M., Taillé, T., Bouré, C., Molina-Peña, R., Boury, F., Cenis, J.L., Garcion, E., Alvarez-Lorenzo, C., 2020. Aerogel sponges of silk fibroin, hyaluronic acid and heparin for soft tissue engineering: Composition-properties relationship. Carbohydrate Polymers 237, 116107. https://doi.org/10.1016/j.carbpol.2020.116107

Nakayama, H., Kusumoto, C., Nakahara, M., Fujiwara, A., Higashiyama, S., 2018. Semaphorin 3F and Netrin-1: The Novel Function as a Regulator of Tumor Microenvironment. Frontiers in Physiology 9.

Nasarre, C., Koncina, E., Labourdette, G., Cremel, G., Roussel, G., Aunis, D., Bagnard, D., 2009. Neuropilin-2 acts as a modulator of Sema3A-dependent glioma cell migration. Cell Adhesion & Migration 3, 383–389. https://doi.org/10.4161/cam.3.4.9934

Nduom, E.K., Weller, M., Heimberger, A.B., 2015. Immunosuppressive mechanisms in glioblastoma. Neuro Oncol 17 Suppl 7, vii9–vii14. https://doi.org/10.1093/neuonc/nov151

Olivier, C., Oliver, L., Lalier, L., Vallette, F.M., 2021. Drug Resistance in Glioblastoma: The Two Faces of Oxidative Stress. Frontiers in Molecular Biosciences 7.

Pirovano, G., Jannetti, S.A., Carter, L.M., Sadique, A., Kossatz, S., Guru, N., Demétrio De Souza França, P., Maeda, M., Zeglis, B.M., Lewis, J.S., Humm, J.L., Reiner, T., 2020. Targeted Brain Tumor Radiotherapy Using an Auger Emitter. Clinical Cancer Research 26, 2871–2881. https://doi.org/10.1158/1078-0432.CCR-19-2440

Porath, K.A., Regan, M.S., Griffith, J.I., Jain, S., Stopka, S.A., Burgenske, D.M., Bakken, K.K., Carlson, B.L., Decker, P.A., Vaubel, R.A., Dragojevic, S., Mladek, A.C., Connors, M.A., Hu, Z., He, L., Kitange, G.J., Gupta, S.K., Feldsien, T.M., Lefebvre, D.R., Agar, N.Y.R., Eckel-Passow, J.E., Reilly, E.B., Elmquist, W.F., Sarkaria, J.N., 2022. Convection enhanced delivery of EGFR targeting antibody-drug conjugates Serclutamab talirine and Depatux-M in glioblastoma patient-derived xenografts. Neuro-Oncology Advances 4, vdac130. https://doi.org/10.1093/noajnl/vdac130

Pouget, J.-P., Constanzo, J., 2021. Revisiting the Radiobiology of Targeted Alpha Therapy. Frontiers in Medicine 8.

Reifenberger, G., Wirsching, H.-G., Knobbe-Thomsen, C.B., Weller, M., 2017. Advances in the molecular genetics of gliomas — implications for classification and therapy. Nat Rev Clin Oncol 14, 434–452. https://doi.org/10.1038/nrclinonc.2016.204

Rich, P.H., 1988. The Origin of Ecosystems by Means of Subjective Selection, in: Pomeroy, L.R., Alberts, J.J. (Eds.), Concepts of Ecosystem Ecology, Ecological Studies. Springer, New York, NY, pp. 19–27. https://doi.org/10.1007/978-1-4612-3842-3_2

Rodrigues, J.C., Gonzalez, G.C., Zhang, L., Ibrahim, G., Kelly, J.J., Gustafson, M.P., Lin, Y., Dietz, A.B., Forsyth, P.A., Yong, V.W., Parney, I.F., 2010. Normal human monocytes exposed to glioma cells acquire myeloid-derived suppressor cell-like properties. Neuro-Oncology 12, 351–365. https://doi.org/10.1093/neuonc/nop023

Rong, Y., Durden, D.L., Van Meir, E.G., Brat, D.J., 2006. "Pseudopalisading" necrosis in glioblastoma: a familiar morphologic feature that links vascular pathology, hypoxia, and angiogenesis. J Neuropathol Exp Neurol 65, 529–539. https://doi.org/10.1097/00005072-200606000-00001

Sadir, R., Baleux, F., Grosdidier, A., Imberty, A., Lortat-Jacob, H., 2001. Characterization of the Stromal Cell-derived Factor-1α-Heparin Complex*. Journal of Biological Chemistry 276, 8288–8296. https://doi.org/10.1074/jbc.M008110200

Sadir, R., Imberty, A., Baleux, F., Lortat-Jacob, H., 2004. Heparan sulfate/heparin oligosaccharides protect stromal cell-derived factor-1 (SDF-1)/CXCL12 against proteolysis induced by CD26/dipeptidyl peptidase IV. J Biol Chem 279, 43854–43860. https://doi.org/10.1074/jbc.M405392200

Salazar, N., Muñoz, D., Kallifatidis, G., Singh, R.K., Jordà, M., Lokeshwar, B.L., 2014. The chemokine receptor CXCR7 interacts with EGFR to promote breast cancer cell proliferation. Molecular Cancer 13, 198. https://doi.org/10.1186/1476-4598-13-198

Sanai, N., 2012. Emerging operative strategies in neurosurgical oncology. Curr Opin Neurol 25, 756–766. https://doi.org/10.1097/WCO.0b013e32835a2574

Santagata, S., Ieranò, C., Trotta, A.M., Capiluongo, A., Auletta, F., Guardascione, G., Scala, S., 2021. CXCR4 and CXCR7 Signaling Pathways: A Focus on the Cross-Talk Between Cancer Cells and Tumor Microenvironment. Frontiers in Oncology 11.

Seeger, F.H., Rasper, T., Fischer, A., Muhly-Reinholz, M., Hergenreider, E., Leistner, D.M., Sommer, K., Manavski, Y., Henschler, R., Chavakis, E., Assmus, B., Zeiher, A.M., Dimmeler, S., 2012. Heparin Disrupts the CXCR4/SDF-1 Axis and Impairs the Functional Capacity of Bone Marrow–Derived Mononuclear Cells Used for Cardiovascular Repair. Circulation Research 111, 854–862. https://doi.org/10.1161/CIRCRESAHA.112.265678

Séhédic, D., Chourpa, I., Tétaud, C., Griveau, A., Loussouarn, C., Avril, S., Legendre, C., Lepareur, N., Wion, D., Hindré, F., Davodeau, F., Garcion, E., 2017. Locoregional Confinement and Major Clinical Benefit of 188Re-Loaded CXCR4-Targeted Nanocarriers in an Orthotopic Human to Mouse Model of Glioblastoma. Theranostics 7, 4517–4536. https://doi.org/10.7150/thno.19403

Sehgal, A., Keener, C., Boynton, A.L., Warrick, J., Murphy, G.P., 1998. CXCR-4, a chemokine receptor, is overexpressed in and required for proliferation of glioblastoma tumor cells. J Surg Oncol 69, 99–104. https://doi.org/10.1002/(sici)1096-9098(199810)69:2<99::aid-jso10>3.0.co;2-m

Semmler, L., Naghilou, A., Millesi, F., Wolf, S., Mann, A., Stadlmayr, S., Mero, S., Ploszczanski, L., Greutter, L., Woehrer, A., Placheta-Györi, E., Vollrath, F., Weiss, T., Radtke, C., 2023. Silk-in-Silk Nerve Guidance Conduits Enhance Regeneration in a Rat Sciatic Nerve Injury Model. Advanced Healthcare Materials 12, 2203237. https://doi.org/10.1002/adhm.202203237

Shimizu, A., Nakayama, H., Wang, P., König, C., Akino, T., Sandlund, J., Coma, S., Italiano, J.E., Mammoto, A., Bielenberg, D.R., Klagsbrun, M., 2013. Netrin-1 Promotes Glioblastoma Cell Invasiveness and Angiogenesis by Multiple Pathways Including Activation of RhoA, Cathepsin B, and cAMP-response Element-binding Protein*. Journal of Biological Chemistry 288, 2210–2222. https://doi.org/10.1074/jbc.M112.397398

Silbergeld, D.L., Chicoine, M.R., 1997. Isolation and characterization of human malignant glioma cells from histologically normal brain. J Neurosurg 86, 525–531. https://doi.org/10.3171/jns.1997.86.3.0525

Staneva, R., Burla, F., Koenderink, G.H., Descroix, S., Vignjevic, D.M., Attieh, Y., Verhulsel, M., 2018. A new biomimetic assay reveals the temporal role of matrix stiffening in cancer cell invasion. MBoC 29, 2979–2988. https://doi.org/10.1091/mbc.E18-01-0068

Staros, J.V., Wright, R.W., Swingle, D.M., 1986. Enhancement by N-hydroxysulfosuccinimide of water-soluble carbodiimide-mediated coupling reactions. Analytical Biochemistry 156, 220–222. https://doi.org/10.1016/0003-2697(86)90176-4

Stummer, W., Pichlmeier, U., Meinel, T., Wiestler, O.D., Zanella, F., Reulen, H.-J., 2006. Fluorescence-guided surgery with 5-aminolevulinic acid for resection of malignant glioma: a randomised controlled multicentre phase III trial. The Lancet Oncology 7, 392–401. https://doi.org/10.1016/S1470-2045(06)70665-9

Stupp, R., Mason, W.P., van den Bent, M.J., Weller, M., Fisher, B., Taphoorn, M.J.B., Belanger, K., Brandes, A.A., Marosi, C., Bogdahn, U., Curschmann, J., Janzer, R.C., Ludwin, S.K., Gorlia, T., Allgeier, A., Lacombe, D., Cairncross, J.G., Eisenhauer, E., Mirimanoff, R.O., 2005. Radiotherapy plus Concomitant and Adjuvant Temozolomide for Glioblastoma. New England Journal of Medicine 352, 987–996. https://doi.org/10.1056/NEJMoa043330

Tokoyoda, K., Egawa, T., Sugiyama, T., Choi, B.-I., Nagasawa, T., 2004. Cellular Niches Controlling B Lymphocyte Behavior within Bone Marrow during Development. Immunity 20, 707–718. https://doi.org/10.1016/j.immuni.2004.05.001

Tsurkan, M.V., Levental, K.R., Freudenberg, U., Werner, C., 2010. Enzymatically degradable heparin-polyethylene glycol gels with controlled mechanical properties. Chem. Commun. 46, 1141–1143. https://doi.org/10.1039/B921616B

Vyas, M., Müller, R., Pogge von Strandmann, E., 2017. Antigen Loss Variants: Catching Hold of Escaping Foes. Frontiers in Immunology 8.

Wang, S., Chen, C., Li, J., Xu, X., Chen, W., Li, F., 2020. The CXCL12/CXCR4 axis confers temozolomide resistance to human glioblastoma cells via up-regulation of FOXM1. Journal of the Neurological Sciences 414, 116837. https://doi.org/10.1016/j.jns.2020.116837

Woerner, B.M., Warrington, N.M., Kung, A.L., Perry, A., Rubin, J.B., 2005. Widespread CXCR4 Activation in Astrocytomas Revealed by Phospho-CXCR4-Specific Antibodies. Cancer Research 65, 11392–11399. https://doi.org/10.1158/0008-5472.CAN-05-0847

Wu, Y.-C., Tang, S.-J., Sun, G.-H., Sun, K.-H., 2016. CXCR7 mediates TGFβ1-promoted EMT and tumor-initiating features in lung cancer. Oncogene 35, 2123–2132. https://doi.org/10.1038/onc.2015.274

Yamahara, T., Numa, Y., Oishi, T., Kawaguchi, T., Seno, T., Asai, A., Kawamoto, K., 2010. Morphological and flow cytometric analysis of cell infiltration in glioblastoma: a comparison of autopsy brain and neuroimaging. Brain Tumor Pathol 27, 81–87. https://doi.org/10.1007/s10014-010-0275-7

Yu, J., Wang, A., Tang, Z., Henry, J., Li-Ping Lee, B., Zhu, Y., Yuan, F., Huang, F., Li, S., 2012. The effect of stromal cell-derived factor-1α/heparin coating of biodegradable vascular grafts on the recruitment of both endothelial and smooth muscle progenitor cells for accelerated regeneration. Biomaterials 33, 8062–8074. https://doi.org/10.1016/j.biomaterials.2012.07.042

Zagzag, D., Esencay, M., Mendez, O., Yee, H., Smirnova, I., Huang, Y., Chiriboga, L., Lukyanov, E., Liu, M., Newcomb, E.W., 2008. Hypoxia- and vascular endothelial growth factor-induced stromal cell-derived factor-1alpha/CXCR4 expression in glioblastomas: one plausible explanation of Scherer's structures. Am J Pathol 173, 545–560. https://doi.org/10.2353/ajpath.2008.071197

Zhou, Y., Larsen, P.H., Hao, C., Yong, V.W., 2002. CXCR4 is a major chemokine receptor on glioma cells and mediates their survival. J Biol Chem 277, 49481–49487. https://doi.org/10.1074/jbc.M206222200

Annexes

6. Annexes

6.1. Publications

1. **Molina-Peña R**, Ferreira NH, Roy C, Roncali L, Najberg M, Avril S, Zarur M, Bourgeois W, Ferreirós A, Lucchi C, Cavallieri F, Hindré F, Tosi G, Biagini G, Valzania F, Berger F, Abal M, Rousseau A, Boury F, Alvarez-Lorenzo C, Garcion E. Implantable SDF-1α-loaded silk fibroin hyaluronic acid aerogel sponges as an instructive component of the glioblastoma ecosystem: Between chemoattraction and tumor shaping into resection cavities. **Acta Biomater. 2024** Jan 1;173:261-282.

   https://doi.org/10.1016/j.actbio.2023.10.022

3. Djoudi A, **Molina-Peña R**, Ferreira N, Ottonelli I, Tosi G, Garcion E, Boury F. Hyaluronic Acid Scaffolds for Loco-Regional Therapy in Nervous System Related Disorders**. IJMS. 2022**; 23(20):12174.

   https://doi.org/10.3390/ijms232012174

4. **Molina-Peña R**, Haji Mansor M, Najberg M, Thomassin JM, Gueza B, Alvarez-Lorenzo C, Garcion E, Jérôme C, Boury F. Nanoparticle-containing electrospun nanofibrous scaffolds for sustained release of SDF-1α. **Int J Pharm. 2021** Dec 15;610:121205.

   https://doi.org/10.1016/j.ijpharm.2021.121205

5. Toullec C, Le Bideau J, Geoffroy V, Halgand B, Buchtova N, **Molina-Peña R**, Garcion E, Avril S, Sindji L, Dube A, Boury F, Jérôme C. Curdlan-Chitosan Electrospun Fibers as Potential Scaffolds for Bone Regeneration. **Polymers. 2021** Feb 10;13(4):526.

   https://doi.org/10.3390/polym13040526

6. Najberg M, Haji Mansor M, Taillé T, Bouré C, **Molina-Peña R**, Boury F, Cenis JL, Garcion E, Alvarez-Lorenzo C. Aerogel sponges of silk fibroin, hyaluronic acid and heparin for soft tissue engineering: Composition-properties relationship**. Carbohydr Polym. 2020** Jun 1;237:116107.

   https://doi.org/10.1016/j.carbpol.2020.116107

6.2. Communications

1. **Molina-Pena R**, Ferreira N, Rousseau A, Najberg M, Roy C, Roncali L, Avril S, Haji-Mansor M, Boury F, Alvarez-Lorenzo C, Garcion E. **Silk-fibroin interventional nano-trap for the treatment of glioblastoma: translation of an ecological trap in cancer therapy.** ***Présentation orale***. New Modalities in Cancer Imaging and Therapy workshop, Cancéropôle Grand Ouest, October 2022, Erquy, France.
2. Ferreira NH, **Molina-Pena R**, Najberg M, Roy C, Roncali L, Avril S, Mansor MH, Boury F, Alvarez-Lorenzo C, Garcion E. **P10.14.A Caught in a trap: Silk fibroin, hyaluronic acid, and heparin sponges to capture residual glioblastoma cells**, Neuro-Oncology, Volume 24, Issue Supplement_2, September 2022, Pages ii51–ii52, https://doi.org/10.1093/neuonc/noac174.179
3. **Molina-Pena R**, Ferreira N, Rousseau A, Najberg M, Roy C, Roncali L, Avril S, Haji-Mansor M, Boury F, Alvarez-Lorenzo C, Garcion E. **Silk-fibroin interventional nano-trap for the treatment of glioblastoma**. ***Présentation orale***. Journées Scientifiques SFR Santé, Juin 2022, Université d'Angers.
4. **Molina-Pena R**, Ferreira N, Rousseau A, Najberg M, Roy C, Roncali L, Avril S, Haji-Mansor M, Boury F, Alvarez-Lorenzo C, Garcion E. **Silk-fibroin interventional nano-trap for the treatment of glioblastoma**. ***Présentation orale***. Journées Scientifiques Ecole Doctorale Biologie Santé, Université Bretagne-Loire, Décembre 2021, Brest, France.
5. **Molina-Peña R**, Haji Mansor M, Najberg M, Thomassin JM, Gueza B, Alvarez-Lorenzo C, Garcion E, Jérôme C, Boury F. **Nanoparticle-containing electrospun nanofibrous scaffolds for sustained release of SDF-1α. Poster**. French Society for Nanomedicine. 7th Annual Meeting, December 2021, Angers, France. sciencesconf.org:sfnano2021:373094.
6. **Molina-Peña R**, Ferreira N, Najberg M, Roy C, Roncali L, Rousseau A, Avril S, Haji Mansor M, Boury F, Alvarez-Lorenzo C, Garcion E. **Silk-fibroin interventional nano-trap for the treatment of glioblastoma. Poster**. French Society for Nanomedicine. 7th Annual Meeting, December 2021, Angers, France. sciencesconf.org:sfnano2021:373079.

Titre : Développement et évaluation de bioimplants interventionnels comme pièges à cellules cancéreuses pour le traitement du glioblastome

Mots clés : Piège à tumeur ; Glioblastome ; Maladie résiduelle ; Bioimplants ; Fibroïne de soie ; Acide hyaluronique ; Nanofibres de chitosane ; Nanoparticules de PLGA-PEG

Résumé : La récidive du glioblastome (GB) est aujourd'hui inévitable. L'échec de la thérapie conventionnelle est dû à la résistance des cellules tumorales et à l'administration sous-optimale des principes actives qui n'arrivent pas à cibler les cellules infiltrantes dans 2 cm de la cavité de résection. Une approche alternative consiste plutôt à attirer la cible à un leurre en modifiant des éléments de l'écosystème du GB. Autrement dit, en remplaçant la niche de choix des cellules residuelles, il pourrait devenir possible de les diriger vers un emplacement contrôlé pour une élimination loco-régionale plus poussée. Ici, l'axe SDF-1α/CXCR4 s'est avéré diriger la migration des cellules U87MG-CXCR4+ humaines. Nous émettons l'hypothèse qu'il est possible d'attirer les cellules de glioblastome infiltrantes dans un piège en implantant un échafaudage à l'intérieur de la cavité de résection. À cette fin, deux nouveaux échafaudages implantables libérant du SDF-1α ont été développés et évalués en tant que pièges à cellules de GB. Le premier échafaudage est une éponge de fibroïne de soie avec de l'acide hyaluronique et de l'héparine, où l'héparine agit comme un agent de complexation pour le SDF-1α. Le second est constitué de SDF-1α nanoprécipité encapsulé dans des nanoparticules de PLGA-PEG intégrées dans une matrice fibreuse de chitosane électrofilé. Dans la présente thèse, la caractérisation et les interactions *in vitro* avec les cellules GB pour les deux systèmes, ainsi que l'évaluation *in vivo* des éponges ont été réalisées. Les avantages et les inconvénients des deux systèmes sont discutés et des perspectives sur le piégeage des cellules GB sont présentées.

Title: Development and evaluation of interventional bioimplants as cancer cell traps for the treatment of glioblastoma.

Keywords: Cancer cell trap, Glioblastoma, Residual disease, Bioimplants, Silk fibroin, Hyaluronic acid, Sponges, Chitosan nanofibers, PLGA-PEG nanoparticles, SDF-1α

Abstract: Glioblastoma (GB) recurrence is inevitable today. It occurs within 2 cm from the resection cavity due to infiltrative GB cells. The failure of conventional therapy is due to tumor cell resistance and sub-optimal delivery of therapeutics. An alternative approach to directly targeting those "guerrilla cells" is rather to convey the target to a lure by altering elements of the GB ecosystem. That is, by substituting GB remnant cell's niche of choice, it might become possible to direct them toward a controlled location for further locoregional elimination. Here, the SDF-1α/CXCR4 axis was found to direct the migration of human U87MG-CXCR4+ cells. We hypothesize that it might be possible to attract GB cells in a trap by implanting a scaffold inside the resection cavity. For this purpose, two novel implantable scaffolds releasing SDF-1α were developed and evaluated as GB cell traps. The first is a silk fibroin with hyaluronic acid and heparin sponge, where heparin acts as a complexation agent for SDF-1α. The second consists of nanoprecipitated SDF-1α encapsulated in PLGA-PEG nanoparticles embedded in an electrospun chitosan fibrous matrix. Here, the characterization and *in vitro* interactions with GB cells for both systems, and the *in vivo* evaluation of sponges were performed. The advantages and disadvantages of both systems are discussed, and perspectives on the trapping of GB cells are presented.